THE UNIVERSITY *of* EDINBURGH

Bacterial Confinement in Microfluidic Micro-Environments

Daniel Taylor

Doctor of Philosophy
The University of Edinburgh
October 6, 2019

Abstract

Microfluidic droplet systems have shown great promise in the study of biological systems. In this thesis I explore the application of a microfluidic droplet system to the study of small bacterial populations and their growth response to antibiotics.

This thesis comprises of three primary results sections. The first section details the development and fabrication of a custom microfluidic system. This microfluidic system is designed to study the growth dynamics of small *Escherichia coli* (*E. coli*) bacterial communities. The second section presents an image processing and analysis workflow that is designed to be used in conjunction with the microfluidic device to extract quantitative growth data of confined bacterial communities with single cell precision. The third section details a study that uses the microfluidic system to measure the growth dynamics of *E. coli* communities encapsulated within microfluidic droplets whilst uninhibited and under the effect of the antibiotic streptomycin.

In the first section, I present the development, design and fabrication of a two-part microfluidic device that is later used to study the growth dynamics of *E. coli* bacteria. The first part of the microfluidic device consists of droplet generating microfluidic geometry that is designed to encapsulate small communities of *E. coli* bacteria (typically 1-5 cells in size) within microfluidic droplets around 30 μm in diameter. The second part of the microfluidic device is composed of a microfluidic reservoir that is designed to store microfluidic droplets. By imaging the droplets in the storage reservoir with a combination of brightfield and fluorescence microscopy, the growth dynamics of the encapsulated bacterial communities can be described.

In the second section of the thesis, I present the development and operating principles of my image processing and analysis workflow. This workflow automatically extracts quantitative bacterial growth data from a gridded array of brightfield and fluorescence microscopy images taken across the microfluidic device during

experimentation. The analysis algorithm is capable of processing upwards of 200 fields of view across 80 time frames. This makes it possible to detect, track and measure the size of upwards of 1000 encapsulated bacterial communities with single cell precision. Droplet boundaries are detected using brightfield microscopy images and each droplet is tracked from one time step to the next using a modified particle tracking algorithm. Bacterial community sizes are measured by counting individual bacteria in thresholded fluorescence microscopy images.

In the final section of this thesis, a study of *E. coli* bacteria was conducted using the microfluidic device. Small communities of bacteria, typically 1-5 cells in size, were confined in microfluidic droplets and observed for 8 hours. The bacteria were grown in the absence of antibiotic, as well as in the presence of the antibiotic streptomycin at various concentrations. A number of metrics of the growth dynamics are extracted from the study and compared with traditional bulk growth techniques.

It is shown that in the absence of streptomycin, the final droplet population size distributions feature extended tails due to large, fast growing bacterial populations. The tails of these distributions are reduced in length in the presence of streptomycin at a concentration below the Minimum Inhibitory Concentration (MIC). A positive correlation is found between initial and final bacterial population size, however this correlation is weak, indicating a highly stochastic growth process. It is also shown that at moderate streptomycin concentrations both around and above the MIC, some bacterial populations are inhibited in a non-lytic manner, whilst other populations underwent lysis. It is also shown that at moderate antibiotic concentrations around the MIC value, there is a bias against bacterial lysis in droplets with large populations. Finally, at low antibiotic concentrations below the MIC, it is shown that some bacterial populations are inhibited but not lysed, whereas some populations are not inhibited.

The microfluidic device and image analysis workflow described in this thesis is a novel experimental system with widespread applicability. The system is able to partition an aqueous solution into a large number of small, compartmentalised liquid volumes and analyse these volumes using both brightfield and fluorescence time-lapse microscopy. This could be used to study the population dynamics of a variety of bacterial strains, and could also be used to explore more general questions relating to stochastic cell biology where encapsulation is experimentally beneficial.

Lay Summary

Traditionally, bacterial research is carried out by growing bacteria in containers between 0.1 ml and 100 ml in volume. This means that when we study how a bacterial population behaves under certain conditions, we are actually studying the behaviour of a bacterial population of over 10 million cells.

This is a problem as bacterial infections can begin with just a single bacterial cell, and single bacterial cells may respond differently to a drug or antibiotic when compared to a large population of 10 million cells.

In this thesis, we designed and fabricated a specialised experimental tool that allowed us to place hundreds of small bacterial populations in microscopic droplets less than one tenth of a millimeter in diameter. By doing this, we were able to measure how small populations of bacteria grew in the presence of an antibiotic. This thesis can be separated into 3 main sections.

The first section of this thesis is dedicated to the design, development and fabrication of a specialised experimental system that allows us to place small bacterial populations in microscopic droplets and study them. This system is made up of two separate devices. The first device places the small bacterial populations in the microscopic droplets at a rate of up to 40 droplets per second. The second device stores these microscopic droplets in an imaging chamber. Once the droplets are stored in the imaging chamber they can then be imaged using a microscope so that the number of bacteria in each droplet can be counted and tracked over time. This experimental system was designed specifically so that it can be fabricated and operated by scientists that have not used this type of system before.

The bacteria that are stored in the droplets have been modified so that they glow brightly when a special type of light is shone upon them. By taking images of the bacteria as they glow, it is possible to count the number of bacteria in each droplet. In the second section of this thesis, we discuss the development of a

computer program that we wrote to automatically count the number of bacteria in over 1000 microscopic droplets for up to 8 hours.

The final section of this thesis presents the results of an experiment that utilised the experimental system and computer program that were covered in sections one and two. We first measured how quickly bacterial populations grew in the microscopic droplets. It was found that on average the bacterial populations grew at a similar rate to bacterial populations that were grown using traditional techniques, this meant that the bacteria were healthy and able to reproduce in the microscopic droplets. An antibiotic called streptomycin was then added to the droplets at a variety of concentrations. Once streptomycin was added, we studied how the droplet populations grew at each antibiotic concentration. It was found that streptomycin affected the droplet populations differently depending on its concentration. It was also found that even at the same streptomycin concentration some droplets reacted differently to the antibiotic. It is currently not known why streptomycin affects certain droplets differently, but it is hoped that with further experiments we might be able to understand this behaviour and even predict it.

The experimental system designed in this thesis allow measurements of bacterial populations to be taken that are not possible using many other techniques. It is possible that this system could be used to study different types of bacteria, different types of antibiotics, or even study different biological systems where it would be useful to store things in microscopic droplets.

Declaration

I declare that this thesis was composed by myself, that the work contained herein is my own except where explicitly stated otherwise in the text, and that this work has not been submitted for any other degree or professional qualification except as specified.

(*Daniel Taylor, October 2019*)

Acknowledgements

First and foremost, I would like to thank my principal supervisors Simon and Rosalind for their guidance and direction. You were always approachable, enthusiastic and endlessly insightful. I could not have asked for better mentors. I would also like to thank Nia, you brought a fresh perspective and optimistic energy to my work, it has been a pleasure handing over my project to you. I would like to thank the population dynamics group for countless stimulating discussions that always proved to be enlightening and thought-provoking.

Next, I'd like to thank and acknowledge Angela Dawson for her unending patience, help and guidance in the biophysics lab, Louis Berridge for his support in all matters Matlab, Peter Lomax for his help fabricating microfluidic device masters, and the Scottish Microelectronics Centre for allowing me to use their facilities. I would also like to thank the SOFI CDT for accepting me onto their stellar doctorate program, Patrick Warren and Unilever for their support, and the EPSRC who funded my project.

Outside of this project but equally responsible for its completion, I would like to thank my friends in Edinburgh. Weightlifters and physicists alike, you brought me joy and contentment in more ways than you could possibly know. I would also like to thank all of my gaming friends across the country for their incredible capacity to help me unwind, and SOFI cohort one for being so much more than just work colleagues.

Finally, I'd like to thank my family, especially my parents, for their unwavering support and encouragement. None of this would have been possible without you.

Contents

Abstract i

Lay Summary iii

Declaration v

Acknowledgements vi

Contents vii

List of Figures xi

List of Tables xvi

1 Introduction 1

2 Background 4

2.1 Introduction 4

2.2 Bacteria 5

2.2.1 *Escherichia coli* 5

2.2.2 Bacterial growth 7

2.2.3 Metabolism and respiration 10

2.3 Antibiotics 11

2.3.1 Antibiotic resistance 12

2.3.2 Ribosome targeting antibiotics and streptomycin 13

2.4 Microscopy 15

2.4.1 Introduction 15

2.4.2 Microscopy fundamentals 15

2.4.3 Brightfield microscopy 17

2.4.4 Fluorescence microscopy 18

2.4.5 Fluorophores 19

Fluorescent proteins 19

2.4.6 State-of-the-art Microscopy . . . 20
2.5 Continuous flow microfluidics . . . 24
2.5.1 Microfluidic theory . . . 24
Dimensionless Quantities . . . 25
Hydraulic Resistance . . . 26
2.5.2 Continuous flow microfluidics - general applications . . . 27
2.5.3 Continuous flow microfluidics - biological applications . . . 28
2.6 Droplet microfluidics . . . 30
2.6.1 Introduction . . . 30
2.6.2 Theory . . . 31
Dimensionless Quantities . . . 31
2.6.3 Droplet generation . . . 32
T-junction . . . 32
Flow-focusing junction . . . 35
2.6.4 Droplet microfluidics - general applications . . . 37
2.6.5 Droplet microfluidics - biological applications . . . 38
Biological applications using microfluidic droplets . . . 38
Biological applications studying cells encapsulated within microfluidic droplets . . . 39
Biological applications studying bacteria-antibiotic interactions within microfluidic droplets . . . 42
2.7 Summary . . . 44

3 Methods, Materials and Fabrication 45
3.1 Introduction . . . 45
3.2 Materials . . . 46
3.2.1 Polydimethysiloxane . . . 46
3.2.2 Carrier oil . . . 47
3.2.3 Droplet surfactant . . . 47
3.2.4 Device hydrophobicity . . . 48
Heat treatment . . . 48
Chemical treatment . . . 51
3.2.5 *E. coli* . . . 52
3.2.6 M9 growth media . . . 52
3.2.7 Agarose Plates . . . 53
3.2.8 Streptomycin . . . 54
3.3 Fabricating a PDMS-based microfluidic device . . . 54
3.3.1 Overview . . . 54

3.3.2 Fabrication protocol - photomask and master mould 55
3.3.3 Fabrication protocol - PDMS-based microfluidic device . . 56
3.4 Equipment 57
3.4.1 Microscope and camera 57
3.4.2 Microfluidic device mount 58
3.4.3 Syringe pumps 59
3.4.4 Plasma oven 60
3.5 Concluding remarks 60

4 Designing a Microfluidic System for the Encapsulation of Bacterial Populations 61
4.1 Introduction 61
4.1.1 Continuous flow microfluidics versus droplet microfluidics . 62
4.2 Designing a microfluidic device 62
4.2.1 Technical detail 63
4.3 General design principles 64
4.3.1 Consider channel dimensions and their transitions 64
Match channel transitions 64
Oversized outlet channels 65
4.3.2 Large inlet/outlet size 65
4.3.3 Minimise hydraulic resistance 65
4.3.4 Separate designs 66
4.3.5 Device support 66
4.4 Device design evolution 67
4.4.1 Microfluidic design 1 67
4.4.2 Microfluidic design 2 72
4.5 Microfluidic design 3 75
4.6 Concluding Remarks 79

5 Image Processing Workflow - From Microscope to Data 81
5.1 Chapter aims and structure 81
5.1.1 Introduction 82
5.1.2 Imaging bacteria in droplets 82
5.1.3 Existing bioimage-processing solutions 84
5.1.4 Microscope output / image processing input 85
5.2 Image processing protocol 87
5.2.1 Stage 1 - image validation and stitching 87
5.2.2 Stage 2 - Brightfield image droplet detection and tracking 91

5.2.3 Stage 3 - Fluorescence image thresholding and bacteria counting . . . 94
Image thresholding . . . 94
Threshold optimisation . . . 94
Bacterial count algorithm . . . 98
Addendum - integrated fluorescence intensity . . . 99
5.2.4 Final data output . . . 100
5.3 Concluding remarks . . . 100
5.4 Designing and fabricating a microfluidic system: thoughts and conclusions . . . 101

6 Device Validation **103**
6.1 Introduction . . . 103
6.1.1 Experimental identification numbers . . . 103
6.2 Bacterial counting errors . . . 104
6.2.1 Crowded droplets . . . 104
6.2.2 Bacterial aggregation . . . 106
Bacterial aggregation - observations in microfluidic droplets 106
Bacterial aggregation - causes and reduction . . . 108
6.2.3 Threshold optimisation and error estimation . . . 108
6.3 Droplet polydispersity . . . 112
6.4 Observation Delay . . . 114
6.5 Spatial correlation of growth . . . 116
6.6 Bacterial fluorescence does not imply life . . . 119
LIVE/DEAD staining . . . 120
6.7 Conclusions . . . 121

7 Encapsulated *E. coli* - a growth and inhibition study **123**
7.1 Introduction . . . 123
7.2 Experimental objectives . . . 123
7.3 Notable results . . . 125
7.4 Experimental protocol . . . 126
7.4.1 Device preparation, operation and image acquisition . . . 126
7.4.2 Image processing . . . 129
7.5 Growth of total bacterial population across all droplets . . . 129
7.5.1 Total population growth curves . . . 130
Results . . . 130
Discussion . . . 133

7.5.2 Total population growth rates and doubling times 135
Results 135
Discussion 137
Bulk growth measurements 138
7.5.3 Minimum inhibitory concentration 140
7.5.4 Analysis of individual droplet populations 140
7.6 Size distributions of bacterial populations growing in droplets . . 141
7.6.1 Initial population size distribution vs. final population size distribution 141
Results 141
Discussion 146
7.6.2 Time evolution of population size distribution 149
Results 149
Discussion 151
7.6.3 Final population size - measured vs. predicted 153
Results 153
Discussion 158
7.7 Time of droplet death 162
Results 162
Discussion 164
7.8 Time of droplet death versus initial population size 169
Results 169
Discussion 171
7.9 Initial droplet population size as a growth predictor 173
7.9.1 Initial droplet population versus final droplet population . 173
Results 173
Discussion 175
7.9.2 Box-plot analysis 176
Results 176
Discussion 178
7.10 Summary 179
7.11 Concluding remarks 180

8 Conclusions **182**
8.1 Summary 182
8.2 Outlook 185

Bibliography **187**

List of Figures

(2.1) Plot: example growth curve of a bacterial population. 9
(2.2) Diagram: ray diagrams of the optical train for a finite tube length microscope and an infinity corrected microscope. . . . 16
(2.3) Diagram: ray diagrams illustrating the imaging focal plane and the illumination focal plane. 17
(2.4) Diagram: an inverted microscope and a filter cube containing a dichroic mirror. 18
(2.5) Diagram: schematic of a confocal microscope. 21
(2.6) Diagram: STORM superresolution imaging sequence. 22
(2.7) Image: conventional fluorescence microscope images compared to superresolution images. 23
(2.8) Diagram: schematic of a T-junction microfluidic droplet generating geometry. 33
(2.9) Diagram: schematic of a flow-focusing microfluidic droplet generating geometry. 35

(3.1) Image: PDMS contact angle measurements. 50
(3.2) Image: aquapel precipitation observed in the channels of our microfluidic system. 51
(3.3) Diagram: the soft lithographic process used when fabricating a PDMS-based microfluidic device. 55
(3.4) Image: microfluidic device mount. 59

(4.1) Diagram: geometries that constitute the first microfluidic design. 68
(4.2) Diagram: microfluidic outlet design of our first generation device. 69
(4.3) Image: high speed microscopy images of our first generation flow-focusing microfluidic droplet generator. 70
(4.4) Image: microscopy image of droplets pinned against the flat surface of support pillars. 71

(4.5) Diagram: geometry of the second microfluidic design. 73
(4.6) Diagram: geometries of the three sub-designs that constitute the third microfluidic device design. 76
(4.7) Diagram: geometries of the inlets of the third generation reservoirs. 77
(4.8) Image: microfluidic master used to fabricate our final microfluidic design. 78
(4.9) Image: final microfluidic device design. 79

(5.1) Diagram: microfluidic droplets in the droplet generating device and the reservoir device. 84
(5.2) Image: microscopy images in both brightfield and fluorescence channels that are out of focus. 89
(5.3) Image: microscopy images in both brightfield and fluorescence channels that show non-circular droplets. 89
(5.4) Image: microscopy images in both brightfield and fluorescence channels that contain fluorescent debris. 90
(5.5) Image: example frame of an experimental sub-section, shown in brightfield. 91
(5.6) Image: microscopy images showing examples of both acceptable and unacceptable boundary detection in the image analysis workflow. 93
(5.7) Image: processed images showing the importance of a well optimised threshold value. 96
(5.8) Diagram: example data array output from an experimental run. 100

(6.1) Image: example microscopy images of droplet populations that are counted correctly and incorrectly dependent on the density of their encapsulate bacterial population. 105
(6.2) Image: microscopy images showing a bacterial aggregate forming in a microfluidic droplet. 106
(6.3) Plot: scatter plot showing the initial population distribution Fano factors for each experimental run as a function of streptomycin concentration. 115
(6.4) Plot: S values plotted as a function of inter-droplet distance. 117

(7.1) Plot: total population growth curves of RJA002 E. coli populations encapsulated in microfluidic droplets, grown in M9 minimal media (part one). 132
(7.2) Plot: total population growth curves of RJA002 E. coli populations encapsulated in microfluidic droplets, grown in M9 minimal media (part two). 133
(7.3) Plot: logarithmically scaled ensemble growth curves of RJA002 E. coli populations encapsulated in microfluidic droplets, grown in M9 minimal media. 136
(7.4) Plot: multiwell plate growth curves of RJA002 *E. coli* grown in M9 minimal media supplemented with glucose. 138
(7.5) Plot: histograms showing the population distributions of droplets at t = 0 mins and t = 474 mins, grown in M9 minimal media (part one). 142
(7.6) Plot: histograms showing the population distributions of droplets at t = 0 mins and t = 474 mins, grown in M9 minimal media (part two). 143
(7.7) Plot: histograms showing the population distributions of droplets at t = 0 mins and t = 234 mins, grown in M9 minimal media (part three). 144
(7.8) Plot: bar plots of the initial and final mean droplet population size for each experimental run. 145
(7.9) Plot: scatter plot showing the Fano factor for each experimental run as a function of streptomycin concentration. . . . 146
(7.10) Plot: colour plots showing the evolution of population size distribution across the course of an experimental run (part one). 150
(7.11) Plot: colour plots showing the evolution of population size distribution across the course of an experimental run (part two). 151
(7.12) Plot: example growth curves of individual droplets populations. 152
(7.13) Plot: measured and predicted final droplet population distributions of RJA002 E. coli populations encapsulated in microfluidic droplets, grown in M9 minimal media. Difference in droplet frequency between the measured and the predicted distributions (part one). 155

(7.14) Plot: measured and predicted final droplet population distributions of RJA002 E. coli populations encapsulated in microfluidic droplets, grown in M9 minimal media. Difference in droplet frequency between the measured and the predicted distributions (part two). 156
(7.15) Plot: measured and predicted final droplet population distributions of RJA002 E. coli populations encapsulated in microfluidic droplets, grown in M9 minimal media. Difference in droplet frequency between the measured and the predicted distributions (part three). 157
(7.16) Plot: histograms showing how droplet death times are distributed over the course of an experimental run (part one). . 163
(7.17) Plot: histograms showing how droplet death times are distributed over the course of an experimental run (part two). . 164
(7.18) Plot: scatter plots showing droplet time of death as a function of initial droplet population size (part one). 170
(7.19) Plot: scatter plots showing droplet time of death as a function of initial droplet population size (part two). 171
(7.20) Plot: scatter plots showing droplet time of death as a function of initial droplet population size, highlighting an area of the graph where no droplet deaths are observed. 172
(7.21) Plot: Scatter plots of initial droplet population sizes vs. Final droplet population size. 174
(7.22) Plot: box plots of initial droplet population sizes vs. final droplet population sizes. 177

List of Tables

(6.1) Summary of all experimental identification numbers and the colour chosen for each experiment to enhance readability throughout this thesis. Strep. Conc. gives the final concentration (w/w) of streptomycin used in each experimental run once added to the M9 growth medium. 104
(6.2) Error measurements for all experimental runs, at t = 0, 114 and 234 minutes. Experimental runs are ordered by streptomycin concentration: green experiments are grown in the absence of streptomycin whilst red experiments are grown at high streptomycin concentrations. 110
(6.3) Measured and calculated droplet radii values for droplet monodispersity testing, each ID represents a full experimental run. 113

(7.1) Summary of details of each experimental run. Strep. Conc. gives the final concentration (w/w) of streptomycin used in each experimental run once added to the M9 growth medium. Droplet count refers to the number of droplets detected within the whole microfluidic device, averaged across all time frames. 124
(7.2) Quantitative summary of ensemble growth behaviour for all experimental runs. *Experimental runs 2.50 - 1 and 50.0 - 1 were ended after 4 hours due to large-scale loss of visible bacteria. 134
(7.3) Calculated growth rates and doubling times of experiments that exhibited net bacterial growth. 136
(7.4) Summary of measured gradient and R^2 values for the data presented in figure 7.21. 174
(7.5) Quantitative summary of data displayed in box plots shown in figure 7.22 178

Chapter 1

Introduction

The discovery of antibiotics transformed modern medicine. With their widespread introduction in the early 1940's, they provided effective treatment to many diseases prevalent at the time[1]. Since then, the list of known antibiotic compounds has expanded massively due to extensive research and their revolutionary positive impact on clinical outcomes. At present, antibiotics underpin the treatment of almost all bacterial infections and are vital in complex clinical procedures such as highly invasive surgeries and chemotherapy. Whilst global antibiotic consumption was not originally tracked or quantified, it is known that antibiotic use was initially accelerated due to their effectiveness at treating *cocci* bacterial infections during World War II[2]. This increase in antibiotic use continued throughout the twentieth century, and statistics show that antibiotic consumption from 2000-2015 increased by 39%[3].

Unfortunately, because of this increase in antibiotic use, the prevalence of bacterial infections that are resistant to antibiotics has similarly skyrocketed. As the rate of antibiotic discovery has slowed over the last 20-30 years, the rate at which bacteria are becoming resistant to these antibiotics has not. It has been suggested that we are currently in the depths of an antibiotic crisis and may be fast approaching a regression back to the "pre-antibiotic" era due to a lack of antibiotics that are able to treat resistant infections. Evidence suggests that healthcare costs are likely to rise rapidly as we require newer, more complex and more expensive therapies for extended hospital admissions[4]: this is unsustainable in the long run.

As such, continued and renewed effort into antibiotic research is increasingly necessary; by furthering our understanding of how antibiotics work and their impact on bacterial populations, it is hoped that the impending clinical crisis can be averted.

Antibiotic research is usually conducted using bulk growth techniques. This means that when bacterial populations are cultured they are grown and studied in large volume containers, such as conical flasks. These methods of bulk culture mask the true heterogeneity of a bacterial population, as individual cells within a given population can vary significantly in their morphology and behaviour. This means that any quantitative measurement extracted from a large population cultured using bulk growth techniques will be an ensemble-average of the entire population. This naturally extends to measurements detailing antibiotic inhibition. This is relevant as clinical infections can begin with just a handful of bacteria from the same bacterial strain in a small biological niche such as the interior of a host cell. The success or failure of the infection or the antibiotic treatment may rest on the dynamics and responses of just a few highly heterogeneous bacteria, as opposed to the ensemble behaviour of a large population.

The aim of the work completed in this thesis was to develop and fabricate a device that encapsulates small bacterial populations within individual, non-interacting environments that mimic *in vivo* biological niches such as eukaryotic cell interiors. This was achieved using a custom-designed microfluidic system that encapsulated bacterial populations within monodisperse emulsion droplets less than 100 μm in diameter. These emulsion droplets were then incubated and imaged using bright-field and fluorescence microscopy. Using these microscopy images, each droplet was tracked over time and its respective bacterial population was measured. By studying large numbers of small bacterial populations simultaneously, we aimed to develop a system that could extract statistical information regarding the heterogeneity of the response of bacterial populations to antibiotic agents.

- **Chapter 2** provides background and context for the work completed in this thesis. An overview of bacterial growth and biological microscopy is given. The basic principles behind continuous flow and droplet-based microfluidics are outlined and previous work in the field is discussed.

- **Chapter 3** details the materials, methods, equipment and protocols used explicitly in the fabrication and use of our microfluidic system. Emphasis is placed on why each material was chosen in relation to the outlined research objectives. Experimental preparation methodologies are also discussed.

- **Chapter 4** outlines the iterative design process used in the development of a custom microfluidic system to be used in the encapsulation and incubation of small bacterial communities.

- **Chapter 5** introduces and summarises the Matlab-based image processing and analysis workflow that was developed to extract quantifiable data from our experimental system.

- **Chapter 6** reviews the testing and validation processes that were completed to ensure the accuracy and integrity of data generated using our microfluidic system.

- **Chapter 7** presents the results of a study into the effects of streptomycin on small *Escherichia coli* populations grown in microfluidic droplets. This study fully utilises the microfluidic system whose development was detailed in the first half of the thesis. The complete experimental protocol used for this study is also outlined.

- **Chapter 8** highlights the key outcomes and findings derived from the work completed in this thesis.

Chapter 2

Background

2.1 Introduction

In this chapter I will outline the ideas and theories that underpin the work completed in this thesis. Key concepts will be established that should allow the reader to correctly understand and interpret the results and methodologies presented in this research project.

Firstly, bacteria will be discussed, followed by an introduction to *Escherichia coli* and its role as a model organism in the field of microbiology. I will then provide an overview of bacterial growth dynamics, including a short introduction to traditional techniques that are used to measure bulk growth. After this, antibiotics will be introduced, focusing on a ribosome targeting antibiotic called streptomycin that is studied in this thesis.

Moving on from bacteria, I will pivot to microscopy. The fundamental operating principles of compound microscopes will then be reviewed before a more technical discussion outlining brightfield microscopy, fluorescence microscopy and biologically relevant fluorophores. After this, I will briefly discuss several pioneering microscopy techniques that are used in microbiological research.

The field of microfluidics will then be examined, beginning with an introduction to basic microfluidic theory. Current and historical applications of continuous flow microfluidics will be reviewed, with a focus on their use in microbiological research. The chapter will then end with an introduction to droplet-based microfluidics, a subset of microfluidic systems that have gained substantial traction

within the general field of microfluidics. The key principles involved in the development of droplet-based microfluidic devices will again be outlined, which will finally be followed by a review of common academic applications, focusing on microbiological research.

2.2 Bacteria

Bacteria are single-celled organisms that are members of the prokaryotic domain. Prokaryotes differ from other single-celled organisms in that they do not possess a membrane-enclosed nucleus[5] and they lack energy producing organelles[6]. Their DNA is exposed to and part of the soup-like internals of the bacterial cell that is also made up of proteins and other macromolecules. Bacterial species used as models in cell biology generally have volumes of around 0.4 - 3 μm^3, however bacterial species that are not used traditionally in the laboratory have been observed with average cell sizes that vary dramatically. For example, ultramicrobacteria have been observed with average volumes of 0.013 μm^3, whilst a single marine sediment–dwelling bacteria has been observed with a volume of 2.2 x 10^8 μm^3[7].

Despite their diminutive size, by virtue of sheer numbers, bacterial biomass outweighs all other life on earth combined[8]. Humans contain approximately 10x as many bacterial cells than human cells, and approximately 100x more bacterial genes than human genes[9]. Bacteria were first identified and studied in a clinical context due to their sometimes negative impact on human health. However, they do not simply exist to infect humans, indeed they exert powerful influences across all facets of the natural world.

2.2.1 *Escherichia coli*

Bacteria are classified as Gram-negative or Gram-positive (with a few exceptions that are not discussed here) based upon the structure of their cell envelope[10]. The cell envelope of Gram-negative bacteria consists of a thin layer (2-3 nm) of the polymer peptidoglycan sandwiched between the outer and inner membranes, whereas the cell envelope of Gram-positive bacteria consists of a much thicker layer (≈30 nm) of peptidoglycan but the outer membrane is absent.

Gram staining

Gram staining is a technique used to distinguish between Gram-positive and Gram-negative bacteria. The assay is named after Hans Christian Gram, who developed the technique in 1884 to distinguish bacterial cells from host tissue cells[11]. The process has three primary steps: cells are first stained using a crystal violet–iodine complex, they are then decolourised using ethanol and acetone before a safranin counterstain is applied. The cell wall structure of Gram-positive cells retains the iodine complex (rendering them a deep purple), whereas Gram-negative cells readily decolourise and are subsequently stained by the safranin (appearing pink)[12][13].

Escherichia coli (*E. coli*) is a rod shaped, Gram-negative bacteria around 2 μm in length and 1 μm in diameter. It typically inhabits the gastrointestinal tract of warm blooded animals, and it has been found to colonise the gut of a human infant within hours of being born[14]. *E. coli* is usually commensal and will co-exist within a human host without problem for many years[14]. It is generally the most prolific facultative anaerobe in the human gastrointestinal tract; however it is still not fully understood how and by what mechanisms *E. coli* occupies this niche so successfully and competitively when compared to other bacterial strains[14].

It could be argued that more is known about *E. coli* than any other organism on the planet, and it is because of this that the *E. coli* genome was one of the first candidates suggested for whole genome sequencing[15]. To emphasise this fact, Jacques Monod, Nobel prize winner famous for his "discoveries concerning genetic control of enzyme and virus synthesis", once claimed:

"All that is true of *E. coli* is also true of the elephant[1]"

E. coli, in particular the K12 strain, is the most common and popular model organism across the entire field of biology[16]. K12 was originally isolated in 1922 and rose to prominence for a number of reasons. Firstly, K12 is prototrophic and therefore easily to grown in defined growth media[17]. Secondly, early studies revealed that K12 was found to be capable of genetic recombination by both conjugation and transduction[18]. K12 is popular due to its historical prevalence,

[1] [translated] - "Tout ce qui est vrai pour le Colibacille est vrai pour l'éléphant"[16]

metabolic robustness and ease of use in the laboratory. Whole genome sequences are available for the two most common K12 variants: MG1655[15] and W3110[17]. MG1655 has been maintained as a standard laboratory strain save a small number of genetic manipulations. Of note, a mutation leads to pyrimidine starvation, resulting in a growth rate 10-15% slower in pyrimidine-free medium[19]. Furthermore, almost all K12 derivatives carry a mutation that results in the absence of O-antigen synthesis[15]. The O-antigen is a polysaccharide that is part of the lipopolysaccharide in the outer membrane of Gram-negative bacteria[20]. It is highly immunogenic, can be used as a receptor for certain bacteriophages, and it is a virulence determinant for the bacteria[21].

There is growing criticism of academia's fondness for K12 as critics argue that there is strong evidence that modern laboratory strains have diverged far from their original, free living ancestors. It is believed that with the introduction of modern high-throughput sequencing, K12 will be removed from its pedestal as the archetypal *E. coli* strain. It is hoped by some that *E. coli* in general will be better understood as just one of many model organisms in the greater context of bacterial diversity[16].

2.2.2 Bacterial growth

When a small bacterial population is exposed to a nutrient rich environment, it will undergo four broadly defined stages of growth. At the point of introduction to their nutrient rich environment, bacteria do not usually begin to divide straight away. Instead, they generally first optimise themselves for further growth, gaining mass as they upregulate protein and ribosome production to maximally exploit their new nutrient dense surroundings[22]. This initial period of little to no growth is called the lag phase.

Once the bacteria have successfully adjusted to their new surroundings they will begin to divide, and their rate of growth will increase as they enter what is known as the exponential or logarithmic growth phase. In this phase, growth is uninhibited by nutrient limitation or waste toxicity. Because of this the number of bacteria in the population (N) increases proportionally to N:

$$\frac{dN}{dt} = kN, \tag{2.1}$$

therefore the population size can be described by simple exponential growth:

$$N = N_0 e^{kt}, \tag{2.2}$$

where N_0 is the initial number of bacteria, t is the time elapsed and k is the specific growth rate. The doubling time of an exponentially dividing bacterial population can be obtained by dividing $ln(2)$ by k. Once the population begins to exhaust key nutrients in their environment (or waste accumulates to toxic levels), then the growth rate of the population will begin to decline and the population size plateaus. This third growth stage is known as the stationary phase. Eventually bacteria will start to die and the bacterial population size will begin to deplete. This final growth phase is known as the death phase. These growth phases can be clearly observed in a bacterial populations growth curve. See figure 2.1 for further information.

Optical Density

Optical density measurements are commonly used to assess the concentration of bacterial suspensions. According to the Beer-Lambert law, the attenuation of light passing through a sample is linked to the optical properties of the attenuating species in the sample material. With correct calibration, a turbidity measurement can therefore be taken to assess the concentration of bacteria in a bacterial suspension[23].

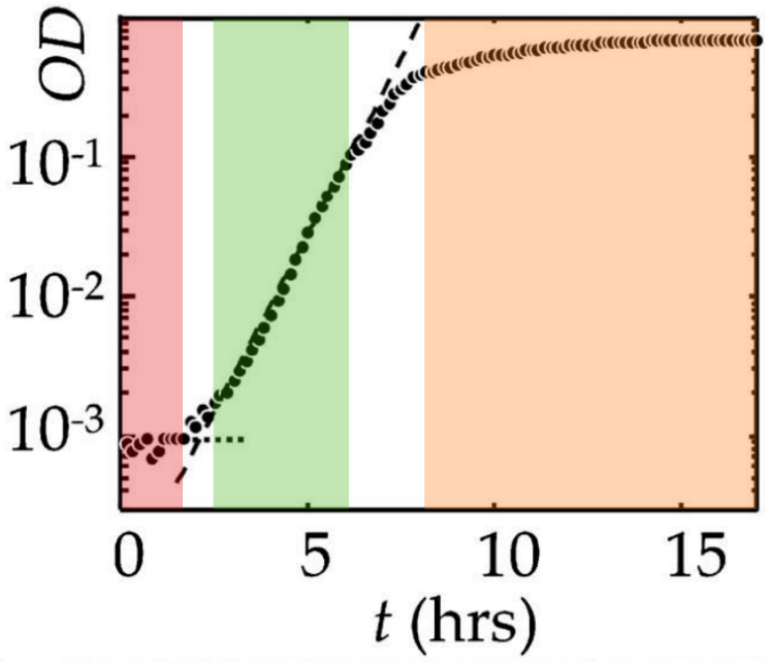

Figure 2.1 *Growth curve of an E. coli population, measured using Optical Density (OD) at 600nm. Log of population size is plotted versus time. The lag phase can be seen in the initial horizontal section of the graph (shown here in red), at this stage population size is unchanged from the initial inoculum. The exponential phase can be seen in the linearly increasing section of this plot (shown here in green), N_0 is defined as the population size at the start of the exponential growth phase. The stationary phase can be seen to begin as the curve levels off to become eventually horizontal (shown here in orange), indicating slower and slower bacterial growth. Adapted from [22].*

Bacterial growth can be quantified experimentally by culturing populations in liquid growth media. Liquid growth media is generally split into two categories: undefined and defined media. Undefined media does not have a well defined chemical composition. As an example, Lysogeny Broth (LB) is a common undefined media that is formulated using yeast extract. Defined media has a well defined chemical composition, this means it is formulated using a precise and controlled recipe of chemical compounds. Defined media is the preferred choice when conducting quantitative bacterial growth measurements as the same growth media can be formulated to the same specification in any laboratory using pure chemicals off the shelf, ensuring standardisation. Different formulations of defined media can be further categorised based on whether they are considered to be rich or poor. Rich media supports fast growth, whereas poor media supports slow growth. A nutrient molecule in rich media provides more energy than a nutrient molecule in poor media.

It is also important to consider the growth applications supported by the liquid media: LB is an ubiquitous undefined and rich liquid growth medium, but it is also auto-fluorescent and is therefore unsuitable for fluorescence based growth studies. In our work we used M9 minimal medium, this is a well defined and poor growth medium, this was chosen as slow growth was convenient when working with our experimental system.

2.2.3 Metabolism and respiration

Bacterial metabolism refers to the set of biochemical reactions that occur in a bacteria. This encompasses the reactions that break down substrate molecules, as well as the reactions that uptake and utilise compounds required for growth and maintenance of the cell[24]. Bacteria are highly specialised energy transformation systems that are able to generate high-energy compounds such as adenosine 5'-triphosphate (ATP) by breaking down substrate molecules. These high-energy compounds store energy in the form of phosphate bonds, which can then be easily processed to provide energy for many different cellular operations.

Across all bacteria, there are a wide variety of metabolic substrates and reactions that can be used to generate energy. Furthermore, a single bacteria can change the metabolic pathway it uses to extract energy dependent on its immediate environment and the availability of different nutrients[25]. Heterotrophic bacteria obtain their energy through the oxidation of organic compounds, such as carbohydrates, proteins and lipids. The carbohydrate glucose is most commonly used to study heterotrophic metabolism. Aerobic bacteria are able to oxidise glucose through the following chemical reaction:

$$C_6H_{12}O_6 + 6O_2 \longrightarrow 6CO_2 + 6H_2O + \text{energy},$$

Where glucose is oxidised completely to CO_2 and H_2O. In aerobic respiration, molecular O_2 acts as the electron acceptor. Practically, aerobic respiration is an efficient ($\approx$55%[24]) energy generation process that oxidises environmental organic substrates and produces primarily carbon dioxide and water.

2.3 Antibiotics

Antibiotics are defined as compounds that inhibit bacteria. Bactericidal antibiotics are defined as antibiotics that kill bacteria with an efficiency of >99.9%[26], whereas bacteriostatic antibiotics prevent further bacterial growth but do not cause cell death[27]. Antibiotics are able to target bacteria by inhibiting or disrupting processes that are unique to prokaryotic cells, such that the eukaryotic cells of the host are not affected. Although this sounds ideal, many bacteria are beneficial to the host's health and wellbeing. This means that a course of antibiotics can significantly change the internal distribution of useful bacteria within a host that are sensitive to a given antibiotic, and it was only recently realised that antibiotics can have long lasting effects on the infected host well beyond the time frame of the initial infection[5].

At the turn of the 20th century, antimicrobial agents were discovered by screening basic synthetic chemicals, with a focus on microbiological dyes and stains[28]. With the discovery of penicillin by Sir Alexander Fleming in 1928[29], these basic chemicals were superseded as a number of bacterial and fungal metabolites were proven to efficiently treat bacterial infections with minimal side-effects[30]. Beginning in the early 1940's, a number of protocols were established in the field of natural drug development and discovery, including the Waksman platform[31]: a screening strategy for the discovery of antibiotics using soil-dwelling bacteria. The method of determining an antibiotics minimum inhibitory concentration in rich media was also standardised during this time.

Minimum inhibitory concentration

The Minimum Inhibitory Concentration (MIC) of an antibiotic is defined as the minimum concentration required to inhibit visible growth of a bacteria after overnight incubation[32].

From the 1940's through to the mid-1960's, many new antibiotics were discovered in what is dubbed the 'golden age' of antibiotic discovery. It is during this time that the majority of known antibiotic classes were discovered[30]. By the mid-1960's antibiotic resistance was becoming a problem in the treatment of bacterial infections, whilst newly discovered antibiotics were becoming increasingly difficult to implement in a clinical environment due to negative pharmacological

or toxicological properties. The golden era of antibiotic discovery gave way to an era of medicinal chemistry, where improved synthetic versions of existing natural antibiotics were the main source of new antibiotics. Whilst lacking in revolutionary discovery, the antibiotic derivatives discovered during this time brought about lower doses, wider generality and the continued avoidance of resistance[30]. For reference, the quinolone class of antibiotics was discovered in the 1960's, it then took over 20 years for the next class of antibiotics to be discovered, with linezolid being approved for use in the United States in 2000[33]. From roughly 2000 through to 2015, antibiotic discovery methods were underpinned by genomic data and high-throughput screening technology, with a distinct focus on target-based antibiotics and the discovery of broad spectrum antibiotics. Whilst not a complete failure, this approach proved to be relatively unsuccessful and in recent years a paradigm shift has refocused efforts on complex combinatorial treatments that more accurately reflect the inherent complexity of *in vivo* bacterial infections. These screening approaches utilise unconventional and unique drug discovery strategies[34].

2.3.1 Antibiotic resistance

As discussed in chapter 1, antibiotic resistance is a global health issue that if left unchecked could have disastrous consequences. Antibiotic resistant bacterial strains were observed almost immediately after the introduction of the first antimicrobial agents[35]. *Streptoccoccus pyogenes* bacteria resistant to sulfonamide emerged in the late 1930's[2], whilst *Staphylococcus aureus* bacteria resistant to penicillin emerged in the late 1940's[36]. This was followed by streptomycin resistant *Mycobacterium tuberculosis*, that were observed just four years after streptomycins discovery[37]. Bacteria resistant to multiple antibiotics (*E. coli, Shigella, Salmonella*) were observed in the 1960's and 1970's[38], and since then the rate of antibiotic resistance has been consistently outpacing the rate of antibiotic discovery[1].

Some bacteria are intrinsically resistant to certain antibiotics by the nature of their physiology. For example, Gram-negative bacteria are generally more resistant to antibiotics, as many of these compounds are unable to cross their outer membrane[39]. Lipopeptide daptomycin is ineffective against Gram-negative bacteria, as the lower proportion of anionic phospholipids in the membrane of Gram-negative bacteria reduces the insertion of the antibiotic into the cell[40].

There are many mechanisms by which bacteria can develop or attain resistance to an antibiotic. These molecular mechanisms are encoded in the DNA of resistant bacteria, and there are multiple ways in which this DNA can be shared amongst bacteria[41]. These resistance mechanisms generally fall into one of three categories[41]. Firstly, bacteria can reduce the intracellular concentration of antibiotic, either by reducing the permeability of the cells membrane, or through active antibiotic efflux. Secondly, bacteria can alter the antibiotic target site through genetic mutation to reduce antibiotic affinity. Thirdly, bacteria can directly inactivate the antibiotic by either destroying the antibiotic molecule or modifying the structure of the antibiotic. An example of this third resistance mechanism was recently reported in *Campylobacter coli*, where genetic material was found that encoded six aminoglycoside-modifying enzymes that confered resistance to multiple aminoglycoside antibiotics[42].

Whilst understanding these molecular mechanisms gives us valuable insight into how bacteria respond to antibiotic agents, it is essential to recognise that microbiological processes (including those that govern antibiotic resistance) are inherently stochastic in nature. As such, it has been shown that antibiotic resistance is a heterogeneous property of a bacterial population[43]. It is critical that we understand this heterogeneity if we hope to effectively improve the clinical applications of both current and future antibiotics. It is the heterogeneous aspect of bacteria-antibiotic interaction that the research project presented in this thesis aims to explore.

2.3.2 Ribosome targeting antibiotics and streptomycin

The ribosome is the most complex piece of enzymatic machinery found in nature. Ribosomes exist within all living cells and their primary purpose is to synthesise proteins[44]. The bacterial ribosome consists of two primary subunits and more than 50 different protein and RNA components. The ubiquity of the bacterial ribosome makes it a prime target for antibiotic inhibition. Furthermore, whilst the eukaryotic ribosome is structurally similar to the bacterial, the size and exact makeup of each subunit is critically different[45]. This means that antibiotics that target bacterial ribosomes do not affect eukaryotic ribosomes, and therefore human cells.

Ribosomal protein synthesis can be divided into 4 primary stages. In the initiation phase, the large and small subunit of the ribosome assemble on a specific region of an mRNA molecule. In the subsequent elongation phase, the mRNA transcoded as it passes through the ribosome and a polypeptide chain is built. Once the ribosome encounters a stop codon, the elongation phase ends and the process undergoes termination. Once complete, the ribosome subunits detach and mRNA is released, completing the final recycling phase [46]. Ribosome targeting antibiotics bind to the ribosome and inhibit this protein synthesis, with the bulk of clinically relevant antibiotics disrupting the elongation stage[47].

Streptomycin is a bactericidal ribosome targeting antibiotic that binds irreversibly to the 30S ribosomal complex (the smaller ribosomal subunit consisting of ≈50,000 atoms larger than hydrogen). This binding inhibits the initiation stage of protein synthesis[48]. We chose to study bacterial inhibition by streptomycin in this research project as work completed by Greulich *et al.* suggested that *E. coli* may respond differently to streptomycin inhibition at the level of individual cells[48]. In this theoretical work, a bistable dependence of growth rate on antibiotic concentration is predicted at the individual cell level in the limit of near-irreversible antibiotic binding (as is the case with streptomycin). This means that across a distinct range of extracellular antibiotic concentrations, two stable growth rate states exist. In this bistable regime, a large fraction of the population grow at a stable rate, whilst a smaller sub-population grow at a comparably reduced rate.

This prediction of a bistable growth regime is purely theoretical, and no experimental evidence for its existence was presented by Greulich *et al.* This provided motivation for us to study streptomycin inhibition using our microfluidic system. We hoped that heterogenous growth behaviours may be experimentally observed and quantified using our microfluidic device, which is not possible to observe using traditional bulk growth techniques.

2.4 Microscopy

2.4.1 Introduction

Microscopy is an experimental technique that is utilised extensively in the work conducted in this thesis. Standard brightfield microscopy is used here in the detection of microfluidic droplet boundaries, whilst fluorescence microscopy is used when counting cells for the purpose of cell growth measurements. In this section I will discuss the basic principles behind brightfield microscopy, before moving onto fluorescence microscopy.

2.4.2 Microscopy fundamentals

The fundamental purpose of a microscope is to produce an image of an object that is too small to resolve with the naked eye. This is achieved by using a series of lenses to manipulate light travelling from a sample to an observer such that the observer perceives a magnified virtual image. A compound microscope attains this magnification using two lens systems, the eyepiece and the objective lenses.

Light is emitted from an illumination source (through a condenser lens) and passes through the sample. This light is then collected by an objective lens, which (after being passed through a tube lens) then forms the light into a magnified real intermediate image. The eye and eyepiece lens then operate in conjunction to form a real image on the retina. This is perceived as a magnified virtual image by the observer[49]. This arrangement can be seen in figure 2.2.

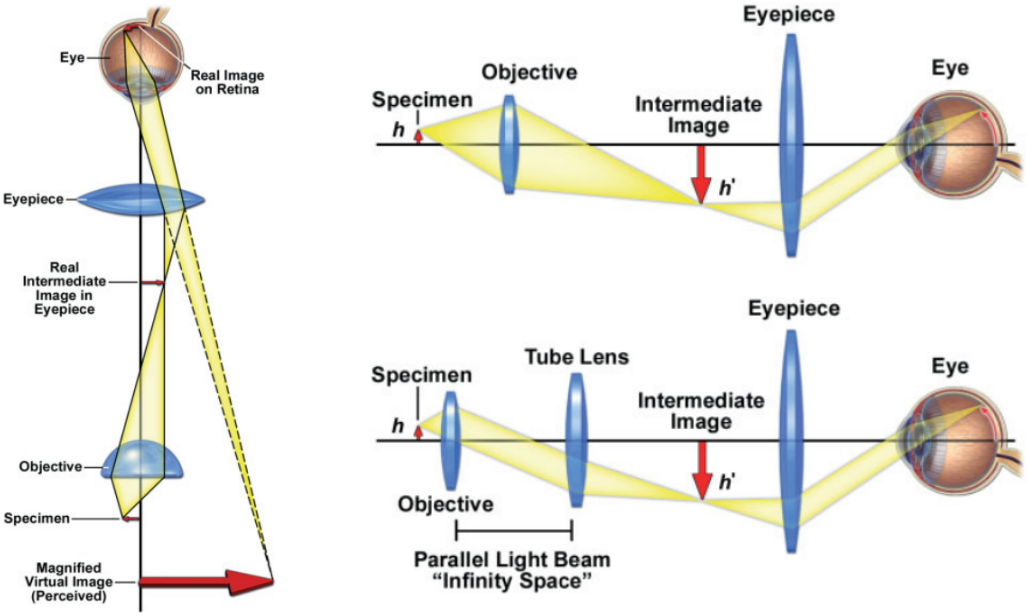

Figure 2.2 *(Left) ray diagram of the basic optical train of a microscope, highlighting how the eye perceives a magnified virtual image. (Upper-right) ray diagram of the optical train for a finite tube length microscope. (Lower-right) ray diagram of the optical train for an infinity corrected microscope. Whilst the tube length of microscopes was traditionally standardised to 160 mm, many newer objective lenses are infinity corrected to allow for the introduction of additional optical components, such as prisms and polarisers, into a parallel optical path. Taken from [49].*

Although the basic principle of microscope operation is shown above, modern compound microscopes are somewhat more complex. Compound microscopes use two conjugate planes of light when imaging a sample. Conjugate focal planes exist when a sample is in perfect focus in one of the planes whilst it is perfectly unfocused in the other[50]. By ensuring the illuminating light source is maximally out of focus at the sample location, whilst the sample is optimally in focus, any variations in the light source are smoothed out and therefore changes in light intensity are entirely the result of the sample. These two light planes are named the illumination and the image-forming planes. Ray diagrams of the imaging focal plane and the illumination focal plane can be seen in figure 2.3.

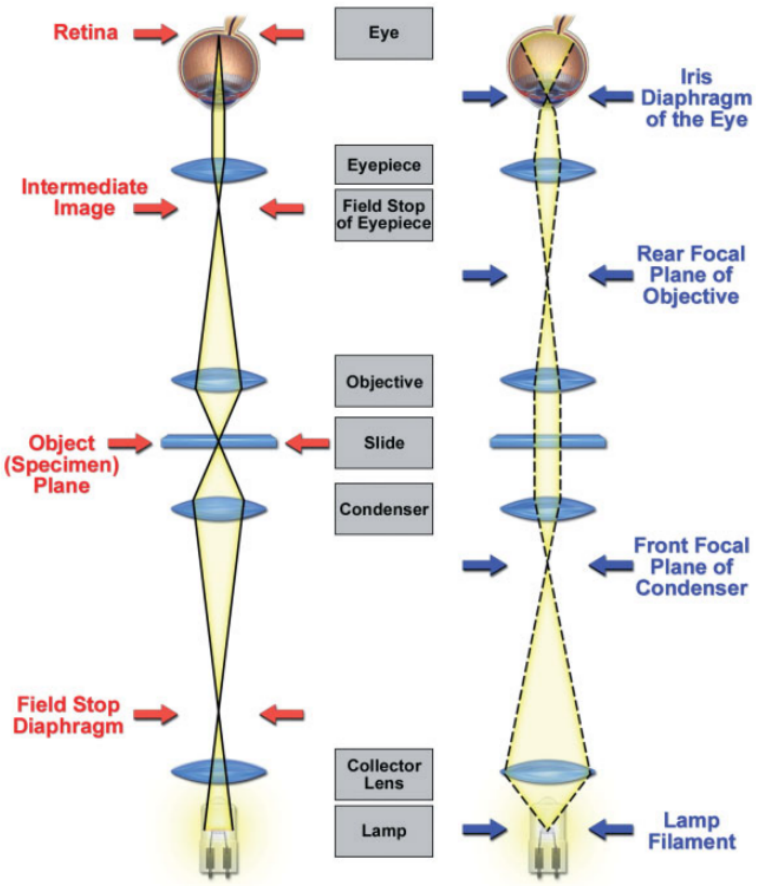

Figure 2.3 *(a) Ray diagram of the imaging focal plane. (b) Ray diagram of the illumination focal plane. Taken from [49].*

2.4.3 Brightfield microscopy

Brightfield microscopy is the most simple form of microscopic imaging. Light is transmitted through or reflected from a sample, and then collected by an objective lens. Different parts of a sample will absorb different amounts of light and it is this contrast that distinguishes the details within a brightfield image. Brightfield imaging often suffers from poor contrast as portions of a sample may not differ significantly in transparency, despite their biological or chemical differences. Historically, stains have been used to improve microscopic contrast, and these can be effective if an isolated component of a sample can be selectively stained.

2.4.4 Fluorescence microscopy

Fluorescence microscopy is a form of imaging that utilises photon emission from electrons that have been transiently raised into a higher molecular energy state. When an electron is excited from its ground state to a higher energy state, it can collapse back to its original state via internal and external energy processes which in turn can emit a photon of light. The process of adsorption and emission occurs over a time period of 10^{-9}-10^{-12} seconds[49]. This initial excitation can be triggered intentionally by irradiating a sample with light at a specific wavelength, if a photon is subsequently emitted it usually has a longer wavelength than the exciting photon that was first absorbed[49].

By irradiating a sample with light of a fixed wavelength that is known to excite a specific fluorescent compound, the subsequently emitted light can be filtered, collected and then formed into an image. This is usually achieved using a filter cube containing a dichroic mirror (see figure 2.4). Fluorescence images are highly valued in biological microscopy due to their high signal:noise ratio, as well as their power to selectively illuminate structures within a sample.

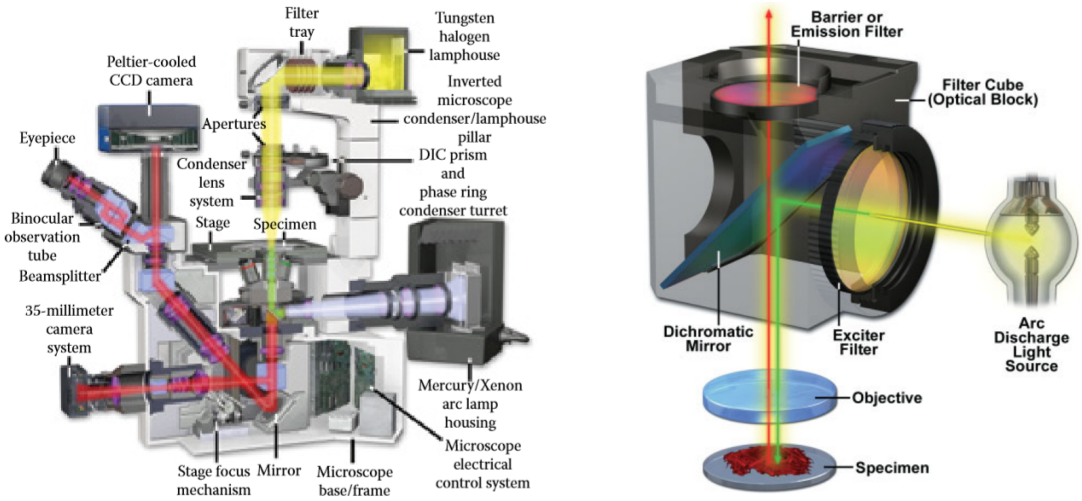

Figure 2.4 *(a) Cutaway diagram of an inverted microscope designed for the purpose of both brightfield and fluorescence microscopy, taken from [50]. (b) Illustration of a filter cube containing a dichroic mirror. Light from a broad spectrum source is first filtered and reflected onto a sample, light subsequently emitted from fluorphores within the sample is then filtered through the dichroic mirror to be collected by the objective lens. Taken from [49].*

2.4.5 Fluorophores

Molecules and compounds that possess the ability to fluoresce are defined as fluorescent. The term fluorophore is used for macromolecules that have been tagged with a fluorescent compound. Fluorophores are primarily defined by their excitation and emission spectra. The difference in wavelength between the peak values of these spectra is known as the Stokes Shift, this value can range from 25 nm to over 200 nm[49]. Fluorophores are also classified using a number of criteria such as their quantum efficiency (ratio of emitted photon quanta to absorbed photon quanta), aqueous solubility and resistance to quenching and photobleaching, which both act to reduce total fluorescence.

Fluorescent proteins

The first example of a naturally occurring fluorescent protein to be isolated was Green Fluorescent Protein (GFP), which was isolated from the North Atlantic jellyfish *Aequorea victoria*[51]. After their discovery, naturally occurring fluorescent proteins quickly became important markers of gene expression[52].

GFP is cylindrical in nature with 11 β-strands forming the walls of the cylinder, with an α-helix inside and helical segments capping the ends of the cylinder. Once formed, GFP is highly stable, requiring treatment with 6M guanidine hydrochloride at 90°C or pH of <4 or >12 for denaturation to be observed[53]. This stability has been attributed to its novel "β can" structure which acts to protect the enclosed chromophore.

These proteins are genetically encoded, allowing fluorescent protein gene expression to act as a reporter of cellular function when transferred into the sequence of another gene. Genetic transfer from one bacteria to another occurs through one of three processes: transformation, transduction or conjugation. Transformation is the process whereby bacteria incorporate naked DNA found in their environment. Transduction is the process of horizontal gene-transfer where a bacteriophage encapsulates a segment of a host cells DNA and acts a vector for the DNA's injection into a recipient cell. Conjugation is a DNA transfer mechanism that relies on cell-cell contact[54]. Fluorescent proteins offer a number of advantages over other fluorophores due to their compatibility with existing biological molecules and structures, their ability to fluoresce independently of external triggers, their low phototoxicity and their inherent ability to achieve subcellular

localisation[49][55]. As no exogenous triggers besides illumination are required to obtain this fluorescence, fluorescent protein expression is often used to monitor gene expression and protein localization in living organisms. The *E. coli* strain used in this thesis produces Yellow Fluorescent Protein (YFP). It was created using transduction, and the YFP gene is controlled by a genetic promoter that does not respond to external stimuli and therefore expresses YFP continuously.

Whilst useful, naturally occuring or "wild-type" fluorescent proteins exhibit some less than ideal experimental characteristics. To address these failings, a number of mutant proteins have been developed for use in the laboratory. Enhanced GFP (eGFP) is a fluorescent protein that features chromophore mutations that improve emission intensities by 35 times over wild-type GFP[52]. Furthermore, it features shifted excitation and emission spectra that more closely matches standard fluorescein isothiocyanate (FITC) excitation-emission filter sets[56]. Lastly, it is codon optimised for higher expression in mammalian cells[52]. GFP+ features mutations and DNA shuffling that improves folding efficiency above 25°C, enhancing brightness of cells by 16 times at 37°C, additionally protein aggregation is reduced and diffusability inside cells is increased[57]. GFP+ also exhibits a 35 times increase in fluorescence when excited at 488 nm.

The red fluorescent protein DsRed, which was isolated from the coral, *Discosoma*, has also been improved through genetic mutation. The obligate tetramerisation of DsRed historically hindered its used as an encoded fusion tag, as this caused the aggregation of almost anything to which DsRed could be covalently bonded[58]. Monomeric red fluorescent protein (mRFP1) is a mutant variety of DsRed that does not form a tetrameric structure[59]. MRFP1 also improves upon the time it takes for DsRed to become fully fluorescent after synthesis, this is known as the fluorescent proteins maturation time. The maturation time is a key experimental parameter that is usually beneficial to minimise[58].

2.4.6 State-of-the-art Microscopy

Whilst only standard brightfield and fluorescence-based microscopy techniques were used in this thesis, there are many more microscopy techniques used in the field of microbiology.

A technique commonly used when imaging biological samples is confocal microscopy. This technique can be used to construct high resolution three dimensional images of a biological sample. Whilst a number of other methods have been developed to image biological samples in three dimensions, they all generally operate by imaging multiple shallow image planes, building up a stack of image slices in the z-axis. Confocal microscopy achieves this by selectively illuminating and imaging small volumes of the sample in three dimensions using a focused scanning laser beam and a combination of pinhole apertures[49][60]. A complete image of the sample in three dimensions is then reconstructed computationally. This confocal arrangement is shown in figure 2.5.

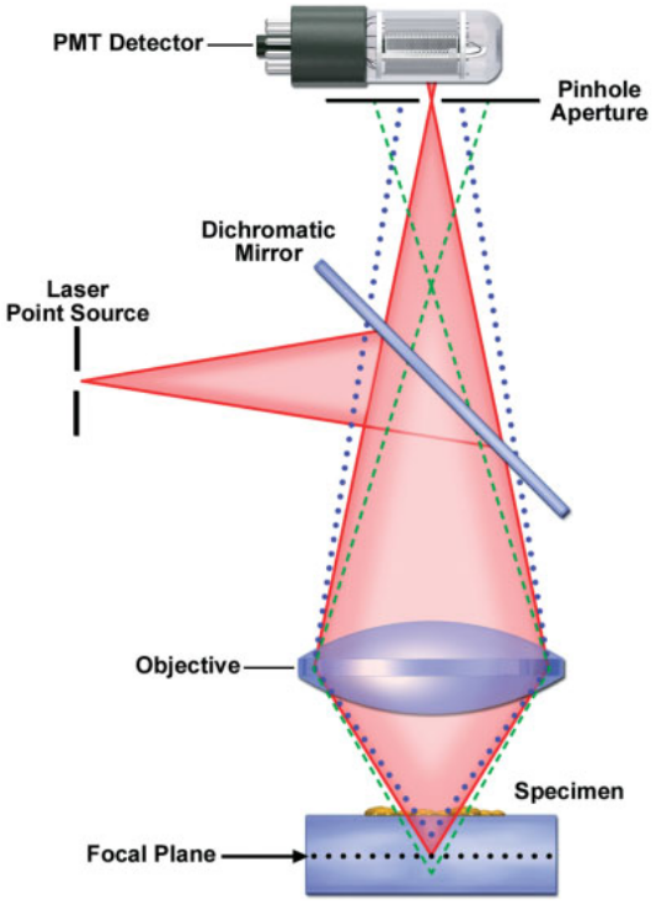

Figure 2.5 *Schematic diagram of a confocal microscope. Using a combination of multiple pinhole apertures and a laser point source, only fluorescent light from a single shallow plane reaches the photomultiplier tube (PMT) detector. Light from above (blue dots) and below (green dots) the focal plane is largely unable to reach the detector. Taken from [49].*

More recently, a focus has been placed on superresolution imaging. The resolution of a microscope at a fundamental level can be described in terms of the ability to distinguish two objects that are in close proximity to one another. In a standard light microscope this resolution is limited by the diffraction of light, and the lateral resolution is limited at around 200-250 nm. To overcome this diffraction limit, state-of-the-art techniques use single-molecule localisation to resolve features down to less than 10 nm[49][61]. This is usually achieved by repeatedly imaging a single field of view which contains fluorescent molecules that stochastically photoswitch using low-power lasers[62]. As the molecules stochastically photoswitch from one image frame to the next, each of the individual localised molecule centres can be determined using statistical fitting techniques. Through this repeated imaging, it is possible to construct a superresolution image by plotting the centroid positions of all observed fluorescent probes[61]. This process is shown in figure 2.6.

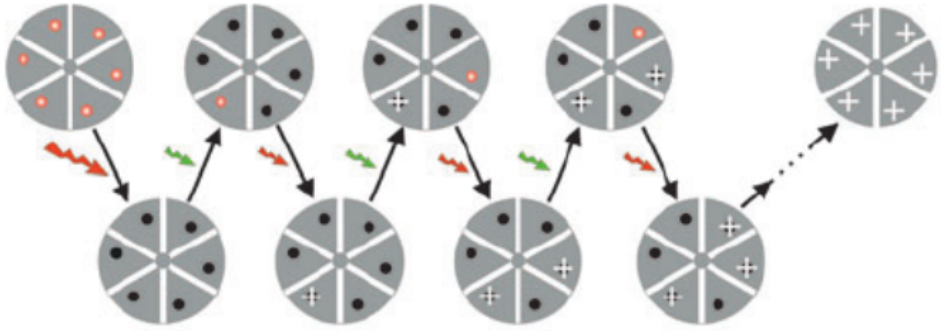

Figure 2.6 *Diagram detailing the imaging sequence used in STORM superresolution microscopy. In this case a hypothetical object labelled with 6 red fluorophores is being imaged. The red fluorophores photoswitch to a bright state using a green laser, and a dark state using a red laser. In each imaging/switching cycle, a green laser pulse is used to stochastically switch on a small fraction of the fluorophores, whose centres are accurately determined, before a red pulse then switches them off. This process is repeated numerous times until near all fluorophore positions can be determined with high accuracy and a superresolution image is constructed. Taken from [61].*

Two highly similar techniques that achieve superresolution in this manner are Photo-Activated Localisation Microscopy (PALM) and Stochastic Optical Reconstruction Microscopy (STORM). Example STORM images are compared to conventional fluorescence images in figure 2.7.

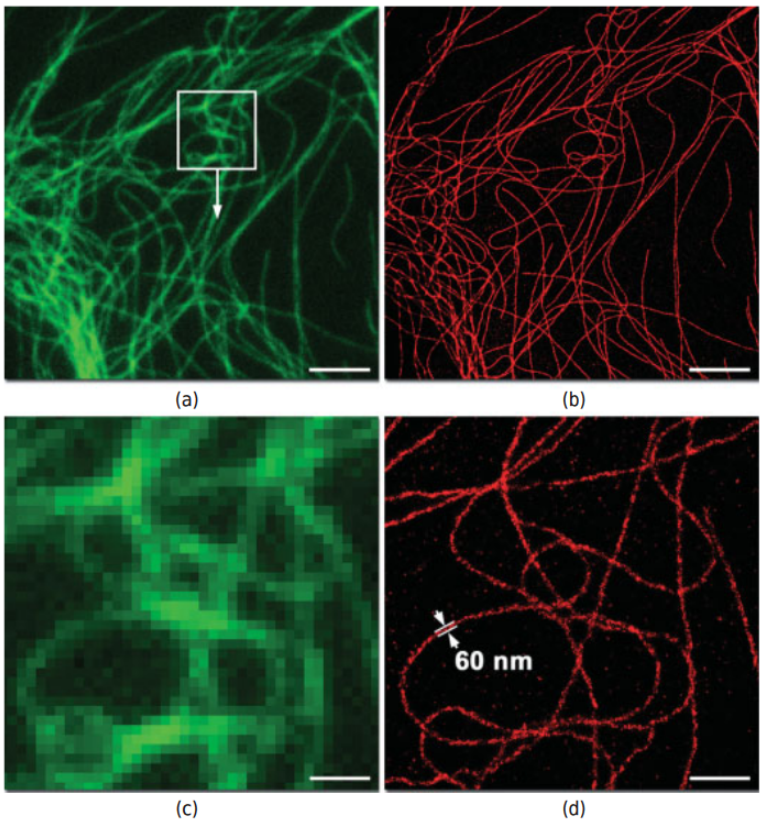

Figure 2.7 *Microcopy images showing the increased resolution obtained using STORM superresolution microscopy when compared to conventional fluorescence microscopy. Microtubules in rat kangaroo kidney cells are imaged using conventional fluorescence microscopy (a) and using STORM superresolution microscopy (b). The boxed section of the image seen in (a) is enlarged in (c), (d) shows a STORM image of the area shown in (c). Scale bar (a) and (b) = 5 μm, Scale bar (a) and (b) = 1 μm. Taken from [49].*

2.5 Continuous flow microfluidics

In this section I will discuss the field of continuous flow microfluidics, focusing on the fundamentals of microfluidic theory followed by an overview of microfluidic research and its applications.

2.5.1 Microfluidic theory

Microfluidics is the study of small volumes of fluids (10^{-9} to 10^{-18} litres)[63] and the systems used to manipulate these small volumes of fluids. Microfluidic systems generally use a series of channels with primary dimensions less than 100 μm to direct microfluidic flows. To understand how these microfluidic systems can be used in creative and novel applications, and the benefits they provide over more traditional fluid manipulation techniques, it is useful to first understand the theoretical principles commonly used to describe and characterise microfluidic flow.

The behaviour of a fluid system is governed by a number of different physical forces that compete with one another for dominance. This competition and its eventual winners dictate the emergent behaviour of the system. To more easily understand the mechanics of a fluid system, a number of dimensionless quantities have been established to quantitatively evaluate the importance of these forces relative to one another. Many of these forces scale with a characteristic length scale of the system. This scaling is critically important when discussing microfluidic systems as these almost always operate at length scales not commonly encountered in the academic laboratory, therefore their behaviour can appear counter-intuitive unless properly understood.

Before discussing these dimensionless quantities, it is important to review the dimensional parameters that govern fluid flow, and the fundamental equation that underpins microfluidic flow: the Navier–Stokes equation. Fluids are continuous materials, and as such are not generally described using discrete quantities. Instead, continuous fields such as density and force density are used (which are described per unit volume). The velocity field for a fluid obeys the Navier-Stokes equation, which can be described as Newton's second law for fluid particles[64].

The incompressible fluid regime is assumed for microfluidics, therefore the Navier–Stokes equation takes the following form:

$$\rho(\partial_t v + (\mathbf{v} \cdot \nabla)\mathbf{v}) = -\nabla p + \eta \nabla^2 \mathbf{v} + \mathbf{f}, \tag{2.3}$$

where ρ is fluid density, $\mathbf{v}$ is fluid velocity, p is pressure, η is the fluid viscosity and $\mathbf{f}$ are body force densities due to external forces such as gravity[64][65]. Inertial acceleration terms appear on the left hand side of the equation, whilst force terms are gathered on the right hand side. When inertial forces are dominated by viscous forces (a condition normally satisfied by microfluidic flow), the non-linear term can be neglected. Under this regime, fluid flow is described by the Stokes Flow equation:

$$\rho \partial_t v = -\nabla p + \eta \nabla^2 \mathbf{v} + \mathbf{f}. \tag{2.4}$$

The Navier-Stokes equation is famously difficult to solve. It is however possible to derive analytical solutions for a small number of simple and idealised cases[64]. These solutions provide a basic and intuitive understanding of fluid flow in microfluidic channels, and it is this fundamental understanding that forms the basis for the dimensionless quantities discussed in the following section.

Dimensionless Quantities

The first and most well known dimensionless quantity associated with microfluidic flow is the Reynolds Number (Re):

$$Re = \frac{f_i}{f_v} = \frac{\rho\, U L}{\eta}, \tag{2.5}$$

where ρ is the density of the fluid, U is the velocity of the fluid with respect to the channel, L is a characteristic length scale over which the fluid forces are influencing and η is the dynamic viscosity of the fluid. Re is the ratio between the inertial forces and viscous forces acting upon a fluid flow. Low Re values imply that viscous fluid forces are dominating over inertial forces. When Re is small the non-linear terms in the Navier-Stokes equations become vanishingly small, resulting in linear, non-turbulent flow.

This means *Re* is most generally used as a predictor for the transition between laminar and turbulent flow regimes. Although a useful quantity more generally, *Re* is a poor tool for the evaluation of microfluidic flows, as almost all microfluidic flows operate in the small *Re* regime. This means that virtually all microfluidic flow is linear and laminar in nature. Interestingly, this has the implication that almost all cellular processes in nature occur in a low *Re* environment. This concept is explored brilliantly in the talk "Life at Low Reynolds Number" by E. M. Purcell[66] - an excellent primer on the sometimes counter-intuitive dynamics of fluids operating in the low *Re* regime.

Whilst the Reynolds number is used to compare the inertial and viscous forces that act upon fluid flows, there are a number of other dimensionless quantities that are also used to characterise microfluidic flow. The Peclet number, for example, compares diffusive and convective forces within a microfluidic flow. Calculation of the Peclet number indicates that diffusion is dominant in almost all microfluidic flows. The laminar nature of microfluidic flows means that mixing can only occur via diffusion. Practically this means that to achieve decreased mixing times in microfluidic flows, one must use carefully chosen microfluidic geometries. Other dimensionless quantities include the Capillary, Weissenberg, Deborah and Weber numbers, which compare the relative magnitudes of different fluid forces and properties such as interfacial tension and polymeric relaxation times. Each of these numbers is used to describe the dynamical behaviour of specific microfluidic systems or geometries, and both the Capillary number and Weber number will be detailed in section 2.6 as they are useful in the characterisation of droplet microfluidic systems.

Hydraulic Resistance

Beyond the dimensionless quantities discussed in this section, two key quantities that must be considered when developing microfluidic systems are hydraulic resistance and conductance. These quantities are defined below, in the Hagen–Poiseuille law:

$$\Delta p = R_{hyd} Q = \frac{1}{G_{hyd}} Q, \tag{2.6}$$

where Δp is the pressure drop of a flow of constant rate Q, with proportionality constants R_{hyd} (hydraulic resistance) and G_{hyd} (hydraulic conductance)[64].

Equation 2.6 is analogous to Ohm's law, which links the voltage drop across a current carrying wire given an electrical resistance. As electrical resistance can be described in terms of energy loss due to heating, hydraulic resistance can be described in terms of energy loss due to mechanical energy dissipation due to internal fluid friction. To further the analogy, it is possible to calculate the hydraulic capacitance of a system (known as the compliance). This compliance is due to the fact that the fluids and materials used to construct a microfluidic device are not perfectly incompressible or rigid, herein energy can be stored.

Furthermore, it is possible to apply the basic laws of circuit theory that describe coupled resistors and capacitors (as described in Kirchhoff's laws) to a microfluidic network[64][67]. This allows good estimates to be made of the total hydraulic resistance of complex microfluidic lab-on-a-chip systems, without the need for numerical simulations. The hydraulic properties (flow rate, hydraulic resistance/conductance, pressure etc.) of a microfluidic system can be related to channel geometry (cross-sectional shape, height, width and length)[67].

Whilst explicit calculations of hydraulic resistance were not made in this thesis, an intuitive understanding of how channel geometry impacted hydraulic properties such as flow rate and pressure was vital in the design of our microfluidic system.

2.5.2 Continuous flow microfluidics - general applications

Complex microfluidic designs are now being integrated into experimental systems to conduct research across many academic fields[63]. These microfluidic systems have furthered the experimental capabilities of many research groups, often improving upon or condensing traditional experimental techniques.

Perhaps the most common and developed application of continuous flow microfluidics is in experimental screening, where many samples are tested for a particular property of interest. For example, a number of microfluidic systems have been developed to benefit the field of drug development, as high-throughput screening techniques are an essential part of the drug discovery pipeline. The integration of multiple reaction steps onto a single microfluidic chip means that serial analysis is attainable in flowing systems[68]. Furthermore, these serial reactions can be parallelised extensively[69]. Microfluidic systems have also been coupled with conventional mass spectroscopy systems to screen laboratory separations[70]. Microfluidic devices also lend themselves well to single molecule detection stud-

ies[71]. These devices can be used in the identification and counting of newly synthesised compounds and could have widespread applicability, especially in bio-analytical fields[72]. Microfluidics devices have also found extensive use in the synthesis and preparation of chemical compounds. By integrating a large number of individual processes into a single "lab on a chip" that sequentially automates a number of complex techniques, it has been possible to synthesise sensitive compounds with a high yield and purity. It is possible for all of this to be accomplished in a shorter time frame than current standardised techniques[73].

Whilst the the numerous applications of continuous flow microfluidics are clearly far reaching and diverse, the field of microbiology is perhaps the greatest benefactor of this experimental technology. Bio-specific microfluidic applications will be introduced and examples detailed in the following section.

2.5.3 Continuous flow microfluidics - biological applications

Microfluidics have proved themselves an invaluable tool in the study of (micro)biological systems[65][74][75][76]. This is in part due to their ability to accurately and reliably manipulate fluids on length scales matching those of *in vivo* biological niches. Another benefit of the microfluidic platform is the ability to integrate a number of preparation and analysis processes into a single "lab on a chip": this has been used to simplify complex biological assays. Finally, the small physical size of microfluidic devices make them suitable for Point of Care (POC) diagnostic devices. This has been taken even further with the introduction of low-cost paper-based microfluidic systems, which in the future may be used in clinical applications in developing nations[77].

By way of example, stem cell researchers have designed a flow based sorting system based on the principles of hydrodynamic filtration to sort marrow-derived mesenchymal stem cells[78]. This approach allows for the rapid sorting of stem cells without damage. Multiple advances have also been made in the field of neurology due to studies using microfluidic devices. One group has developed a microfluidic multi-electrode array that could perform high-resolution extra-cellular recordings of brain slices whilst remaining optically compatible with calcium imaging - this had not been possible using traditional macro-scale experimental systems[79]. Minimal "organs on chips" have also been developed to closely

replicate the environments inside functional organs so that bio-mimetic research can be completed. Jang *et al.* mimicked a kidney using a simple multi-layer microfluidic device consisting of microfluidic channels and a porous membrane substrate. It was found that renal tubular cells developed inside the artifical kidney grew as they would *in vivo*, suggesting that the microfluidic organ emulated the target biological conditions well[80]. This study could have practical implications in the fields of drug screening and tissue engineering.

More relevant to the work completed in this thesis, microfluidics can be used to manipulate and immobilise individual cells for imaging in ways that were previously impossible using more traditional microbiological techniques. A simple and effective example of this can be seen in the popular "mother machine"[81][82], a microfluidic geometry that constrains cells in long channels wide enough for just a single cell to pass through. When bacteria are confined in these long channels, daughter cells can be tracked with relative ease and lineage monitoring is possible for over 200 generations. This is a 10x improvement in observation time over traditional methods using agar pads[81]. Lee *et al.* have adapted this design in a microfluidic dissection platform for yeast cells. In this adapted design, yeast cells are trapped between PDMS-based microfluidic pads and a glass cover slip. Fresh media is then passed over the cells, simultaneously providing nutrients to the trapped mother cells and removing the smaller daughter yeast cells. This supersedes a 50 year old technique described as "laborious and time-consuming" where individual yeast cells are manually extracted and dissected at different stages in the yeast cell lifespan[83].

Microfluidic systems are becoming popular in the study of bacterial population dynamics, often with the aim of using microfluidic geometries to mimic biological niches. For example, Austin *et al.* fabricated a linear array of coupled, micro-scale growth "patches" that were inoculated with bacterial populations[84]. Nutrients and waste were exchanged with an external reservoir using nano-scale slits and stress could then be applied to each of the populations by restricting nutrient exchange. It was found that growth patches and their associated bacterial populations interacted through extinction and colonisation processes, and by varying stresses across the growth patch landscape, adaption was seen in high stress areas. Another prominent study published by the same group took this design further by fabricating a microfluidic device consisting of 1200 hexagonal growth chambers[85]. The growth chambers were connected by 10 μm wide channels that allowed for bacterial movement from one chamber to the next. Antibiotic could be

applied uniformly across all growth chambers, or as a gradient across the growth chambers, using nano-scale slits at the perimeter of the microfluidic device. This artificial set of linked environments mimics a number of micro-scale biological niches well; porous materials, large cells and biological emulsions are examples of micro-environments that confine bacteria but also allow interaction through diffusion. It was found that bacterial growth was completely inhibited under uniform antibiotic application, however antibiotic resistance rapidly emerged when the antibiotic was applied as a gradient. By further studying this rapid emergence of antibiotic resistance across heterogeneous growth landscapes, it may be possible to better understand *in vivo* bacterial infections.

Although these studies are but a tiny fraction of the current research being completed in the field of biologically oriented continuous flow microfluidics, they nonetheless reveal the positive disruptive impact that microfluidics is having on current techniques in experimental microbiology.

2.6 Droplet microfluidics

2.6.1 Introduction

Droplet-based microfluidics is a rapidly expanding field within the more general domain of microfluidics. These types of microfluidic systems use specialised channel geometry to generate and manipulate droplets with diameters typically in the range of 10-100 μm. These droplets are suspended in a secondary immiscible continuous phase and due to the low-Reynolds number behaviour that characterises microfluidic systems, it is possible to quickly generate upwards of 1000 droplets per second with a diameter polydispersity of less than 3%[86].

In this section I will introduce two commonly used dimensionless quantities that can be used to quantitatively describe droplet-containing microfluidic flows. I will then detail two experimental microfluidic geometries that are commonly used in the generation of microfluidic droplets. Lastly, I will summarise a number of studies that use droplet microfluidics, focusing on biological applications that involve cellular confinement.

2.6.2 Theory

When considering the behaviour of fluids in microfluidic droplet devices, we almost exclusively discuss interactions occurring in the low Re regime. As is standard with fluid dynamics, the behaviour of droplets generated and manipulated in a microfluidic device can be generally characterised using a variety of dimensionless numbers. These numbers are designed to compare the relative strengths of the physical forces and interactions that govern microfluidic flow.

Although I have already described some of these dimensionless quantities in the previous section, there are two numbers often used when describing droplet microfluidics specifically.

Dimensionless Quantities

The Capillary number (Ca) compares viscosity to interfacial tension, and is perhaps the most useful dimensionless quantity when describing microfluidic droplet generation and flow.

$$Ca = \frac{\mu U}{\gamma}, \tag{2.7}$$

where μ is generally the viscosity of the most viscous fluid, U is the characteristic fluid velocity and γ is the interfacial tension. When Ca is low, this implies that interfacial stresses are dominating over viscous stresses. In this scenario droplets will attempt to minimise their surface area, resulting in spherical fluid interfaces wherever possible. At large values of Ca, viscous stresses are dominating over interfacial stresses. This results in droplets deforming into non-spherical, asymmetric shapes. This will become highly relevant when discussing methods of droplet generation.

The Weber number (We) compares inertia to interfacial tension, and is generally useful in characterising the formation of droplets or bubbles, or in describing thin film flows.

$$We = \frac{\rho U^2 l}{\gamma}, \tag{2.8}$$

where ρ is the density of the continuous fluid, U is the fluid velocity, l is the characteristic length of the system (usually droplet diameter) and γ is the interfacial tension. This dimensionless number is usually small in microfluidic flow, but inertial effects can become relevant in high speed flows. The Weber number is often used to characterise droplet breakup processes when viscous stresses are dominated by capillary pressures and inertial forces[87], and it has been experimentally linked to the transition between droplet generation regimes[88].

In summary, these dimensionless quantities are very useful in describing the microfluidic flow of droplet generation and offer a convenient method of mapping the transitions between droplet generation regimes.

2.6.3 Droplet generation

Generally, the most complex and dynamic process within a microfluidic droplet device is the generation of the droplets themselves, i.e. the point at which two immiscible phases first interact to form an emulsion of dispersed droplets within a continuous fluid phase. Devices for droplet generation are usually based around the principles of co-flowing or cross flowing geometries.

T-junction

Of the many geometries designed to generate a monodisperse emulsion of microfluidic droplets, the T-junction (a form of cross flowing geometry) is the most popular, most likely due to its inherent simplicity[87][89][90][91]. This method of monodisperse microfluidic droplet generation was first demonstrated by Thorsen *et al.*[92]. The T-Junction droplet generating geometry operates by flowing one fluid into a second, cross flowing immiscible fluid at an orthogonal junction[93][94][95]. A basic schematic of the T-junction geometry is shown in figure 2.8.

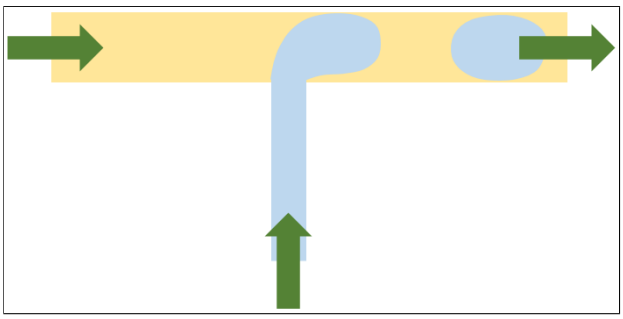

Figure 2.8 *Schematic displaying the basic geometry of a cross flowing T-junction microfluidic droplet generator. The dispersed phase (bottom) can be seen entering the cross flow of an immiscible continuous phase (left). As the dispersed phase enters the cross flow, the head distorts downstream until the neck thins and breaks, resulting in droplet formation.*

The generation of droplets in a cross flowing T-junction is deceivingly complex. First, the dispersed phase enters the flow of the cross flowing continuous phase and an increasing pressure [89] and shear gradient is established [93]. These gradients cause the head of the dispersed phase to elongate into the direction of the continuous phase flow. As the head of the dispersed phase is distorted along the channel, the neck of the dispersed phase thins and breaks, generating droplets[89].

It has been observed that when generating monodisperse microfluidic droplets, the T-junction geometry usually operates under one of two regimes. In the first dripping regime, the continuous phase channel width significantly exceeds that of the dispersed phase channel width. The capillary number is large, which generally signifies a fast flowing continuous phase. Under these circumstances, the droplets are formed before the head of the dispersed phase can span the continuous phase channel, breaking off when viscous shear stresses dominate over interfacial stresses[96]. When the channel width ratio of the two phases approaches one, and the capillary number is reduced (signifying a lower continuous phase velocity), the T-junction transitions into the squeezing regime[89]. Here the dispersed phase is able to almost completely span the continuous phase channel. A rapid increase in upstream pressure forces the fluid interface to pinch off, forming a plug-like droplet[96].

Whilst I will mention a number of studies that explore this process in more detail, it should be noted that there are currently no empirical or theoretical treatments that accurately predict the transition between the various droplet generating regimes. Scaling laws that predict the rate of droplet production have been proposed that agree well with experiments[97]. Despite this, there are no studies that accurately describe droplet size or rate of production of a generalised cross flowing droplet generating system[96].

A numerical investigation of the dripping to squeezing transition has been completed by Menech *et al.* This found that the squeezing regime operated largely independently of material properties such as fluid viscosities, but they observed that the dripping regime was far more fragile and only functioned correctly across a small range of capillary numbers[98]. Garsteki *et al.* predicted that the droplet length would be independent of the continuous phase viscosity across a wide range of values[89], but more contemporary numerical[99] and experimental[97][100] studies have shown the viscosity ratio can be influential in cross-flowing droplet generation under certain conditions. Steegmans *et al.* noted that whilst the channel depth and the capillary number impacted generated droplet size, the dispersed phase velocity was largely unimportant[101]. An experimental study completed by Guillot *et al.*[102] found a transition from droplet generation to stable parallel flows could not be predicted by capillary number alone.

I have acknowledged here just a handful of studies that attempt to provide insight into the generation of droplets using a cross flowing microfluidic junction. Despite the intense investigation into this method of droplet generation, there is still no general consensus on the exact physical parameters that govern the mechanics of droplet breakup at a T-junction.

The T-junction method of microfluidic droplet generation is often used due to its simple design, but once this geometry has been finalised this approach offers limited control over droplet size. This has been addressed in designs that implement additional moving elements such as mechanical[103] or pneumatic[104] microvalves, or by tuning internal surface tensions and viscosities through the integration of heating elements[105]. Despite these innovations, these complex designs sacrifice device simplicity and can reduce droplet generation frequency significantly.

Flow-focusing junction

Another effective method of microfluidic droplet generation is through the use of a flow-focusing junction. In this geometry three separate fluid flows are simultaneously passed through a constricting orifice. The dispersed phase is fed through a central channel, whilst the continuous phase occupies two channels either side of the central channel[76][106], as illustrated in figure 2.9.

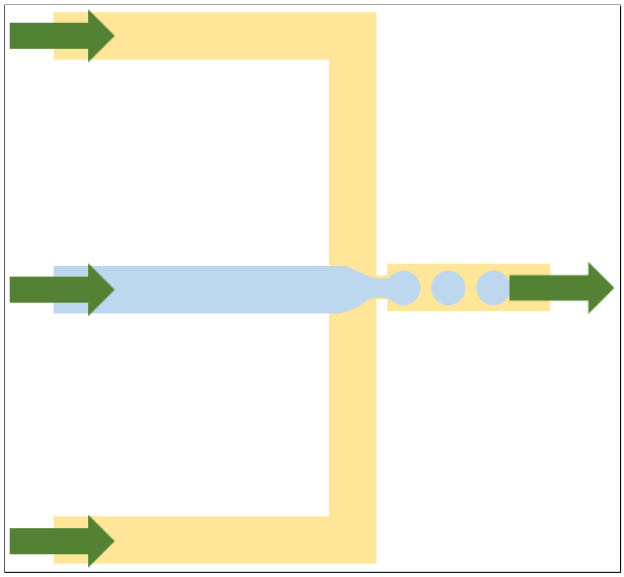

Figure 2.9 *Flow-focusing geometry for droplet generation in a microfluidic device. Three channels are positioned beside one another, the outer channels (top, bottom) carrying the continuous phase whilst the centre channel (middle, left) carries the dispersed phase. Each phase is simultaneously forced through a constricting orifice. Droplet generation can occur upstream, downstream or within the confines of the constriction.*

As the dispersed phase flow is squeezed between the two continuous phase flows, increasing pressure gradients cause symmetric shearing forces as all three flows pass through the constricting orifice[94]. Viscous stresses and pressure cause droplets to be formed in elongation-dominated flows[103].

It has been shown that flow-focusing droplet generating junctions optimally operate in one of two droplet generation regimes[93][107][108]. The dripping regime can be characterised by droplets being generated within one orifice-diameter of the constricting orifice[109], and the generated droplet diameters being smaller than the constricting orifice. The droplets generated in this regime are also

highly monodisperse (less than 2% polydisperse)[87]. The jetting regime occurs when droplets are generated at a point over three orifice-diameters from the constricting orifice [109]. The outer continuous phase wraps around the elongated neck of the dispersed phase, stabilising it such that it stretches downstream of the constriction (likened to a jet) and this neck eventually breaks into droplets. Comparatively large and polydisperse droplets are formed under this regime[108]. A number of additional breakup regimes have also been observed [87]. Understanding the transition from the dripping to jetting generation regime is non-trivial. Multiple studies have aimed to both qualitatively and quantitatively describe the underlying physical phenomena that trigger this transition. Utada *et al.* argue that the dripping regime will transition to the jetting regime when the timescale for visco-capillary pinchoff roughly matches the timescale for growth of the jet, leading to a critical transitional capillary number[109]. In similar fashion, Zhou *et al.* argues that dripping will transition to jetting when interface disturbances are convected downstream before amplification occurs[88]. Zhou's approach predicts a critical scaling behaviour, but this has not been tested empirically[87]. Physical parameters such as droplet generation rate, droplet spacing and droplet velocity have also been investigated and empirical relationships between these variables have been predicted successfully using geometrical arguments[110].

A predictive model for the generated droplet size does not exist[93], but multiple studies have shown that droplet size is affected by junction geometry, flow rates, viscosity and interfacial tension[93]. As inertial contributions are typically negligible in microfluidic flows, it has been hypothesised that a combination of viscous stresses and capillary pressures primarily control droplet generation processes[93] [103].

Despite the increased geometrical complexity demanded by the flow-focusing junction (in comparison to the passive T-junction geometry), the effective geometry of the flow-focusing junction can be tuned significantly by adjusting the dispersed and continuous phase inlet flow rates[111]. This affords a greater flexibility in the generated droplet size alongside reduced polydispersity when compared to the T-junction geometry.

2.6.4 Droplet microfluidics - general applications

The idea of manipulating small droplets in microfluidic channels is appealing both academically and industrially. Chemists and biochemists successfully used droplet emulsions as pseudo-microreactors long before the advent of microfluidics[112][113]. Droplet microfluidics builds upon this basic premise by offering a method of tightly controlling the generation of these droplet emulsions and further manipulating them in ways that were not previously possible. Additionally, the contents of microfluidic droplets can be modified through the controlled splitting or fusion of droplets using both passive[114][115] and active methods[116][117][118].

In many cases, microfluidic droplets are treated as individual "test tubes" - isolated environments that benefit from low reagent utilisation, rapid mixing and automated droplet manipulation[108]. Whilst both continuous flow microfluidics and droplet microfluidics lend themselves well to many mutual areas of research, some applications naturally benefit more obviously from the compartmentalised nature of microfluidic droplet emulsions. Across the next two sections, I will discuss a number of studies and applications that utilise microfluidic droplet technologies.

One of the primary applications of microfluidic droplets is in the area of chemical synthesis. In this role, droplets behave like compartmentalised reaction vessels that are able to encapsulate an entire reaction process. Reagent consumption is heavily reduced due to the sub-nanolitre volumes typical of microfluidic droplets, and the rapid accumulation of reaction products decreases analysis and detection times. Scaling reactions down so that they are performed in highly parallelised micro-reactors also reduces the risk of performing exothermic reactions in bulk. This allows reactions to be completed more quickly due to shorter diffusion, heat and mass transfer distances[94]. In the microfluidic literature, there are numerous examples of microfluidic droplet systems being used as a platform for multiphase reactions such as titration[119] and precipitation[120]. Ahmed *et al.* performed a simple biphasic hydrolysis reaction in a two-phase droplet microfluidic device. It was found that reaction rate was dependant on multiple factors such as droplet size and flow rate. When using the segmented microfluidic flow, it was found that the efficiency was dramatically improved when compared to the same reaction performed in a single phase conventional reaction flask[121].

Droplet microfluidics are also finding use in the fabrication of special materials - mostly solid or gel particles. These fabrication techniques generally operate using the same basic principles; reactants are first encapsulated within microfluidic droplets and then dispersed into a continuous phase, material formation is then triggered whilst the reactants are encapsulated within the microfluidic device[111]. These reactions can be initiated using external triggers such as UV exposure, temperature or simple time delay. Winterton *et al.* presented a novel microfluidic reactor for the high temperature synthesis of semiconductor nanocrystals. Nanocrystals were synthesised inside of droplets that were passed in and out of a number of temperature controlled zones that could be tuned to the requirements of the synthesis[122]. By tuning the temperature of each reaction zone and its associated droplet residence time, this droplet microfluidic device could be used to optimise many forms of chemical processes. More complex mechanisms of reaction initiation have been demonstrated that utilise droplet injection or coalescence to merge a number of reagents during multiphase reactions[111][114]. Frenz *et al.* demonstrated this in their work producing synchronised droplet pairs that they mixed using electrocoalescence to fabricate magnetic iron oxide nanoparticles[123], which have applications in magnetic resonance imaging and high density data storage.

2.6.5 Droplet microfluidics - biological applications

Whilst both chemical synthesis and nanomaterial fabrication are prolific areas of research using microfluidic droplet systems, the applications of this technology to the field of quantitative microbiology are numerous and fruitful.

Biological applications using microfluidic droplets

Droplet microfluidics are well suited to biological screening and digital assays. Current bottlenecks exist in microbiological research due to the need to screen large numbers of individual reactions. Molecular screening for the purpose of drug discovery requires the ability to screen millions of compounds, and this is typically completed using a high-throughput pipetting robot using a 1536 well plate, at a rate of $\approx$1 Hz, with minimal sample volumes of 100 nL[76]. Due to these limitations, it is financially impossible to use molecular screening analysis for all but the most valuable research targets [124]. Droplet microfluidics offers

the ability to screen reactions at an ultra-high-throughput with rates reported above 1 kHz using ≈1 pL of reagant per reaction[125][126]. This high-throughput methodology coupled with increased sensitivity due to the small volume/high density regime means that droplet microfluidics can dramatically increase the productivity of bioassays and combinatorial biochemical reactions. An example is provided by a study completed by the Weitz group, where droplet microfluidics were used for the directed evolution of the enzyme horseradish peroxidase. The study found mutants of the enzyme that exhibited catalytic rates ten times greater than that of their parent. Furthermore the entire assay was completed in less than one thousandth of the time and one millionth of the cost of the comparable state-of-the-art robotic screening system[127].

Polymerase chain reactions (PCR) are an effective and reliable method of DNA amplification, a process often harnessed in biological diagnostics. Whilst PCR was first reported by Mullis *et al.* in 1987[128], the technique has been significantly improved in multiple ways using both continuous flow and droplet microfluidics[129]. Droplet-based PCR is capable of single-molecule DNA analysis, enabling the rapid detection of rare mutation sequences without the signal being washed out by more abundant DNA sequences[93]. DNA fragments can also be isolated, stored and amplified without the possibility of recombination. Droplet PCR is perhaps the most commercially successful application of droplet microfluidics to date [108] - multiple companies currently offer microfluidic droplet systems tailored toward PCR[130].

Biological applications studying cells encapsulated within microfluidic droplets

It has been shown that monodisperse microfluidic droplets can act as micro-environments for the purpose of growing living cells[43][131]. Through the use of biocompatible oils and surfactants, it has been shown that bacteria and eukaryotic cells can survive droplet encapsulation for days[126]. This is done by passing a suspension of cells in aqueous growth media through a microfluidic droplet generator.

In this process, cell encapsulation is expected to follow Poisson statistics[132]:

$$P(\lambda; n) = \frac{\lambda^n e^{-\lambda}}{n!}, \tag{2.9}$$

where $P(\lambda; n)$ is the probability of n cells being found in a droplet given the average number of cells per droplet is λ. This is because bacteria suspended in a liquid growth media will arrive at a microfluidic droplet generating junction randomly and independently of one another. Furthermore, the average bacterial arrival rate is fixed per unit time, and can be determined from the density of the initial bacterial suspension[133]. Experimentally λ is tuned by adjusting the concentration of the initial suspension, this allows the study of low-density bacterial populations in microfluidic droplets. Moreover, by carefully selecting the concentration of the initial suspension it is possible to obtain a distribution of droplets which contains droplets encapsulating single cells. To surpass the inherent Poisson efficiency limitations imposed by random loading, a number of groups have taken advantage of both active techniques and passive hydrodynamic phenomena to increase single cell loading efficiency up to ∼80%[132][134][135]. Whilst methods have been developed to improve single cell loading efficiency, many studies choose not to employ these complex geometries[43][131][136][137], instead empty droplets are removed in additional sorting steps or simply ignored in further analysis. Whilst this produces a large number of empty droplets when studying small bacterial populations, this is generally not a problem due to the high-throughput nature of microfluidic droplet production and screening[138].

The ability to quantitatively study large populations of cells has revolutionised our understanding of stochastic cellular functions and has found increasing use in diagnostics[138]. Cells with desired characteristics can be detected using fluorescence markers that are used to determine protein expression and these can then be isolated using Fluorescence-Activated Cell Sorting (FACS)[139]. This methodology is unfortunately limited if the "detection molecule" (usually the product of an internal cellular process) is released by the cell. This limitation is removed if each cell is instead encapsulated within a microfluidic droplet, as the reagents and secreted molecules are contained in a diffusionally opaque compartment.

Shim *et al.* designed a microfluidic device that encapsulated bacteria in microfluidic droplets and analysed the gene expression and enzymatic activity of each droplet using fluorescence measurements. They demonstrated the use of the device in the context of directed evolution.

Their microfluidic device gave them the ability to study the statistical heterogeneity of cells that were cultured identically[136].

Köster *et al.* demonstrated the encapsulation of single mammalian cells in microfluidic droplets for the purpose of antibody detection. It was shown that antibody secretion from single cells reached detectable levels within 6 hours, moreover the cells were recoverable from the droplets post-encapsulation and were fully viable[138]. Each of the individual processes that constituted the experimental workflow (encapsulation, incubation, detection) were separated onto individual microfluidic chips that were linked after fabrication. This modular design meant that the assay could be customised with the exchange/addition/removal of individual microfluidic sub-devices. This "microfludic toolbox" approach to device design is advocated by a number of groups[126], and we followed this philosophy when designing our own microfluidic device.

In recent years, one of the most innovative applications for microfluidic droplets is in the field of ultra-high-throughput single-cell RNA sequencing. In this application, a cell suspension is prepared using a tissue sample and the individual cells are encapsulated using microfluidic droplets. In the droplets, each cell is encapsulated with a companion microparticle that is tagged with an identifying DNA-barcode. The cells are then lysed and the mRNAs of each cell bind to their companion microparticle. These mRNAs are then reverse transcribed and amplified, and through the use of the bound DNA-barcode, each mRNA transcript can be linked to a single cell-of-origin. The Drop-Seq[140], inDrop[141] and Genomics Chromium[142] systems are three popular platforms that are capable of performing this ultra-high-throughput single cell analysis[143]. Whilst the purpose of each system is largely the same, each of them differ subtly in the materials they use and the order in which the steps of their protocol are completed. In their seminal paper, Macosko *et al.* demonstrated this ultra-high-throughput single-cell RNA sequencing process by analysing complex neural tissue[140]. 44,808 cells were processed and 39 distinct cell populations were detected, each of which consisted of closely related cell types. This cutting edge implementation of microfluidic technology improves upon existing techniques by over two orders of magnitude in both speed and cost. Beyond the simple identification of cell types, it is hoped that this RNA sequencing process will provide a high-throughput method of connecting specific gene function and expression to the diverse families of cellular sub-populations that compose a given tissue.

Biological applications studying bacteria-antibiotic interactions within microfluidic droplets

Finally, and of critical relevance to the work completed in this thesis, microfluidic droplets have also been used to study bacteria-antibiotic interactions in small bacterial populations. Studies that utilise microfluidic droplets for this purpose are discussed below. Ultimately, there is considerable overlap in the objectives of the research discussed below and the work completed in this thesis, so it is important to consider the relative strengths and weaknesses of the different experimental approaches and methodologies.

Tang *et al.* have developed a microfluidic device to detect small sub-populations of bacterial cells that naturally exhibit resistance to a given antibiotic; a phenomenon known as heteroresistance[43]. To measure this heterogeneity a bacterial population is dispersed into a microfluidic droplet emulsion and the resulting droplets are then incubated and later measured for growth. Droplets containing initially resistant bacteria will multiply into a healthy bacterial population. This microfluidic system combined 3 separate devices to achieve its goal. First, a flow focusing microfluidic droplet generator encapsulated an aqueous mixture of bacteria and antibiotic solution within a droplet emulsion dispersed within a continuous fluorocarbon oil phase. After incubation, these droplets are then passed to a second device that uses pico-injection to inject a dye into the droplets that indicates cell viability. After a final incubation, the droplets are then passed to an ultra-high-throughput fluorescence detection device that uses fluorescence of the dye to detect bacterial growth at a rate of around 1600 droplets per second. This device was successful in the rapid phenotyping of antibiotic resistance with high resolution, and moving forwards it is hoped that this microfluidic system will be used to study the evolution of heteroresistance and the conditions that support it. Clinically, this information might be used to influence therapeutic decisions, using data more suitable than population-averaged measurements.

A droplet based microfluidic system has been developed by Konry *et al.* to perform phenotypic-based antimicrobial susceptibility testing [137]. This device generated microfluidic droplets that contained equal parts urine sample (containing live bacterial cells), and antibiotic solution. Using an initial bacterial concentration of 5×10^4 CFU ml^{-1}, bacteria were distributed amongst the droplets such that 14% of droplets contained no bacteria, 68% of droplets contained less than 4 bacteria and 18% of droplets contained more than 4 bacteria. These

droplets were then passed to a temperature controlled 1000 droplet "docking array", where they were imaged. Bacterial population sizes and cell morphologies were measured. Changes in bacterial number and bacterial length were calculated for 50 populations at each experimental condition. This study demonstrated an early proof-of-concept microfluidic device that was used successfully in antibiotic susceptibility testing of clinically relevant *E. coli*. This approach significantly improves upon the readout times of standardised bulk antimicrobial susceptibility testing which requires more than 16 hours for completion. This microfluidic system provided actionable readouts within 1 hour of on-chip incubation. It is hoped that this microfluidic system could form the basis of a high-throughput platform for antimicrobial susceptibility testing. Although this device can only test a single condition at a time, efforts are being made to parallelise this microfluidic testing platform.

Postek *et al.* have developed a droplet-based microfluidic device to encapsulate small populations of bacteria within droplets in order to study an extreme case of the inoculum effect observed at low bacterial concentrations[131].

Inoculum effect

The inoculum effect is a behaviour observed in antibiotic research where the MIC of an antibiotic significantly increases with an increase in initial bacterial inoculum[144].

This was accomplished by using a droplet generating microfluidic device to encapsulate bacteria, aqueous growth media and the antibiotic cefotaxime within microfluidic droplets. These droplets were then incubated off-chip. After incubation, the droplets were introduced to a second microfluidic device that detects and records a fluorescence intensity value for each droplet, which is used as a measure of total growth. An inoculum effect was observed in the droplets as initial bacterial concentration was increased. Bacterial aggregation was also observed at high antibiotic concentrations. The group believe this device could be used in a variety of studies to further our understanding of the inoculum effect in small bacterial populations, as well as find use in more general research that requires a large number of reaction chambers per set of reaction conditions.

2.7 Summary

In this chapter, I have summarised a number of core topics that I feel are important to the work completed in this thesis.

First, I discussed the importance of antibiotic research and why renewed and continued efforts into this field are critically significant moving forwards. Moving on from this, I discussed the principles underpinning brightfield and fluorescence based microscopy, as well as outlining several state-of-the-art microscopy techniques that are used in quantitative microbiology. I then introduced microfluidics and some of the basic theoretical concepts that underpin our understanding of fluid flow at the micro-scale. In the process I defined the dimensionless Reynolds number, further explaining why flow in the low Reynolds number regime is relevant to microbiology. After this I presented a number of studies that utilised continuous flow microfluidics as an experimental platform, first focusing on more general applications before discussing applications with direct microbiological relevance.

I then discussed the field of droplet microfluidics at length - an experimental technique that takes advantage of the unique properties of microfluidic flow to manipulate materials encapsulated within micro-scale droplets. This began with another introduction to microfluidic theory, this time highlighting the Weber number and the Capillary number: dimensionless quantities that are especially useful when describing the behaviour of microfluidic droplets. The concept of microfluidic droplet generation was explored. The two primary methods of microfluidic droplet generation: the T-junction and the flow-focusing junction, were outlined. Emphasis was placed on the numerous experimental and theoretical studies that have been conducted to further our understanding of these deceivingly complex microfluidic geometries. Finally, the many applications of droplet microfluidics were discussed, beginning with more general implementations such as chemical synthesis before moving onto biologically focused applications and studies. Three investigations were referenced[43][131][137] that utilised droplet microfluidics to study the effects of antibiotic inhibition on small bacterial populations, these works are of critical relevance to this thesis and will be referred back to in subsequent chapters.

Chapter 3

Methods, Materials and Fabrication

3.1 Introduction

In this chapter, I present the common materials, techniques and fabrication protocols used throughout this thesis. To begin, I will outline all of the materials used in the fabrication of the microfluidic system that we designed for this research project. Similarly, I will summarise all of the materials required to use our microfluidic system to study bacterial growth in the presence of antibiotic. Alongside this I will outline the microbiological protocols that are used to prepare these materials. After this, I will present the fabrication protocol of our microfluidic master mould, and then the protocols used in the fabrication of the microfluidic devices that make up our system. Lastly, I will discuss ancillary equipment that was used to obtain experimental data using our microfluidic system.

Whilst the materials and methods are described here in relative abstraction, they will provide key context to subsequent chapters. In particular, the materials and methods that we chose to employ when fabricating our microfluidic system had a direct and tangible impact on the design choices and processes detailed in chapter 4.

3.2 Materials

When fabricating a microfluidic device it is important to use materials that complement the objectives of the research that will be conducted using the device. All the materials used in the fabrication of our microfluidic devices were primarily chosen to promote the effective generation of microfluidic droplets for the express purpose of encapsulating biological cells. A secondary emphasis was placed on ease of fabrication: prioritising the use of techniques and materials that are readily available to academics working in a non-specialist laboratory.

3.2.1 Polydimethysiloxane

Our microfluidic device is primarily fabricated using Polydimethylsiloxane (PDMS). PDMS is a silicone elastomer, generally supplied as a base and curing agent that are mixed at a ratio of 10:1 to produce an elastomeric polymer[111]. PDMS is often used as the base material in biological microfluidic research due to a plethora of favourable physical characteristics[76][111]. In particular, PDMS is optically clear down to 240 nm[145], allowing straightforward operation in conjunction with a number of microscopy techniques[146]. PDMS also possesses good bio-compatibility[75] and is non-toxic to cells [146]. It is gas permeable[76], permitting the exchange of gaseous products with the surrounding environment. Finally, PDMS is simple to work with: it is soft, flexible and chemically inert[75][76]. PDMS was purchased as Sylgard 184 flowable silicon elastomer in 1.1 kg quantities.

Although PDMS is the most common material used in the fabrication of academic microfluidic devices, there are a number of alternatives. Silicon and glass have long been used in the fabrication of microfluidic devices, however the associated material costs combined with the complex process of chemical etching results in an expensive fabrication procedure that requires the use of specialist equipment. The use of other polymeric materials is also commonplace; polyvinyl chloride (PVC) and polymethylmethacrylate (PMMA) are used frequently in the manufacture of microfluidic devices. These materials are generally inexpensive, robust and biologically inert. We felt that whilst many of the properties of these materials were attractive, there were some significant drawbacks associated with these materials. For example, fabricating these types of polymeric microfluidic devices requires the use of specialist equipment not generally available in an aca-

demic laboratory. They are also gas impermeable, resulting in a device that does not allow for the exchange of gaseous materials into and out of the microfluidic device. Furthermore these devices are generally re-used from one experiment to the next, necessitating the use of additional sterilisation protocols when biological materials are passed through them.

3.2.2 Carrier oil

Despite the many positive physical attributes of PDMS listed in the previous section, PDMS suffers from swelling when introduced to many organic solvents. This swelling can render a device unusable, therefore in the context of droplet microfluidic systems, organic carrier phases such as hexadecane and mineral oil cannot be used[111]. To avoid this problem, aqueous microfluidic droplet emulsions are often suspended in a fluorinated oil carrier fluid[147]. Fluorinated oils also benefit from being biologically inert[148][149], with a low solubility for many biological reagents. Fluorinated oils also possess a high gas permeability [119][150], allowing gaseous waste products to diffuse from a droplet whilst allowing oxygen to reach the droplet interior.

We chose to use FC40 as the fluorinated oil carrier phase in our microfluidic droplet experiments[137][151][152]. FC40 is a fluorinated oil commonly used as a carrier phase when encapsulating biological material within microfluidic droplets, and possesses all of the positive physical characteristics detailed above. FC40 was purchased from Sigma-Aldrich in 100 ml quantities.

3.2.3 Droplet surfactant

A surfactant is required to stabilise the droplet interface between the FC40 carrier oil and the aqueous growth media encapsulated by each droplet. This drastically reduces the rate at which droplets coalesce (even when confined in close contact with one another), whilst also ensuring biological reagents do not adsorb to the oil-water interface[148][150]. There are a number of commercially available surfactants suitable for use in fluorocarbon systems, as well as literature detailing the synthesis of specialised fluorocarbon surfactants[148].

We use the commercially available fluorosurfactant Pico-Surf 1[152][153][154][155]. It is a biocompatible fluorosurfactant consisting of a perfluoropolyether tail and

a polyalkylene oxide unit headgroup[156], it is stable across an extensive range of temperatures and supports a variety of biological conditions. This has been used successfully in a number of separate studies and is designed to be compatible with the Pico-Glide 1 surface treatment we use to ensure channel hydrophobicity (see section 3.2.4). Pico-Surf 1 was purchased in 10 ml quantities at a concentration of 5% (w/w), in FC40. It was diluted to a concentration of 2.5% (w/w) using FC40.

3.2.4 Device hydrophobicity

During droplet generation it important that the aqueous phase does not wet or pin against the microfluidic channel as this can cause droplet coalescence, or worse, completely prevent the production of a monodisperse emulsion [90][157]. During droplet storage and imaging, it is crucial that the aqueous droplets do not wet the surface of the microfluidic channels as this would allow encapsulated bacteria to interact directly with the channel surfaces of the microfluidic device. To prevent the aqueous phase wetting onto the channels of our microfluidic device, it is essential that the walls of the PDMS device are highly hydrophobic and if possible, fluorophilic.

Freshly cured PDMS is naturally hydrophobic, therefore polar fluids such as water cannot easily wet its surface. Plasma treatment is required to bond PDMS to a glass substrate during the fabrication of a microfluidic device. Unfortunately when PDMS is plasma treated it is rendered hydrophilic[158][159]. This is due to surface oxidation forming a brittle, silica-like SiO_x-rich layer[160][161]. There are two common methods used to revert the channels of a PDMS-based microfluidic device to their original hydrophobic state; heat treatment and chemical treatment.

Heat treatment

It has been shown that PDMS will naturally revert to a hydrophobic state after plasma treatment. This reversal is due to the migration of low molecular weight PDMS chains from the bulk of the material to the oxidised surface[158]. This process takes between 200 and 1000 hours[161], however this can be expedited by baking the PDMS at a high temperature (e.g. 65°C for several days)[76].

When plasma treating our first generation microfluidic devices, we found that sufficient hydrophobicity was recovered by simply baking our microfluidic devices at 80°C for 24 hours. Unfortunately, as we began testing more complex microfluidic designs, the aqueous phase began to wet/pin to the surface of some microfluidic channels. This was most apparent when passing droplets through highly constricted microfluidic features with a channel depth of 11 μm. This aqueous pinning caused droplet coalescence.

Contact angle measurements

Contact angle measurement is a common technique used to quantify the wettability of a solid by a liquid[162]. The contact angle can be geometrically described as the angle formed by a liquid at the three-phase boundary i.e. at the intersection of a liquid, solid and gas.

In this thesis, static contact angle measurements were taken using the sessile droplet method, where droplets of deionised water are delivered to a PDMS surface using a calibrated syringe and subsequently imaged.

To quantify this change in hydrophobicity, contact angle measurements were taken of desionised water on the surface of freshly cured PDMS. These measurements were then compared to contact angle measurements of a PDMS surface that was exposed to oxygen plasma (using the same experimental parameters as detailed in section 3.4.4) and then heat treated at 80°C for 40 hours. These measurements showed that, as anticipated, freshly cured PDMS is highly hydrophobic with a contact angle of 118.8° (measured using an elliptical approximation). After 40 hours of heat treatment, plasma exposed PDMS had not fully recovered its hydrophobic character, with a measured contact angle of 95.4°. This is consistent with literature measurements which have measured the contact angle of pristine PDMS to be between 100° and 120°[158][162][163]. These measurements can be seen in figure 3.1.

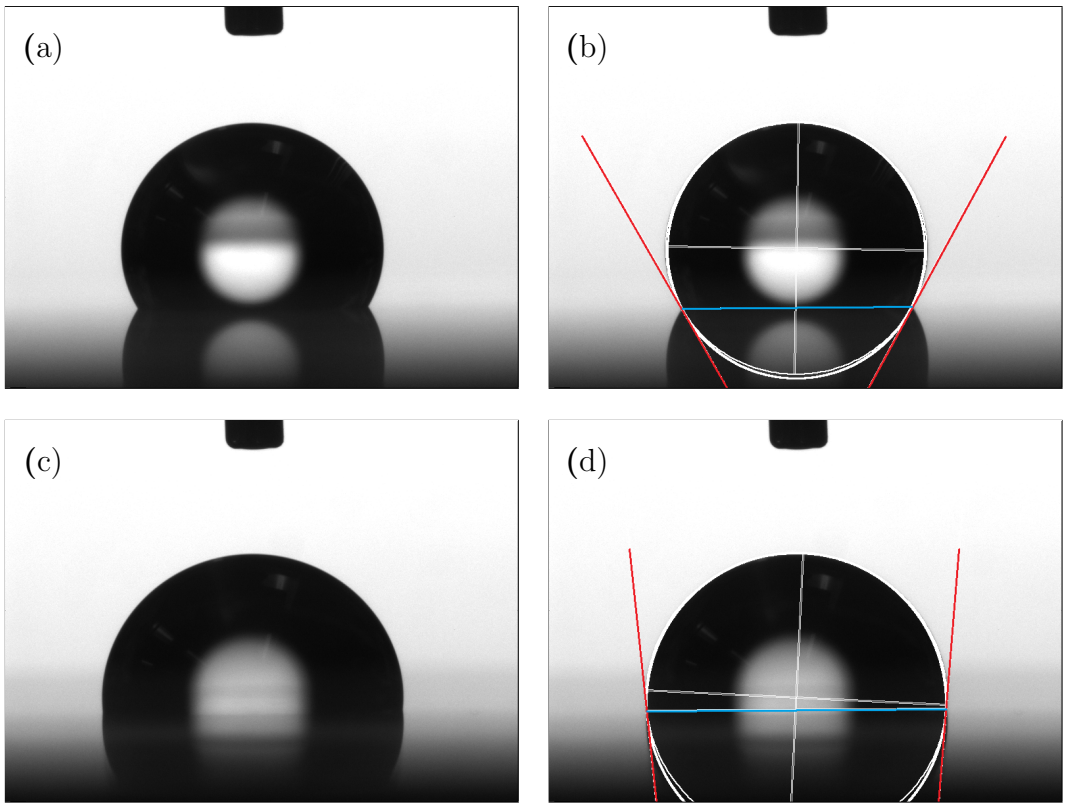

Figure 3.1 *Images showing wetting of deionised water on the surface of a PDMS coated glass slide. (a) and (b) show a droplet of water on a freshly cured PDMS surface, the contact angle measured using an elliptical approximation is 118.8°. (c) and (d) show a droplet of water on a PDMS surface that has been exposed to oxygen plasma (50 seconds at 35 W) and then heat treated for 40 hours, the contact angle measured using an elliptical approximation is 95.4°.*

Furthermore, studies have shown that whilst PDMS surfaces exposed to oxygen plasma revert back to a hydrophobic state, full recovery to the same level of hydrophobicity/wettability has not been observed[158][161]. Because of this, we explored alternative solutions that would promote full hydrophobic recovery of PDMS after plasma treatment.

Chemical treatment

It is possible to restore high levels of hydrophobicity to plasma treated PDMS-based microfluidics using chemical treatments[76][111]. These are generally specialist solutions that contain surface active species that interact with plasma treated PDMS surfaces[164] to render them hydrophobic[165]. Generally, these chemical treatments are flushed through the device as a pre-treatment prior to use.

"Aquapel" is a chemical marketed as a rain repellent treatment for glass. It is commonly used as a hydrophobic surface treatment in microfluidic research due to its low cost and efficacy as a hydrophobic PDMS surface treatment[152][166]. Despite its widespread use in microfluidic research, we found Aquapel to be unsuitable for use in our more complex microfluidic designs. When it is passed through long channels of low cross-sectional area, prolonged exposure to air causes the Aquapel to precipitate[152], rendering the channels functionally useless.

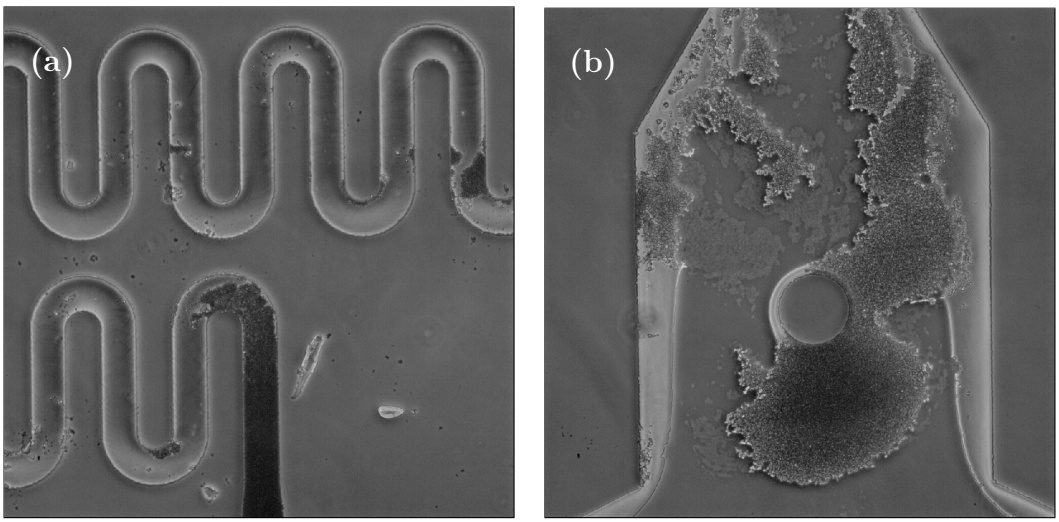

Figure 3.2 *Aquapel precipitation observed in the channels of our microfluidic system. This was observed most frequently in, or directly after, long channels of low cross-sectional area.*

Due to this, I instead used a commercially available solution called Pico-Glide 1, which is manufactured by Dolomite Microfluidics[155][167]. Pico-Glide 1 contains a fluorinated polyether polymer at a concentration of 0.5% w/w and is chemically reactive to plasma treated PDMS and glass. During treatment, PicoGlide interacts with microfluidic channels to form a covalently bonded, dense fluorophilic layer that enhances droplet stability.

Although substantially more expensive than Aquapel, I have found PicoGlide to be effective at reducing droplet wetting and increasing long term droplet stability. Pico-Glide 1 was purchased in 10 ml quantities at a concentration of 2% (w/w) in FC40, and was used as received.

3.2.5 *E. coli*

The bacterial strain used exclusively in this thesis is an *E. coli* mutant named RJA002[168][169]. This mutant was created in the Edinburgh laboratory by Pl transduction from strain MRR (supplied by the Elowitz lab [170]) and selection on chloramphenicol. This mutant contains the gene for YFP integrated on its chromosome at loci *intC*. The YFP gene is under the control of the phage lambda Pl promoter, which is constitutively expressed - this means that RJA002 produces YFP continually.

3.2.6 M9 growth media

M9 minimal growth media (M9) is a liquid growth media commonly used in the cultivation of *E. coli*. It is an inexpensive, well defined and minimal media that needs to be supplemented with a carbon source and can be further augmented with additional metabolites. M9-based media are preferred in imaging applications due to their low levels of auto-fluorescence.

M9 X4 salt stock was prepared by mixing 28 g Na_2HPO_4, 12 g KH_2PO_4, 2 g NaCl and 4 g NH_4Cl with 1 l dH_2O. M9 minimal media was prepared by mixing 100 ml of M9 X4 salt stock with 300 ml dH_2O, 800 μl of 1 M $MgSO_4$ and 40 μl of 1 M $CaCl_2$ is then added. 8 ml of 20% w/v glucose is added, bringing the carbon source to a concentration of 0.4%. Herein M9gl refers to M9 minimal media supplemented with glucose at a concentration of 0.4%.

3.2.7 Agarose Plates

Agarose (agar) plates are petri dishes that contain agar supplemented with nutrients to form a solid growth medium. Selection pressures can be applied with the addition of compounds such as antibiotic. Agar plates are seeded with a bacterial strain by streaking bacteria across the surface in a controlled manner, this streaking process is used to reproducibly isolate single bacteria to obtain isogenic starting populations.

Streaking an agar plate

Streaking an agar plate is a method of isolating, growing and storing small isogenic bacterial populations. These can then be extracted from the agar plate and used as starting colonies in experimental microbiological work. A small volume of frozen bacterial stock is streaked across a subsection of an agar plate using an inoculation loop. The loop is sterilised and then streaked through the initial subsection into a fresh subsection of agar. This process is repeated 4 times in total, each time streaking through the previously streaked subsection. Correctly streaking a plate should result in the growth of individual colonies on the final path of the inoculation loop.

Agar plates supplemented with M9gl were used for the mid-term storage of isogenic bacterial stocks. These were made by mixing M9 X4 salt stock with 300 ml of liquid agar preheated to a temperature of 60°C. $MgSO_4$, CaCl and glucose was then added in quantities matching those given for the liquid growth media. Once the liquid agar had been prepared, multiple plates were made simultaneously by pouring the agar mixture into plastic petri dishes to a depth of ≈5 mm. These were then covered with their respective lids and allowed to cool for 30 minutes. Once the agar had solidified, the petri dishes and lids were inverted and placed in an oven at ≈40°C until all condensation had evaporated. The plates were then sealed using plastic paraffin tape, stored at 4°C, and used within 6 weeks.

Bacteria were added to the plates by streaking with the required strain taken from freezer stock. They were then sealed with plastic paraffin tape and incubated in a stationary incubator until individual colonies were visible (usually between 24 and 36 hours). The plates were then stored at 4°C, and used within 2 weeks.

3.2.8 Streptomycin

Stock streptomycin solutions were prepared by mixing streptomycin sulfate salt with dH_2O to a concentration of 500 μg ml^{-1}. These stock solutions were then sterilised using a 0.22 μm filter, stored at -20°C and used within 3 months. Further stock solutions of streptomycin at lower concentrations were prepared for each experimental run from the original 500 μg ml^{-1} stock. These were stored at -20°C and discarded after 3 freeze-thaw cycles or after 3 months, whichever came first.

3.3 Fabricating a PDMS-based microfluidic device

3.3.1 Overview

In this section, I will outline the protocol that was developed to fabricate our microfluidic system. This is split into two primary sections: the fabrication of a microfluidic master mould using a photomask, and the fabrication of a fully functional microfluidic device using this microfluidic master mould. A microfluidic master mould, herein referred to as a microfluidic master, is a mould that can be used to repeatedly cast a microfluidic device from an elastomeric material.

Soft lithography refers to a set of techniques that can be used to fabricate structures from elastomeric materials, and it is used heavily in the fabrication of our PDMS-based microfluidic devices. This multi-stage process is outlined in figure 3.3.

The fabrication protocol used to produce the microfluidic devices developed in this thesis contains multiple critical stages that must be completed correctly to produce a functioning microfluidic system. Faults and defects introduced during the fabrication process can result in immediate and obvious device failure, although some faults may only become apparent under device operation. It was vital that a reliable fabrication protocol was developed and followed to avoid wasting both time and resources on the fabrication of a faulty microfluidic device.

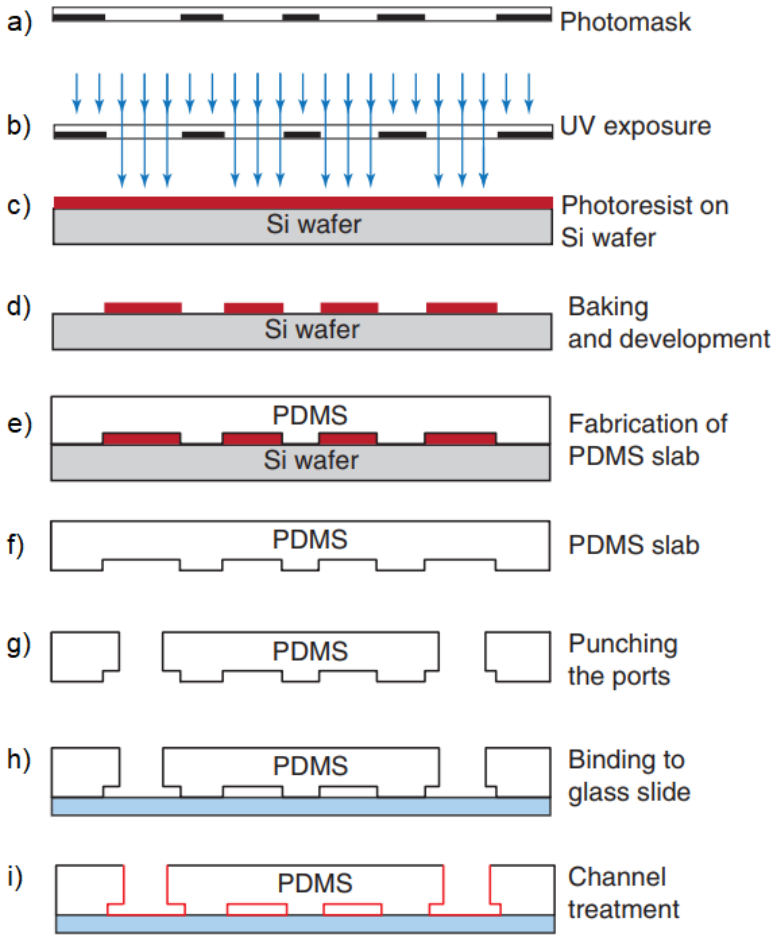

Figure 3.3 *Diagram outlining the soft lithographic process used when fabricating a PDMS-based microfluidic device. In (a) - (d), a microfluidic master mould is fabricated using a photomask. In (e) - (g) a PDMS-based mircofluidic device is cast using the master mould. In (h) and (i) a microfluidic device is bound to a glass substrate and prepared for use. Taken from [152].*

3.3.2 Fabrication protocol - photomask and master mould

The fabrication of a microfluidic master is a highly technical process that involves the use of a custom microfluidic photomask. This is the only procedure in our fabrication protocol that requires the use of specialist equipment not generally available to those working in an academic laboratory. The custom microfluidic photomask that we used in the master fabrication process was made by JD-PhotoData. It is a 4″ low reflective chrome photomask printed onto a 1.5 mm soda lime glass base substrate at a resolution of 128k DPI.

Our final microfluidic design required the fabrication of two microfluidic masters, one with a channel depth of 34.5 μm and the other with a channel depth of 11.5 μm. The microfluidic masters were fabricated in collaboration with the Scottish Microelectronics Centre.

They were made by first spin coating SU8-3010 on a 4″ silicon wafer. The SU8-3010 was spun for 2 minutes at 2000rpm to achieve a channel depth of 34.5 μm and for 2 minutes at 4000rpm to achieve a channel depth of 11.5 μm. Following spin coating, the wafers were pre-baked for 1 minute at 65°C followed by a soft bake for 10 minutes at 95°C. After this, the wafers were exposed to UV light through a photomask for 2 minutes and then baked a second time for 1 minute at 65°C and then 2 minutes at 95°C. Finally, the microfluidic masters were rinsed in propylene glycol methyl ether acetate (PGMEA) until only the crosslinked SU8-3010 remains, usually after around 4 minutes.

3.3.3 Fabrication protocol - PDMS-based microfluidic device

Making microfluidics for this application does not require the use of a clean room, but care does need to be taken to reduce contamination at all stages of device fabrication. All microfluidic devices were stored in sterile disposable petri dishes when not being handled directly.

To make a device, 30 g of PDMS was prepared by mixing the 2 part product in a ratio of 10 parts elastomer to 1 part crosslinking agent. The two components were mixed thoroughly for 5 minutes, ensuring the crosslinking agent was completely combined with the elastomer. Care was taken to avoid contamination of the liquid PDMS as dust mixed into the PDMS can cause issues when using the microfluidic device. Bubbles of air introduced during the mixing process were removed by placing the PDMS mixture under vacuum for 30 minutes. The vacuum was vented every 5 minutes as this acts to burst the bubbles of air once they have risen to the surface of the PDMS. The microfluidic master was placed into a glass petri dish. The PDMS was then poured to a depth of 15 mm over the master and then placed under vacuum until all bubbles on the surface of the microfluidic master had been removed. The master was covered using the petri glass lid and then baked for 90 minutes at 80°C until fully cured.

A scalpel was used to remove the excess PDMS from each of the microfluidic designs. Inlet and outlet holes were then punched into the microfluidic designs using a biopsy punch. 20 mm lengths of glass capillary were then inserted into the freshly punched holes, leaving the excess length of capillary protruding from the opposite face of the PDMS to the microfluidic design. Contaminating debris from the punching process was removed from the inlets and outlets by flushing the capillaries with compressed air. The surface of the PDMS devices featuring the design were then cleaned using compressed air and the repeated, gentle application of adhesive tape.

A microfluidic design and glass microscope slide was placed into a Diener Zepto plasma oven, feature side exposed. These were then exposed to an oxygen plasma for 55 seconds at a power of 35 W. The plasma oven was then vented and the contents were removed. The feature side of the microfluidic design and the exposed face of the glass slide were brought together. With the gentle application of pressure the two surfaces were permanently bonded to one another. Once the microfluidic device had been bound to the glass substrate, the perimeters of the glass capillaries were sealed to the PDMS with the application of a 2-part epoxy resin.

The final stage in device fabrication was to treat the device with PicoGlide, a chemical treatment that makes the surfaces of the microfluidic channels both highly hydrophobic and fluorophilic. 500 μl of PicoGlide was manually flowed into the device using a 1 ml syringe. The channels were filled completely and the device was left for 60 minutes. The channels were then flushed free of PicoGlide and the device was stored in a sealed, clean environment until use.

3.4 Equipment

3.4.1 Microscope and camera

The microscope used in this project was a Nikon Eclipse Ti epi-fluorescent inverted microscope. For all imaging, a Nikon Plan Fluor 20x/0.5 objective was used. The camera used for both brightfield and fluorescence microscopy was a Hamamatsu Orca-Flash4.0 V2 (C11440-22CU). This camera uses a CMOS image sensor that has a 6.5 μm x 6.5 μm pixel size and 2048 x 2048 imaging pixels. A 2 x 2 pixel binning regime was used, reducing image size to 1024 x 1024 pixel^2.

The exposure times for brightfield and fluorescence imaging was 10 ms and 50 ms, respectively. When using fluorescence microscopy to image bacteria expressing YFP (*E. coli* strain RJA002), illumination was provided by a broad spectrum Mercury lamp used in conjunction with a Chroma EYFP filter (λ_{em} = 500 nm, λ_{em} = 535 nm).

A computer controlled motorised microscopy stage was used to automatically scan across the microfluidic reservoir device during imaging. The microcopy stage used was a Prior Scientific H117 motorized precision stage (H117P1N4/F), this stage has a travel range of 114 mm x 75 mm, a resolution of 0.01 μm and a mean uni-directional repeatability of $\pm$0.2 μm. The microscope stage was controlled by a Prior Scientific ProScan III controller in conjunction with a Prior Scientific PS3J100 Interactive Control Centre.

3.4.2 Microfluidic device mount

The high gas permeability of PDMS is useful as it allows gaseous waste products produced by bacteria (see section 2.2.3) to escape from a PDMS-based microfluidic device. Unfortunately, a consequence of this gas permeability is that it allows for the evaporation of the aqueous phase from the microfluidic device[145][171]. Evaporation is a significant problem when culturing bacterial populations as even small reductions in droplet volumes can significantly increase the osmolality of the confined aqueous environments. This is problematic as changes in osmolality can significantly disrupt important cellular functions such as growth rate, metabolism [172] and gene expression[173].

In initial testing, we immediately noticed this aqueous evaporation. When storing our microfluidic droplets, they would steadily decrease in volume, losing more than half their volume over the course of a few hours. To retard this evaporative effect, many groups seal their microfluidic devices using sticky tape or some other non-permeable material, or prime their device by storing the device in water before/during experimentation[174]. We chose to utilise the second method as it afforded us an additional benefit: by submerging the device in a temperature controlled water bath we could eliminate droplet evaporation whilst regulating the temperature of our microfluidic system during experimental runs.

To accomplish this goal, we designed a custom microscope mount that incorporated a reservoir we could couple with an external temperature controlled water bath. The device mount was designed and modelled in FreeCAD. We chose to 3D-print the device mount for multiple reasons. Firstly, 3D-printing is highly time efficient; by using this fabrication technique it was possible to repeatedly and rapidly prototype multiple iterations of a design with turnaround times of less than a day. Secondly, the process is labour efficient; we did not require a university workshop for repeated fabrication of prototype designs. Finally, 3D printing is cheap and scalable at the academic level: material costs can be a fraction of those for traditional fabrication techniques and once the design has been finalised it is available for others to print and use themselves.

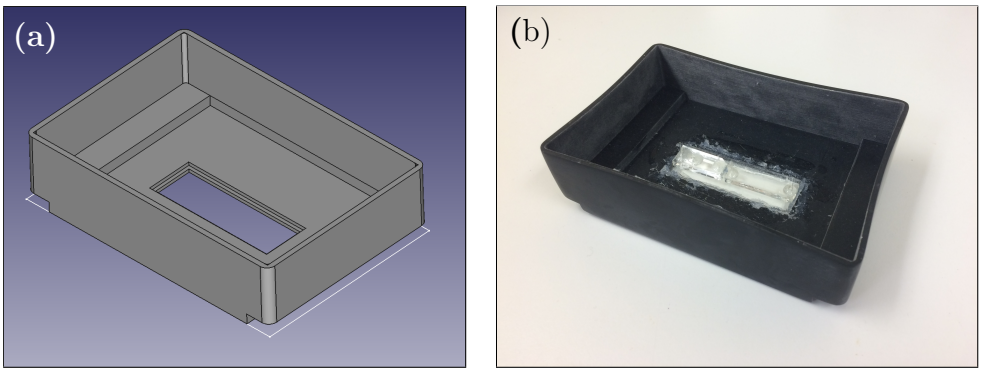

Figure 3.4 *Images of the microfluidic device mount. (a) Shows the 3D model of the device mount that was sent to the 3D printing service, (b) shows the final printed device mount, in this example image a microfluidic device has already been mounted and sealed.*

3.4.3 Syringe pumps

As discussed in chapter 2, the size distribution of droplets generated in a flow focusing junction is intrinsically linked to the fluid velocities of the two fluid phases. Because of this, it is vital that the flow into the microfluidic device is steady and controlled to ensure a truly monodisperse droplet emulsion.

Flow rates less than 10 μl hr^{-1} are commonplace in the field of microfluidics[134], so the minimum flow rate of 20 μl hr^{-1} used in this thesis does not require particular focus or attention. Two "New Era NE-1002X" microfluidic single syringe pumps were used to control the delivery of the aqueous and oil phases.

These are designed to provide smooth linear pumping at flow rates as low as 0.008 nl hr^{-1}[175]. During droplet generation the oil phase was pumped at a flow rate of 80 μl hr^{-1}, whilst the aqueous phase was pumped at a flow rate of 20 μl hr^{-1}.

3.4.4 Plasma oven

Oxygen plasma is used to bond the PDMS microfluidic device to a glass substrate, thus sealing the microfluidic channels[176]. Oxidised PDMS readily bonds to an oxidised glass surface upon contact to form an irreversible seal. This seal is believed to be the result of surface oxidation developing silanol groups (at the expense of methyl groups). These silanol groups form bridging siloxane (Si - O - Si) bonds via condensation reactions when brought into contact[162][177]. A Diener Zepto plasma system was used to bond the microfluidic devices to a glass cover slip. PDMS and glass components were exposed to oxygen plasma for 55 seconds at a power of 35 W.

3.5 Concluding remarks

The materials and fabrication techniques we used to fabricate our microfluidic system were chosen as their strengths and weaknesses optimally matched the experimental objectives of the system. Furthermore, they provided a high degree of bio-compatibility such that the microfluidic devices we have developed could be used to study different biological systems in the future. Finally, the materials, tools and techniques used in the fabrication process did not require specialist knowledge or understanding of microfluidic fabrication protocols. We believe that our choices of materials and fabrication techniques are complementary to both our experimental objectives and our requirement that the device be accessible to the non-specialist.

Chapter 4

Designing a Microfluidic System for the Encapsulation of Bacterial Populations

4.1 Introduction

In this chapter, the design process of our microfluidic device will be detailed. The development of our microfluidic system was an iterative process which involved the design, fabrication and testing of multiple microfluidic geometries.

I will first discuss why we chose to design a droplet-based microfluidic system for our research. After this I will outline a number of key microfluidic design principles that we found to be important in the creation of efficient, reliable and useful microfluidic designs. These rules of good practice are tailored towards droplet based microfluidics, but many of them are also applicable to the optimisation of any single layer microfluidic design. This will be followed by a chronological account of the development of our microfluidic device. In this development process we incrementally improved the design of our device over three generations before arriving at a device design that we felt was fully appropriate for our research and needs. Finally, I will detail our final microfluidic device design, focusing on how we implemented our rules of good practice to produce a device that fulfills our project requirements whilst remaining reliable and easy to use.

4.1.1 Continuous flow microfluidics versus droplet microfluidics

After reviewing the numerous microfluidic systems discussed in section 2.5, we chose to use a droplet-based microfluidic system in our research. A key requirement of our microfluidic system was that it needed to generate large numbers of bacterial environments that are identical, and critically, independent. We could not find a literature example of a single-level, continuous flow microfluidic device that was able to encapsulate and isolate small bacterial communities. Whilst the work completed by Austin *et al.* used continuous flow microfluidic geometries to study small bacterial populations[84][85], this was in the context of connected bacterial populations that were able to exchange individual cells. The "mother-machine" microfluidic system was considered, however in this design each of the confined bacterial populations are not strictly independent from one another. It is entirely feasible that nutrient and antibiotic availability to each bacterial population would not be equal and could be affected by other nearby populations. Likewise, toxic metabolic products from large bacterial populations may begin to impact the growth dynamics of nearby bacterial populations. Furthermore, studies have shown that the mechanical forces experienced by bacteria trapped in the channels of a mother machine cause varying increases in doubling times when compared to bulk growth techniques[178].

In contrast, it is possible to create thousands of isolated and independent bacterial environments using microfluidic droplets. These droplets can be moved, manipulated and studied using a variety of standard microfluidic geometries and techniques[76][94]. Additionally, bacterial populations encapsulated within the droplets are not mechanically confined in the same manner as those stored in the standard mother machine. As such, we decided that for our use case it was more appropriate to use a droplet-based microfluidic platform in our research.

4.2 Designing a microfluidic device

The first step in creating a microfluidic device using is the process of designing its two-dimensional geometry. This design outlines the channels and features of the microfluidic device from a top-down perspective. There are many factors to consider when designing a microfluidic device, each of which can drastically

affect its functionality and experimental reliability. Well designed microfluidic devices allow for fast fabrication and reliable operation under a robust set of conditions. Poorly designed microfluidic devices can be difficult to fabricate, take a long period of time to prepare and only function under a very specific subset of operating conditions.

4.2.1 Technical detail

For the fabrication of a custom microfluidic photomask, a design file is required that details the exact dimensions of every channel and feature encompassed within the microfluidic design. This is usually generated using a CAD-based design software package.

There are a number of resources available that allow researchers to download pre-validated microfluidic designs that can be used for a number of purposes[179]. These pre-validated designs were not used in the work completed in this thesis for two primary reasons. Firstly, the final microfluidic system that we designed for this project combines a number of standard microfluidic geometries with novel geometries. It was felt that whilst the aforementioned pre-validated designs may have served as good starting points for our microfluidic system, they would require significant modification and integration to fully satisfy our experimental objectives. This is compounded by the fact that our final microfluidic system needed to be designed to operate in conjunction with the specific equipment available to our research group. Secondly, we believed that by designing our microfluidic systems from the ground up, we would derive a far better and more intuitive understanding of microfluidic droplet behaviour. We hoped that this would allow us to troubleshoot and diagnose experimental problems more efficiently, whilst being able to more effectively improve the microfluidic design if necessary.

For these reasons, all of the microfluidic designs used in this thesis were designed from scratch. We have found the KLayout[180] software package to be a powerful platform on which to design single layer microfluidics. By taking advantage of KLayout's hierarchical drawing structure, it was possible to quickly and efficiently implement the extensive repeating structures common to microfluidic designs.

4.3 General design principles

Through the continued iterated improvement of our microfluidic devices, we developed a set of generalised design principles that ensured our designs produced efficient and reliable microfluidic devices that were easy to fabricate and use. We focused on designing robust droplet-based microfluidic devices that could be fabricated and used within a traditional academic laboratory without the need for specialist equipment, techniques or handling requirements. These design guidelines were primarily established during the iterative development of our first two microfluidic designs. Our final microfluidic design incorporates all of the design principles detailed below.

4.3.1 Consider channel dimensions and their transitions

Match channel transitions

Generally, when a fluid flows from a channel of lower cross-sectional area to a channel of higher cross-sectional area, it will experience a decrease in flow velocity. If this transition is sudden, then droplets being carried in the fluid will experience a rapid decrease in velocity. This can cause high speed droplet collision and coalescence. To avoid such droplet collisions, when designing a transition from a channel of lower cross-sectional area to a channel of higher cross-sectional area it is important to graduate the transition using a cone/funnel geometry. Likewise, to avoid droplet compression and coalescence events occurring when transitioning from a channel of higher cross-sectional area to a channel of lower cross-sectional area, channel geometry should also be graduated.

Oversized outlet channels

It was observed that when trying to evacuate large numbers of droplets from wide (1000 μm) storage channels through narrower (100 μm) outlet channels, droplets could jam against one another and become immobilised. This caused droplets to back up toward the inlet and coalesce under compression. In extreme instances, droplets caused significant channel deformation and the microfluidic device eventually burst under pressure. As such, it is recommended that outlet channels have a greater total cross-sectional area than inlet channels to support a higher flow throughput.

4.3.2 Large inlet/outlet size

When the inlets and outlets of a microfluidic device are fabricated using a biopsy punch, PDMS in the immediate vicinity can become deformed. Due to the stark transition in scale when an inlet/outlet interfaces with a microfluidic device, these PDMS deformations can cause nearby microfluidic channels and features to become permanently warped or misshapen. To ensure this does not happen, it is important to design large inlet/outlet areas that remove the potential for PDMS deformations to affect nearby microfluidic structures. In the microfluidic designs used in this thesis, a minimum inlet/outlet size of 3000 μm x 3000 μm is used.

4.3.3 Minimise hydraulic resistance

Long channels and tight constrictions both act to increase microfluidic flow resistance through a microfluidic device. This high resistance increases internal pressure, which in turn can cause PDMS channels to deform. This deformation under high pressure means that changes in flow rates can take an excessive period of time to equilibrate and stabilise, this causes the microfluidic device to feel unresponsive when changing input flow rates. Therefore, when designing a device the channel dimensions should be optimised such that experimental objectives can be accomplished whilst channel lengths and constrictions are minimised. Minimising resistance leads to a device that is easy to use and responds quickly to flow rate changes, allowing droplet size adjustments to be made without significant delay.

4.3.4 Separate designs

It is often beneficial to repeat the structure of a single device multiple times across a microfluidic photomask, as this allows multiple devices to be fabricated from a single PDMS cast. If the repeat designs are positioned too close to one another however, then it can become difficult to manually detach the designs from one another using a scalpel. This negates the casting efficiency gain by increasing device fabrication failure rate. I found that a spacing of 3 mm allowed designs to be detached from one another easily whilst maintaining efficient use of space on the microfluidic master.

4.3.5 Device support

Channels without vertical support can flex considerably due to the elastic nature of PDMS. This can cause the "roof" of a microfluidic device to bow upwards due to internal pressure or sag downwards from the weight of the PDMS above[181]. Measurements have shown that microfluidic channels with a width/depth value greater than 20 generally require rigid backing support or the addition of supporting columns in the microfluidic design to avoid this disruptive phenomena[182]. This deformation can cause problems when imaging a microfluidic channel as it may allow objects being imaged (typically a droplet) to move unpredictably along the z-axis, in some cases out of the imaging focal plane completely. To prevent the roof of our microfluidic structures from flexing, I incorporated pillar structures into the design where appropriate.

4.4 Device design evolution

Throughout this project our microfluidic device was repeatedly revised and improved, iterating toward a design that we felt adequately met the needs of our experimental objectives. Our initial aim was to design a microfluidic device that could encapsulate small bacterial populations within a monodisperse emulsion of microfluidic droplets. Furthermore, we needed the microfluidic droplets to be stored inside the device so that it was possible to image the encapsulated bacterial populations on a droplet-by-droplet basis. It was our intention that through the use of microfluidics we could significantly improve upon traditional microbiological techniques. Unfortunately, we feel that the widespread adoption of experimental microfluidic systems are currently being hampered by unnecessarily high barriers to entry. As such, parallel to these experimental objectives, we strived to create a microfluidic system that was accessible in both design and fabrication to researchers who have not had extensive experience with microfluidics.

4.4.1 Microfluidic design 1

Our first microfluidic master was an exercise in fundamental droplet microfluidic device design. The device consisted of multiple smaller sub-designs, each intended to test a different aspect of droplet microfluidics. The overall design consisted of two droplet generating designs alongside three designs intended to test how a monodisperse emulsion of droplets would behave under a variety of conditions. The complete set of microfluidic designs can be seen in figure 4.1.

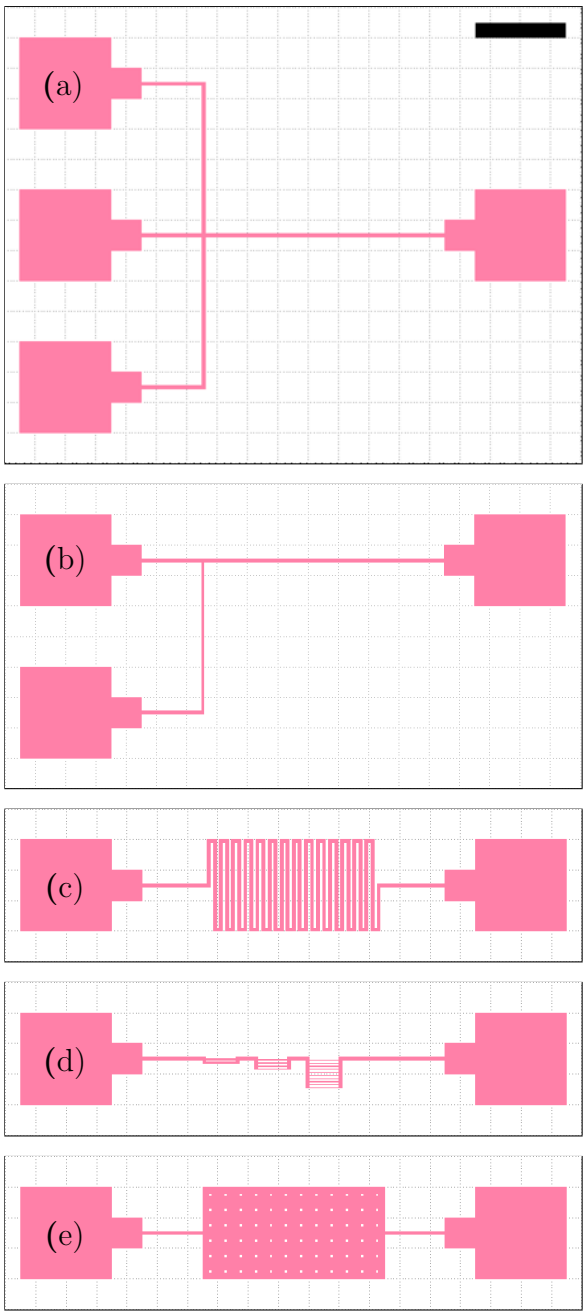

Figure 4.1 *Images detailing the geometries that constitute the first microfluidic design, inlets are shown on the left, whilst outlets are shown on the right. (a) shows the flow-focusing geometry, (b) shows the T-junction geometry, (c) shows the serpentine channel design, (d) shows the microfluidic sieve design, (e) shows the microfluidic reservoir. Scale bar = 3000 µm.*

It was intended for monodisperse emulsions produced by the droplet generation designs to be passed to the testing designs by connecting the outlet of one to the inlet of another. Unfortunately, due to a common design flaw across all of the designs, this was not entirely possible. It was found that a flow transition from a highly constricted channel to a larger channel of much greater cross-sectional area caused a rapid decrease in fluid velocity. This resulted in droplet coalescence due to high speed droplet collisions. This flow transition occurred at the outlet of all of the microfluidic sub-designs in our first generation device (see figure 4.2).

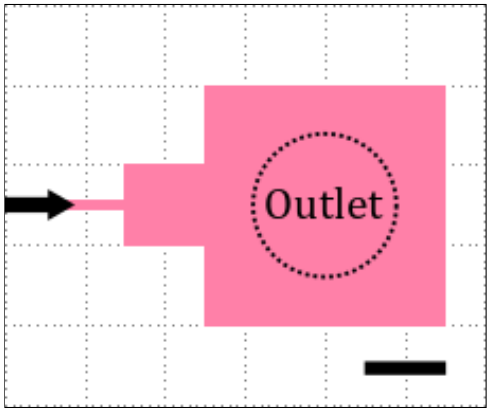

Figure 4.2 *Microfluidic outlet design of our first generation device. Droplets flow in the direction of the arrow toward the outlet which is punched into the device from above. Droplets experience a near-instantaneous decrease in velocity when moving from the channel of 100 μm width to the outlet channel of 1000 μm width. Scale bar = 1000 μm.*

Despite this limitation, it was still possible to test the droplet generation capabilities of our microfluidic designs as well as some of the more basic properties of the other test designs.

Figure 4.1(a) shows the first sub-design, a flow-focusing droplet generating geometry. This microfluidic design was largely a success and was not changed significantly in subsequent designs. This geometry consistently produced size-tunable droplets (30-100+ μm) with low polydispersity at rates of up to 42Hz. It was noted that this design was susceptible to failure if debris blocked the 20 μm constriction at the droplet generating junction, this was remedied in subsequent designs. High speed microscopy images of this flow-focusing droplet generation geometry can be seen in figure 4.3.

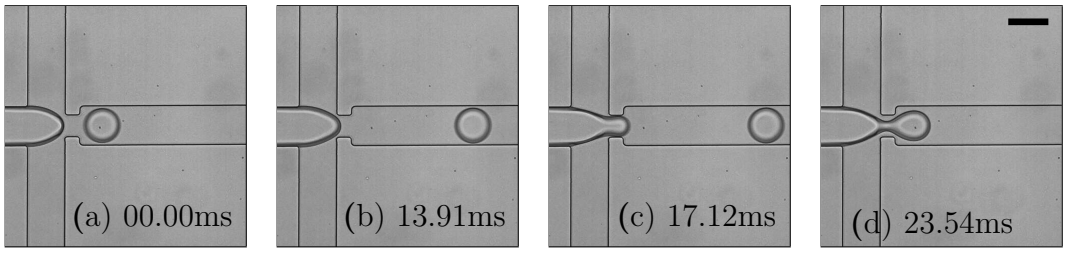

Figure 4.3 *High speed microscopy images of our first generation flow-focusing microfluidic droplet generator. Droplet generation can be seen in images (a) - (d), the relative time between each image is shown. Droplet generation occurs once per 24.61ms, or at a rate of 42Hz. Channels are 100 μm in width. Scale bar = 100 μm.*

Figure 4.1(b) shows the second sub-design, a T-junction droplet generating geometry. Whilst this design was successful in creating an emulsion of microfluidic droplets with low polydispersity, it was found that droplet size did not significantly change even with considerable adjustments to the flow rates.

Comparing the two droplet generation geometries, we decided that the flow-focusing geometry was most suited to our research requirements. Droplet size tunability was highly desirable for our use case, therefore the versatility afforded by the flow-focusing droplet junction was prioritised. All of our subsequent microfluidic designs that generated microfluidic droplets used a flow-focusing junction. The T-junction geometry was not revisited.

Figure 4.1(c) shows the third sub-design, a microfluidic serpentine channel. It has been shown that the contents of microfluidic droplets passing through a serpentine channel are mixed rapidly and efficiently[94][183]. Droplets passing from one section of a microfluidic device to another via a serpentine channel are also delayed in time, with the time delay controlled by the length of the serpentine channel. Despite being unable to pass a monodisperse emulsion of microfluidic droplets through the channel, we were able to observe thorough mixing of bacterial populations inside droplets passing through a serpentine segment. Furthermore the serpentine channels did not cause further coalescence of the emulsion.

Figure 4.1(d) shows the fourth sub-design, a microfluidic "sieve" that was designed to pass droplets through channels of decreasing cross-sectional area. This was intended to test how resistant droplets were to splitting and coalescence under extreme spatial confinement. Unfortunately testing of this sub-design was limited due to the fact we were not able to generate a monodisperse emulsion of droplets at this stage of the project.

Figure 4.1(e) shows the fifth and final sub-design of this microfluidic device which was the first iteration of a microfluidic reservoir. The reservoir consisted of a large rectangular reservoir supported by an array of square pillars. The transition from a channel of low cross-sectional area to a channel of high cross-sectional area meant that fluid flow rapidly decreased in velocity as it entered the reservoir. This caused droplet coalescence at the reservoir entrance. A secondary design flaw inherent to this design was the use of square support pillars in the reservoir. It was observed that once droplets came to a halt against the flat side of a pillar they became pinned, unable to move from this position despite a continual flow past them. The microfluidic flow then seemed to equilibrate around pinned droplets, such that they required a significant transfer of momentum from incoming droplets to be dislodged (see figure 4.4).

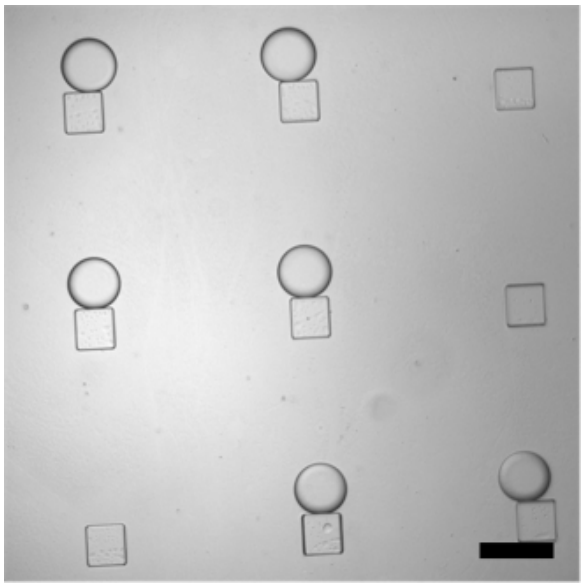

Figure 4.4 *Microscopy image of droplets pinned against the flat surface of support pillars despite continuous flow. This phenomena was avoided in future designs by using support pillars with circular cross-sections. Scale bar = 200 μm.*

4.4.2 Microfluidic design 2

Our second microfluidic device design integrated a number of the previous sub-designs into a single device whilst eliminating the flaws observed in the first set of designs. By integrating the sub-designs into a single device, we hoped that experimental complexity would be reduced. We also aimed to better match the transitions between channels of different cross-sectional area and by extension reduce droplet coalescence. With this design we intended to generate a monodisperse emulsion of microfluidic droplets (containing small bacterial populations) and then store them in a reservoir. We then aimed to observe the encapsulated bacterial communities using brightfield and fluorescence microscopy. This second microfluidic design can be seen in figure 4.5.

This design generates a monodisperse microfluidic droplet emulsion using a flow-focusing junction fed by aqueous phase and oil phase inlets. The droplet emulsion is then passed through a serpentine channel to a reservoir section. Once the droplets have progressed through the reservoir, they are then passed into a second serpentine channel before being removed from the device via a single outlet. By designing a single inlet for the oil phase that split into two channels, the oil phase could be pumped into the microfluidic device using a single syringe pump. This significantly improved ease of use whilst also ensuring that the flow rates of the two oil channels being fed into the droplet generating junction were matched.

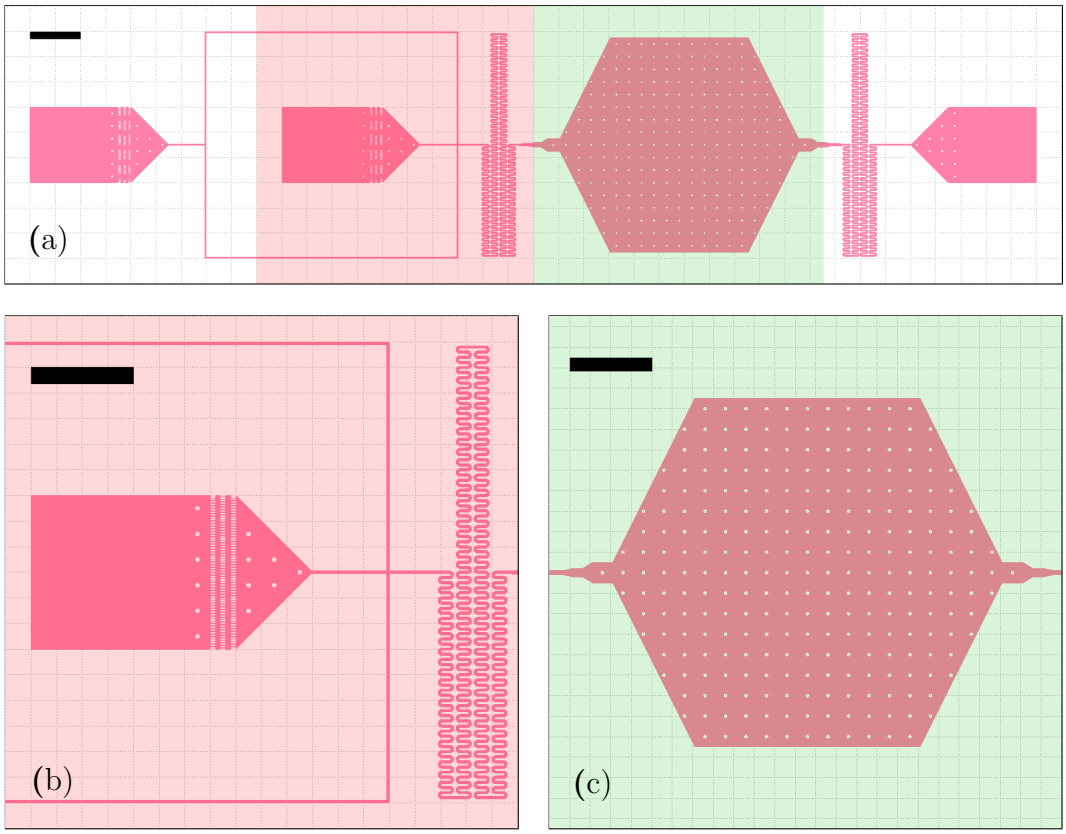

Figure 4.5 *A detailed view of our second microfluidic design. (a) Shows an overview of the entire microfluidic design. From left to right: the inlet, the droplet generation geometry, the first serpentine channel, the reservoir, the second serpentine channel and lastly the outlet. Highlighted in red, (b) shows a subsection of the device including the aqueous inlet, the droplet generating flow-focusing junction and the first of the two serpentine channels. Highlighted in green, (c) shows the microfluidic reservoir. Scale bars = 2000 μm.*

As can be seen in figure 4.5(b), the inlets featured an integrated filter: small microfluidic channels 10 μm in width that were designed to stop fabrication debris reaching the flow-focusing junction. In practice the sieve was very fragile; the channels often broke or collapsed during fabrication, rendering them either unusable or unable to stop debris from reaching the droplet generating junction. The flow-focusing junction was unchanged from the previous design.

Extended serpentine channels were also introduced before and after the reservoir. This ensured the droplets were well mixed before entering the reservoir. It also delayed droplets arriving and leaving the reservoir for around 10 seconds, this was beneficial should the flow not immediately halt when the syringe pumps were turned off. The serpentine channels were found to mix the droplets effectively, but

it was found that when the syringe pumps were turned off, residual pressure in the system could maintain flow inside the device for many minutes. As a consequence, the serpentine channels were ineffective in delaying droplets entering and leaving the reservoir.

The second generation reservoir design shown in figure 4.5(c) features graduated transitions at the entrance and exit to better match flow resistance and therefore flow rate. This gradually changing channel width ensures that droplet velocity slowly decreases and increases at the entrance and exit of the reservoir. This decreases the probability of high speed droplet collisions and therefore droplet coalescence. Additionally, the supporting pillars of the reservoir are circular in cross section so that droplets cannot become pinned as with our first design.

Despite improving upon the first generation reservoir design in multiple ways, the second design also did not function entirely as desired. The constricted reservoir outlet was prone to clogging, as the dense emulsion of monodisperse droplets stored inside the reservoir would often jam causing the microfluidic reservoir to rupture under high pressure. To remedy this, an outlet was manually punched into the reservoir, allowing droplets to easily escape the microfluidic reservoir at the cost of reducing the storage capacity of the device by over 30%. The presence of the manually punched outlet also caused droplets entering the reservoir to disperse poorly, often following a path of least resistance to the outlet, rather than filling the reservoir efficiently.

Finally, it was with this microfluidic design that we first attempted to generate microfluidic droplets that encapsulated bacterial populations, transfer them to an imaging reservoir, and quantitatively measure the size of each bacterial population. Unfortunately, we found that due to the standard 50 μm depth of this microfluidic device, bacteria were able to swim in and out of the focal plane of the microscope. This behaviour meant that at any given time an unknown proportion of each bacterial population was not visible, this introduced significant error to bacterial counting measurements. In an effort to circumvent this problem, an image processing workflow was developed that used the fluorescence intensity of each droplet as a proxy for the number of bacteria contained within the droplet. Unfortunately, this technique failed to accurately measure bacterial counts at the single cell level (see section 5.2.3 for further details).

To address the core issue of bacteria swimming in and out of the focal plane, we also attempted to reduce the channel depth of the entire microfluidic design. Unfortunately this introduced excessive hydraulic resistance to the system. This meant that the time required for the pressure inside the system to equilibrate was significant, and monodisperse droplet generation was not a robust process when flow rates were altered. Therefore, in the third microfluidic design the reservoir geometry was separated from the droplet generation geometry. This allowed us to adjust and optimise the channel depth of each microfluidic sub-design separately.

4.5 Microfluidic design 3

Using the general design principles outlined in section 4.3, I designed our third and final microfluidic device. This design again incorporated multiple geometries onto a single microfluidic master: a single droplet generation sub-design and two reservoir sub-designs. As discussed in the previous section, the decision was made to separate the sub-designs to make it possible to reduce the channel depth of one sub-design relative to another. This would allow us to compress droplets in the reservoir to a depth approximately equal to the focal depth, which was empirically tested to be 12-14 μm. Although this decision made it more time consuming to fabricate and use these microfluidic devices, the flexibility afforded by this decision was invaluable during use. The three microfluidic sub-designs can be seen in figure 4.6.

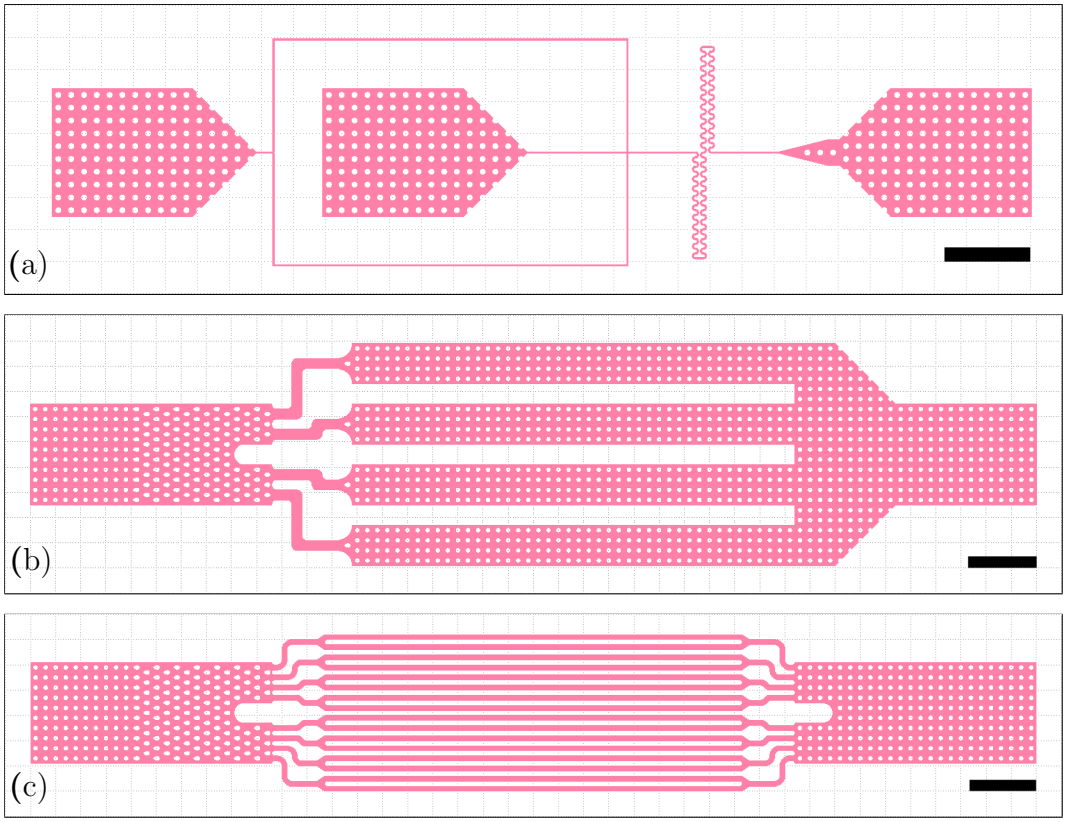

Figure 4.6 *Images showing the three sub-designs that constitute the third microfluidic device design, inlets are shown on the left, whilst outlets are shown on the right. (a) shows the third generation droplet generating sub-design, which consists of two inlets, a central flow focusing junction followed by a serpentine mixing channel, and finally a single outlet. (b) and (c) show the third generation microfluidic reservoir sub-designs. Scale bars = 2000 μm.*

Figure 4.6(a) shows the droplet generation sub-design. This was largely unchanged from the previous version, however the serpentine mixing channel was reduced in length. This change was made as efficient mixing was observed in serpentine channels over short distances in previous designs, and by reducing the length of the serpentine channel we could reduce microfluidic resistance without repercussion. We actively worked to reduce microfluidic resistance in the droplet generation design as droplet size tuning relies on fast response times to flow rate adjustments.

Figure 4.6(b) shows the first of the two microfluidic reservoir sub-designs. Rather than storing droplets in a single large reservoir, droplets passing through this design are stored in four parallel channels. This was done to combat the problem of droplets not efficiently filling a large single microfluidic reservoir. To further this aim, the inlet geometry and support pillars were designed to disperse droplets randomly across the width of the inlet, so that each of the four channels are equally filled. This dispersion was achieved using teardrop shaped support pillars that encouraged lateral droplet movement perpendicular to the microfluidic flow (see figure 4.7). This reservoir design performs well, monodisperse emulsions of droplets are distributed evenly between the four observation channels. Droplets freely exit the device from the large outlet, allowing the device to store a large number of droplets without the possibility of jamming. Once the inlet tubing is cut, droplet movement is arrested almost completely, improving the accuracy of droplet tracking significantly.

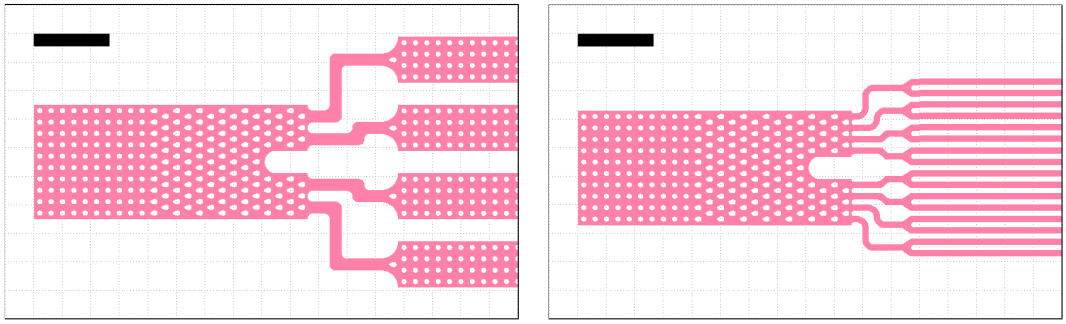

Figure 4.7 *Images showing the inlets of the third generation reservoirs in further detail. Both inlets are designed to disperse the incoming droplets such that the reservoir channels are filled equally. Note the teardrop shaped support pillars designed to encourage lateral droplet movement within the channel. Scale bars = 2000 μm.*

Figure 4.6(c) shows the second microfluidic reservoir sub-design. This design is similar to the first reservoir design, however separates the incoming droplet emulsions into twelve 200 μm wide observation channels rather than the previous four. It was intended for this design to provide an alternative to the first reservoir design, should the first design suffer from compression or crowding problems due to its less structured storage environment. Unfortunately, it was found that this second design was overly constrictive. As the storage channels were approximately equal to the droplet diameter, droplets within each channel essentially acted as plugs, meaning that the oil phase could not freely pass around the droplets.

The unforeseen consequence of this was that the device was sensitive to residual pressure after the inlet tubing had been severed. Residual flow caused the droplets in the channels to continue moving after imaging had started, sometimes out of the device altogether. Coupling an inefficient use of storage space with the aforementioned design flaw, this reservoir design was not used, with the second more open reservoir design being utilised instead.

A photograph of the microfluidic master used to fabricate all of our third generation sub-designs can be seen in figure 4.8.

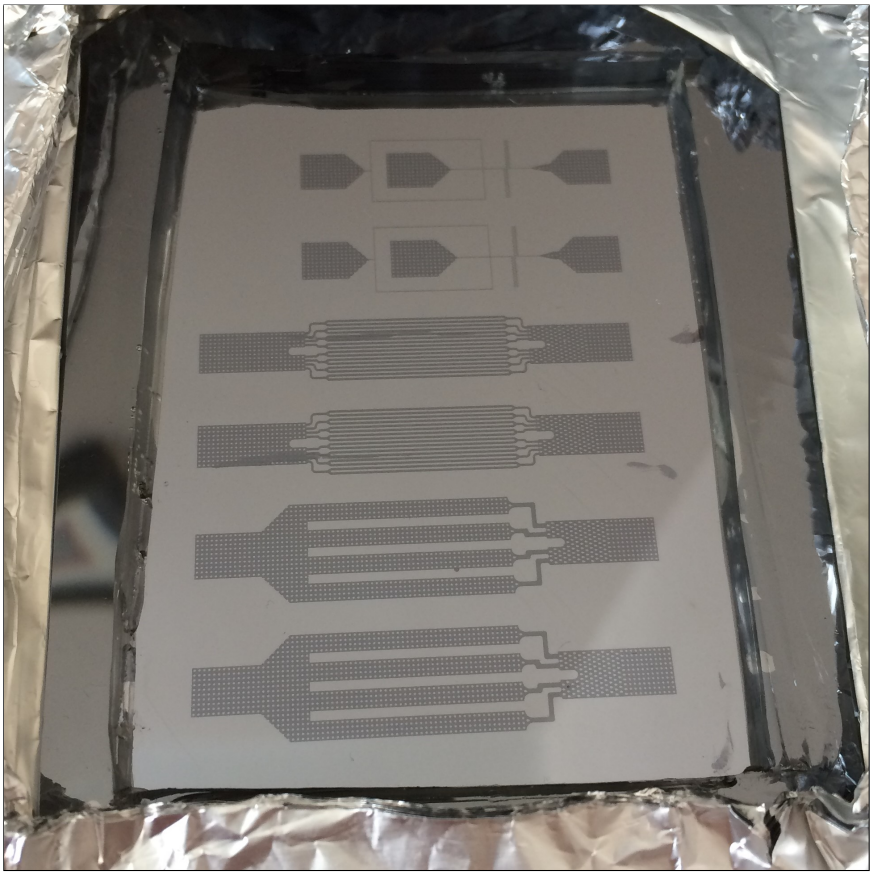

Figure 4.8 *Image of a microfluidic master that features all of our third generation sub-designs. From top to bottom: two droplet generation designs (as seen in figure 4.6(a)), two droplet reservoir designs (as seen in figure 4.6(c)) and lastly two further droplet reservoir designs (as seen in figure 4.6(b)).*

4.6 Concluding Remarks

Through an extensive design optimisation process, we have developed a microfluidic system that satisfies our experimental requirements. This system is comprised of two microfluidic devices, the first generates a microfluidic droplet emulsion whilst the second acts as a droplet reservoir for the purpose of imaging and analysing droplet-based bacterial populations. Through the use of tested design principles, we believe we have designed a device that can be fabricated in an academic laboratory by a non-expert user, without the need for clean room facilities. The device is easy to use and robust when operated across a wide range of conditions. The complete microfluidic system design can be seen in figure 4.9.

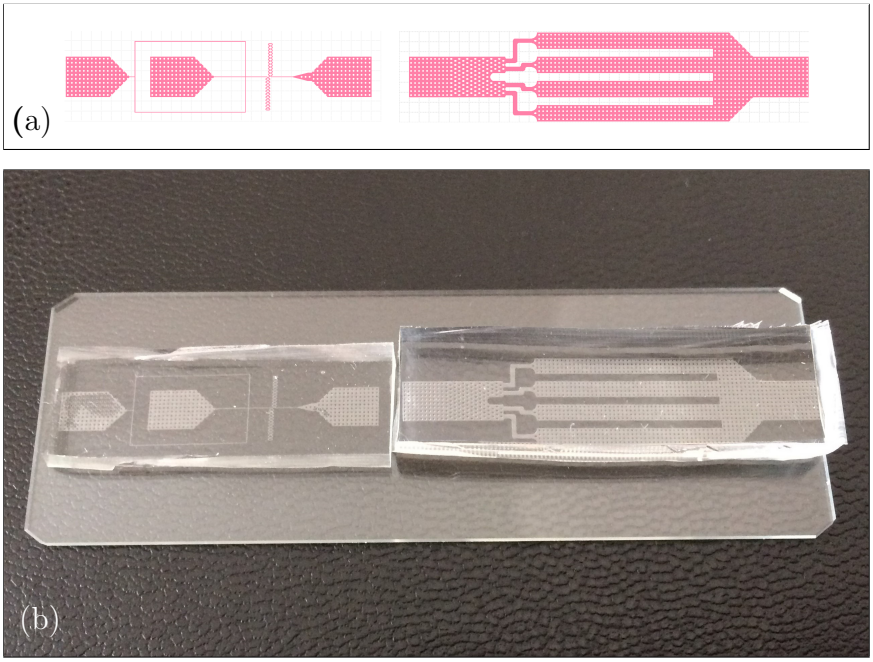

Figure 4.9 *Images showing the final, full microfluidic device design. (a) shows the droplet generation geometry (left) alongside the reservoir geometry (right). (b) shows a partially fabricated microfluidic device with the two designs cast in PDMS and bound to a glass slide.*

The microfluidic system we designed was split into two devices. This was done so that it was possible to alter the channel depth of the two subsystems independently of one another without the need for a multi-layer microfluidic design. This fabrication technique was avoided as it adds significant complexity to the design and fabrication process. We desired the ability to change the channel

depth from one microfluidic sub-system to the next as this would allow us to generate droplets using a channel depth that does not add excessive resistance to the flow-focusing geometry, whilst allowing us to store droplets at a channel depth optimal for microscopy. In the final microfluidic system, the microfluidic droplet generating device had a channel depth of 34.5 μm and the imaging reservoir device had a channel depth of 11.5 μm. We recognise that by splitting the microfluidic system into two devices, a time delay was introduced when droplets pass from the generator to the reservoir. We felt that this time delay was a necessary compromise, one that was justified when our goal of designing an accessible microfluidic system is taken into account.

Chapter 5

Image Processing Workflow - From Microscope to Data

5.1 Chapter aims and structure

This chapter discusses the development of an efficient, accurate and reliable image processing workflow that is designed to be used in conjunction with the microfluidic system outlined in chapter 4. The objective of this image processing workflow is to take brightfield and fluorescent images of bacterial populations encapsulated in microfluidic droplets (that are stored in a microfluidic reservoir), and extract quantitative data about their growth. Specifically, this extracted data will provide the growth and population size dynamics of each bacterial population with single cell precision over a period of 8 hours, with measurements being recorded every 6 minutes.

First, I will discuss existing software solutions that are used to detect bacteria in microscopy images, outlining why these solutions were not fully appropriate for this project. I will then analyse the difficulties of imaging objects inside spherical droplets. After this, I will outline the structure of the microscopy images that are input into the image processing workflow. Moving forwards, I will detail the full image processing protocol that was developed for this research project, which is separated into the key stages: image validation, droplet detection and bacterial counting. Following the conclusion of this protocol, I will briefly review and discuss the general process of designing and fabricating a full microfluidic system for the purpose of experimental microbiology.

5.1.1 Introduction

Our experimental system consists of a reservoir that is able to store 1000-2000 microfluidic droplets. Each of these microfluidic droplets is able to encapsulate a population of fluorescent bacteria that is trapped within the confines of the droplet volume. Brightfield images are taken of the droplets to track their position and size. Fluorescence images are taken of the droplets to detect the bacteria encapsulated within them.

The complete image processing workflow can be separated into 3 sub-sections that operate one after another to extract quantitative population size measurements of the encapsulated bacterial populations. The first sub-process consists of a manual image validation step that ensures the microscopy images are of a high enough quality for further analysis. This is followed by an image stitching step that prepares the images for further processing. The second sub-process takes the validated brightfield images and detects all droplet positions and boundaries in them across all time steps. The detected droplet boundaries and positions are then used to track each droplet from one time frame to the next, over as many time steps as possible. The third sub-process takes the droplet boundaries detected from the brightfield images and uses them in conjunction with the fluorescence images to count the number of bacteria encapsulated by each droplet at each time step. By combining this information with the droplet tracking data, the growth dynamics of the bacterial populations within each droplet can be measured to single cell precision.

5.1.2 Imaging bacteria in droplets

Changes in the refractive index of a sample can cause optical distortions when imaged using light microscopy[184]. In the context of this research project, this is a cause for concern when imaging bacteria inside a droplet of a given refractive index, which is suspended in a carrier fluid of a different refractive index. In their work studying the radial distribution of motile bacteria in droplets, Poon *et. al* modelled the confocal imaging of objects in a droplet of aqueous buffer (refractive index $n_w = 1.33$) suspended in sunflower oil (refractive index $n_o = 1.46$)[185]. In the upper hemisphere, significant distortions were found when imaging the droplet boundary and when imaging objects inside the droplet. The imaged droplet boundary had a smaller radius when compared to its actual value, and

the location of the objects inside the droplet were incorrect. Furthermore, in the lower hemisphere significant positional errors were observed which increased as the angle from the central axis increased. This meant that objects at the equator could be imaged twice. Finally, it was noted that objects near the equator could also be missed entirely due to "blind regions" that result from light being unable to enter the droplet beyond a critical angle.

By design, the experimental system designed and used in this thesis negates many of the issues described above. Firstly, when stored in the reservoir each droplet is compressed into a disk-like shape, with a diameter of ≈55 μm and a depth of ≈11.5 μm (see figure 5.1). This means that the vast majority of each droplet is imaged through a flat droplet surface, rather than a spherical droplet surface as modelled by Poon *et. al.* This reduces the distorting effect of the aqueous-oil interface. Additionally, the fluorocarbon oil phase used in this research has a refractive index of 1.29[186], which is far closer to the refractive index of aqueous growth media[23] when compared to the sunflower oil ($n_o = 1.46$) used in the model.

For these reasons, we did not believe that the aqueous-oil interfaces present in our experimental would introduce significant errors to our bacterial counting measurements. To confirm this, high framerate (60 fps) videos were recorded of low density bacterial populations stored in droplets inside our microfluidic reservoir. Over multiple ≈30 second videos, the highly motile bacteria swam both in the flat central area of the droplet and in the curved edge areas of the droplet. Through manual inspection and the analysis of individual video frames, the number of bacteria in each droplet was not observed to change at any point. This analysis reaffirmed our belief that when imaging bacteria inside our compressed droplets, the bacterial count was not significantly affected by the optical distortions described above.

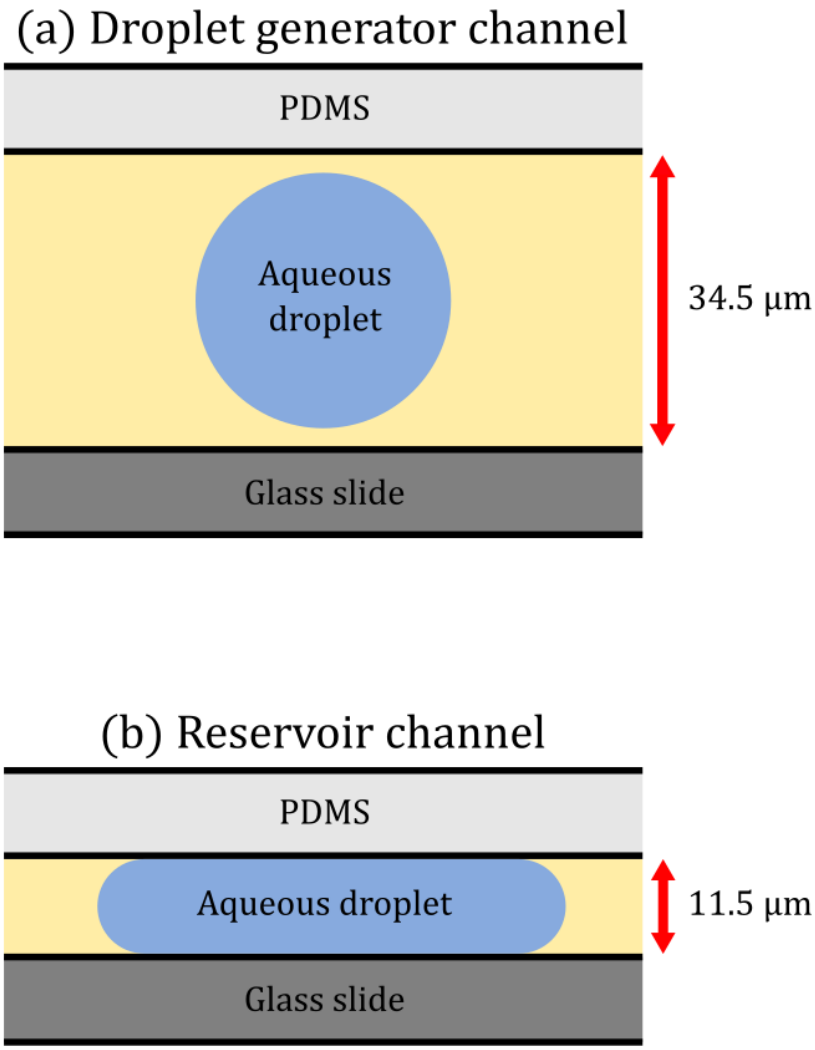

Figure 5.1 *Scale diagram of microfluidic droplets in the channels of the (a) droplet generating device and (b) reservoir device. Droplets are generated with a diameter approximately equal to the channel depth of the droplet generating device (34.5 µm). When these droplets are stored in the reservoir, they are compressed to the channel depth of the reservoir device (11.5 µm).*

5.1.3 Existing bioimage-processing solutions

Detecting, segmenting and tracking cells in microscopy images is a difficult task that can be used to gain biological insight from time-lapse recordings of cell growth, movement and behaviour[187]. Software packages such as Schnitzcells[188], MicrobeJ[189] and TLM-Tracker[190] are able to segment, track and perform lin-

eage analysis of low-motility bacteria growing in a 2D plane. These packages are often used to analyse the behaviours and growth of bacterial populations using phase-contrast or fluorescence microscopy at high magnification (typically 60x to 100x). Unfortunately, these software solutions are inappropriate for the images produced by our experimental system, which are (comparatively) low resolution time-lapse images of highly motile bacteria.

A number of studies have automated the detection of bacteria in droplets. Unfortunately, many of these fluorescence measurements are binary in nature, only capable of detecting whether bacteria are present in a droplet or not[43][131]. Whilst bacterial population sizes in droplets have been measured with single cell precision, these measurements are completed manually[137]. Due to the labour intensive nature of manual inspection, these measurements are therefore highly limited in throughput. The absence of existing solutions to this problem may be because droplet microfluidic systems generally store droplets in a spherical state, this means that three-dimensional imaging techniques must be used to accurately detect the bacteria stored in each droplet. Generally these three-dimensional imaging techniques are slower, as a specimen must be sampled multiple times to build up a complete image[191]. As such, this limits the throughput of the system, negating many of the benefits afforded by using a microfluidic system. As discussed in section 5.1.2, this problem was circumvented in our system by compressing the droplets, such that the entire population of a droplet can be imaged using standard epifluorescence microscopy.

We are not aware of any software analysis package designed to measure and track droplet encapsulated bacterial populations with single cell precision. Furthermore, we are not aware of any work that has measured droplet-encapsulated bacterial population size with single cell precision across many (>100) droplets. As such, we felt it was necessary to develop a custom image processing workflow to maximally utilise the experimental strengths of our microfluidic system.

5.1.4 Microscope output / image processing input

Before exploring the details of the processing workflow, it is important to consider the structure of the images produced by the microscope, as these images act as the data input for the entire image processing workflow that follows.

As discussed previously, due to the size of the reservoir it is not possible to image all droplets in a single field of view whilst maintaining the resolution required to count bacterial populations with single cell precision. The microfluidic device is therefore imaged by stitching multiple smaller fields of view together. This is done by scanning across the device along a predetermined grid. A single field of view images approximately 670 μm x 670 μm. A typical experimental run uses a field of view grid size of 18 x 14, this corresponds to a total imaged area of $\approx$1 cm^2. A 2 x 2 pixel binning regime was used to ensure a signal-to-noise ratio that allowed individual bacteria to be resolved accurately.

Pixel Binning

Pixel binning is the technique of combining adjacent pixels on an image sensor to produce a single super pixel. This has the effect of increasing both the pixel intensity and the signal-to-noise ratio within an image, which is useful for fluorescence microscopy. However, this process does reduce overall image resolution. All images taken using the automated experimental process in this thesis use a 2 x 2 pixel binning regime, combining every block of 4 pixels on the camera sensor into a single image pixel.

For each field of view, two images are taken; one using brightfield illumination and the other using YFP fluorescence. The whole microfluidic reservoir is imaged once per 6 minutes and a full experimental run is 8 hours long. Therefore, each grid position is imaged 80 times in both the brightfield and fluorescence illumination channels. This protocol outputs a total of 30,000-40,000 1024 pixel x 1024 pixel images per experimental run, depending on the imaging grid size used. In principle, the image analysis conducted in this chapter could be completed manually; however in practice the large volume of data necessitates the use of multiple semi-automated protocols. The optimisation of these automated processes is discussed in detail in the upcoming sections.

5.2 Image processing protocol

5.2.1 Stage 1 - image validation and stitching

A mantra often repeated in the field of image analysis is that the data you extract from an image is only as good as the image under scrutiny. Even with complex analysis tools it can be near-impossible to extract accurate and quantitative data from images of poor quality. With this is mind, before any images are fed into the processing algorithm they are first checked and validated for experimental errors and issues that could adversely affect data integrity later on in the image processing pipeline. Each field of view is checked and validated in both the brightfield and fluorescence channels, across all time frames. All fields of view that are flagged as unsuitable in this process are replaced with blank image stacks such that they do not interfere with the analysis of adjoining fields of view.

During this image checking process, four issues occur most commonly. These are detailed below and examples can be seen in figures 5.2, 5.4 and 5.3.

- **The field of view is out of focus.** The microscope is focused manually at the beginning of each experimental run, this is then maintained using a hardware-based automatic focusing system. Whilst this system is generally effective, a small number of imaging fields of view will be focused incorrectly consistently. When focused incorrectly, brightfield images are largely unaffected (due to brightfield features being large in comparison to the focal length), however bacterial fluorescence signals are blurred significantly. When this happens it is not possible to resolve multiple bacteria in close proximity, and single bacteria are able to swim out of focus completely (both of these issues can result in incorrect bacterial counting). As such, if a field of view is consistently incorrectly focused in the fluorescence channel then it is discarded. See figure 5.2.

- **The field of view does not image a microfluidic channel.** Depending on the specific positioning of the image grid it is possible that some fields of view do not contain a microfluidic channel. Whilst not an imaging issue that would cause problems for subsequent analysis processes, any empty fields of view can be immediately discarded without loss of information, thus improving image processing times.

- **The droplets within the field of view are distorted or non-circular.** Droplets can become distorted/non-circular because of spatial compression. This compression can occur when droplet flow is impeded by debris or uneven channel depth caused by defects in the microfluidic. Droplets can also become non-circular if they wet on the internal surface of a microfluidic channel. This can happen if the hydrophobic character of the PDMS microfluidic device has not been fully restored after plasma treatment. Droplet wetting was negligible when the microfluidic device had been treated with Pico-Glide 1 (see section 3.2.4).

  If the droplets are non-circular due to spatial compression or surface wetting, the subsequent droplet boundary identification process will be unable to fit boundaries to the droplets correctly. Incorrectly fitted droplet boundaries will cause significant bacterial population miscounts. The negative impact that this would have on data accuracy and integrity means that fields of view containing non-circular droplets are removed. See figure 5.3.

- **The field of view is contaminated with debris.** During the fabrication phase, it is possible for debris to contaminate the channels and reservoir of the microfluidic device. The majority of this debris is flushed from the device as the continuous oil phase passes through the reservoir. However, some pieces become trapped and these can cause a variety of issues during image processing. Debris can cause droplet compression and concomitant deviation from circularity, but most importantly, we observe that some debris fluoresces under YFP illumination resulting in highly inaccurate bacterial counts later on in the processing procedure. Fields of view that contain disruptive debris fragments are therefore removed. See figure 5.4.

  By automatically removing fields of view with fluorescent objects sorted by size/morphology, it may have been possible to automate the removal of fields of view containing fluorescent debris. However because each field of view was being assessed for a number of imaging issues (some of which would have been much more difficult to validate in an automated manner), it was decided that the implementation of an automated fluorescent debris check would realistically save very little time.

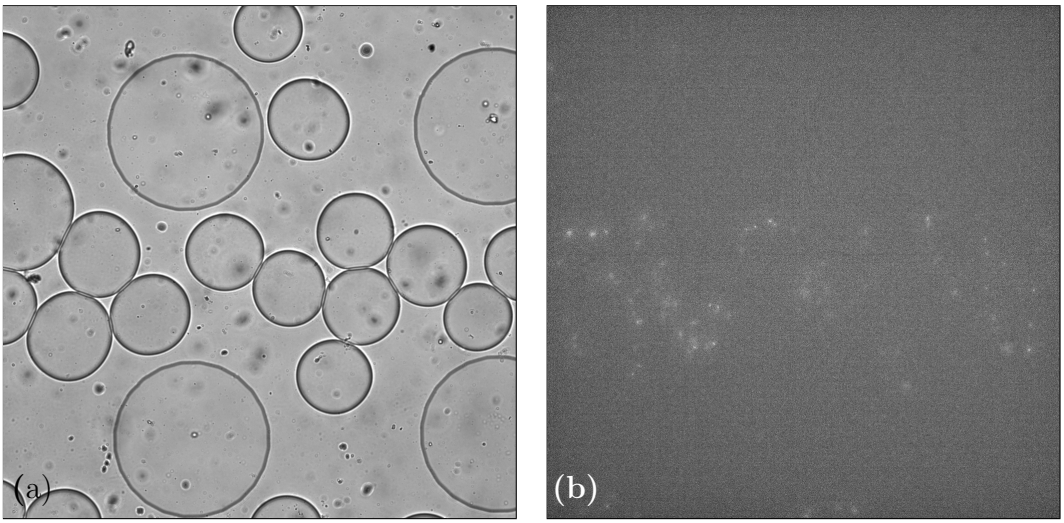

Figure 5.2 *Poor focus can disrupt processing for both brightfield and fluorescence channels. (a) Shows a brightfield image of microfluidic droplets in a reservoir, (b) shows a fluorescence image of the same field of view at the same focus. Whilst the features visible in the brightfield image appear to be focused to a reasonable standard, it can clearly be seen in the fluorescence image that the focusing is incorrect, and individual bacteria are difficult to resolve. This focusing issue will cause automated bacterial counts to be incorrect.*

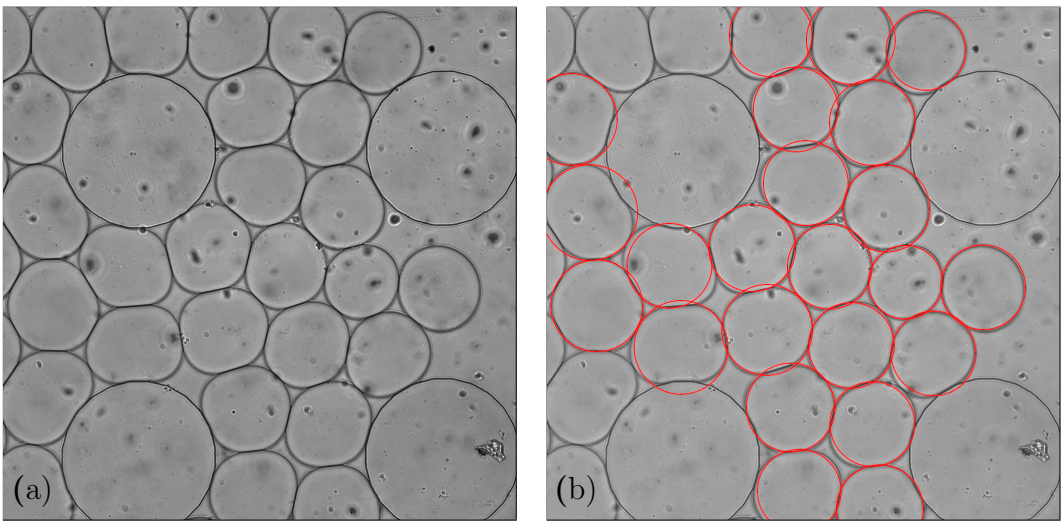

Figure 5.3 *The boundaries of distorted droplets cannot be approximated by a circle of known centre and radius. (a) Shows an unprocessed brightfield image of spatially distorted microfluidic droplets in a reservoir, (b) reveals the poor boundary detection that results when images containing non-circular droplets are processed.*

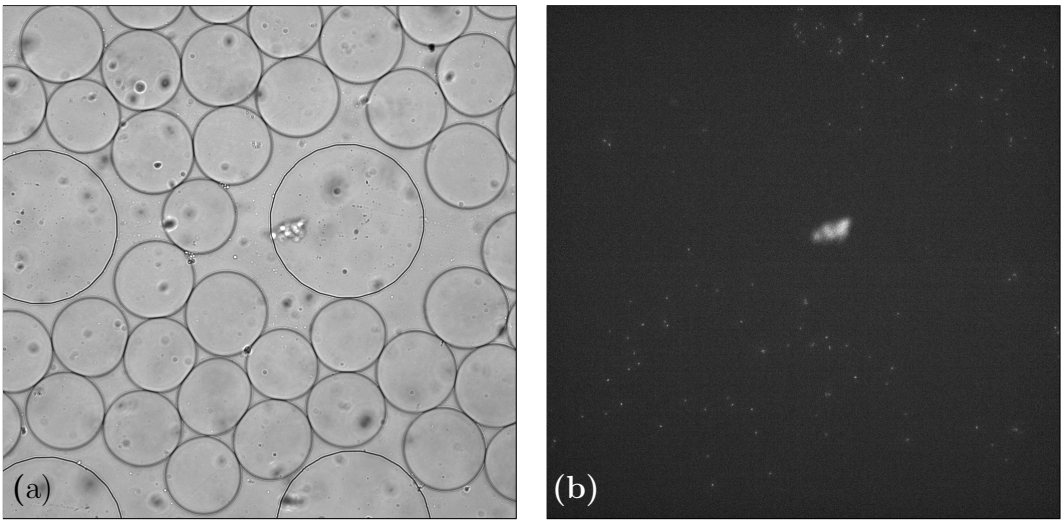

Figure 5.4 *Fluorescent debris can distort nearby droplets and will cause incorrect image exposure due to high pixel intensities. (a) Shows an unprocessed brightfield image of microfluidic droplets in a reservoir (a large piece of debris can be seen in the centre of the image), (b) shows an unprocessed fluorescence image of the same field of view (the large piece of disruptive fluorescent debris can be seen more clearly in fluorescence).*

The manual validation of each field of view is a labour intensive process. For each field of view, the first 10 image frames are checked for the common issues detailed above. The following 60 frames are then scanned through quickly to ensure that excessive droplet movement is not observed, which can cause droplet compression and tracking failures. The final 10 frames are then checked to ensure the lighting and focal properties of the images have not changed over the 8 hour duration of an experimental run. As described earlier in this section, a typical dataset consists of ≈250 fields of view. This validation process takes around 1 minute per vield of view, factoring in additional time for file management processes, it was found that the total validation process for a single experimental run takes around 6 hours.

Whilst this level of manual intervention is not ideal, we felt it was reasonable considering the high level of automation this process enabled (see section 5.2.2 and 5.2.3). Although it may have been possible to automate these validation processes, it was decided that the minimal time that would be saved by this automation (compared to total processing time) did not warrant the significant additional work that this would involve.

Once the experimental images have been successfully validated, they are stitched together to form larger composite image stacks that can be more efficiently processed. This step produces two stacks of 2D images, one for brightfield and the other for fluorescence, containing all fields of view over all time steps for each channel.

An example frame of an experimental sub-section, shown in brightfield, is shown in figure 5.5.

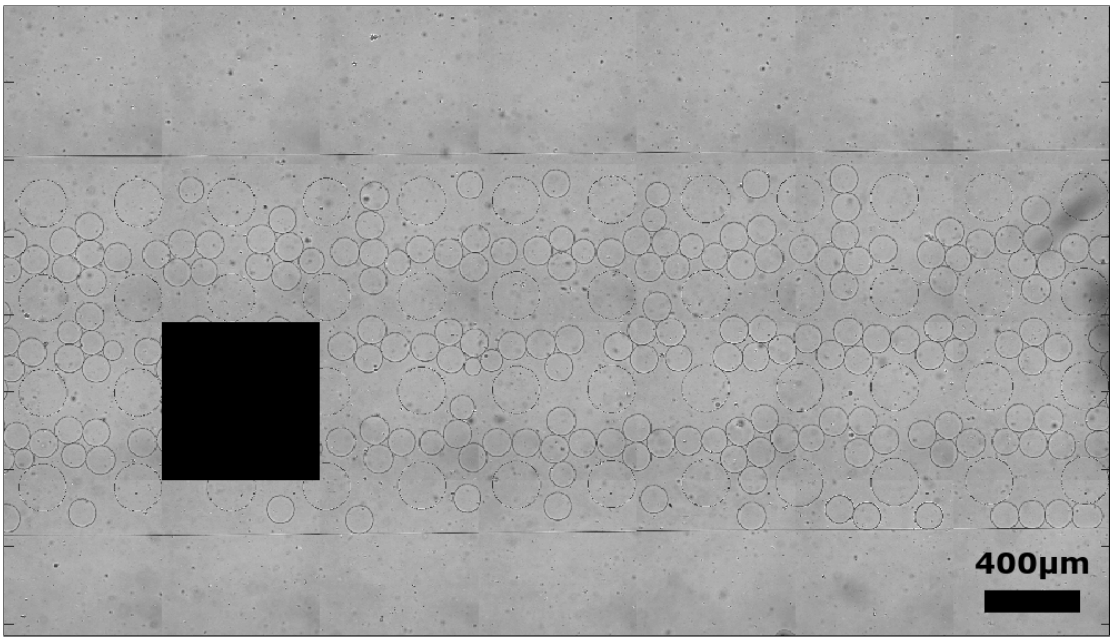

Figure 5.5 *An example frame of an experimental sub-section, shown in brightfield. The black square is a field of view that was removed during the validation stage of image processing.*

5.2.2 Stage 2 - Brightfield image droplet detection and tracking

Once each image has been validated and stitched, the brightfield images are passed through a circle detection algorithm standard to Matlab - the `imfindcircles` function. This is used to detect the locations and size of the microfluidic droplets in each frame of the image stack.

The `imfindcircles` function[192][193] searches for circular objects in an image using a circular Hough transform[194]. This fits boundaries to the droplets and outputs a data array describing all circles found in the image - listing their centres and radii. A sensitivity factor and edge threshold value are adjusted to optimise droplet boundary detection (see figure 5.6). These variables are optimised manually to ensure that the droplet detection algorithm only fits a single circular boundary to each droplet that is the correct size and does not overlap with its neighbours. The detected circles can be further filtered by a minimum and maximum radius, allowing for the exclusion of rare non-monodisperse droplets and circular features in the microfluidic device structure, such as reservoir supports.

Hough Transform

A Hough Transform is a common image analysis technique used to extract information about certain features in an image. Originally intended as a method of detecting lines in an image, the classical Hough transform has been extended to identify a number of shaped features such as circles and ellipses. The circular Hough transfer searches within an image for objects with high degrees of radial symmetry, allowing for the detection of even incomplete circles.

This circle detection algorithm is used to find the droplet boundaries in the brightfield microscopy images, and is repeated for every image at every time step such that a data set is produced that contains the position and radius of every droplet detected across a full experimental run.

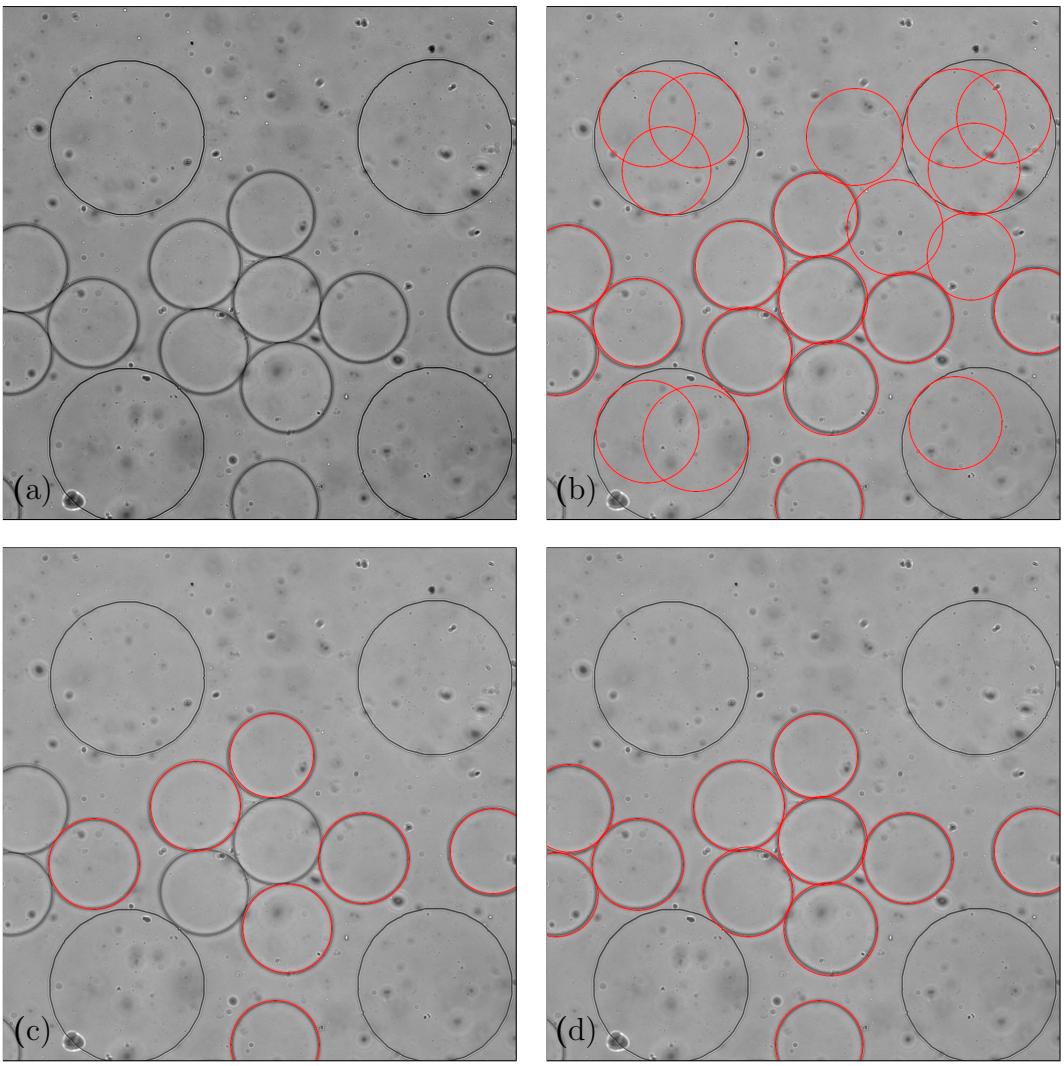

Figure 5.6 *Correct boundary detection is a vital step in the image analysis workflow. (a) Shows an unprocessed brightfield image of microfluidic droplets in a reservoir, (b) and (c) exhibit poor droplet detection due to poorly optimised sensitivity factors and/or edge threshold values, (d) exhibits correct droplet boundary detection.*

To accurately measure the bacterial populations in each droplet across all time steps we also needed to track droplets from one time step to the next. This is achieved using an adapted particle tracking algorithm[195]. Each image set is taken 6 minutes apart and during an optimised experimental run the majority of droplets do not displace themselves by more than their own radius within this time interval. This allows the tracking algorithm to track the majority of the droplets stored in the reservoir.

Upon completion of both the droplet boundary detection algorithm and the droplet tracking algorithm, a data array is output. This array contains the centre position and radius of every droplet across all time steps. In the array, each droplet is also assigned an identification number that allows it to be followed in time, from one frame to the next.

5.2.3 Stage 3 - Fluorescence image thresholding and bacteria counting

Image thresholding

To automatically count the number of bacteria in a fluorescence image it is necessary to threshold the image. This allows the perimeter of each bacterial cell in the image to be defined. A binarised thresholded image will consist of islands of connected 1-pixels (which represent detected fluorescent bacteria) on a background of 0-pixels.

Image Thresholding

Thresholding is an image processing technique whereby a grayscale image is binarised, such that every pixel within the image is set to either 0 or 1. All pixels with an intensity value above a set threshold value are set to 1, whereas all those whose intensity is below the threshold value are set to 0. The threshold value can be set to any chosen pixel value, however a threshold optimisation algorithm is commonly used to define a threshold value suitable for the application.

Threshold optimisation

An optimal threshold intensity value is essential for accurate counting of bacteria. If the threshold value is too low then small fluctuations in background fluorescence could be miscounted as additional bacteria; too high and bacteria with low fluorescence will not be counted at all.

The optimal threshold value changes from one experimental run to the next, this is because the experimental conditions from one experiment to the next are not identical. Small changes in experimental details such as optical focus or background fluorescence will impact the threshold value required to optimally detect fluorescent bacteria. Because of this, the process of threshold optimisation is repeated for each experimental run, producing unique optimal threshold values.

To optimise the threshold value the output of the bacterial counting algorithm must be compared to a "true" value of the bacterial count. This "true" bacterial count is obtained by manual inspection, i.e. counting the bacteria by eye.

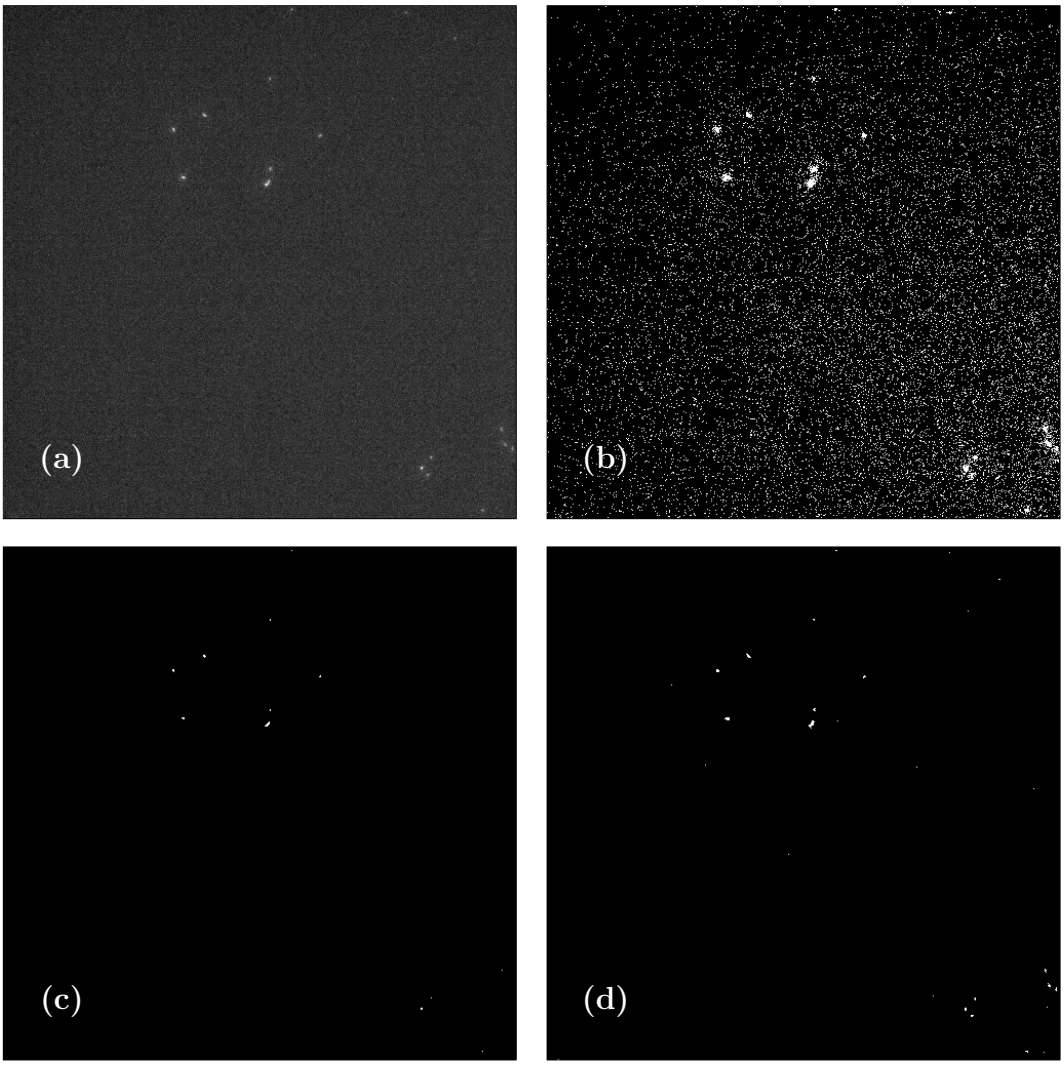

Figure 5.7 *Choosing an optimal threshold value is vital for the automation of bacterial counting. (a) Shows an unprocessed fluorescence image of bacteria encapsulated within microfluidic droplets, (b) shows the same image thresholded with a value below the optimum, (c) shows the image thresholded with a value above the optimum, (d) shows the image thresholded using the optimum threshold value. Note that single isolated pixels are not considered to be bacteria by the automated counting algorithm.*

A small change in threshold value can cause a large drop in the accuracy of bacterial counting. Therefore it is vital that the threshold value chosen takes into account the inherent variations in both the ambient and bacterial fluorescence from one experiment to the next. To ensure this is the case, the following optimisation process is carried out prior to the image processing of each experimental run.

1. **Select 4 fields of view across the microfluidic device and extract the corresponding images at a predetermined time frame** The time at which the fields of view are extracted is decided according to the general behaviour of the bacteria in a given experimental run. By way of example, if all the bacteria in a given experimental run are driven to extinction by 240 minutes, the fields of view are extracted half way between t = 0 minutes and this limiting behaviour at t = 240 minutes, i.e. t = 120 minutes. The 4 fields of view should be representative of the device as a whole. Therefore they are generally selected from locations that span the microfluidic reservoir. This is done to account for illumination and fluorescence fluctuations on a scale greater than a single field of view.

2. **Run the droplet detection algorithm on these images.** The bright-field images are passed to the droplet detection algorithm, and the position and radius of all droplets across the 4 images are recorded.

3. **Manually count and record the number of bacteria in the detected droplets.** The "true" bacterial count is obtained by eye by inspecting the raw fluorescence images with the detected droplet boundaries overlaid. Each droplet is assigned a bacterial count value.

4. **Threshold the fluorescence images.** The fluorescent images are initially thresholded using an arbitrarily low threshold value. Although this will almost certainly yield an incorrect initial automated bacterial count, it ensures that the optimal threshold value is eventually found by the optimisation process.

5. **Run the thresholded image through the bacterial count algorithm (described in the following section).** The bacterial count algorithm uses the thresholded image and attempts to measure the number of bacteria it can detect in each droplet.

6. **Compare the automated bacteria count values with the "true" values.** The difference between the "true" bacterial counts and the automated bacterial counts are calculated for all droplets and recorded. The smaller the difference between these two values, the better the threshold value is at accurately counting individual bacterial cells.

7. **Repeat steps 4, 5 and 6 - increasing the threshold value between each successive pass.** As the threshold value is increased, the accuracy of the bacterial counting algorithm is monitored. By plotting the difference between the automated count values and the optimal count value as a function of threshold value, a global optimisation curve is produced. This curve will feature a single minimum, where the automated count deviates least from the true count. The threshold value corresponding to this minimum is designated as the most optimal one.

Once the most optimal threshold value has been discovered, the entire fluorescence image stack of the experimental run is thresholded using the optimised threshold value.

Bacterial count algorithm

After the fluorescence images have been optimally thresholded, they are passed to an algorithm that counts the number of bacteria observed in each droplet. The automated bacterial counting algorithm functions by overlaying the droplet boundary information on top of the fluorescence images, and then counting the number of pixel islands that are not 8-connected within each droplet. Each pixel island is assumed to be a single bacterium, therefore the number of islands counted within a droplet is assumed to equal the number of bacteria encapsulated by the droplet. This is the algorithm used in step 5 of the threshold optimisation protocol detailed in the previous section. The same algorithm is used with the optimised threshold value to obtain the final bacterial count results.

Pixel Connectivity

Pixel connectivity is a method of describing how pixels are spatially related to their neighbours. Describing pixels as "8-connected neighbours" means that a pair of pixels is described as 8-connected if one of them occupies any of the 8 pixels that surround the other. This contrasts with 4-connected pixels that are only deemed to be neighbours if one of the pair occupies one of the 4 face positions surrounding the other.

Using the bacterial counting algorithm, the number of bacteria in each droplet, for each time step, is measured and recorded. As the droplets have been assigned an individual ID number that tracks them from one time step to the next, it is then possible to track the growth of the bacterial populations in specific droplets, with single cell precision, over the duration of a complete experimental run.

Addendum - integrated fluorescence intensity

In early versions of the microfluidic design, it was not possible to count individual bacteria within a droplet as the bacteria could swim in and out of the focal plane. This was due to the fact that earlier versions of of the device had deeper reservoirs channels. Because of this, alternative methods of measuring the bacterial population size were implemented, including an algorithm where the integrated fluorescence intensity of each droplet was used as a proxy for the number of bacteria contained within the droplet.

This approach assumed that an individual bacteria would emit a constant and consistent value of fluorescence intensity. Therefore, by integrating the total fluorescence intensity of a droplet (accounting for droplet size and uniform background intensity) one should obtain a total intensity which should scale linearly with bacterial population size. It was found that although the method described the general growth trends of the encapsulated bacterial communities well, this method had a low signal-to-noise ratio and failed to accurately measure bacterial counts at the single cell level. We believe this is due to the inherent heterogeneity between individual bacteria that can cause a variation in fluorescence intensity over time, particularly as they leave the exponential growth phase. Since the device allows us to autonomously image 1000+ droplets at a resolution high enough to distinguish individual bacteria it was felt a key strength of the system was not being exploited by using this integrated fluorescence method of measurement. Therefore, key changes were made to the microfluidic reservoir that allowed for direct measurement of bacterial population sizes. Critically, the reservoir was made shallower (reduced to 11.5 μm) to prevent bacteria swimming out of the focal plane.

5.2.4 Final data output

Once the image thresholding and bacterial counting sub-process have been completed, the image processing workflow comes to an end. The final output data structure contains 6 pieces of information for each droplet found at each time step - its identification number, (x, y) position, radius, bacterial population size and finally the time step at which these variables were measured. An example data structure output from the image analysis pipeline is shown in figure 5.8.

	x-position (px)	y-position (px)	time (min)	droplet ID	droplet radius (px)	number of bacteria
6216	8122.795599	1407.564319	84	423	91	1
6217	8122.907219	1407.616034	90	423	89	1
6218	8122.309915	1406.731203	96	423	90	1
6219	8121.844311	1407.538964	102	423	90	1
6220	8123.155365	1409.978301	108	423	90	1
6221	8120.798618	1411.312037	114	423	90	2
6222	8121.429962	1410.938771	120	423	90	2
6223	8121.369207	1411.553312	126	423	90	2
6224	8120.107545	1411.550238	132	423	90	2
6225	8120.722069	1411.949605	138	423	90	2
6226	8120.823653	1411.845977	144	423	89	2
6227	8122.378587	1413.612324	150	423	87	2
6228	8120.992623	1412.712346	156	423	89	2
6229	8122.170508	1412.987571	162	423	88	2
6230	8121.429132	1414.83637	168	423	90	3

Figure 5.8 *An example section of data output from an experimental run. For each droplet ID at a given time, the x-position, y-position, droplet radius and the number of bacteria detected in the droplet at that time is recorded.*

5.3 Concluding remarks

The development of an effective image processing protocol was a non-trivial task. On the one hand, our image processing algorithm required a level of sophistication that allowed for the counting and tracking of individual bacterial cells confined within hundreds of microfluidic droplets. On the other hand, our image processing algorithm must be simple and/or efficient enough to process large volumes of data within a reasonable time frame.

We were limited by the time resolution of our experimental system. Due to the large number of images that are taken across the reservoir at each time step, every image taken at a single location is separated by a six minute interval. Whilst this six minute interval is small enough to accurately track droplets in time (droplets tend not to move significantly on this time scale), it is far too long to track bacteria such that individual bacteria can be differentiated from one time step to the next (bacterial positions lose correlation within seconds).

We have developed an effective image processing workflow that efficiently detects, tracks and measures microfluidic droplets within our experimental system, as well as accurately counting the number of bacteria encapsulated by each droplet. Despite the relative complexity of the image processing algorithm, our image processing workflow remains computationally minimal: we have found it can be ran on a standard desktop computer with an entire experimental run taking less than 4 days to fully process (including manual validation and optimisation steps).

5.4 Designing and fabricating a microfluidic system: thoughts and conclusions

When designing and planning our microfluidic device, we sought to satisfy a particular set of experimental objectives.

1. Encapsulate a large number of small bacterial communities within isolated micro-environments.
2. Track each of these micro-environments, and by extension, their encapsulated bacterial population.
3. Measure the size of each bacterial population with single cell accuracy, over an extended period of time.

These objectives were chosen because we wanted to quantify the growth dynamics of small bacterial populations in the presence of antibiotic with high levels of precision. Due to the inherently stochastic nature of bacterial growth, we also wanted to obtain parallel repeats of these measurements on a scale not yet achieved in previous work. This would allow for statistically significant growth measurements of small bacterial populations that resemble those found *in vivo*.

Over the previous three chapters, I have discussed in detail the experimental processes and procedures that were used to design and fabricate a system that accomplishes these objective. First, I explored the materials, techniques and experimental protocols used in the fabrication of our microfluidic system. Second, I reviewed the iterative design process that was undertaken to produce an effective and reliable droplet-based microfluidic device. Third, I detailed the image processing protocol we implemented to extract quantitative growth data from brightfield and fluorescence images of bacteria that were grown in droplets using our microfluidic system.

Whilst there are multiple examples of other experimental systems that can track large numbers of bacterial populations, many of them are not able to measure the populations with single cell accuracy. These systems often rely on indirect measurement methods to assess population size; using fluorescence intensity or the results of a scattering technique as a proxy for cell number[43][131]. Similarly, whilst there are numerous experimental systems that can quantitatively measure the size of small bacterial populations with single cell accuracy, precise measurements of small bacterial populations are often limited to a small number of populations in total[137]. This usually results in results that lack statistical significance, especially when probing a highly stochastic biological growth process.

Our experimental system can generate upwards of one thousand microfluidic droplets which together encapsulate a low density bacterial suspension. The system is then able to simultaneously image, detect and track each droplet and the size of the bacterial population it encapsulates, with single cell accuracy. With the accomplishment of our original experimental objectives, we believe that we have developed a device that can offer a unique insight into the stochastic growth dynamics of small bacterial populations.

Chapter 6

Device Validation

6.1 Introduction

Before I present the results of the experimental work that has been completed using our microfluidic system, there are a number of experimental validations, assumptions and caveats that must be discussed to ensure that any conclusions drawn from our microfluidic system are valid and accurate. Whilst I will use data and measurements from chapter 7, the analysis will remain as abstract as possible and context will be included where required.

6.1.1 Experimental identification numbers

For clarity, each experimental run presented in the following two chapters has been given an identification number. These ID numbers are used to quickly and clearly distinguish each experimental run throughout the rest of this thesis. The ID number contains two pieces of information: the streptomycin concentration used in the experimental, and the repeat number of the experimental run at that streptomycin concentration. For example, experimental ID "0.50 - 2" is an experimental run conducted at a streptomycin concentration of 0.50 μg ml^{-1}, and is the 2^{nd} repeat at this concentration. Furthermore, the antibiotic concentrations are colour coded according to their growth behaviour to enhance readability (see table 6.1 for all experimental identification numbers and their associated colour).

Experiment ID	Strep. Conc. (μg ml^{-1})
0.00 - 1	0
0.00 - 2	0
0.05 - 1	0.05
0.50 - 1	0.5
0.50 - 2	0.5
2.50 - 1	2.5
50.0 - 1	50

Table 6.1 *Summary of all experimental identification numbers and the colour chosen for each experiment to enhance readability throughout this thesis. Strep. Conc. gives the final concentration (w/w) of streptomycin used in each experimental run once added to the M9 growth medium.*

6.2 Bacterial counting errors

The process of counting encapsulated bacterial populations in our microfluidic reservoir is a semi-automated procedure that only requires user input for validation and variable optimisation, as shown in chapter 5. This semi-automated workflow is one of the key strengths of our experimental system.

In the image analysis process, bacteria are detected and counted through the use of image thresholding. Whilst computationally efficient, this process lacks the complexity required to differentiate between bacteria that are in extreme close proximity to one another. This is rarely a problem in droplets that contain small numbers of motile bacteria, as it is highly unlikely that in any given time frame the bacteria are in close enough proximity to falsely register as a single bacteria. Unfortunately, our microfluidic droplets do not always exclusively contain small populations of motile bacteria.

6.2.1 Crowded droplets

Bacterial populations that undergo significant logarithmic growth can form dense suspensions within the 8 hour time frame of a single experimental run. Under these crowded conditions, the image processing algorithm will incorrectly assign a single cell count to multiple bacteria that are in close proximity. This can be seen clearly in figure 6.1.

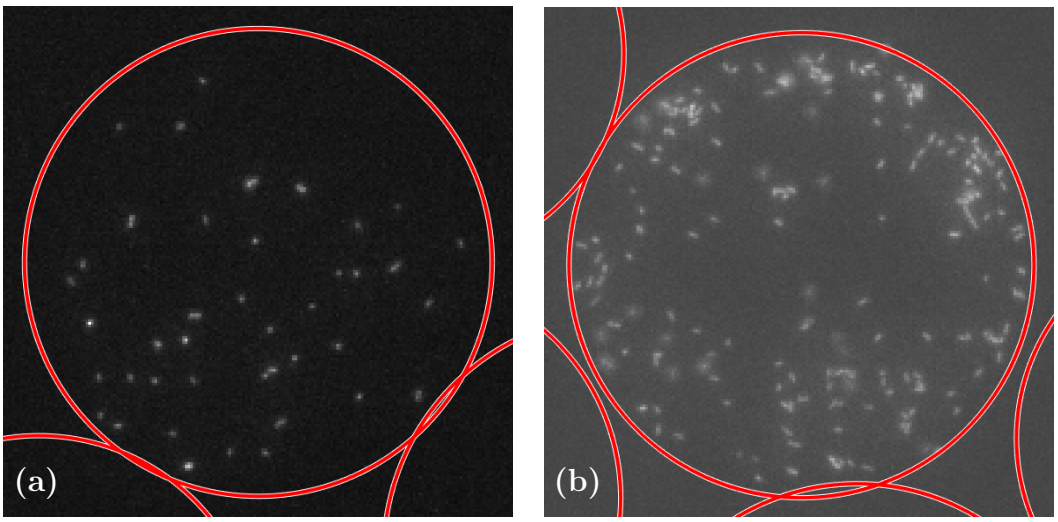

Figure 6.1 *(a) Shows an example of a bacterial population in which all individual bacteria are well detected using our bacterial thresholding algorithm. Bacteria are highly fluorescent and well dispersed, (true bacterial count = 40, automated bacterial count = 40). (b) Shows an example of a very large bacterial population that is poorly detected using our bacterial thresholding algorithm. Bacteria are densely packed and bacteria are in close proximity, making it difficult to differentiate individual bacteria from one another, (true bacterial count ≈ 158, automated bacterial count = 129).*

Whilst these well-dispersed but dense bacterial populations result in bacterial miscounts, we are not overly concerned with their impact on the accuracy of our experimental data. This form of bacterial miscounting will only impact the extracted data of fast growing, uninhibited bacterial populations that reach high number densities. Droplet populations of this density are rare (see figure 7.5).

For a well-dispersed bacterial suspension of a fixed cell density, it may be possible to calculate how likely it is for the individual bacteria in the suspension to overlap. As such, it should also be possible to calculate bacterial overlapping probability (and therefore bacterial counting error) as a function of droplet population density. If an acceptable error threshold value was defined, this could be correlated to an acceptable population density, above which the counting error of the algorithm used to detect the bacteria would be deemed unacceptable. Unfortunately, as discussed in section 6.2.2, the counting error introduced by this proximity-based overlapping is small in comparison to the counting error introduced by bacterial aggregation.

Because of this, defining an acceptable error threshold according to a population density value would not be useful given the larger error introduced by aggregation which is heterogeneous, unpredictable, and not directly proportional to population density.

6.2.2 Bacterial aggregation

Bacterial aggregation - observations in microfluidic droplets

It has been repeatedly observed that some bacteria will spontaneously stop moving whilst continuing to fluoresce and replicate. Daughter cells of these immotile bacteria often remain stationary after replication, and this process continues until a static bacterial aggregate is formed. In these cases, the extreme close proximity of progenitor cells causes incorrect cell counting. An example of this behaviour is shown in figure 6.2.

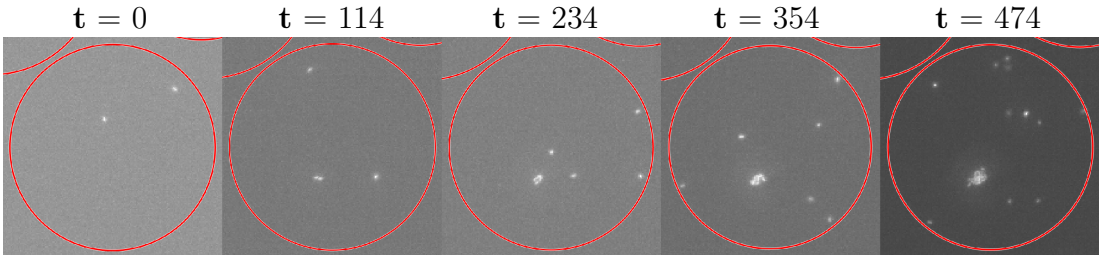

Figure 6.2 *Example of bacterial aggregation in a droplet encapsulated bacterial population, aggregation formation can be observed to begin as early as 60 minutes into an experimental run. Time is given in minutes.*

We believe that bacterial aggregation is the primary cause of bacterial counting errors in our experimental system. Bacterial aggregation appears to be a spontaneous process, with aggregate formation beginning at any time in an experimental run from 60 minutes onwards. De-aggregation has been observed on rare occasions, and it is possible for highly motile daughter cells to leave their birth aggregate. However once an aggregate has begun to form it will generally remain static and grow until the conclusion of the experimental run. Aggregation also appears to be experimentally difficult to predict as it has been observed to occur apparently at random in almost every type of droplet population, regardless of growth rate or antibiotic concentration.

We do not see a simple method of resolving the number of bacteria in these aggregates given the high throughput nature of our microfluidic system. From an experimental perspective, it is not possible to increase magnification or use a more complex microscopy technique as this would severely limit the total number of droplets we could observe with reasonable time resolution. From an image processing perspective, given that it is not possible to manually count the number of bacteria contained within some aggregates, it is most likely not possible for any simple thresholding algorithm to differentiate and count the number of bacteria within a dense aggregate.

Fortunately, this problem only affects droplets that undergo significant bacterial growth. If previously motile bacteria in a droplet became attached to a growing bacterial aggregate, it is possible that bacterial aggregation could cause an apparent net loss in visible bacteria whilst the population was actually undergoing growth. Fortunately, manual inspection of droplets that contain bacterial aggregates all show an increase in detected population size with time. Furthermore, the behaviour of a droplet population is usually most dynamic and stochastic at low population numbers. This means that whilst the automated size count of a fast growing population may be inaccurate later on in time due to bacterial aggregation, the more general behaviour of the droplets growth will be recorded correctly.

Given these reasons, we decided to take a pragmatic approach to the possibility of bacterial miscounting. Whilst our system has been proven to accurately count small bacterial populations encapsulated within microfluidic droplets, we are aware that this accuracy decreases when measuring large bacterial populations and aggregated bacterial populations. By their very nature, these counting errors more commonly impact the accuracy of large population size measurements and rarely influence the accuracy of measurements that are used to quantify key dynamics that occur early on in an experimental run. Moreover, these mechanisms exclusively cause an underestimation of bacterial population sizes. This allows these errors to be more easily taken into consideration when conclusions are being drawn from quantitative trends and measurements of bacterial growth dynamics.

Bacterial aggregation - causes and reduction

The surface properties of bacteria such as *E. coli* vary significantly from one strain to the next[196]. This variation can affect their adhesive properties to both surfaces and other bacteria. The surface protein antigen 43 (Ag43) has been linked to the aggregation of *E. coli* suspensions. It is hypothesised that Ag43 molecules on the surface of adjacent bacteria interact in a head-to-tail conformation - the L-shaped structure of Ag43 enabling "velcro-like" adhesion between cells, facilitating aggregation[197].

There are a number of techniques that can be used to reduce bacterial aggregation. Bacterial mutants have been developed that alter the L-shaped structure of Ag43, these deletion mutants do not exhibit auto-aggregation and bacterial clumping[197]. Other mutants that feature surface bound fimbriae (rod shaped organelles approximately 7 nm in width and 1 μm in length) have also been shown to abolish Ag43-mediated autoaggregation[198]. Outside of strain variation, it is also possible to retard auto-aggregation through the use of compounds that are added to aqueous bacterial suspensions.

6.2.3 Threshold optimisation and error estimation

To obtain accurate bacterial counts, the threshold value for each experimental run must be chosen so that the image processing algorithm can optimally detect bacteria with single cell accuracy. If this threshold value is too low, then background fluorescence fluctuations will be registered as bacterial counts. If the threshold value is too high, then weakly fluorescing bacteria will not be detected at all. Using the threshold optimisation process detailed in chapter 5, an optimal threshold value is chosen for each of our experimental runs based on a set of sample images taken from that experimental run. Whilst this threshold value is optimal given a set of test images, the overall error when the counting algorithm is applied to a complete experimental run is unknown.

To calculate an error estimate for our automated bacterial counting algorithm, we begin by selecting 3 fields of view from each experimental run. For each field of view, the automated bacterial count data is extracted for t = 0 minutes, t = 114 minutes and t = 234 minutes. These times are chosen so that error estimates can be compared across all experimental runs, including experimental runs 2.50 - 1 and 50.0 - 1 that were stopped after 234 minutes. These images are man-

ually assessed and the number of visible bacteria in each droplet is measured. The manually assessed bacterial counts are then compared with the automated bacterial counts. This process essentially repeats the threshold optimisation process detailed in chapter 5, but instead of minimising the output differences with respect to a set of test images, we are measuring the difference when the process is applied to a set of random images. Error estimates for all experimental runs have been calculated using this method. These are tabulated in table 6.2.

It is prudent to note that this error analysis is only capable of estimating errors in the automated counting process, i.e. it is only able to evaluate the accuracy of the thresholding process that measures bacterial population sizes using fluorescence microscopy images. If bacterial cells are not visible in the fluorescence microscopy images due to poor focus, lack of fluorescence or incorrect droplet boundary detection, it is not possible for this analysis to quantify these failures. See chapter 5 for further details on the extensive validation processes that were completed to avoid these issues before the automated counting process was used to obtain data. Error measurements at t = 0 mins, 114 mins and 234 mins for all experimental runs are tabulated below.

Experimental ID	Time (mins)	Droplets measured	True count	Auto. count	Count error	Percentage error (%)
0.00 - 1	0	33	33	35	2	+6
0.00 - 1	114	33	95	97	2	+2
0.00 - 1	234	31	169	154	-15	-9
0.00 - 2	0	42	14	14	0	0
0.00 - 2	114	42	33	25	-8	-24
0.00 - 2	234	42	74	59	-15	-20
0.05 - 1	0	42	74	70	-4	-5
0.05 - 1	114	42	175	155	-20	-11
0.05 - 1	234	41	276	241	-35	-13
0.50 - 1	0	46	12	12	0	0
0.50 - 1	114	45	7	7	0	0
0.50 - 1	234	46	4	3	-1	-25
0.50 - 2	0	26	50	48	-2	-4
0.50 - 2	114	25	39	37	-2	-5
0.50 - 2	234	26	26	23	-3	-8
2.50 - 1	0	18	26	27	1	+4
2.50 - 1	114	18	16	14	-2	-13
2.50 - 1	234	19	7	5	-2	-29
50.0 - 1	0	44	19	19	0	0
50.0 - 1	114	46	3	3	0	0
50.0 - 1	234	49	1	1	0	0

Table 6.2 *Error measurements for all experimental runs, at t = 0, 114 and 234 minutes. Experimental runs are ordered by streptomycin concentration: green experiments are grown in the absence of streptomycin whilst red experiments are grown at high streptomycin concentrations.*

In experimental runs 0.00 - 1, 0.00 - 2 and 0.05 - 1, the total number of visible bacteria increased from t = 0 minutes to t = 234 minutes. Maximal percentage errors of -20% and -24% can be seen in experimental run 0.00 - 2, where the automated counting algorithm underestimated the number of bacteria by 8 and 15 bacteria respectively. It was observed that almost all miscounting errors were due to aggregation events, further supporting our hypothesis that the primary source of bacterial miscounts was due to this phenomena.

In experimental runs 0.50 - 1 through 50.0 - 1, the total number of visible bacteria decreased from t = 0 minutes to t = 234 minutes. In these experiments the maximal count error was -3 (0.50 - 2 at t = 234) where 26 bacteria across 26 droplets were miscounted as 23 bacteria by our automated algorithm. The maximal percentage error was -29% (2.50 - 1 at t = 234) where a total of 7 bacteria across 19 droplets were miscounted as 5 bacteria by our automated algorithm.

The automated counting algorithm was perfectly accurate at identifying droplets that contained no bacteria. Of the the 493 empty droplets that were manually assessed across all experimental runs and time frames, 0 were falsely identified as containing bacteria.

Despite the automated counting error values appearing somewhat random, there are a number of metrics, trends and observations that can be examined. Firstly, both absolute and percentage-based bacterial counting errors broadly increase as a function of time. This is consistent with our intuition that the primary cause of counting errors is bacterial aggregation, which increases in frequency and magnitude as time passes. Secondly, automated counting errors are lower in experimental runs that did not exhibit net bacterial growth. This intuitively matches our expectations: without net bacterial growth there are simply not as many bacteria to count incorrectly. Furthermore, due to the lack of growth it is not possible for bacteria to reach high densities where bacterial overlap becomes a problem (as discussed earlier in this chapter), and it is also not possible for large numbers of bacteria to form aggregates. Finally, bacterial counting errors become increasingly negative as a function of time. At t = 234 minutes none of the bacterial counting errors are positive, this indicates that the automated bacterial counting algorithm is underestimating bacterial population sizes at later time frames. This behaviour is independent of the total number of visible bacteria, apart from experimental run 50.0 - 1 that ended with only 1 bacteria visible at t = 234 minutes. This consistent underestimation again supports our hypothesis that bacterial aggregation is a major cause of automated counting errors.

Whilst it is critical to understand and quantify the errors that exist in our automated bacterial counting algorithm, the context of these error measurements must be appreciated. Firstly, when manually assessing the number of bacteria in droplets that exhibited aggregation, it was often difficult to accurately count multiple bacteria in close proximity. If it is not possible to manually count the number of bacteria in an aggregate, it is unreasonable to expect that an automated algorithm could perform this task more accurately. This means that to

solve this problem, an attempt to reduce aggregation may be more successful than an attempt to improve the accuracy of the counting algorithm. Furthermore, in the process of analysing the experimental data presented in chapter 7, the automated counting algorithm will measure the bacterial populations of over 7000 droplets. These 7000 droplets will be measured up to 80 times per experimental run, resulting in a total of ≈525,000 population measurements. For the error estimations calculated here, over 750 droplet populations were manually assessed, but this still pales in comparison to the total number of bacterial droplets that the automated counting algorithm will process in the full analysis of our experimental data. As such these error measurements should be treated as order of magnitude estimations. These error estimations should serve to guide the conclusions we draw from any data that is produced using this automated process.

In summary, automated counting error estimates were calculated at t = 0, 114 and 234 minutes for each of the experiments that will be presented in chapter 7. These counting errors increase as a function of time, and almost exclusively underestimate droplet population sizes. For this reason, automated bacterial population counts at later time steps should be treated as lower bound estimations. It has been hypothesised that the primary cause of automated counting error is bacterial aggregation.

6.3 Droplet polydispersity

So that bacterial populations encapsulated by droplets can be quantitatively compared to one another, the assumption is made that the size of every droplet within an experimental run is equal. If this is true, then the space and nutrients available to each bacterial population is consistent from one droplet to the next. To test this size assumption, the droplet monodispersity for each experimental run is calculated. A standard measure of droplet monodispersity is the coefficicent of variation (CV), which is the ratio of droplet diameter standard deviation to mean[199]. A microfluidic droplet emulsion is considered monodisperse if the CV value is below 5%[200].

Given that the droplets are imaged in a microfluidic channel that is 11.5 μm deep, we first measure an "observed" average droplet radius in pixels for the first time frame of each experimental run. After converting these radii in pixels to μm, estimated volumes for these average droplets are calculated by approximating the droplets as disks 11.5 μm in depth. Using these average droplet volumes, estimated average spherical droplet radii are then calculated. This was done to allow our monodispersity measurements to be compared with literature values.

Experimental ID	Observed disc radius (pixels)	Observed disc radius (μm)	Estimated spherical volume (pL)	Estimated spherical radius (μm)
0.00 - 1	90 ± 5	58 ± 3	120 ± 14	31 ± 1
0.00 - 2	88 ± 5	56 ± 3	115 ± 13	30 ± 1
0.05 - 1	76 ± 4	49 ± 3	86 ± 10	27 ± 1
0.50 - 1	73 ± 3	47 ± 2	79 ± 7	27 ± 1
0.50 - 2	85 ± 6	54 ± 4	107 ± 16	29 ± 2
2.50 - 1	93 ± 6	59 ± 4	127 ± 16	31 ± 1
50.0 - 1	77 ± 7	49 ± 5	87 ± 16	28 ± 2

Table 6.3 *Measured and calculated droplet radii values for droplet monodispersity testing, each ID represents a full experimental run.*

The CV values for each experimental run ranged between 3% and 7%, sitting at the the limit of what is considered monodisperse. We deemed these CV values acceptable for multiple reasons. To start, due to the nature of bacterial loading into microfluidic droplets, the average size of a bacterial population encapsulated within a droplet will scale with droplet size. This means that smaller droplets will on average have smaller initial populations, and larger droplets will on average have larger initial populations. As a consequence of this, the average space and nutrients available to each bacteria in a droplet population will remain relatively consistent, regardless of droplet size.

Secondly, the observed droplet size measurements were recorded when the droplets were confined within a microfluidic channel that was significantly wider than it was deep. Small variations in channel height could cause the observed droplet size to vary considerably. These channel height variations may occur due to defects in the microfluidic master or because of the elastomeric nature of PDMS: observed droplet size was seen to change significantly when droplets passed through microfluidic channels with known defects.

Finally, and perhaps most importantly, one of our experimental aims was to test the growth of numerous small bacterial populations encapsulated in micro-environments and compare this to the growth of a single large bacterial population that is grown using traditional bulk techniques. The difference in volume between those found in our microfluidic droplets ($\sim 1 \times 10^{-10}$ l) and those found in bulk growth techniques ($\sim 1 \times 10^{-3}$ l) is considerable. This volume difference dwarfs the droplet volume variations calculated in table 6.3, therefore the volume variations can be considered negligible when considering our experimental objective.

6.4 Observation Delay

Prior to droplet generation, 10 ml of fresh M9gl growth media was inoculated using 25 μl of high density starting culture. This 10 ml volume was then placed in a shaking incubator (37°C, 200 rpm) for 1.5 hours. This bacterial suspension is then pumped into the microfluidic device, where it is encapsulated into microfluidic droplets. Once these droplets are generated in the first microfluidic device, they are then transferred into the second reservoir device via a piece of connecting tubing. This transfer of droplets from one device to the next introduces a time delay between droplet generation and droplet imaging of around 90-120 minutes.

To assess the impact of this time delay, we use a statistical measure called the Fano factor. The Fano factor is a measure of the dispersion of a random process and is defined as the variance divided by the mean. The distribution of bacteria from a bulk suspension into microfluidic droplets is expected to be a Poisson process[132], for which the mean and variance of the droplet population sizes will be equal, and the Fano factor will equal 1. If the droplet populations have undergone significant changes from encapsulation to imaging, the Fano Factors for our droplet population size distributions would diverge significantly from 1. The initial Fano factors for all experimental runs can be seen in figure 6.3.

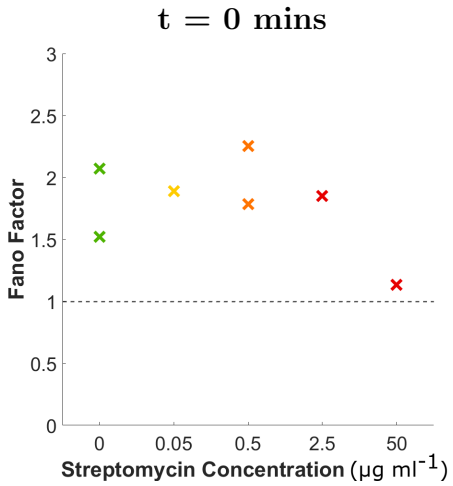

Figure 6.3 *Scatter plot showing the initial population distribution Fano factors for each experimental run as a function of streptomycin concentration.*

The initial Fano factors for all experimental runs were between 1 and 2.5, a slight increase over the Fano factor of 1 predicted by a Poisson process. This indicates that the population size distributions at the start of each experimental run exhibited a higher variance than expected, given the Poissonian encapsulation process. Given the doubling time of RJA002 in M9gl has been found to be ≈112 minutes[201] (see section 7.5 for further inmformation), this increased variance is most likely explained by small amounts of growth in the delay between encapsulation and imaging. Despite this, we do not believe that this time delay hides significant population growth dynamics for two principal reasons. Firstly the growth exhibited during this imaging delay is small in comparison to the growth that occurs during a full experimental run. Secondly, the small changes in Fano factor during this imaging delay does not appear to correlate with streptomycin concentration, whereas the changes in Fano factor during each experimental run correlate strongly with streptomycin concentration.

For these reasons, we believe that the Fano Factors of our droplet population size distributions are strong indicators of significant changes in the distribution of population sizes. Furthermore, we are confident that the time delay discussed here does not hide important bacterial population growth dynamics. Nonetheless, we are mindful that this time delay is an inherent property of our microfluidic system and consider its potential impact when drawing conclusions from the bacterial growth dynamics observed in our microfluidic droplet populations.

6.5 Spatial correlation of growth

When interpreting our experimental results, we assumed that all confined bacterial populations existed independently. This meant that we assumed zero exchange of information or resources from one droplet to the next, and by extension we assumed that the growth dynamics of one droplet population would not impact that of another.

This is an important assumption that must be validated. For example, competition for depleted nutrients and the accumulation of metabolic waste products could impact the growth of two populations in close proximity. Furthermore, bacteria have been shown to display co-operative behaviours that could also impact bacterial populations near to one another. Quorum sensing is a phenomena where individual bacteria release signalling molecules that initiate cooperative behaviours at high bacterial densities[202][203]. Given the nature of this experimental system, it is plausible that quorum sensing signalling molecules from a high density population could impact the growth of a different population. This would invalidate our assumption that encapsulated bacterial populations are independent, and we would not be able to treat our droplets as distinct and individual experimental repeats.

As such, we wanted to explore our assumption that each droplet population is independent, and that the growth of one bacterial population does not impact that of another. To do this, we define a metric S that is used to quantify whether final droplet population sizes are correlated with one another at a given distance, i.e. whether droplets at a given distance exhibit similar growth behaviours. S is calculated using the following steps. First, the centre-centre distances between all droplet pairings in a sub-section are measured. The difference in final population size is then recorded for each droplet pairing. The droplet pairings are then binned according to their absolute inter-droplet distance and the differences in their respective population sizes are summed and normalised according to the total number of droplet pairings discovered in that distance bin. At this point, a set of S values has been calculated for a number of inter-droplet distances, for each sub-section. So that the S values for different sub-sections can be compared, they are each normalised according to the average value of S for each sub-section. Only droplets that were detected for all 80 time steps were included in this analysis.

We chose to calculate S values for experimental runs conducted at streptomycin concentrations of 0 μg ml^{-1} (0.00 - 1 and 0.00 - 2) and 0.5 μg ml^{-1} (0.50 - 1 and 0.50 - 2), as we wanted to check that the population growth in a particular droplet is independent of the population growth in other droplets both in the absence and presence of streptomycin. Experimental runs conducted at higher streptomycin concentrations exhibited almost total net loss of visible bacteria, meaning that almost no droplets contained bacteria in the final time frames of those experimental runs. Consequently, the S values for these experimental runs provided little information and were therefore excluded.

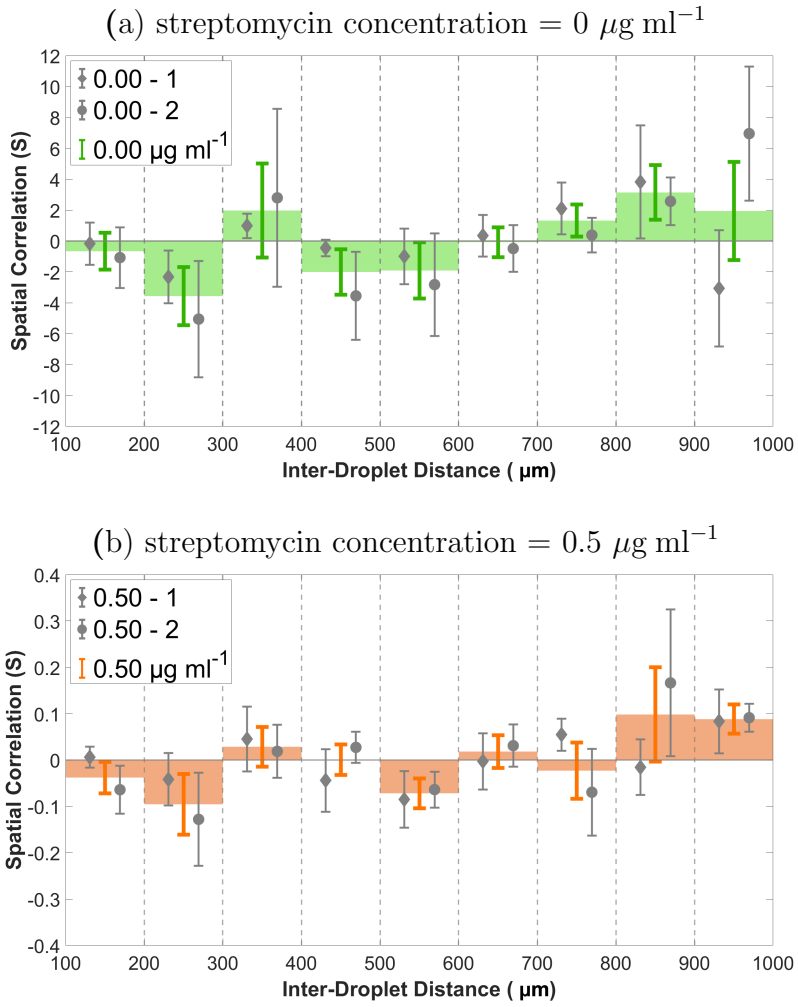

Figure 6.4 *S values plotted as a function of inter-droplet distance, for experimental runs conducted at (a) 0 μg ml^{-1} (experimental runs 0.00 - 1, 0.00 - 2) and (b) 0.5 μg ml^{-1} (experimental runs 0.50 - 1, 0.50 - 2). The error bars represent the standard error of S values across all subsections at a given distance.*

To briefly summarise our interpretation of S:

- If the S value decreases at a given distance, this implies that at that distance it is more likely for droplets to have convergent population sizes. This may happen if droplets that finish with large final populations are clustered close to one another.
- If the S value increases at a given distance, this implies that at that distance it is more likely for droplets to have divergent population sizes. This may happen if droplets that finished with large final populations were surrounded by droplets that finished with small final populations.
- If the S value is uniform across all distances, then this implies that it is no more or less likely for a droplet population to experience growth or death due to another droplet population at any given distance.

As can be seen in figure 6.4 (a) and (b), the calculated S values both in the absence and presence of streptomycin are stable across a range of inter-droplet distances, fluctuating between both positive and negative values. The S values in both cases do not appear to follow any consistent trend, with the majority of standard errors spanning a value of zero. This means that we do not believe there is any significant spatial correlation between the final population sizes of the droplets we measured.

The S value fluctuations observed in the absence of streptomycin (figure 6.4 (a)) are roughly one order of magnitude larger than the S value fluctuations observed in the presence of streptomycin (figure 6.4 (b)). This is unsurprising, as bacterial population growth rates in the absence of antibiotic vary considerably. This results in a wide distribution of final droplet population sizes and therefore large S values due to large differences in droplet populations. In contrast to this, bacterial population growth rates in the presence of antibiotic are suppressed. This results in final droplet populations that do not differ significantly in size, leading to smaller S values. For further detail regarding final population size distributions see section 7.6.

This analysis provided us with the confidence that bacterial population growth in our microfluidic droplets is independent of growth in any other droplets. This is a key assumption of the work shown in chapter 7, as well as numerous studies by other groups that use microfluidic systems and materials common to this work.

6.6 Bacterial fluorescence does not imply life

In the work presented in chapter 7, we use bacterial fluorescence to assess population growth. This approach is based upon the fundamental assumption that healthy, living bacteria fluoresce, making a measurement of fluorescence a proxy measurement of population size. We need to be aware, however, that dead or dying bacteria may, in principle, also fluoresce.

As discussed in section 2.4.5, fluorescent proteins are highly stable. It has been shown that following maturation, fluorescent proteins are highly resistant to degradation and turnover by specialist housekeeping enzymes that are able to break down proteins and peptides[204]. As such, fluorescent proteins typically have an *in vivo* degradation half-life of 24 hours[205]. Through the addition of short peptide chains, protein variants have been developed that are highly susceptible to degradation by specific intracellular proteases. The degradation half-life of these variants are reduced significantly - as low as 40 minutes[206][207]. These susceptible variants are used in studies exploring temporal gene expression where rapid degradation and turnover is essential.

The fluorescent protein produced by the *E. coli* strain used in this thesis (RJA002) is not an unstable, susceptible protein variant. As such, unless a bacterial cell experiences total lysis, it can be assumed that the fluorescent proteins manufactured by a bacterium before death will continue to fluoresce for the entirety of an 8 hour experimental run. This means that dead bacteria may generate fluorescence with sufficient intensity for detection. In summary, it cannot be assumed that when a bacteria undergoes death due to antibiotic inhibition it will cease to be detected as though it were still alive.

In our experimental system it is therefore not possible to distinguish between healthy fluorescent bacteria and bacteria that continue to fluoresce following death. This constraint impacts our interpretations of the growth dynamics discussed in chapter 7. However, it has still proven possible to draw meaningful and interesting conclusions from our data whilst acknowledging this limitation.

LIVE/DEAD staining

There are a number of stains available that are capable of discriminating live bacteria from dead bacteria. A popular and commercially available epifluorescent staining method is the LIVE/DEAD Bacterial Viability Kit (Baclight)[208], which consists of two stains.

The first stain, SYTO 9, binds to DNA and RNA, emits green fluorescence, and is able to penetrate all bacterial membranes. The second stain, propidium iodide (PI), similiarly binds to nucleic acids however is only able to penetrate damaged cytoplasmic membranes[209]. When PI is able to penetrate a cell that has been pre-stained with SYTO 9, the emission properties of the SYTO 9 stain changes due to stain displacement and quenching. This stain mixture produces red fluorescence. It is this altered emission state that is used to differentiate between bacterial cells that are alive and dead. If the membrane of a cell is intact - it fluoresces green and it is therefore assumed to be alive. If the membrane of a cell has been compromised - stain-mixing causes the cell to fluoresce red and it is therefore assumed to be dead.

Whilst this staining methodology is highly popular and used by a wide range of researchers across many fields of microbiology, it hinges on the assumption that cell membrane integrity is directly correlated with cell viability. This assumption holds true for membrane-compromised cells[210], however the assumption that cells with intact membranes are alive is not always valid[211].

There are a number of alternative techniques that can be used to determine whether cells in a bacterial suspension are living or dead. For example cell viability reagent alamarBlue uses a resazurin-based solution to assess the reducing power of live cells, which can be used as a quantitative measure of cell viability and health[212].

A cell viability indicator was not used in the research conducted for this thesis. This was because it would add significant complexity to both the fabrication and operation of our microfluidic system. Firstly, to introduce external reagents to our microfluidic droplets after encapsulation would require the addition of complex microfluidic geometries to our system. Therefore to use a viability indicator with our current microfluidic system, it would be need to be added to the bacterial suspension prior to encapsulation. It is unknown how a viability indicator would interact with the numerous components present in our microfluidic system

(continuous oil phase, surfactant, antibiotic). These interactions could potentially impact droplet stability and bacterial growth. Secondly, the additional fluorescence channel(s) necessitated by a viability indicator would substantially complicate imaging and analysis processes.

We did not feel that substantial complexity introduced by these indicators justified the additional information they would provide. Therefore, we decided not to use a viability indicator such as Baclight or alamarBlue. It was found that meaningful and novel results could be obtained with our microfluidic system despite the limitations discussed in this section, but acknowledge that once the system has been fully characterised and validated, LIVE/DEAD staining could be implemented in future iterations of our microfluidic system.

6.7 Conclusions

In this chapter, I have discussed a number of experimental checks, assumptions and error estimations that are necessary to consider when using the microfluidic system we have designed to quantitatively study small bacterial populations.

To start, sources of errors in the bacterial counting process were discussed and error estimations were made for the automated bacterial counting algorithm. The counting algorithm was found to increasingly underestimate bacterial population sizes as time passed. It is hypothesised that bacterial aggregation is the primary source of this automated counting error.

This was followed by a discussion of some of the technical limitations of our microfluidic device. Droplet diameter coefficients of variation ranged from 3% to 7%, this was judged to be acceptable given the experimental objectives of our research. Fano factors were calculated for initial bacterial population distributions. Fano factors above 1 were observed for all initial bacterial population distributions, indicating that a small amount of bacterial growth occurred during the delay from droplet encapsulation to droplet imaging. This growth was not considered critical as it was extremely limited in comparison to the population changes observed during the full experimental runs. Furthermore, this growth was not correlated with streptomycin concentration.

After this, droplet-to-droplet growth correlations were examined. It was shown using a spatial correlation of growth metric that changes in droplet population sizes over the course of an experimental run were not correlated with inter-droplet distance. This means that the growth dynamics of any given droplet population do not impact the growth dynamics of any other droplet populations.

Finally, the use of bacterial fluorescence as a measure of population growth and death was reviewed. It was concluded that it is not possible to use fluorescence microscopy to distinguish between healthy bacteria that are actively dividing, and dead bacteria that have not lysed. This is a critical distinction that impacts the conclusions and interpretations we can draw from the results presented in chapter 7. Despite this limitation, we found that we were still able to identify a number of novel growth dynamics using our microfluidic system.

Chapter 7

Encapsulated *E. coli* - a growth and inhibition study

7.1 Introduction

As discussed in chapter 1, the aim of my work was to develop an experimental system that could be used to investigate the heterogeneity in response of small bacterial populations to antibiotics. To this end, we have designed and fabricated a complete microfluidic system that allows us to encapsulate small bacterial populations and antibiotic within microfluidic droplets and then track bacterial growth on a droplet-by-droplet basis. We hope that by studying the growth dynamics of small bacterial populations, we will be able to better understand *in vivo* growth, antibiotic response and the factors that affect them.

7.2 Experimental objectives

In this chapter, the population growth dynamics of small bacterial populations grown in the presence of streptomycin at five different concentrations is compared. These concentrations are 0 μg ml^{-1}, 0.05 μg ml^{-1}, 0.5 μg ml^{-1}, 2.5 μg ml^{-1} and 50 μg ml^{-1}. Repeat experimental runs were conducted at streptomycin concentrations of 0 μg ml^{-1} and 0.5 μg ml^{-1} to give seven total experimental runs suitable for analysis.

Details of each experimental run are given in table 7.1, with each experimental run being given an experimental identification number as detailed in section 6.1.1. Whilst each experimental run was imaged using comparable grid sizes, the number of droplets successfully processed varies considerably between experiments due to fields of view being discarded in the validation stage, as discussed in chapter 5.

Experiment ID	Strep. Conc. (μg ml^{-1})	Droplet Count
0.00 - 1	0	687
0.00 - 2	0	1474
0.05 - 1	0.05	919
0.50 - 1	0.5	1796
0.50 - 2	0.5	883
2.50 - 1	2.5	439
50.0 - 1	50	1129

Table 7.1 *Summary of details of each experimental run. Strep. Conc. gives the final concentration (w/w) of streptomycin used in each experimental run once added to the M9 growth medium. Droplet count refers to the number of droplets detected within the whole microfluidic device, averaged across all time frames.*

The seven experimental runs discussed in the chapter were critically important as they were used to validate our experimental systems as a viable platform for the quantitative study of bacterial populations (see chapter 6 for further information). These data sets represent preliminary studies that explore the growth dynamics of small bacterial populations when exposed to streptomycin. Furthermore, they highlight the flexibility and utility of our microfluidic system as a more general tool for use in quantitative microbiology. The analyses discussed in this chapter showcases the variety of quantitative metrics that can be extracted from the data generated by our microfluidic system. These metrics are not possible to measure or calculate using traditional microbiological techniques, further underscoring the utility of our microfluidic system.

In this chapter we observe, measure and quantify a variety of novel bacterial growth phenomena using our microfluidic system. Understanding the observed variability between repeat data sets (0.00 - 1 and 0.00 - 2, 0.50 - 1 and 0.50 - 2) represents a research project in itself, and further studies are already underway to fully understand the growth dynamics in these small encapsulated populations and determine the factors that impact inter-experiment variability. It is

hoped that this research might also provide insight into the mechanisms behind the variable growth dynamics observed when using bulk growth techniques (see figure 7.4). These studies are being undertaken by Nia Verdon at the University of Edinburgh, under the supervision of Prof. Rosalind Allen and Dr. Simon Titmuss.

Beyond these opening investigations, Nia is interested in using our microfluidic system to study the heterogeneous response of small bacterial populations when exposed to different classes of antibiotics. A unique feature of our microfluidic system is the ability to image large numbers of small bacterial populations with single cell precision. Nia hopes to analyse the large scale statistics of bacterial growth both in the presence and absence of inhibiting agents, which has been shown to be highly heterogeneous when using bulk growth techniques (see section 7.5.2). Alongside this macro-scale statistical analysis, Nia will be able to simultaneously observe the underlying behaviours that may cause this growth heterogeneity at the single cell level.

7.3 Notable results

Where appropriate, results that we feel are particularly notable are highlighted. Some of these notable results are important as they further validate our microfluidic device. In these results, growth metrics are compared to values measured using bulk growth techniques. Other results are noteworthy as they offer insight into unique population dynamics exhibited by small bacterial populations that are not possible to observe or quantify using bulk growth methodologies. These notable results are visually emphasised by a blue text box, an example of which can be seen below.

Example notable result.

In blue text boxes such as this, the details of a notable result are discussed. Generally, each notable result will be supported by a number of analyses which will also be reference and summarised.

7.4 Experimental protocol

In this section I will outline the full experimental protocol used to generate the results discussed in this chapter. In this section, the beginning of the experiment (t = 0) is defined as the point at which imaging/data recording begins. Whilst every effort was made to standardise our experimental protocol, it was not possible to ensure certain processes completed within a certain time. As such, the timings detailed below should be treated as guidelines. These timings represent expected values based on our experience of working with the microfluidic system.

7.4.1 Device preparation, operation and image acquisition

At t = -22.5 hours, a 5 ml volume of M9 growth media supplemented with 0.4% glucose (M9gl) was inoculated with a single colony of RJA002 *E. coli* taken from an M9gl agar plate. The 5 ml volume was then placed in a shaking incubator (37°C, 200 rpm) for 18 hours, producing a high-concentration starting culture of *E. coli*.

At t = -4.5 hours, a 10 ml volume of fresh M9gl growth media was inoculated with 25 μl of bacterial suspension taken from the starting culture. This 10 ml volume was then placed in a shaking incubator (37°C, 200 rpm) for 1.5 hours. The 1.5 hour duration of this incubation period was found to consistently produce a low density bacterial suspension that produced droplet populations with a mean population size of ≈1-2 cells when encapsulated into microfluidic droplets.

By inoculating the 10ml volume of fresh M9gl growth media with the 25 μl of starting culture, then incubating for 1.5 hours, it was intended that the bacterial suspension would be in the exponential growth phase during the 8 hour observation period that would follow.

Logarithmic Growth

The logarithmic growth phase (or exponential phase) is a period of uninhibited bacterial population growth in which population doubling occurs at a constant rate. Exponential growth is preferred in bacterial studies as bacteria in this state reproduce most consistently. See chapter 2 for further information regarding bacterial growth.

When appropriate, the antibiotic streptomycin was added at a pre-determined concentration to the 10 ml volume of M9gl after the 1.5 hour incubation period. It was then incubated again in a shaking incubator (37°C, 200 rpm) for 10 minutes to ensure adequate mixing, and the standard experimental protocol was then resumed.

Streptomycin

Streptomycin is a bactericidal ribosome targeting antibiotic. We chose to use streptomycin in our research as it has been suggested that individual *E. coli* cells may respond differently to streptomycin inhibition at the level of individual cells[48]. For further information regarding antibiotics and streptomycin, see section 2.3.

At t = -3.5 hours, 500 μl of the oil phase is drawn into a 1 ml plastic syringe and connected to the microfluidic device via a syringe pump. This was then pumped into the microfluidic device at 50 $\mu\mathrm{l\,hr^{-1}}$, ensuring that the oil phase reaches the interior of the microfluidic device before the aqueous phase and purges any remaining air from the oil inlet.

At t = -3 hours, after the 10 ml volume of M9gl had been incubated for 90 minutes, 1 ml of the bacterial suspension was drawn into a 1 ml plastic syringe and connected to the microfluidic device using a second syringe pump, the aqueous bacterial phase was then flowed into the microfluidic chamber at 50 $\mu\mathrm{l\,hr^{-1}}$. The microfluidic device mount was then filled with water and brought to 37°C using a water bath and peristaltic pump. The water level and temperature was then adjusted regularly throughout the experiment to ensure the microfluidic device and inlet tubing were maintained at a temperature of 37°C.

At t = -2 hours, once both the aqueous and oil phase reached the flow focusing junction and droplet generation had begun, the device was left for 15 minutes so that pressure levels within the device could equilibrate. This allowed droplet production to settle into a steady, monodisperse state. After the 15 minute equilibration period had concluded, the flow rates were adjusted. The flow rate of the aqueous phase was reduced to 20 μl hr^{-1}, whilst the flow rate of the oil phase was increased to 80 μl hr^{-1}. The device was then left for a second 15 minute equilibration period, ensuring the stable production of a monodisperse droplet emulsion. Droplet production was continued until the monodisperse droplet emulsion began to flow into the microfluidic reservoir. This process usually took between 1.5 and 2 hours.

As the monodisperse droplet emulsion travelled from the droplet generation device to the reservoir device, a number of imaging preparation processes were completed. The imaging grid was initialised to optimally cover the microfluidic reservoir. Microscopy settings were then adjusted to optimise image quality. Brightfield channel exposure was set to 10 ms, fluorescence exposure was set to 50 ms and the pixel binning of both channels was set to 2 x 2.

Once the reservoir was full of monodisperse droplets of the correct size, the syringe pumps were stopped. The inlet and bridge tubing were then severed, arresting all droplet movement within the microfluidic reservoir. Automatic focus was adjusted for optimal imaging of bacteria bacteria viewed in the fluorescence channel across multiple fields of view, correct focus in the fluorescence channel ensured the high image contrast required for bacterial counting whilst maintaining an adequate focus for the boundary detection algorithm using the brightfield channel.

The imaging acquisition process was then started (t = 0), during the following 8 hours the images were continually monitored for imaging or automation problems. The temperature of the water immersing the device was maintained at 37°C by adjusting the water bath temperature to ensure optimal uninhibited growth.

7.4.2 Image processing

Once each experimental run was completed, the data was segmented into a number of sub-sections that were processed individually (see chapter 5 for further details regarding the segmentation process). Once each sub-section had been passed through the image processing algorithm independently, the resultant data was recombined to create a complete data set for each experimental run.

7.5 Growth of total bacterial population across all droplets

A fundamental measure of the growth dynamics of a bacterial population is provided by the growth curve, which is a plot of population size/density as a function of time.

Colony-Forming Units

Under the correct growth conditions, an individual cell placed onto an agar growth plate will proliferate and form a macroscopic colony visible to the naked eye. In this context, the progenitor cell is defined as a Colony-Forming Unit (CFU). CFUs can be used to estimate the density of viable progenitor cells in a bacterial suspension[213].

This is achieved by spotting samples from the serial dilution of a cell suspension onto agar plates that have been supplemented with growth media. After an incubation period, the agar plates are then examined and where CFUs can be identified individually, they are counted. By correlating this CFU count with the dilution factor of the sample, an order of magnitude estimate of the viable cell density can be made. Determining viable cell density by manually counting CFU's is a time-consuming and laborious task that is prone to error[214]. As such, indirect methods of measuring cell density are often used, these proxy measurements are then calibrated against CFU measurements.

To measure the growth curve of a bacterial population, a proxy variable is usually measured that is assumed to be intrinsically linked to population size or density, such as fluorescence intensity or optical density. This value is then plotted versus time and the growth dynamics of large bacterial populations are able to be quantified. With our microfluidic system, it is possible to count the bacterial population directly in a highly accurate and time-efficient manner. So that we could compare the growth behaviour of our droplet populations with the growth behaviour seen in standard bulk cultures, we begin our analysis by examining total population growth curves observed in our microfluidic device.

Bacterial Growth

As described in chapter 2, bacterial growth can be divided into four distinct phases: an initial lag phase, an exponential growth phase, a stationary and a death phase. Experiments are often designed such that the bacterial population is in the exponential growth phase. In this phase growth rates and doubling times for a bacterial population are easily calculated.

7.5.1 Total population growth curves

Results

To quantify and compare the overall growth dynamics of our droplet populations with those observed in bulk growth experiments, total population growth curves for each experimental run have been plotted. These were calculated by first summing the total number of bacteria detected across all droplets at each time frame of an experimental run. This total count was then plotted versus time to produce a growth curve.

A sampling error estimate for each growth curve is also shown. This error estimate was determined by randomly selecting a subset of droplets from the pool of droplets that were successfully tracked across all time frames of their experimental run. The total bacterial population of this droplet subset was then calculated for all time steps. This sampling process was then repeated multiple times, and the standard deviation of the population size at each time step was calculated across the droplet subsets. This standard deviation was then scaled according

to the number of bacteria measured in each experimental run. For each experimental run, each randomly selected droplet subset was one third the size of the overall droplet set, and 10 droplet subsets were used to calculate the standard deviation at each time frame.

Growth curves for all experimental runs can be seen in figures 7.1 and 7.2. As discussed in section 7.4, t = 0 herein refers to the time at which the image acquisition process is started. This is after monodisperse droplets have been isolated in the microfluidic reservoir and fluid flow has been stopped.

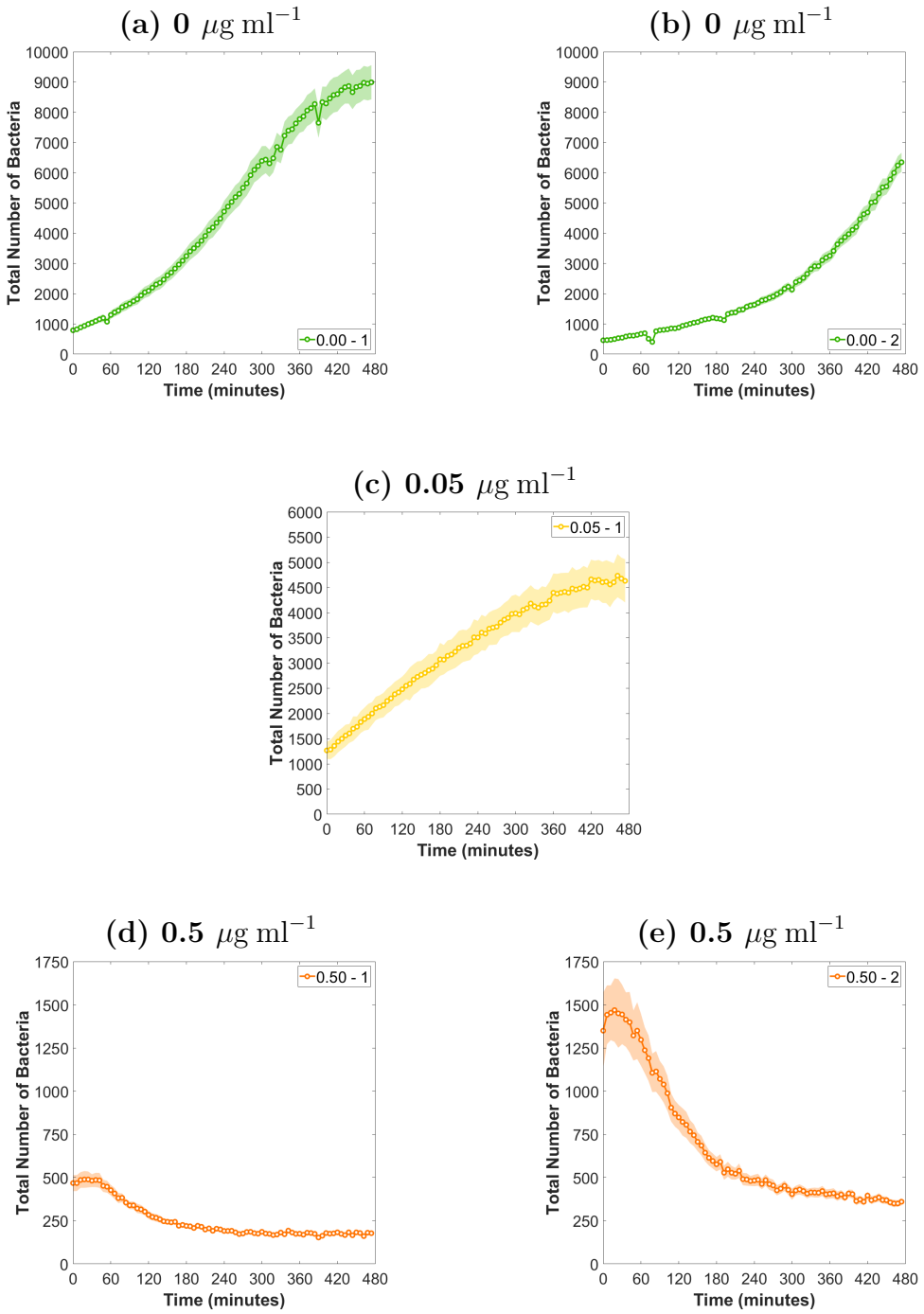

Figure 7.1 *Total population growth curves of RJA002 E. coli populations encapsulated in microfluidic droplets, grown in M9 minimal media. Each graph represents a complete experimental run.*

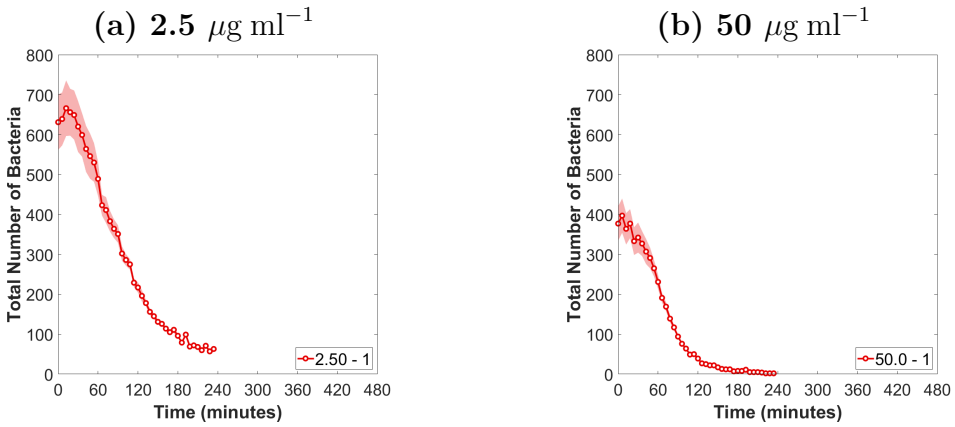

Figure 7.2 *Total population growth curves of RJA002 E. coli populations encapsulated in microfluidic droplets, grown in M9 minimal media. Each graph represents a complete experimental run.*

Discussion

The experimental runs have been separated into 4 distinct classes according to their total population growth behaviour. These are described below. The colour-based identification system is used throughout this chapter for the purpose of clarity.

Uninhibited - logarithmic growth

Bacteria encapsulated in the absence of streptomycin (experimental runs 0.00 - 1, 0.00 - 2) (figure 7.1) exhibited uninhibited logarithmic growth (see figure 7.3 for further details). Experimental run 0.00 - 1 appears to enter the stationary phase of growth around 5 hours into the experiment. This may be due to its comparatively large initial population sizes (see section 7.6) and short population doubling times (see section 7.5.2). Experimental run 0.00 - 2 exhibited logarithmic growth throughout the entirety of the 8 hour observation.

Weakly inhibited - linear growth

Bacteria encapsulated in the presence of streptomycin at a concentration of 0.05 μg ml^{-1} (experimental run 0.05 - 1) (figure 7.1) exhibited weak inhibition, as characterised by a lower total population growth rate (see section 7.5.2) and net bacterial growth. At this concentration the total bacterial population size appears to grow in a linear fashion.

Weakly inhibited - loss of visible bacteria

Bacteria encapsulated in the presence of streptomycin at a concentration of 0.5 μg ml^{-1} (experimental runs 0.50 - 1, 0.50 - 2) (figure 7.1) exhibited weak inhibition with a net loss of observable bacteria. However, a significant sub-population of bacteria are observed to fluoresce throughout the 8 hour observation.

Strongly inhibited - loss of visible bacteria

Bacteria encapsulated in the presence of streptomycin at concentrations of 2.5 μg ml^{-1} and 50 μg ml^{-1} (experimental runs 2.50 - 1, 50.0 - 1) (figure 7.2) exhibited strong inhibition with an almost total loss of observable bacteria. At these concentrations, streptomycin appears to be bactericidal, leaving very few bacteria remaining visible.

Experiment ID	Strep. Conc. ($\mu g\ ml^{-1}$)	Initial Population	Final Population	Percentage Change
0.00 - 1	0	790	8991	+ 1038.1%
0.00 - 2	0	460	6347	+ 1279.8%
0.05 - 1	0.05	1267	4631	+ 265.5%
0.50 - 1	0.5	468	178	- 62.0%
0.50 - 2	0.5	1350	360	- 73.3%
2.50 - 1	2.5	631	63*	- 90.0%
50.0 - 1	50	377	2*	- 99.5%

Table 7.2 *Quantitative summary of ensemble growth behaviour for all experimental runs. *Experimental runs 2.50 - 1 and 50.0 - 1 were ended after 4 hours due to large-scale loss of visible bacteria.*

The variation in total population growth with antibiotic concentration is in line with our basic expectations - as antibiotic concentration increased growth was increasingly inhibited. At high streptomycin concentrations loss of visible bacteria was observed, which we attribute to cell lysis. Unexpectedly, at moderate streptomycin concentrations (0.5 $\mu g\, ml^{-1}$) we observed a sub-population of bacteria that did not divide, but remained fluorescent until the end of the 8 hour experimental run. Counter to the literature[215] this could imply that streptomycin at this concentration is bacteriostatic in nature for populations of this size, or it may indicate that the bacteria have died but not lysed and are therefore still visible in fluorescence. Both of these explanations are very interesting, as we are not aware of any prior work that has reported two alternative death pathways for bacteria inhibited by streptomycin: lysis or non-lysis. This phenomena is explored further in subsequent analyses.

7.5.2 Total population growth rates and doubling times

Results

To further quantify the growth of the total population, bacterial growth rates and doubling times have been calculated for the experimental runs that exhibited net growth (0.00 - 1, 0.00 - 2 and 0.05 - 1). These were calculated using population size data from the first 234 minutes of each experimental run, this ensured that the transition to stationary phase observed in experimental run 0.00 - 1 was not included in the growth rate calculations. Plots of the logarithm of the total population size as a function of time are shown in figure 7.3; growth rates and doubling times were calculated from the gradients of these plots. The plotted errors shown in these plots is the same sampling error estimate that was calculated for figures 7.1 and 7.2. For the non-logarithmic data the error is omitted for visual clarity.

The calculated growth rate errors shown in table 7.3 are the standard errors for prediction, obtained from the linear fit made to the logarithmically scaled population size data. The calculated growth rates and associated doubling times are tabulated in table 7.3. Whilst experimental run 0.05 - 1 did not exhibit logarithmic growth, an approximate doubling time was still calculated for further comparison.

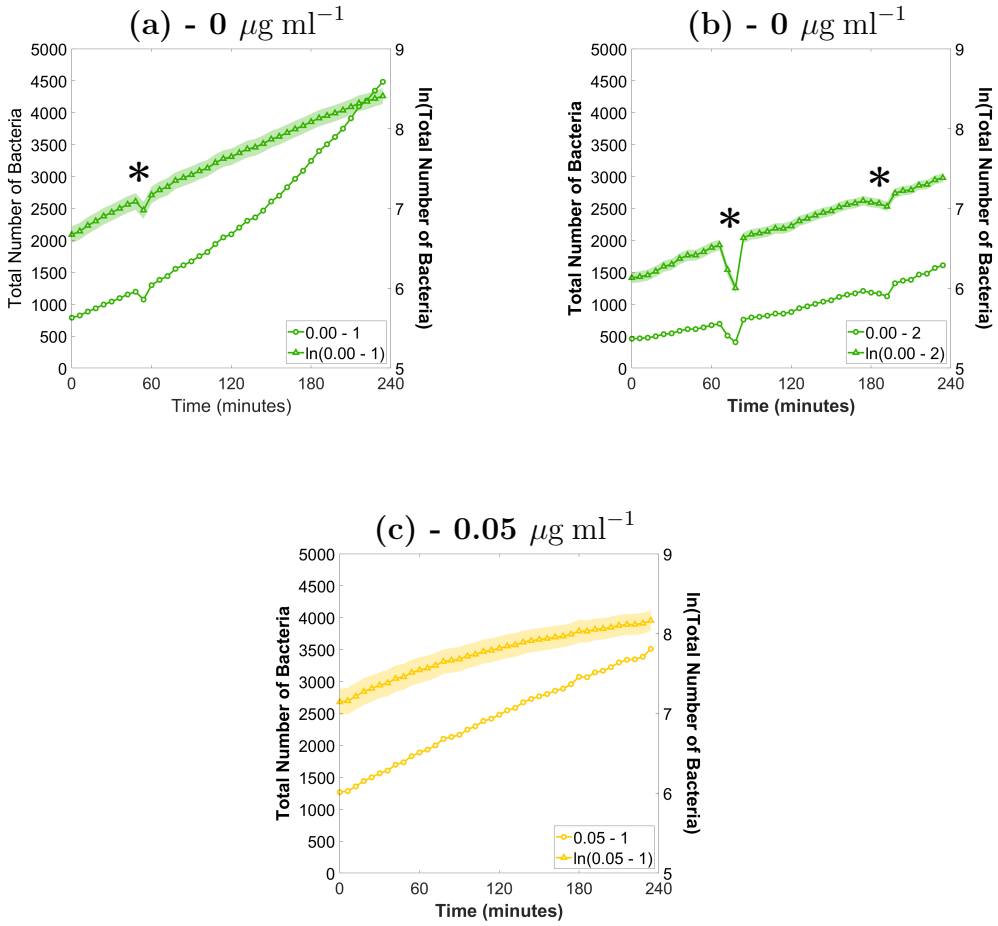

Figure 7.3 *Logarithmically scaled ensemble growth curves of RJA002 E. coli populations encapsulated in microfluidic droplets, grown in M9 minimal media at streptomycin concentrations of 0 μg ml^{-1} and 0.05 μg ml^{-1}. Each graph represents a complete experimental run. *Dips in the data are due to brightfield lighting fluctuations causing droplet boundary detection failures. These points are removed for the calculation of growth rates and doubling times.*

Experiment ID	Strep. Conc. (μg ml^{-1})	Growth Rate - (λ) (min^{-1})	Doubling Time (mins)
0.00 - 1	0	0.0075 ± 0.0001	93 ± 1
0.00 - 2	0	0.0053 ± 0.0001	131 ± 2
0.05 - 1	0.05	0.0042 ± 0.0001	165 ± 4

Table 7.3 *Calculated growth rates and doubling times of experiments that exhibited net bacterial growth.*

Discussion

The total population growth rates and doubling times were calculated for all experiments that exhibited net bacterial growth (table 7.3).

The total population doubling time of encapsulated bacterial populations grown in the absence of antibiotic (experimental runs 0.00 - 1, 0.00 - 2) was found to be 93 ± 1 minutes and 131 ± 2 minutes, respectively. Despite experimental runs 0.00 - 1 and 0.00 - 2 being performed under the same growth conditions, they show a significant difference in growth rate. There are numerous potential explanations for this difference. For example, each experimental run is initiated with a bacterial culture taken from a different colony on an agar plate (see chapter 3 for more information): it is possible that one of these colonies had picked up a mutation that affected its growth rate. In the future we would like to repeat the experimental runs conducted in the absence of streptomycin to determine whether the variability in growth rate between replicate runs persists. Regardless of the observed difference in total population growth rate between experimental runs 0.00 - 1 and 0.00 - 2, they both exhibited logarithmic growth, with growth rates larger than any other experimental run that exhibited a net increase in bacterial population size.

The approximate total population doubling time of encapsulated bacterial populations grown in the presence of streptomycin at a concentration of 0.05 μg ml^{-1} was found to be 165 ± 4 minutes.

M9 Minimal Media

The growth media encapsulated within our microfluidic droplets was M9 minimal media supplemented with glucose to a final concentration of 0.4% w/v.

Bulk growth measurements

Waclaw *et al.* at the University of Edinburgh reported a growth rate for RJA002 *E. coli* grown in M9gl of 0.0062 ± 0.0004 min^{-1}, corresponding to a doubling time of 112 ± 7 minutes[201]. These measurements were obtained using a 96 well plate-reader, and the growth rate value is the mean of 24 experimental repeats. These growth curves can be seen in figure 7.4.

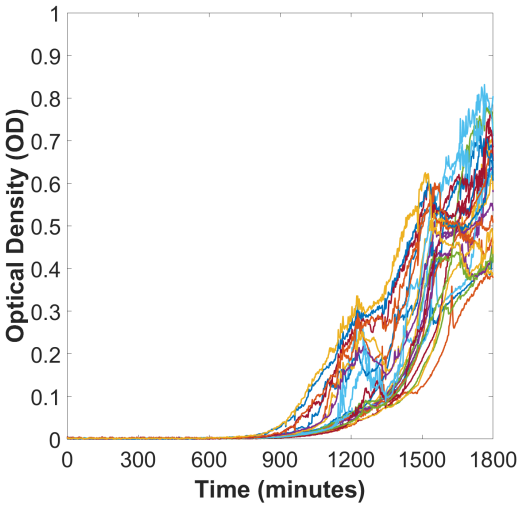

Figure 7.4 *Multiwell plate growth curves of RJA002 E. coli grown in M9 minimal media supplemented with glucose. Plotted using data provided by Waclaw et al.[201]. Exponential growth is visible at OD < 0.1.*

A significant lag phase can be seen in the growth curves obtained using a plate reader, which were plotted using data provided by Waclaw *et al.*[201]. This is not observable in the growth curves obtained using our microfluidic system. This is primarily because measurements begin in plate reader experiments almost immediately after the initial low-concentration bacterial suspension is produced. In contrast, measurements begin in our microfluidic system ≈4.5 hours after the initial low-concentration bacterial suspension is produced. During this 4.5 hours time delay, the bacterial suspension is passed into the microfluidic device where it is then encapsulated into a monodisperse microfluidic droplet emulsion. These droplets are then moved into the microfluidic imaging reservoir. See section 7.4.1 for further information regarding the complete experimental protocol and the timings associated with this process.

The calculated doubling times for RJA002 growing in our microfluidic droplets are 93 ± 1 minutes (experimental run 0.00 - 1) and 131 ± 2 minutes (experimental run 0.00 - 2). These values are 17% shorter and 17% longer than the bulk growth measurement of 112 minutes reported by Waclaw *et al.* The error value for the growth rate obtained by Waclaw *et al.* was calculated by assessing the growth rate variation across 24 experimental repeats. The error values for the growth rates we obtained using our microfluidic system are the standard errors for prediction, obtained from the linear fit made to the logarithmically scaled population size data (figure 7.3). As such, the bulk measurement error estimation is significantly higher than the errors calculated for our microfluidic system.

To accurately compare the total population growth rates (and errors) of our microfluidic system with those obtained using traditional bulk techniques, it would be necessary to perform additional repeat experiments using our droplet system. This would allow us to obtain a statistically significant inter-experimental error estimation, further validating this system for use in microbiological research (see section 7.2 for further discussion).

Logarithmic growth was observed that was consistent with bulk measurements, indicating that the process of encapsulation and growth using our microfluidic system did not inhibit growth.

In experimental runs 0.00 - 1 and 0.00 - 2 (streptomycin concentration of 0 μg ml^{-1}) logarithmic growth was observed (figure 7.3). Growth rates and doubling times of these experimental runs were consistent with literature values obtained using bulk measurement techniques[201] (table 7.3). This suggests that bacterial populations grown using our microfluidic system are not significantly inhibited by their environment. Furthermore, access to oxygen and the accumulation of toxic waste products does not appear to be limiting bacterial growth inside our microfluidic system.

7.5.3 Minimum inhibitory concentration

The MIC of streptomycin has been measured for RJA002 in glucose-supplemented minimal media repeatedly using bulk growth techniques. Reported MIC values lie within 1 order of magnitude, with measurements ranging from $\approx 0.2\ \mu g\ ml^{-1}$[48] to $\approx 2\ \mu g\ ml^{-1}$[216]. From the experimental data presented in this section, it is clear that the experimental MIC measured for these droplet encapsulated populations is between $0.05\ \mu g\ ml^{-1}$ (net bacterial growth) and $0.5\ \mu g\ ml^{-1}$ (net reduction in observed bacteria).

Greulich et al. have shown that the MIC value of streptomycin exhibits a dependence on growth rate[48]. Given that bulk measurement growth rates differ from our calculated growth rates presented in table 7.3, it follows that our MIC value might also be expected to differ from the bulk measurement MIC values. By comparing our antibiotic-free growth rate values with those found in the work of Greulich *et al.* we predict a streptomycin MIC value of around $0.3\ \mu g\ ml^{-1}$. This is consistent with the observed effects of the different streptomycin concentrations on the total population growth behaviour shown earlier in this section.

7.5.4 Analysis of individual droplet populations

Whilst the total population growth rate measurements provide insight regarding the macro-scale behaviour of the bacterial populations, an advantage of using our microfluidic device is the ability to accurately quantify the growth dynamics of many small populations simultaneously. It is our goal to study the micro-scale behaviour that occurs at the individual droplet level so that we can then understand how the growth dynamics in these individual droplets gives rise to the total population growth dynamics that have been described here. To do this, it is necessary to analyse the growth in the droplet populations separately, thereby building a more nuanced statistical picture of the overall stochastic bacterial growth.

7.6 Size distributions of bacterial populations growing in droplets

7.6.1 Initial population size distribution vs. final population size distribution

Results

As discussed in chapter 2, it is well understood that the initial population size distribution in our droplets is expected to follow a Poisson distribution[132]. Despite this statistical understanding of the initial population size distribution, it not known how the population size distribution evolves as each droplet population undergoes stochastic growth.

Figure 7.5, 7.6 and 7.7 show histograms of the distribution of the bacterial population sizes at the start and end of each experimental run.

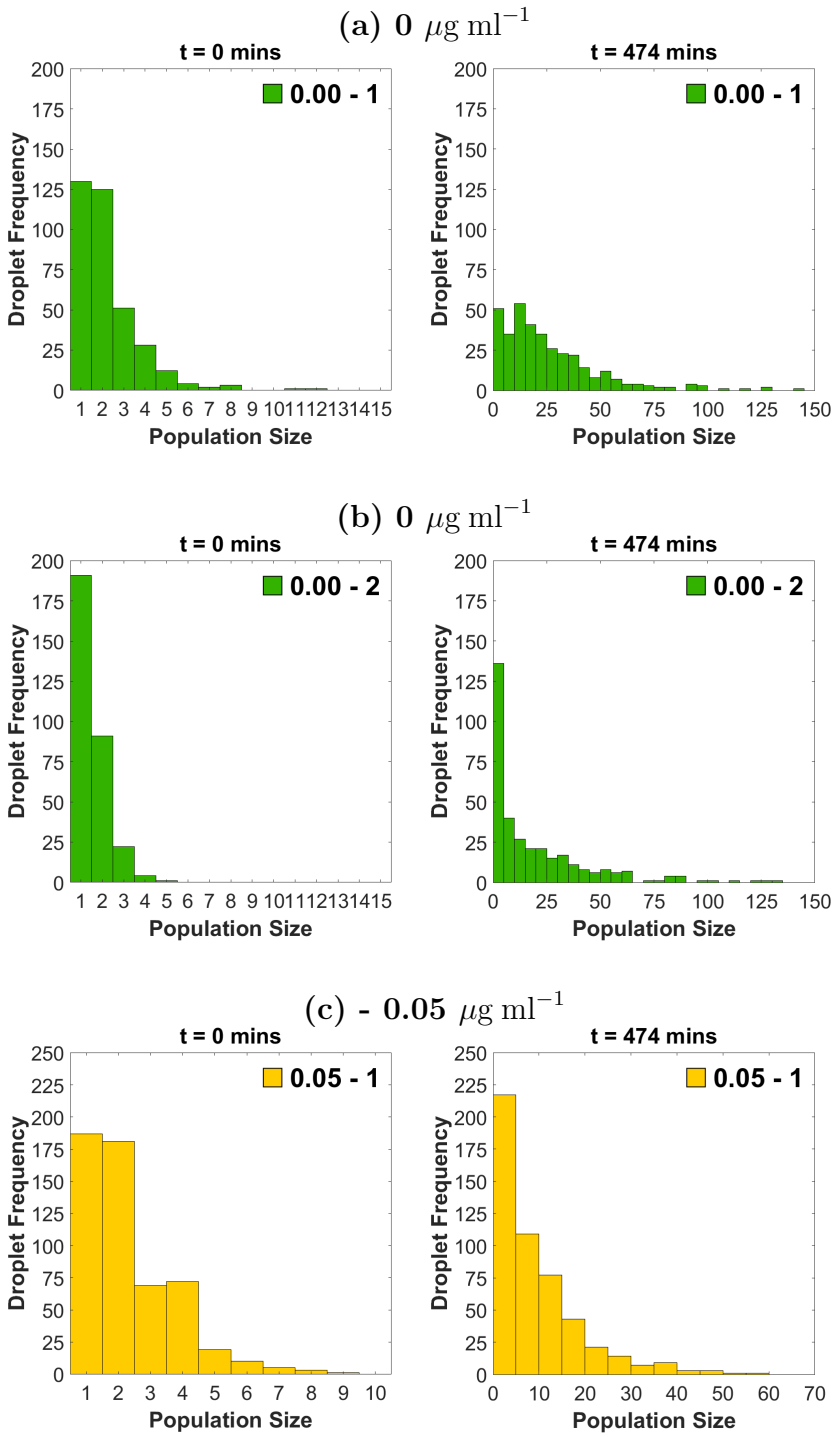

Figure 7.5 *Histograms showing the population distributions of droplets at $t = 0$ mins and $t = 474$ mins, grown in M9 minimal media at streptomycin concentrations of (a,b) 0 μg ml^{-1} and (c) 0.05 μg ml^{-1}. The number of detected, populated droplets included in each histogram at [$t = 0$ mins, $t = 474$ mins] is (a) [357, 355], (b) [309, 339], (c) [547, 522].*

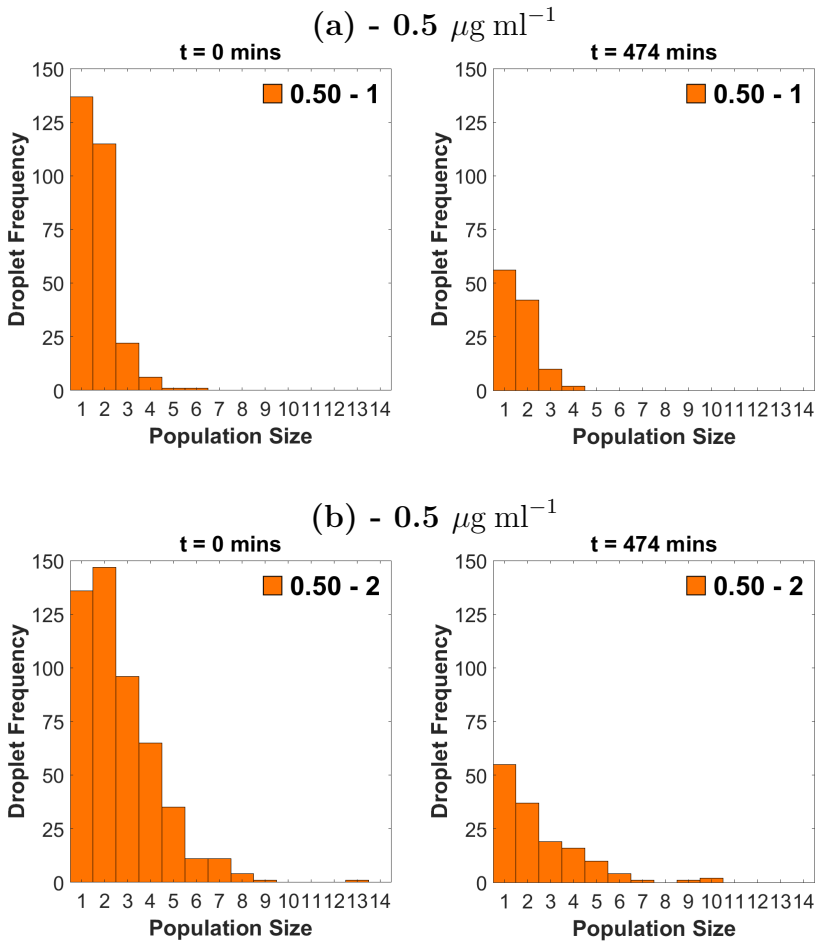

Figure 7.6 *Histograms showing the population distributions of droplets at $t = 0$ mins and $t = 474$ mins, grown in M9 minimal media at a streptomycin concentration of 0.5 μg ml^{-1}. The number of detected, populated droplets included in each histogram at [$t = 0$ mins, $t = 474$ mins] is (a) [282, 127] and (b) [507, 226].*

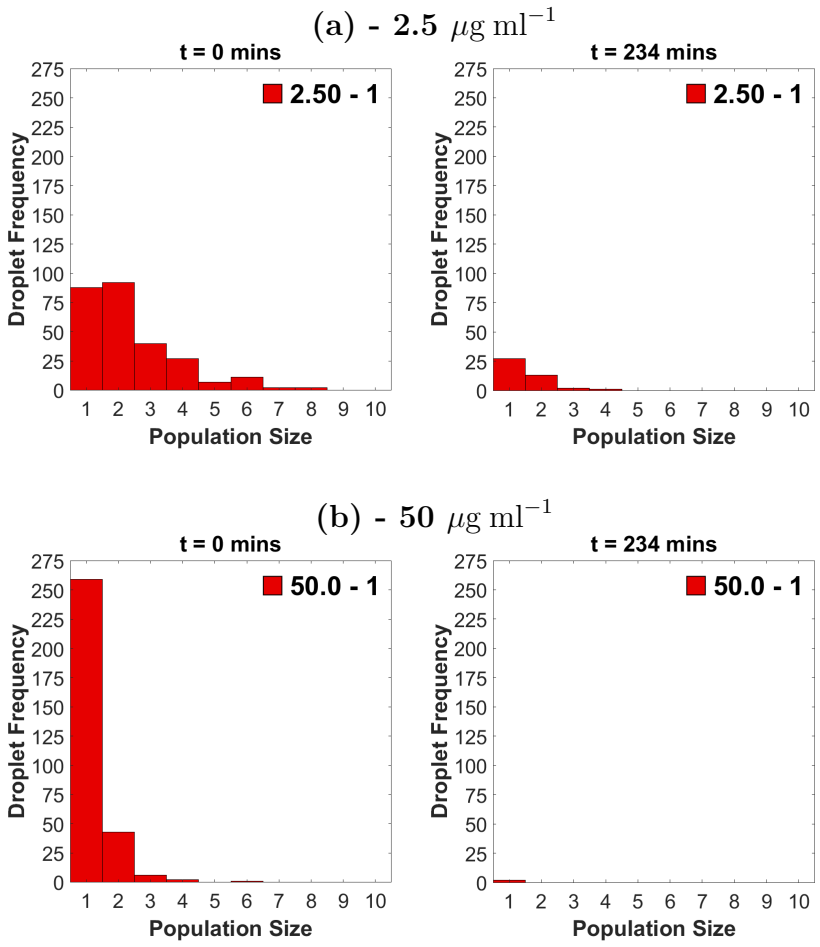

Figure 7.7 *Histograms showing the population distributions of droplets at $t = 0$ mins and $t = 234$ mins, grown in M9 minimal media at streptomycin concentrations of (a) 2.5 μg ml^{-1} and (b) 50 μg ml^{-1}. The number of detected, populated droplets included in each histogram at [$t = 0$ mins, $t = 234$ mins] is (a) [268, 43] and (b) [311, 2].*

The mean and standard deviation was calculated for the initial and final population size distributions. These are plotted in figure 7.8

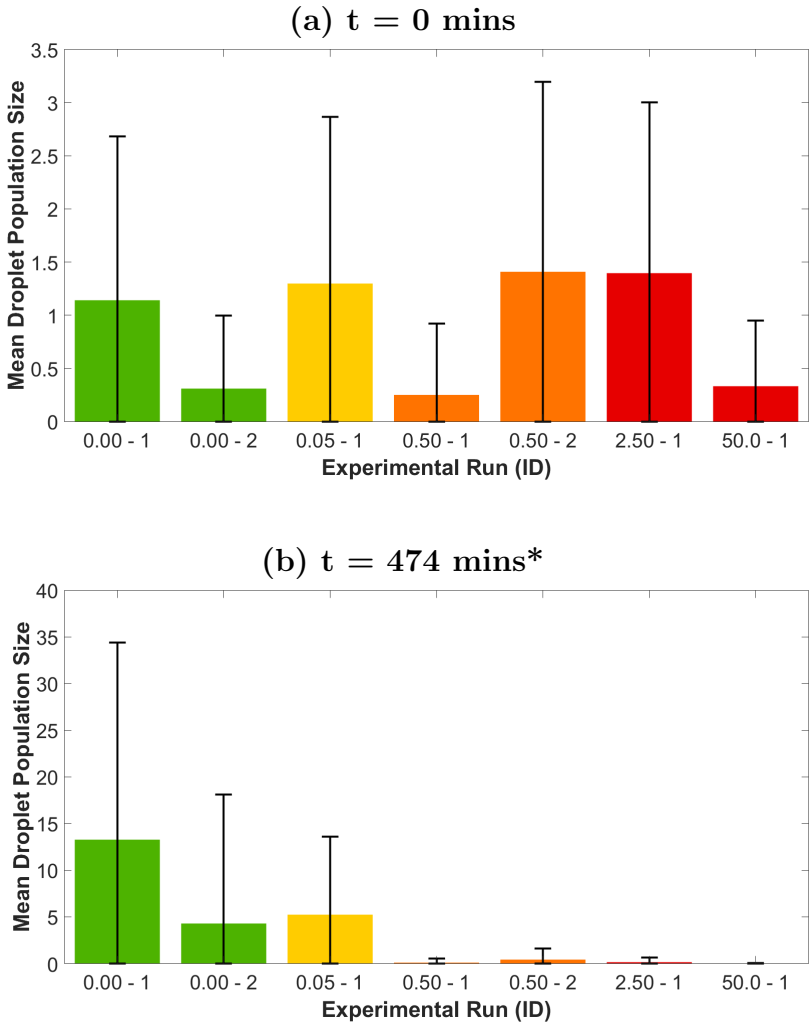

Figure 7.8 *Bar plots of the initial and final mean droplet population size. (a) displays the initial mean population size for each experimental run, (b) displays the final mean population size for each experimental run. Error bars represent standard deviation. *t = 234 mins for experimental run 2.50 - 1 and 50.0 - 1.*

For a Poisson distribution, the mean and variance are equal. The Fano factor for the initial and final population size distributions was plotted as a function of streptomycin concentration. This can be seen in figure 7.9.

To further this analysis, a "predicted" final population distribution was calculated for each experimental run. This was achieved by calculating a deterministic growth rate for each experimental run, using the initial and final total bacterial population size. Each of the initial population distributions were then "grown" using the deterministic growth rate to produce a predicted final population distribution. The mean, variance and Fano factor for each of these predicted final population distributions was then calculated, and then compared to the observed final population distributions. These predicted Fano factor values are also plotted in figure 7.9.

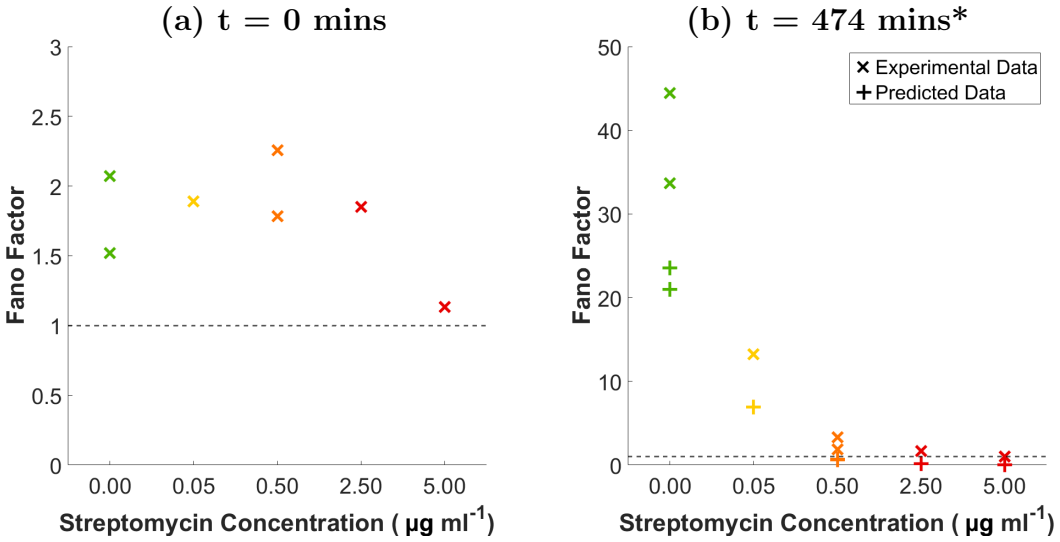

Figure 7.9 *Scatter plot showing the Fano factor for each experimental run as a function of streptomycin concentration. (a) Displays the initial experimental population distribution Fano factors, (b) displays the final experimental and predicted population distribution Fano factors. *t = 234 mins for experimental run 2.50 - 1 and 50.0 - 1.*

Discussion

For experimental run 0.00 - 1 (streptomycin concentration of 0 μg ml^{-1}) the mean population size increases dramatically over the course of the experimental run, consistent with the observed logarithmic growth. The initial Fano factor is 2.07, indicating the population distribution has a Poisson character, although the variance is ≈2x greater than the mean population size would predict given a Poisson encapsulation process. This discrepancy was discussed in chapter 6. The

final Fano factor is 33.70, indicating a large increase in variance with respect to the mean. This variance can be seen clearly in the extended distribution tail at large population sizes.

In experimental run 0.00 - 2 (streptomycin concentration of 0 μg ml^{-1}) the mean population size also increases significantly over the course of the experimental run. The initial Fano factor is 1.52, again indicating a higher variance than would be anticipated given the starting mean. The final Fano factor is 44.44, again indicating that uninhibited logarithmic growth raises increases the variance away from that predicted by Poisson statistics. Despite experimental run 0.00 - 2's lower growth rate, the final Fano factor of experimental run 0.00 - 2 is greater than the final Fano factor of experimental 0.00 - 1. This means that the variance in experimental run 0.00 - 2 increases more than experimental run 0.00 - 1 (over the course of an experimental run) when normalised by the mean population size. Experimental run 0.00 - 1 was, however, observed to enter the stationary phase of growth after around 5 hours, this could explain the decreased Fano factor of this experimental run with respect to experimental run 0.00 - 2.

For experimental run 0.05 - 1 (streptomycin concentration of 0.05 μg ml^{-1}), the mean population size increases during the run, but not to the same degree as the experimental runs completed at 0 μg ml^{-1}. A key difference can be seen in the final distribution - the tail is much shorter (failing to extend beyond 70 cells), despite the initial distribution being skewed to larger populations than other experimental runs. The initial Fano factor is 1.89, consistent with the values obtained in the absence of streptomycin. The final Fano factor is 13.25, again implying a comparatively large increase in variance with respect to the mean. Although the final Fano factor indicates an increased variance with respect to the mean, it is less than half of the final Fano factors calculated for experimental runs 0.00 - 1 and 0.00 - 2, indicating even low antibiotic concentrations may significantly limit the growth of high population droplets.

For experimental runs 0.50 - 1 and 0.50 - 2 (streptomycin concentrations of 0.5μg ml^{-1}), the mean droplet population size decreases over the course of each 8 hour experimental run. Interestingly, despite the loss of observable bacteria in these experimental runs, a number of droplets with moderate bacterial populations continue to visibly fluoresce and these populations appear to remain stable in size. The Fano factor for experimental run 0.50 - 1 increases from 1.78 to 1.84 over the course of the experimental run. This indicates that the droplet population size variance doesn't change significantly over the course of the experimental

run, when normalised according to the mean. The Fano factor for experimental run 0.50 - 2 increases from 2.26 to 3.34 over the course of the experimental run, indicating a small increase in variance with respect to the mean.

For experimental runs 2.50 - 1 and 50.0 - 1 (streptomycin concentrations of 2.5 μg ml^{-1} and 50 μg ml^{-1}), the final population mean decreases significantly during the run, consistent with the net bacterial death observed in their total population growth curves. The initial Fano factor for experimental run 2.50 - 1 is 1.85, which is consistent with the previously discussed experimental runs. This decreases to 1.65 after the 4 hour experimental run, indicating a decrease in variance with respect to the mean. The initial Fano factor for experimental run 50.0 - 1 is 1.13, indicating a population size distribution that has a strong Poisson character. This Fano factor decreases to 1.00, however this is misleading as the vast majority of droplets contain 0 bacteria, with only 2 droplets containing 1 bacteria each.

Aside from the initial Fano factors being higher than anticipated given a Poisson process (see chapter 6), some of the most interesting results from this data are the Fano factors calculated for experimental runs 0.50 - 1 and 0.50 - 2. For context, in experimental runs that exhibited net bacterial growth (0.00 - 1, 0.00 - 2, 0.05 - 1), the Fano factors increased over the course of the experimental run, indicating an increase in variance with respect to the mean. In experimental runs that exhibited a significant net loss of total visible bacteria (2.50 - 1, 50.0 - 1), the Fano factors decreased over the course of the experimental run, indicating an decrease in variance with respect to the mean. Counter to these trends, experimental runs 0.50 - 1 and 0.50 - 2 exhibited a net loss of total visible bacteria, but the Fano factors increased over the course of these experimental runs. This implies that whilst the mean droplet population size decreased, the variance normalised with respect to this mean increased. An explanation for this increase in Fano factor could be that whilst on average the droplet populations decreased in size, streptomycin at this concentration does not inhibit droplet populations equally. It could be that droplet populations with large initial populations are inhibited less than droplet populations with small initial populations, driving an increase in Fano factor. This hypothesis is supported by further analysis that will be described later on in this section.

The predicted Fano factor values for the deterministic final population distributions can be seen in figure 7.9(b). The predicted final population Fano factor values are all lower than their respective experimental values. This implies that the variance of the final population distributions are larger than would be ex-

pected given the initial population distributions and deterministic growth. In the experimental data, increased growth results in an increased Fano factor value. This generally holds true for the predicted data too, however they do not scale linearly with their associated experimental value. For example, the final experimental Fano factor for run 0.00 - 1 is 33.66 and its predicted value is 23.58 (70%), whereas the final experimental Fano factor for run 0.00 - 2 is 44.44 and its predicted value is 20.98 (47%). The concept of comparing the exhibited growth with deterministic growth is explored in further detail in section 7.6.3, where the final experimental population distributions are compared with their deterministic counterparts.

7.6.2 Time evolution of population size distribution

Results

Figures 7.10 and 7.11 are 3-dimensional colour plots that show the evolution of each experimental run's population distribution as a function of time. At each point in time (x-axis), it is possible to see how many droplets were observed (z-axis) with a given population size (y-axis).

These colour plots were created by binning each droplet according to its population size (at a given time frame). This process was then repeated for all time frames of each experimental run. This allowed the frequency of droplets with a given population size to be measured, and the 3-dimensional colour plots were then generated. Note that the droplet frequency colour-scale (z-axis) of each plot is scaled logarithmically, allowing low frequency populations to remain visible whilst also allowing more general high frequency trends in the distributions to be visualised.

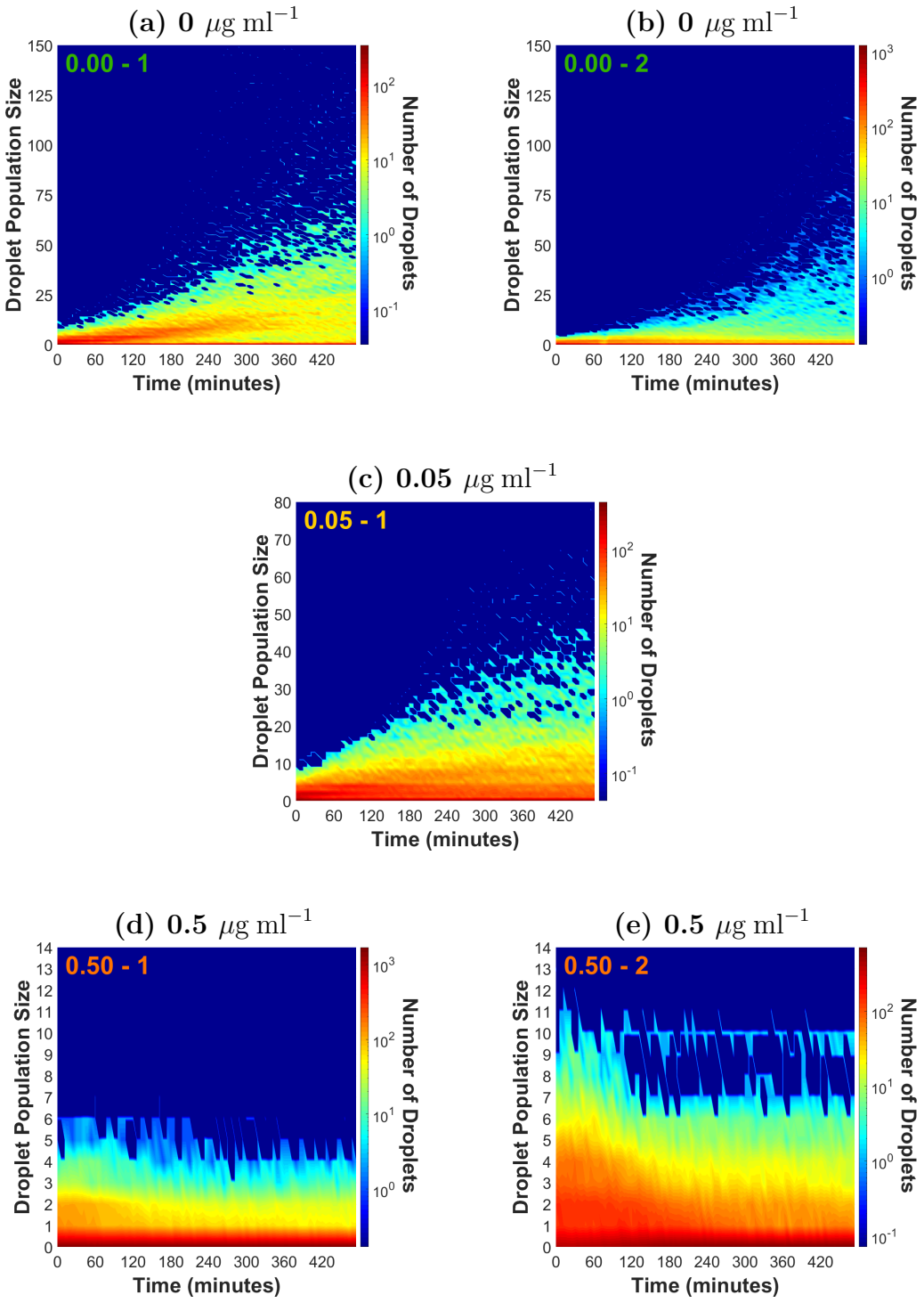

Figure 7.10 *Colour plots showing the evolution of population size distribution across the course of an experimental run. Bacteria grown in M9 minimal media at streptomycin concentrations of (a,b) 0 μg ml^{-1}, (c) 0.05 μg ml^{-1} and (d,e) 0.5 μg ml^{-1}. Each graph represents a complete experimental run.*

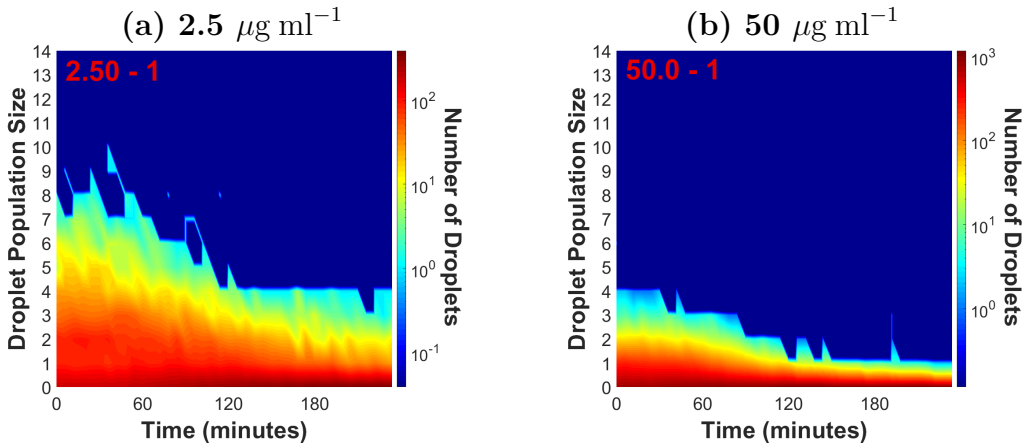

Figure 7.11 *Colour plots showing the evolution of population size distribution across the course of an experimental run. Bacteria grown in M9 minimal media at streptomycin concentrations of (a) 2.5 μg ml^{-1} and (b) 50 μg ml^{-1}. Each graph represents a complete experimental run.*

Discussion

For experimental runs 0.00 - 1 and 0.00 - 2 (streptomycin concentration of 0 μg ml^{-1}), droplet population sizes increase dramatically over the 8 hour experimental run. The red band visible in figure 7.10(a) indicates that in experimental run 0.00 - 1 a large number of droplet populations initially grow at the same rate. However after approximately 300 minutes these populations diverge in growth rate.

For experimental run 0.05 - 1 (streptomycin concentration of 0.05 μg ml^{-1}), the droplet population sizes increase steadily over the course of the 8 hour experimental run. This experimental run uniquely exhibits a subset of droplets with stationary bacterial populations. The number of visible bacteria in these populations does not change over time, resulting in horizontal bands of colour that can be seen against the background of the evolving population distribution beyond 120 minutes. This can be seen most prominently for bacterial populations between 1 and 10 bacteria. These populations do not significantly diverge in size over the course of the experimental run. Example growth curves of individual droplets that exhibit this behaviour can be seen in figure 7.12.

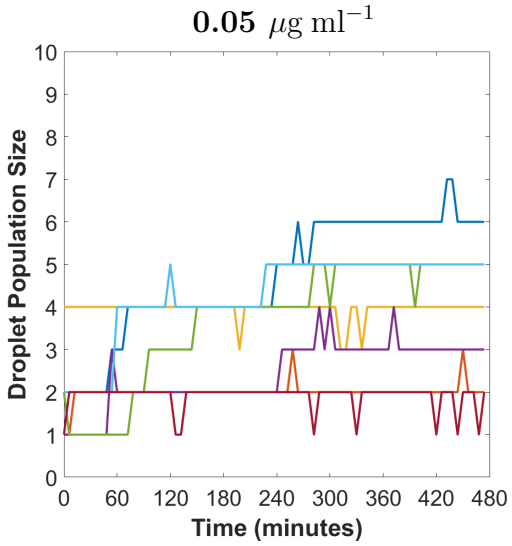

Figure 7.12 *Example growth curves of individual droplets with near-stationary populations in experimental run 0.05 - 1. Bacteria grown in M9 minimal media at a streptomycin concentration of 0.05* μg ml^{-1}.

It is not clear why this subset of bacterial populations remain roughly stationary in size. Streptomycin is classified as a bactericidal antibiotic. It acts by binding irreversibly to bacterial ribosomes, inhibiting their function. The static growth behaviour observed in this subset of droplet populations is therefore not anticipated according to this classification. This band of static/slow-growing bacteria may be connected to the bistable dependence of growth rate on antibiotic concentration at the individual cell level predicted by Greulich *et al.*[48] (see section 2.3.2). To further explore this phenomena, additional techniques would be required to discern whether these static bacterial populations are alive but not dividing, or if they are dead but not lysed (see section 6.6). If we confirmed that the observed subset of static/slow-growing droplet populations were indeed alive, it would be possible to quantify the exact conditions under which this bi-stable growth rate dependence existed. This would not be possible using traditional bulk growth techniques. Furthermore, we may be able to isolate bacteria from these fast-growing and static/slow-growing subpopulations, allowing us to perhaps understand the microbiological mechanisms behind this heterogeneous response.

For experimental runs 0.50 - 1 and 0.50 - 2 (streptomycin concentration of 0.5 μg ml^{-1}), we also obtain interesting results. There is a net loss of visible bacteria throughout the first 120 minutes of each experimental run. After the first 120 minutes, the number of low population droplets slowly decreases, but the number of large population droplets does not seem to decrease significantly in this time. This can be seen in figure 7.11 (d) and (e), where the orange bands decrease with time whilst the teal bands do not.

For experimental runs 2.50 - 1 and 50.0 - 1 (streptomycin concentrations of 2.5 μg ml^{-1} and 50 μg ml^{-1}), the number of visible bacteria in all droplets decreases rapidly over the course of the 4 hours of observation.

7.6.3 Final population size - measured vs. predicted

Results

By evolving the initial population size distribution of an experimental run according to its total population growth rate, it is possible to calculate a predicted final population size distribution, for a given initial size distribution, based upon an assumption of deterministic growth. This predicted final distribution can then be compared directly to the observed final distribution, similar to the analysis detailed in section 7.6.

This was achieved by first calculating a total population growth multiplier for an experimental run, e.g. the initial population size for experimental run 0.00 - 1 is 790, the final population size is 8991, therefore the growth multiplier for this experimental run is 11.381. Each initial droplet population was then artificially "grown" using this growth multiplier, e.g. droplets that began with 1 bacteria are predicted to end with 11.381 bacteria, droplets that began with 2 bacteria are predicted to end with 22.762, and so on. The predicted final droplet populations were then binned and plotted in a histogram alongside the measured final values.

This prediction assumes deterministic growth, meaning that all populations that start with the same population size will end with the same population size. Therefore, if there are only 6 distinct initial population sizes, there will only be 6 predicted final population sizes. So that the predicted and measured population distributions could be compared, the number of bins they were both separated into was matched. The number of bins was chosen to equal the number of initial population sizes, e.g. if an experimental run starts with 6 population sizes, the predicted and measured final populations are separated into 6 bins.

The predicted and measured final population sizes are plotted and quantitatively compared in figures 7.13, 7.14 and 7.15. Error bars are derived from the sampling error estimates detailed in section 7.5.1.

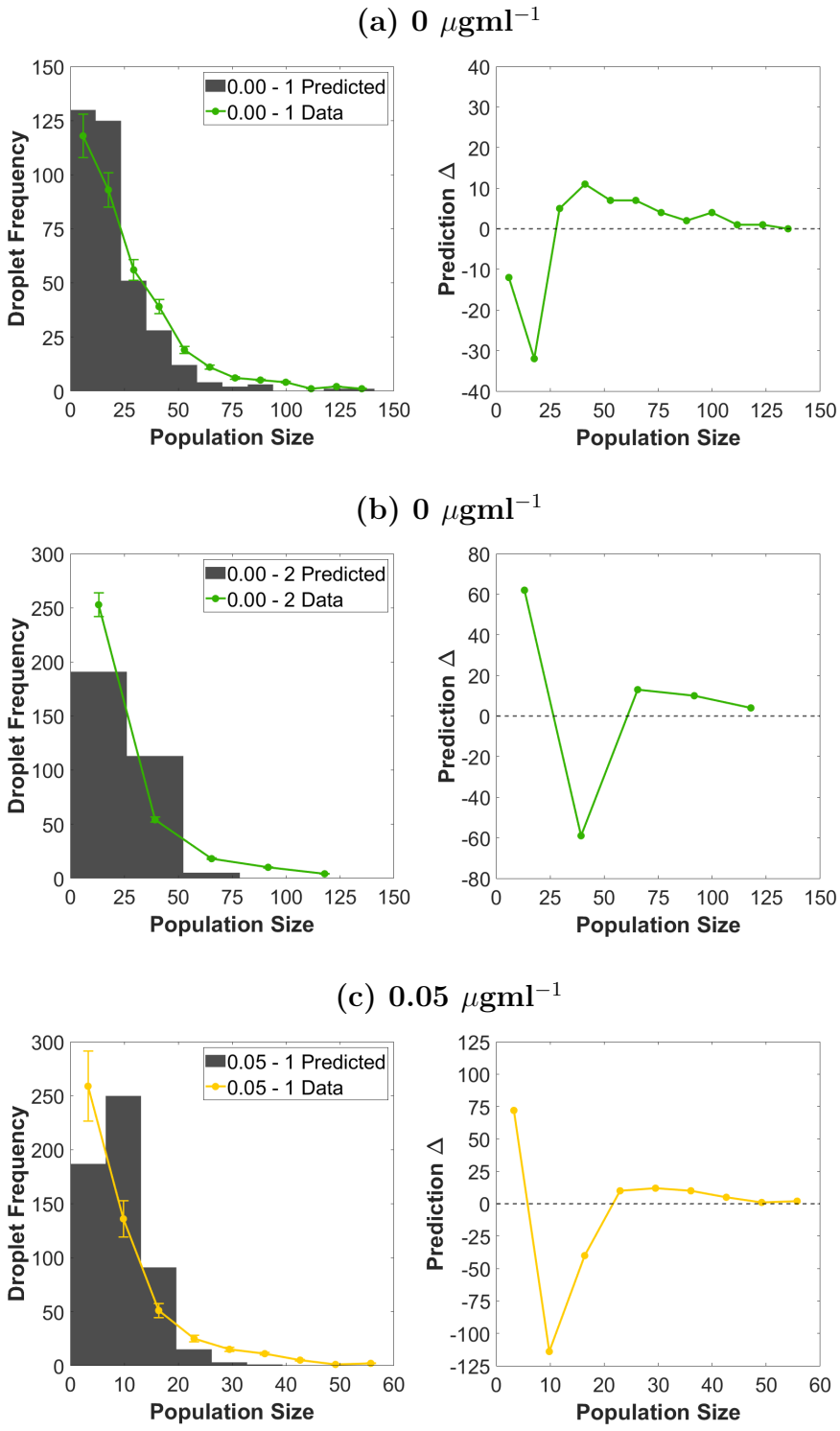

Figure 7.13 *(left) Measured and predicted final droplet population distributions of RJA002 E. coli populations encapsulated in microfluidic droplets, grown in M9 minimal media at streptomycin concentrations of (a,b) 0 μg ml^{-1} and (c) 0.05 μg ml^{-1}. (right) Difference in droplet frequency between the measured and the predicted distributions, positive Δ values imply the measured droplet frequency is greater than the predicted droplet frequency.*

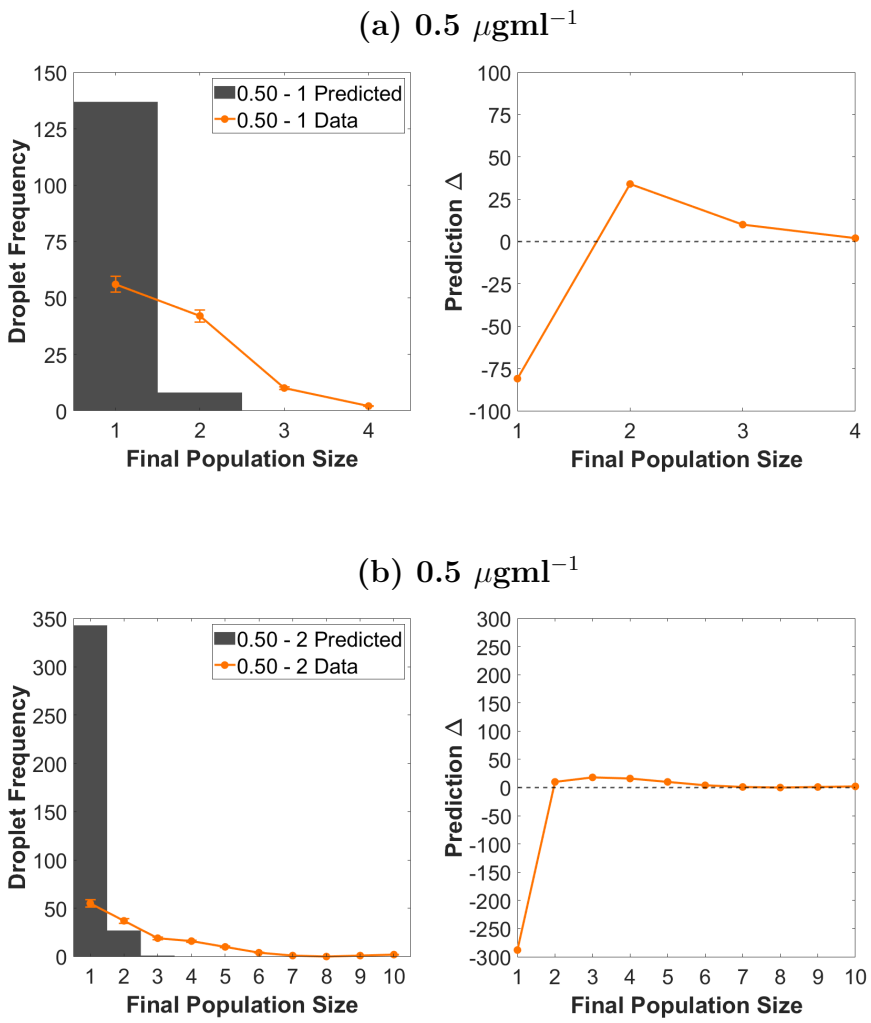

Figure 7.14 *(left) Measured and predicted final droplet population distributions of RJA002 E. coli populations encapsulated in microfluidic droplets, grown in M9 minimal media at a streptomycin concentration of 0.5* μg ml^{-1}*. (right) Difference in droplet frequency between the measured and the predicted distributions, positive* Δ *values imply the measured droplet frequency is greater than the predicted droplet frequency.*

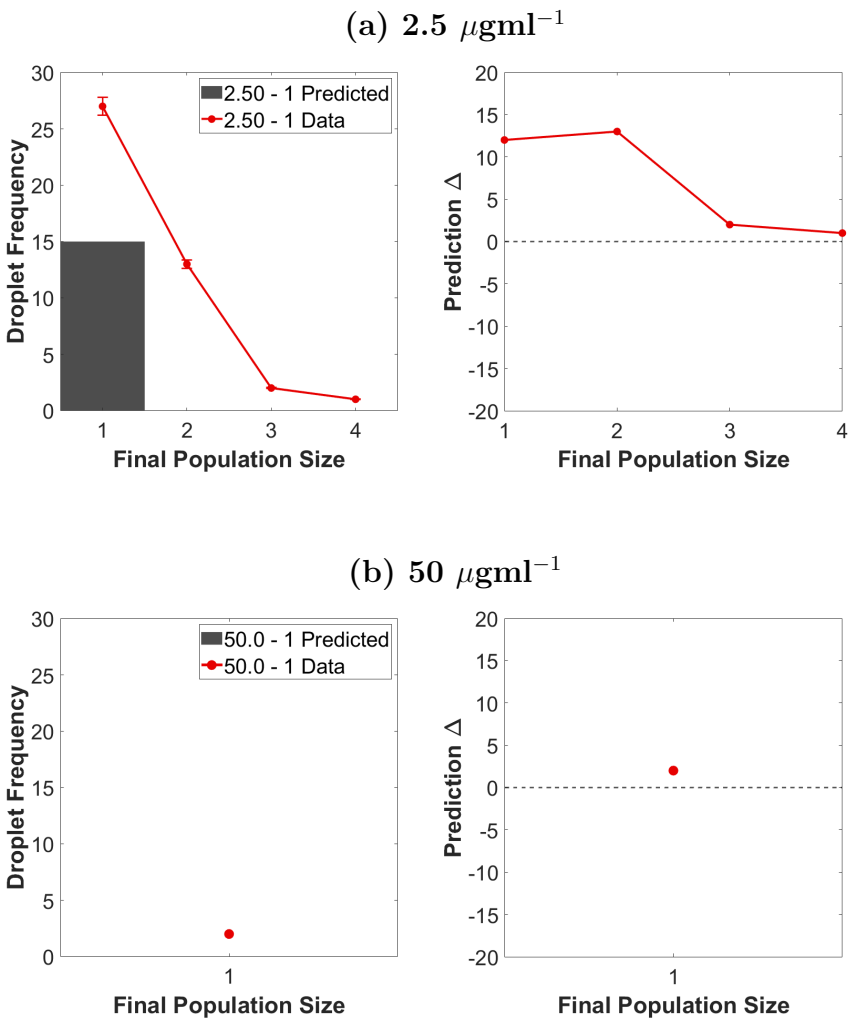

Figure 7.15 *(left) Measured and predicted final droplet population distributions of RJA002 E. coli populations encapsulated in microfluidic droplets, grown in M9 minimal media at streptomycin concentrations of (a) 2.5 μg ml^{-1} and (b) 50 μg ml^{-1}. (right) Difference in droplet frequency between the measured and the predicted distributions, positive Δ values imply the measured droplet frequency is greater than the predicted droplet frequency.*

Discussion

For experimental runs 0.00 - 1 and 0.00 - 2 (streptomycin concentration of 0 μg ml^{-1}), the predicted final droplet population distribution appears similar to the measured distribution. For the majority of population size bins, a decrease in measured droplet frequency is mirrored by a decrease in predicted droplet frequency. However, there are some key differences. In experimental run 0.00 - 1, the predicted data overestimates the number of low population droplets (<26 bacteria). In experimental run 0.00 - 2, the predicted data this time underestimates the number of low population droplets (<26 bacteria) whilst overestimating the number of moderate population droplets (26-52 bacteria). Common to both experimental runs, the predicted distribution significantly underestimates the number of high population droplets, both in number of droplets and in the maximum population size. This observation indicates that a number of droplets contain populations that grow significantly faster than the mean total population growth rate would predict.

For experimental run 0.05 - 1 (streptomycin concentration of 0.05 μg ml^{-1}), the predicted and measured distributions differ more significantly than any other experimental run that exhibited net growth. The predicted population distribution estimates the number of droplets with population sizes between 0 and 6 bacteria at the end of the run to be 187, whilst the measured number is 259 - underestimating the actual value by 28%. Counter to this, the predicted population distribution estimates the number of droplets with population sizes between 7 and 13 bacteria at the end of the run to be 250, whilst the measured number is 136 - overestimating the actual value by 84%. We believe this is linked to the subset of populations visible in figure 7.10(c) that seem to have static population sizes with bacterial counts below 6. This would explain why the number of moderate sized bacterial populations at the end of the run (7 - 18 bacteria) is underestimated by the deterministic growth, as deterministic growth predicts that the smaller of these static bacterial population bands (0 - 6 bacteria) would grow into the 7 - 18 bacteria band, were they not static. Similar to experimental runs 0.00 - 1 and 0.00 - 2, the predicted population distribution significantly underestimates the number of high population droplets. We also note that although the initial droplet population distribution features a large step (figure 7.5), in the measured final droplet population distribution this step has been completely smoothed out over the 8 hour experimental run.

For experimental runs 0.50 - 1 and 0.50 - 2 (streptomycin concentration of 0.5 μg ml^{-1}), the predicted distributions dramatically overestimate the number of droplets containing 1 bacterium that are present at the end of the run. Conversely, the number of droplets measured with bacterial population sizes greater than 1 exceeds the predicted values. It appears at this streptomycin concentration, which is close to the estimated MIC, that droplets beginning with relatively large population sizes (2-7 bacteria) manage to maintain their population size. In contrast, the deterministic assumption predicts mass inhibition of the majority of droplets to small but non-zero values.

For experimental runs 2.50 - 1 and 50.0 - 1 (streptomycin concentrations of 2.5 μg ml^{-1} and 50 μg ml^{-1}), the measured droplet populations exceed those predicted across all population sizes. Unfortunately, the measured data is extremely limited as very few droplets are populated by the end of each experimental run.

In the absence of streptomycin, final droplet population distributions featured extended tails at high population values. These extended tails were due to high population droplets that grew significantly faster than the population mean. At a streptomycin concentration of 0.05 $\mu g\,ml^{-1}$, this extended distribution tail was still present, but significantly reduced in magnitude.

The final population distributions for experimental runs 0.00 - 1 and 0.00 - 2 (streptomycin concentration of 0 $\mu g\,ml^{-1}$) featured extended tails consisting of large population droplets. These extended distribution tails can he seen in the histograms plotted in figure 7.5.

As seen in section 7.6.1, experimental runs 0.00 - 1 and 0.00 - 2 exhibited final Fano factors of 33.7 and 44.44, respectively. This indicates that the final population variance increased significantly relative to the mean. Experimental run 0.05 - 1 (streptomycin concentration of 0.05 $\mu g\,ml^{-1}$) exhibited a final Fano factor value of 13.25 This indicates that the final population size distribution has a moderately increased variance relative to the mean. This difference can be seen in the largest population droplets of each experiment: whilst experimental runs 0.00 - 1 and 0.00 - 2 featured multiple droplet populations stretching out to ≈150 bacteria in size, in experimental run 0.05 - 1 the maximum final population size was less than 70 bacteria in size. This implies that even at the low concentration of 0.05 $\mu g\,ml^{-1}$, streptomycin limited the growth rate of fast growing droplet populations.

In section 7.6.3, the total population growth rate was used to predict the final droplet population size distribution. This prediction consistently underestimated the number of droplets that were found at large population sizes, whilst overestimating the number of droplets that were found with low-moderate population sizes. This again emphasised the large subset of droplet populations that routinely outperformed the growth rate of the population when it was treated as a total growth measurement.

At a streptomycin concentrations of 0.5 μg ml^{-1}, there is a bias against lysis for large droplet populations.

In experimental runs 0.50 - 1 and 0.50 - 2 (0.5 μg ml^{-1}), it appears that droplets beginning with large numbers of visible bacteria were more likely to maintain their population size, suggesting a bias against lysis for large droplet populations at this antibiotic concentration.

This can be seen in their colour plots (figure 7.10 (d) and (e)), where the number of droplets with small populations slowly decreased after 120 minutes, whereas the number of droplets with larger population sizes stayed more static.

This is supported by the predicted final distribution plots for these experimental runs (figure 7.14). In these plots, the frequency of large population droplets was consistently underestimated by the prediction, implying that the bacteria in large population droplets consistently remained visible when the total population bacterial death rate suggested that their populations should have decreased considerably in size.

This result is further underpinned by the mean and variance measurements for these experimental runs, which is detailed in section 7.6.1. It was found that whilst the mean population size decreased over the course of both experimental runs, the Fano factors actually increased. This means that the variance of the final droplet population sizes increased relative to their respective means. This behaviour is counter to all other experimental runs, and implies there is a process driving an increase in the Fano factor despite the mean population size decreasing. We believe this process is the bias against lysis for large population droplets.

7.7 Time of droplet death

Results

A unique metric that we are able to extract from our experimental data is the time of droplet death. Here I define the time of droplet death as the time frame when a droplet which initially had a non-zero population size is reduced to a population size of zero. It is important to remember here that this only occurs when all bacteria in a droplet population have lysed (as opposed to bacteria dying but remaining fluorescent). To mitigate against counting errors at low bacterial counts, a droplet death is only recorded when the visible population in a droplet is reduced to 0, and remains zero for the following 4 time steps (i.e. droplet population is recorded as 0 for 5 consecutive time steps).

Time of death distributions for each experimental run are shown in figure 7.16 and 7.17. Only droplets tracked across all 80 times frames are used in this analysis. In each plot, the droplet death frequency is normalised with respect to the total number of initially populated droplets. The data is binned using a bin width of 18 minutes, or 3 time frames.

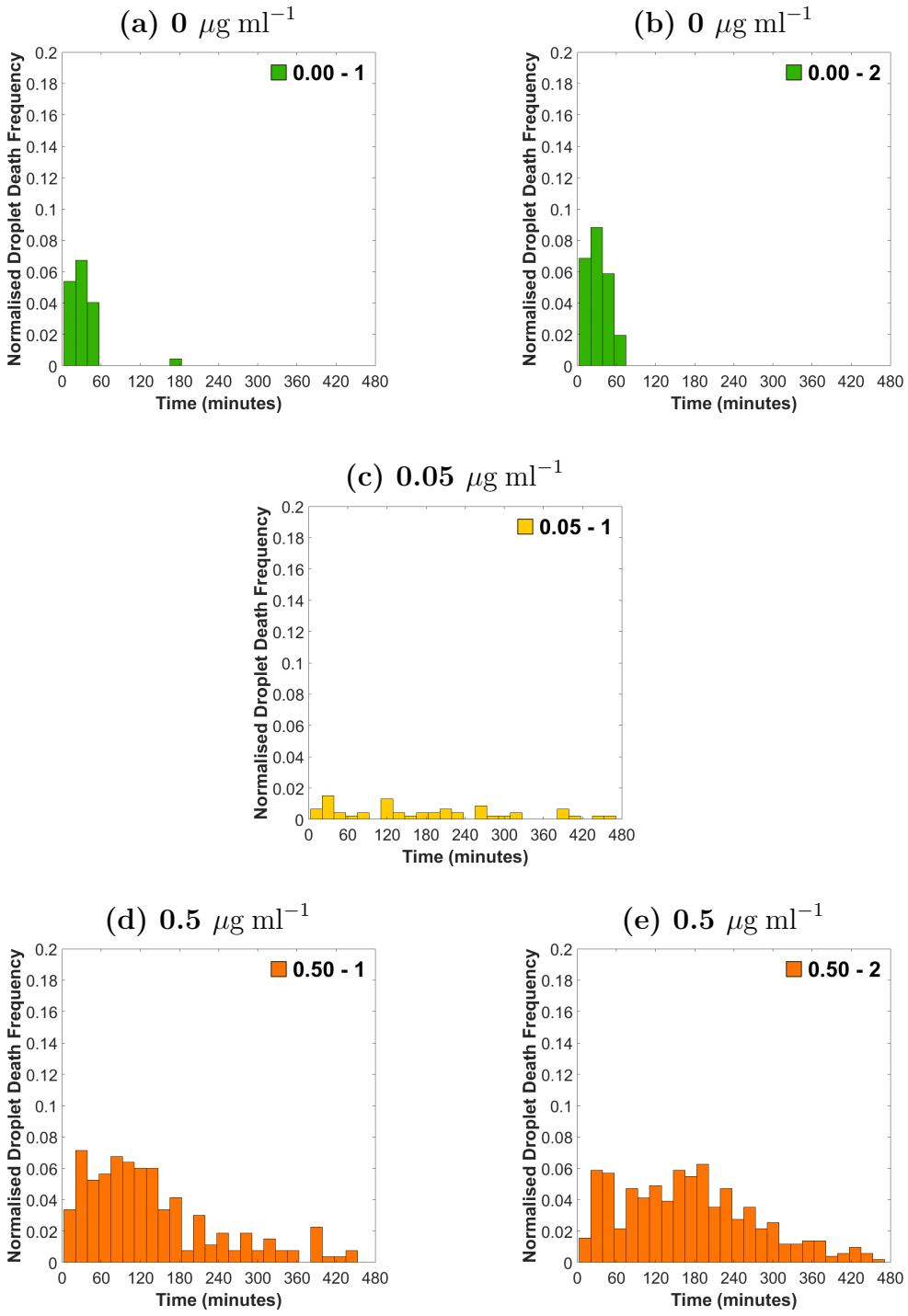

Figure 7.16 *Histograms showing how droplet death times are distributed over the course of an experimental run. Bacteria grown in M9 minimal media at multiple streptomycin concentrations. Each graph represents a complete experimental run.*

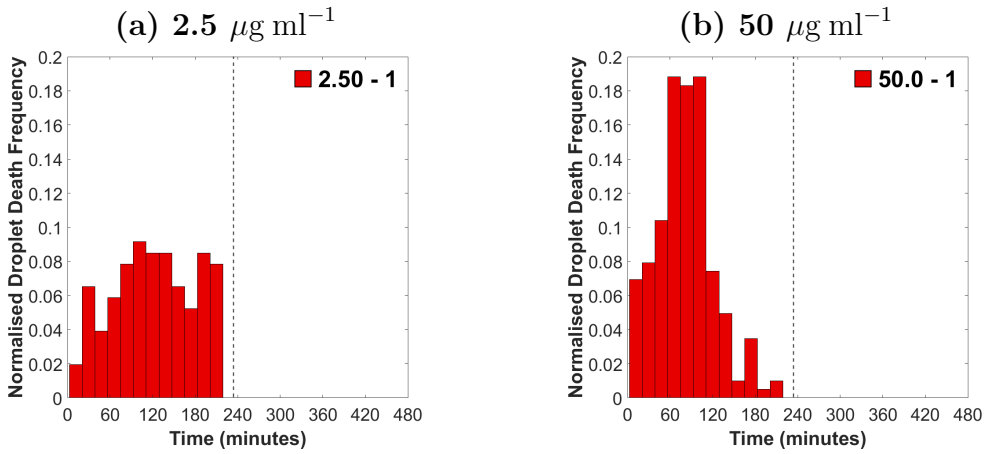

Figure 7.17 *Histograms showing how droplet death times are distributed over the course of an experimental run. Bacteria grown in M9 minimal media at streptomycin concentrations of (a) 2.5 μg ml^{-1} and (b) 50 μg ml^{-1}. Each graph represents a complete experimental run.*

Discussion

The time of death distributions for experimental runs 0.00 - 1 and 0.00 - 2 (streptomycin concentration of 0 μg ml^{-1}), show a number of droplet deaths within the first 60 minutes of both experimental runs. After this, there are essentially no droplet deaths for the remainder of the 8 hour experimental run. This seems reasonable: given a finite probability that a bacterium lyses instead of dividing, there is a reasonable possibility that the bacteria of a small bacterial population of 1 or 2 bacteria in a droplet could stochastically fail to divide and lyse, causing the population in that droplet to become extinct. However, once a population reaches a critical value, it is highly unlikely that all bacteria in that droplet will consistently fail to divide across multiple generations without the influence of external factors. The small fraction of bacteria that fail to divide therefore become insignificant and the droplet survives.

Another point of interest when examining the time of death distributions for experimental runs 0.00 - 1 and 0.00 - 2, is that ≈15% of all tracked droplets go extinct (even though they are being grown in the absence of antibiotic). It is not clear why these droplets are going extinct without an inhibiting agent present. Unfortunately, it is not possible to compare this bacterial death rate to bulk growth measurements. This is because it is not possible to accurately track the deaths of individual bacteria in a bacterial suspension using traditional bulk

growth techniques. Furthermore, any deaths that occur in low density regimes such as this will quickly be obscured by the rapid growth of the rest of the population.

We are not concerned by these droplet deaths, primarily because the total population growth rate observed when using our microfluidic system is comparable to the total population growth observed when using bulk growth techniques (see section 7.5.1). We believe this fact indicates that the bacteria we are using are not significantly stressed by the process of droplet encapsulation and subsequent storage within our microfluidic system.

Experimental run 0.05 - 1 (streptomycin concentration of 0.05 μg ml^{-1}) exhibits a unique droplet death profile. In all growth metrics shown so far, experimental runs performed at streptomycin concentrations of 0 μg ml^{-1} and 0.05 μg ml^{-1} exhibit similar dynamics. However, there are significant differences in the droplet death time distributions of these experimental runs. Experimental runs 0.00 - 1 and 0.00 - 2 displayed initial droplet death followed by essentially zero death, whereas experimental run 0.05 - 1 displays a uniform, low rate of droplet death over the course of an experimental run. Examining this data further raises more questions: experimental run 0.05 - 1 exhibits consistent and uniform droplet death, but the total population is increasing linearly (see figure 7.1). This appears contradictory, but can be explained if the lysing droplet populations are small and have been small for a significant period of time before death. If this is the case, then these droplet deaths would not significantly affect the total population size, allowing the total population size to steadily increase as large population droplets continue to grow. This is supported by the colour plot of experimental run 0.05 - 1 (figure 7.10) which shows a subset of droplets with small populations that do not increase in size. If these droplets populations were to slowly but steadily reduce to zero, it would produce the droplet death distribution described here whilst also not significantly affecting the total population growth. These observations additionally imply that streptomycin inhibits the bacterial populations in some droplets differently to others. Whilst some droplets remain static and their visible populations very slowly decrease over time, some droplets experience relatively uninhibited and rapid growth.

For experimental runs 0.50 - 1 and 0.50 - 2 (streptomycin concentration of 0.5 μg ml^{-1}), the droplet death times follow a consistent pattern: droplet death initially increases to a maximal value over the first 60 minutes, then slowly tails off over the following 7 hours. This is noteworthy as the total population shows a

small amount of growth in the first 30 minutes of these experimental runs. This suggests that whilst a number of droplets undergo droplet death early in the experimental run, a number of droplet populations are also increasing in size at a rate that outstrips this droplet death, resulting in a short burst of total bacterial growth.

Finally, in experimental runs 2.50 - 1 and 50.0 - 1 (streptomycin concentrations of 2.5 μg ml^{-1} and 50 $\mu g\, ml^{-1}$) droplet death is observed almost immediately from the beginning of each experimental run. Although droplet death is initially moderate, it increases to a maximum after approximately 80 minutes. Droplet death decreases drastically after 100 minutes at a streptomycin concentration of 50 μg ml^{-1}; however this is simply because almost all droplet populations at this stage in the experimental run have been reduced to zero - there are no populations left to undergo death.

Interestingly, the number of droplet deaths in experimental run 2.50 - 1 reaches a maximal value at around 80 minutes, and then seems to maintain a steady rate until the experiment ends after 4 hours. This behaviour may appear to be contradictory to the total population growth curve shown in figure 7.2, where the total population declines sharply from 30 to 180 minutes and then declines much more slowly from 180 to 234 minutes. The number of droplet deaths are constant, whilst the rate of loss of bacteria slows down considerably. This implies that early on in the experiment, low population droplets are becoming extinct whilst higher population droplets are also being reduced in size, therefore the total population size is decreasing significantly with time. In contrast, later on in the experiment, a subset of low population droplets are still being driven to extinction, but as the total population is only declining slowly at this point, the rest of the droplet populations must be static in population size.

At streptomycin concentrations of 0.5 μg ml^{-1} and 2.5 μg ml^{-1}, which is above the estimated MIC value, streptomycin appeared to be either bacteriostatic or non-lytic.

It can be seen in the growth curves for experimental runs 0.50 - 1 and 0.50 - 2 that bacterial populations were significantly inhibited at a streptomycin concentration of 0.5 μg ml^{-1} (figure 7.1). This inhibition results in a net loss of visible bacteria. Despite this, a significant number of droplet populations remained visible throughout the entire 8 hour observation period. This could be due to streptomycin acting in a bacteriostatic fashion, or because at this concentration streptomycin induced cell death but not lysis (allowing the bacteria to continue to fluoresce in death). It is not possible to distinguish between these two possibilities using our current microfluidic system, but it is entirely conceivable that an additional process could be integrated into our microfluidic system that tests bacterial metabolic function and/or viability after extended antibiotic exposure.

In figure 7.2, it can be seen for experimental run 2.50 - 1, at a higher streptomycin concentration of 2.5 μg ml^{-1}, the rate of bacterial lysis changed over the course of the experimental run. However in figure 7.17, the rate of droplet death can be seen to remain relatively constant. Early on in the experimental run, rate of bacterial lysis was high, implying that low population droplets were being driven to extinction whilst higher population droplets were being reduced in size. Later on in the experiment, low population droplets were still undergoing droplet death however the total population was declining very slowly. This implies that almost all higher population droplets were static in population size.

At a streptomycin concentration of 0.05 μg ml^{-1}, streptomycin was both non-inhibiting and bacteriostatic/non-lytic.

In experimental run 0.05 - 1 (streptomycin concentration of 0.05 μg ml^{-1}), there was a significant subset of droplets whose population sizes appeared to remain static.

This can be seen in the colour plot for this experimental run (figure 7.10(c)), which showed a horizontal band of droplets with populations that remained stationary between roughly 1 and 10 bacteria.

This was further emphasised in the prediction plot for experimental run 0.05 - 1, which can be seen in figure 7.13(c). In this plot, the number of measured droplets with population sizes between 0 and 6 bacteria far outweighed the number of predicted droplets (which was based on the total population mean growth). This stationary behaviour contrasts with a number of high population droplets that exhibited large growth rates, and the total population size which increased linearly with time. We believe these two conflicting behaviours can be reconciled if one subset of droplet populations is inhibited by streptomycin, whilst another subset is mostly unaffected.

This conclusion is supported by the droplet time of death distribution for experimental run 0.05 - 1 (figure 7.16(c)). This distribution exhibited a uniform, low rate of droplet death throughout the entire observation period. This droplet death distribution again initially appeared to contradict the total population growth data - how was the total droplet population of the experimental run increasing linearly with time whilst also experiencing consistent droplet death? We suggest that droplet death occurred only in the stationary droplets with small populations. These droplet deaths would not impact the total population size significantly, as each droplet death would only deduct a small number of bacteria from the total population size. Furthermore it means that growth of the large population droplets responsible for the linear increase in total population are not as strongly inhibited.

7.8 Time of droplet death versus initial population size

Results

In this section, we are able to further utilise the droplet time of death metric. Here, droplet time of death is plotted versus initial droplet population size for each experimental run. Only droplets tracked across all 80 times frames are used in this analysis. The first 5 time frames of each droplet were then averaged to give an initial droplet population size. This was done to smooth out counting fluctuations which can be prominent at low and high bacterial populations. These plots can be seen in figures 7.18 and 7.19.

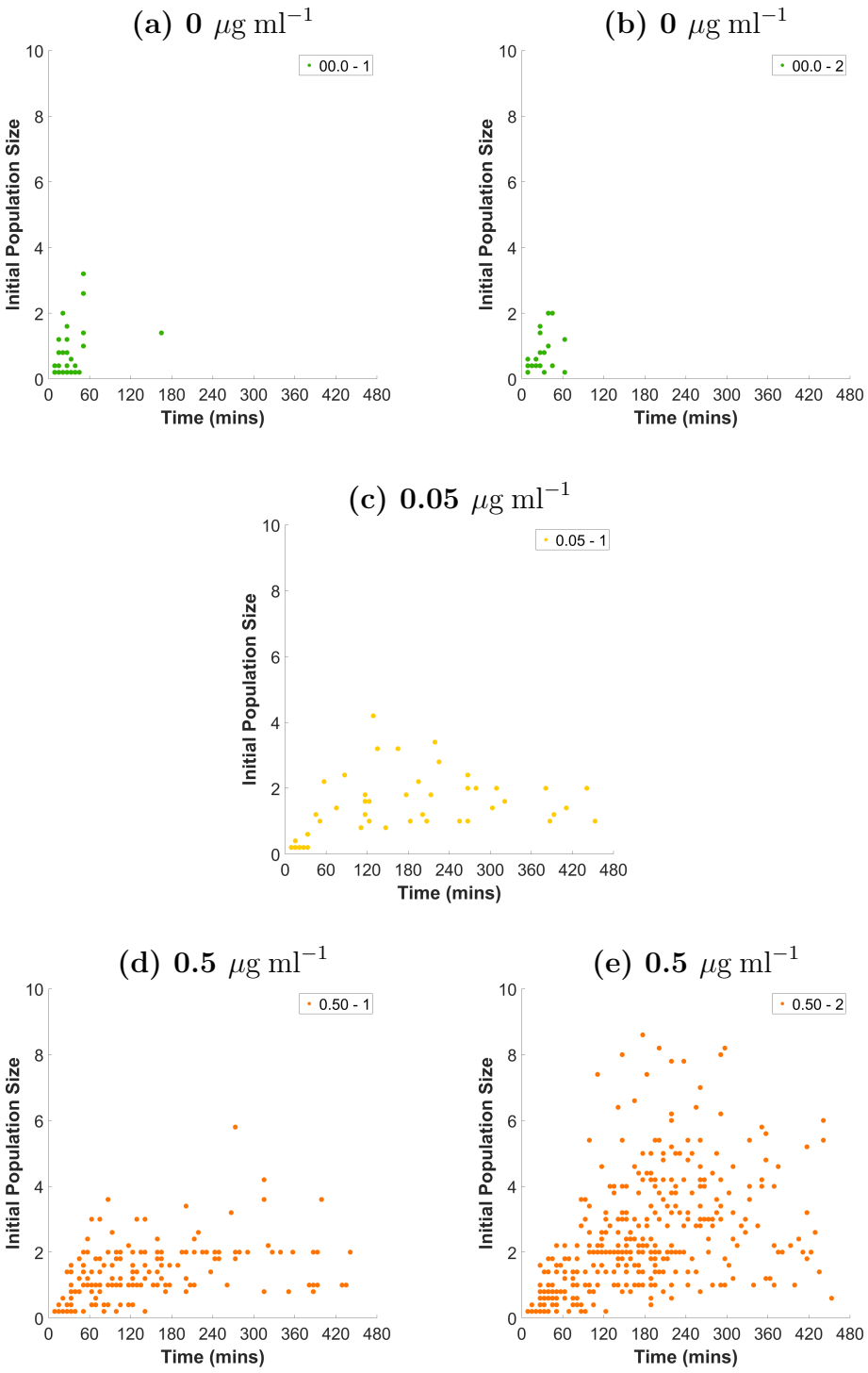

Figure 7.18 *Scatter plots showing droplet time of death as a function of initial droplet population size. Bacteria grown in M9 minimal media at a streptomycin concentration of (a,b) 0 μg ml^{-1}, (c) 0.05 μg ml^{-1} and (d,e) 0.5 μg ml^{-1}. Each graph represents a complete experimental run.*

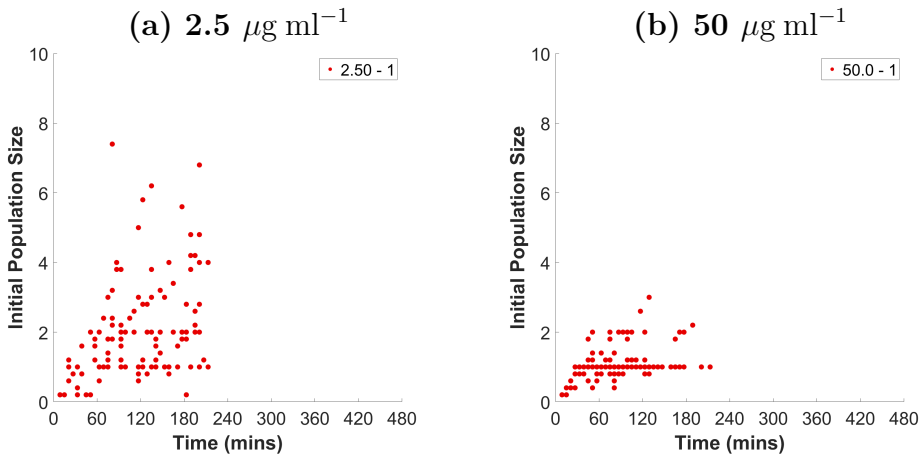

Figure 7.19 *Scatter plots showing droplet time of death as a function of initial droplet population size. Bacteria grown in M9 minimal media at a streptomycin concentration of (a) 2.5* μg ml^{-1} *and (b) 50* μg ml^{-1}*. Each graph represents a complete experimental run.*

Discussion

Droplet time of death is plotted versus initial droplet population size for experimental runs 0.00 - 1 and 0.00 - 2 in figure 7.18 (a) and (b). In these runs bacterial droplet populations are grown in the absence of streptomycin. Droplet death can be seen to occur almost exclusively in the first 66 minutes. Furthermore, the vast majority of these droplet deaths are the result of droplet populations with initial droplet population sizes of <2 bacteria, despite both experiments featuring a significant proportion of droplets with initial population sizes of >2 bacteria (see figure 7.5). In section 7.7, it was postulated that droplet deaths that occurred in the absence of streptomycin were the result of small population droplets stochastically dying off. This is supported by the results shown here.

Plots showing droplet time of death versus initial droplet population size for experimental runs conducted in the presence of antibiotic can be seen in figures 7.18 (c,d,e) and 7.19 (a) and (b). In all of these plots, it is apparent that droplets with large initial populations are driven to extinction later in an experimental run than droplets with small populations. In each of the experimental runs conducted in the presence of streptomycin, droplets with initial population sizes ≤ 2 undergo droplet death almost continually throughout the experimental run. In contrast to this, droplets with initial population sizes >2 undergo droplet death later on in the experimental run, generally beyond 60 minutes.

This absence of high population droplet deaths early on in each experimental run can be seen as an empty triangle in each plot above and to the left of the main cluster of droplet deaths. See figure 7.20 for a visualisation of this empty space.

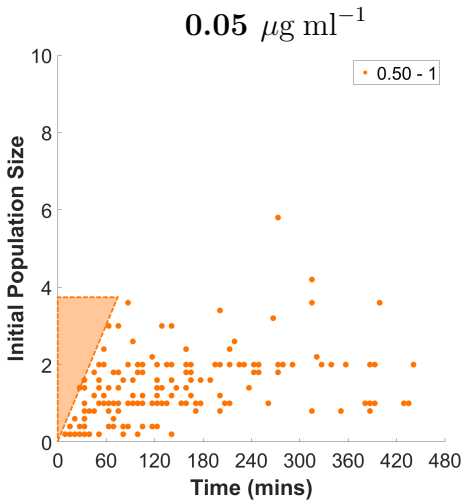

Figure 7.20 *Scatter plot showing droplet time of death as a function of initial droplet population size for experimental run 0.50 - 1. Bacteria grown in M9 minimal media at a streptomycin concentration of 0.5 μg ml^{-1}. The shaded light orange area highlights an area of the graph where no droplet deaths are observed. This triangular area is observed in all experimental runs conducted in the presence of streptomycin.*

The cause of this consistently empty space in the death time versus initial population plots is not clear. It may be that some form of inoculum effect is present, allowing droplets with large initial populations to survive longer than droplets with small initial populations. Likewise, it may simply be the result of stochastic droplet death: given a set probability of droplet death per unit time, large populations of droplets are more likely to contain bacteria that are not killed or lysed quickly. Although it would require further experimental runs to judge the significance of this effect and discern the cause of these empty triangles, this analysis nonetheless highlights the utility of our microfluidic device in comparison to bulk growth techniques, and the power of population tracking with single cell precision.

7.9 Initial droplet population size as a growth predictor

7.9.1 Initial droplet population versus final droplet population

Results

We were also interested in testing if there is a correlation between an individual droplet's initial population size and its final population size. To measure this effect, droplets were screened to ensure suitability for the study - only droplets that were detected for more than 70 time frames were included. The first and final 5 time frames of each droplet were then averaged to give an initial and final droplet population size. This was done to smooth out counting fluctuations which can be prominent at low and high bacterial populations. A scatter plot was then made to detect correlations between initial and final droplet population size. Using a linear regression model, a line of best fit was then calculated for each data set. This was completed for experimental runs 0.00 - 1, 0.00 - 2 and 0.05 - 1 as these all exhibited net total population growth.

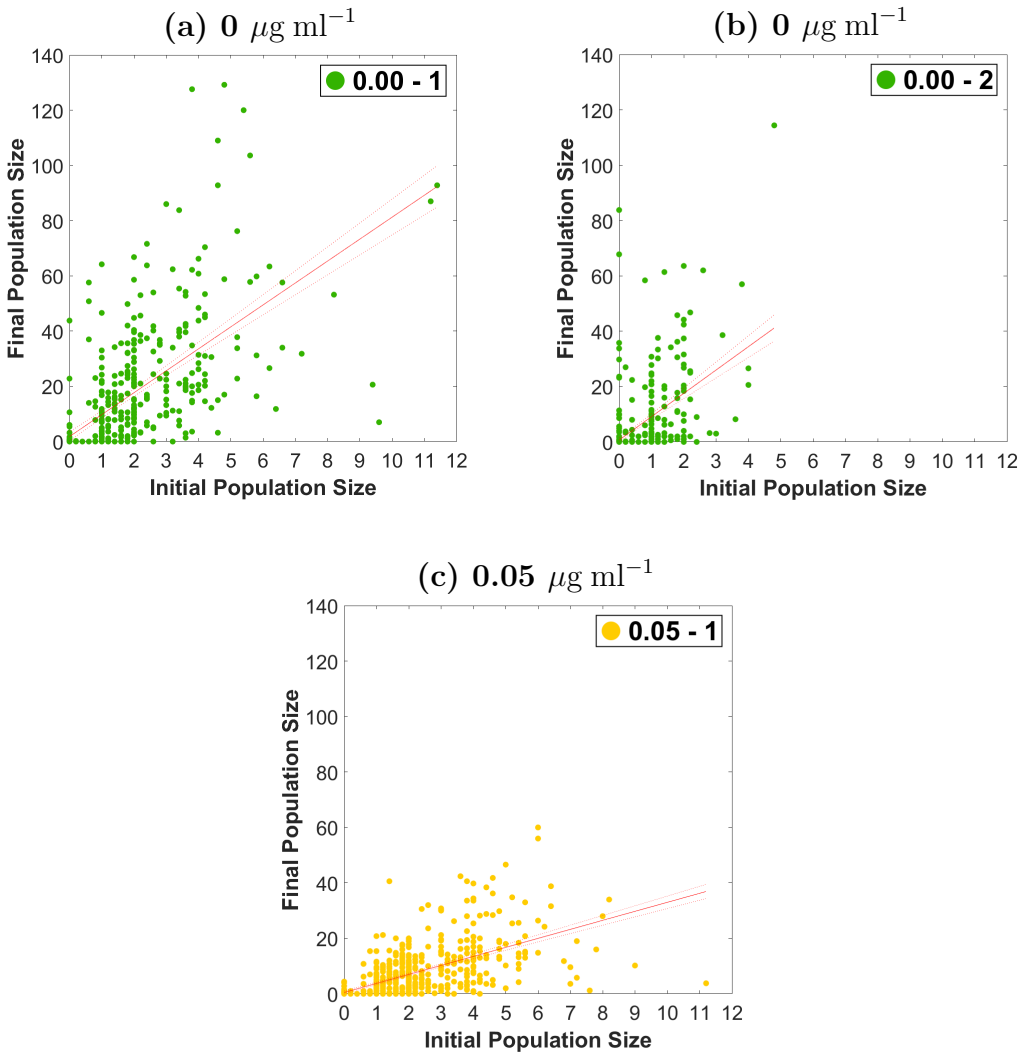

Figure 7.21 *Scatter plots of initial droplet population sizes vs. Final droplet population sizes for experimental runs (a) 0.00 - 1, (b) 0.00 - 2 and (c) 0.05 - 1.*

From these plots, a gradient and correlation coefficient is calculated for each data set.

Experiment ID	Strep. Conc. ($\mu g\ ml^{-1}$)	Gradient	R^2
0.00 - 1	0	7.9426	0.4548
0.00 - 2	0	8.4348	0.2986
0.05 - 1	0.05	3.2504	0.4329

Table 7.4 *Summary of measured gradient and R^2 values for the data presented in figure 7.21.*

Discussion

A large correlation coefficient (R^2) suggests a strong correlation between the initial and final droplet populations sizes. If growth was purely deterministic then this value would equal 1. The R^2 values shown in table 7.4 indicate a weak, but positive correlation between initial and final droplet population sizes. This correlation strength varies considerably from one experimental run to the next and appears to be independent of antibiotic concentration. The implication of this weak, positive correlation is that droplets with an initially large population size are more likely to grow into droplets with a large final population size (as expected); but there is significant variability in this trend. In only one experimental run (0.00 - 2) did the largest initial droplet population end as the largest final droplet population, and in another experimental run (0.05 - 1), the largest initial droplet population barely managed to survive the 8 hour observation.

A large measured gradient suggests strong growth from the initial to the final population size (if every droplet was tracked correctly across all time steps and included in this analysis, the gradients calculated in this section would equal $e^{\lambda t}$, i.e. they would be proportional to the total population growth rate). As anticipated from the growth curves shown previously in this chapter, the measured gradient values for experimental runs that underwent logarithmic growth (0.00 - 1 and 0.00 - 2, streptomycin concentration = 0 $\mu g\, ml^{-1}$) are large in comparison to the experimental run that exhibited lesser and linear growth (0.05 - 1, streptomycin concentration = 0.05 $\mu g\, ml^{-1}$).

A positive but weak correlation was found between initial and final droplet population size in experimental runs that exhibited net growth.

As can be seen in table 7.4, in all experimental runs that exhibited net growth (0.00 - 1, 0.00 - 2 and 0.05 - 1) a positive correlation was found between initial droplet population size and final droplet population size. Calculated correlation coefficients for this relationship ranged from 0.30-0.45 and were independent of antibiotic concentration. This showed that whilst droplets with large initial populations would generally grow to become larger in number than droplets with small initial populations, there were a significant number of droplets that both under- and over-performed compared to their expected final value.

7.9.2 Box-plot analysis

Results

Figure 7.22 shows box plots that compare initial and final population size, for droplets grouped by their initial population size. The data used to generate these box plots is summarised in table 7.5. This analysis is only completed for droplets that started with an initial population size of 1 - 5 bacteria (1 - 4 bacteria for experimental run 0.00 - 2) as there were only a small number of droplets with initial populations larger than these. The median final population sizes are shown, alongside their 25th and 75th percentile. Values deemed statistical outliers with greater spread than would be anticipated from the whole population are shown as red crosses.

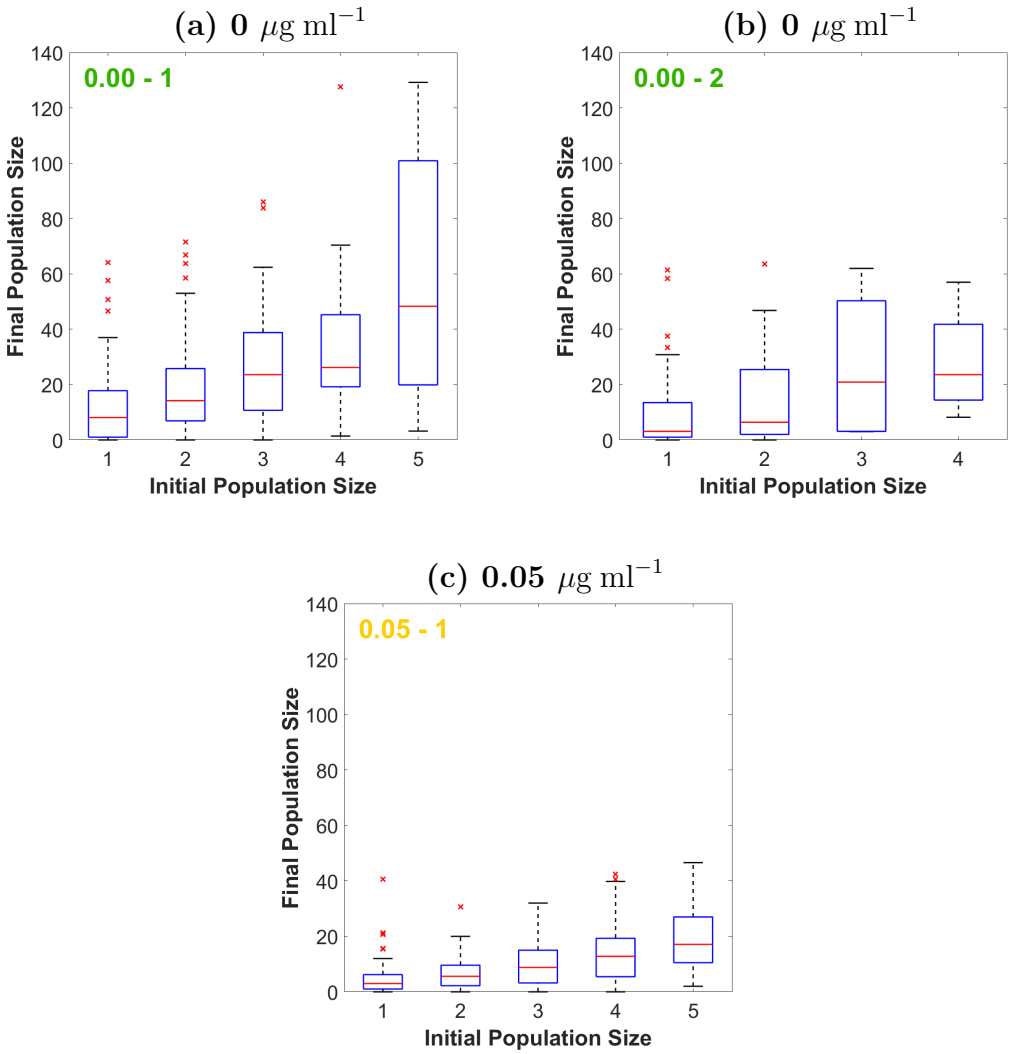

Figure 7.22 *Box plots of initial droplet population sizes vs. final droplet population sizes for experimental runs (a) 0.00 - 1, (b) 0.00 - 2 and (c) 0.05 - 1.*

Experimental ID	Initial population size	Median final population size	25th percentile value	75th percentile value	Inter - quartile range
0.00 - 1	1	8.1	1.0	17.8	16.8
0.00 - 1	2	14.2	6.9	25.8	18.9
0.00 - 1	3	23.6	10.7	38.8	28.1
0.00 - 1	4	26.2	19.2	45.3	26.1
0.00 - 1	5	48.3	19.9	100.9	81
0.00 - 2	1	3.1	1.0	13.5	12.5
0.00 - 2	2	6.4	2.0	25.5	23.5
0.00 - 2	3	20.9	3.1	50.3	47.2
0.00 - 2	4	23.6	14.4	41.8	27.4
0.05 - 1	1	3.0	1.0	6.2	5.2
0.05 - 1	2	5.6	2.2	9.6	7.4
0.05 - 1	3	8.8	3.2	15.0	11.8
0.05 - 1	4	12.8	5.5	19.3	13.8
0.05 - 1	5	17.1	10.5	27.0	16.5

Table 7.5 *Quantitative summary of data displayed in box plots shown in figure 7.22*

Discussion

This final box-plot analysis quantitatively evaluates the data presented in the previous section, seen in figure 7.21. In all experiments the median final population increases as initial population size increases. This is consistent with the positive correlation observed between initial and final population sizes. The final population size inter-quartile range also increases with initial population size (apart from in droplets of initial size 4 in experimental runs 0.00 - 1 and 0.00 - 2) suggesting increased variation in the final population of droplets with large initial populations.

Whilst a general positive correlation exists between initial and final population size, it appears that droplets with low population sizes (1 - 2 bacteria) regularly exceed the average growth of their counterparts. This can be seen in the numerous outliers that are present at these initial population sizes.

Finally, it is apparent that whilst the overall growth of experimental run 0.05 - 1 (0.05 μg ml^{-1}) is suppressed in comparison to experimental runs 0.00 - 1 and 0.00 - 2 (0 μg ml^{-1}), growth patterns and trends appear to be more uniform. Only at this streptomycin concentration of 0.05 μg ml^{-1} do the median final population size, 25th percentile value, 75th percentile value and inter-quartile range all consistently increase with initial population size.

7.10 Summary

In this work, small bacterial populations were encapsulated within microfluidic emulsion droplets both in the absence and presence of the antibiotic streptomycin. The droplets were incubated and imaged over the course of an 8 hour observation period. The growth dynamics of the incubated droplets were measured and recorded. Experimental runs were conducted at streptomycin concentrations of of 0 μg ml^{-1}, 0.05 μg ml^{-1}, 0.5 μg ml^{-1}, 2.5 μg ml^{-1} and 50 μg ml^{-1}. The results of these experimental runs were presented in detail in this chapter, and their analysis consisted of 5 primary studies:

- In the first analysis, we investigated how the total bacterial population changed over the course of each experimental run. Total population growth curves were plotted. Growth rates and doubling times were calculated for all experimental runs that exhibited net growth.
- In the second analysis, we studied how the distribution of droplet population sizes evolved over the course of each experimental run. The initial and final droplet population distributions were plotted and compared. The mean and variance for each distribution was calculated. Colour plots were used to visualise how each initial population distribution evolved across its 8 hour experimental run. A deterministic final droplet population distribution was predicted for each experimental run and compared with the final measured population distribution.
- In the third analysis, we explored how time of droplet death changed with antibiotic concentration. For each experimental run, droplet death frequency was plotted as a function of time.

- In the fourth analysis, we looked at the relationship between droplet death time and initial droplet population. For each experimental run, droplet death time was plotted versus initial droplet population.
- In the fifth and final analysis, we investigated the correlation between initial droplet population size and final droplet population size. Initial population size was plotted versus final population size for each experimental run. Using a linear regression model, a line of best fit was then calculated for each data set. Box plots were used to further compare the spread of bacterial growth from droplets sorted by their initial population size.

7.11 Concluding remarks

Using our microfluidic system, we successfully encapsulated a large number of small bacterial populations in monodisperse emulsion droplets. These droplets were incubated at 37°C and their encapsulated bacterial populations were measured and tracked with single cell accuracy every 6 minutes for a total of 8 hours. Bacterial populations were encapsulated both in the absence of and presence of streptomycin at a range of antibiotic concentrations.

Using this data, a number of novel statistical studies were completed that were designed to investigate the stochastic growth dynamics of bacterial populations growing in the presence of streptomycin. There is strong evidence to support the notion that small bacterial populations can be heterogeneous in their response to moderate concentrations of antibiotic, and whilst the observed growth dynamics were statistically diverse, distinct trends and common behaviours emerged from the large volume of data we acquired.

Whilst there are numerous examples of experimental systems that can study small bacterial populations with a higher throughput than we have shown here, they are generally not able to track population size as a function of time with single cell accuracy. Conversely, there are many systems that are capable of measuring the growth dynamics of single bacteria in extensive detail, tracking advanced growth metrics such as cell motility, morphological information and the populations genealogical tree. Unfortunately these systems tend to rely on extensive manual corrections and are not capable of analysing more than a handful of populations at once.

We have confidence that the results obtained in this chapter successfully validate our microfluidic system and image processing workflow, the development of which is detailed in chapters 3, 4 and 5. We have successfully observed numerous novel behaviours in large numbers of small bacterial populations that were not previously possible to quantify using other experimental systems or bulk measurement techniques.

Chapter 8

Conclusions

8.1 Summary

This thesis details the design and fabrication of a microfluidic device that is used to quantitatively measure the growth dynamics of small *Escherichia coli* populations encapsulated in emulsion droplets in the presence and absence of streptomycin.

In chapter 3 the materials, techniques and protocols that are used to construct our microfluidic device are detailed. A number of key decisions regarding the material and techniques used in the fabrication of our microfluidic system are discussed. These decisions are explained in the context of our specific experimental objectives, as well as in the wider context of fabricating a versatile system that is compatible with a wide variety of biological systems.

Polydimethylsiloxane was chosen as the base elastomer for our microfluidic system as it possesses a number of favourable physical characteristics that complemented our research objectives. Ancillary experimental materials and processes were tested and selected. Additionally, a microfluidic device mount was designed and 3D printed. This mount is used to hold our microfluidic system in place during imaging whilst also maintaining the temperature of the experimental assembly at 37°C.

In chapter 4, the iterative design process of our microfluidic system is outlined. Focus was placed on the development of a microfluidic system that would be straightforward to fabricate and accessible to researchers that did not possess extensive experience in the field of microfluidics. One of the primary benefits of PDMS-based microfluidics is the ability to rapidly prototype and fabricate experimental systems. Through the continued testing and improvement of our microfluidic system, we developed a number of guiding principles that were used to produce our final microfluidic design.

The microfluidic system consists of two devices. The first device is a microfluidic droplet generator, this is used to encapsulate small bacterial populations in aqueous emulsion droplets suspended in a fluorocarbon oil. These droplets are passed to the second device, a microfluidic droplet reservoir. This reservoir stores the droplets so that they can be imaged using both brightfield and fluorescence microscopy. This microfluidic system is easy to fabricate and operate, whilst also being robust across a wide range of experimental conditions.

In chapter 5, the image processing and analysis workflow that we developed to be used in conjunction with our microfluidic system is outlined. The work flow comprises three stages: image validation and stitching, droplet detection and tracking, and finally image thresholding and bacterial counting.

A number of manual pre-processing validation steps are undertaken to ensure that images with experimental defects are not passed forward to subsequent image processing algorithms. After this, brightfield microscopy images are used to detect and track microfluidic droplet boundaries and positions throughout the course of each experimental run. Finally, fluorescence images are thresholded and analysed to detect bacterial population sizes for each droplet with single cell precision. This workflow was designed from the ground up to measure the growth dynamics of 1000+ independent small bacterial populations with single cell accuracy.

In chapter 6, a number of experimental validations, checks and caveats are examined to ensure that the conclusions drawn from the results presented in chapter 7 are accurate. Error measurements and calculations are presented that establish the limitations of our bacterial counting algorithm.

Automated bacterial counting errors have been quantified, and the trends in these errors are discussed. It was hypothesised that bacterial aggregation was the primary source of bacterial counting error. Bacterial aggregation causes population sizes to be increasingly underestimated as time passes. The impact of further

experimental limitations such as droplet polydispersity and imaging delays are discussed. An investigation into growth correlation between droplets based on their relative spatial proximity was conducted. No significant correlation between droplet population growth and relative droplet proximity is observed, validating our assumption that each bacterial population existed independently with no transfer of information or resources between droplets.

In chapter 7, the growth dynamics of small *E. coli* populations were measured both in the absence and presence of the ribosome targeting antibiotic streptomycin. A number of statistical measurements were extracted from the data that detailed the growth dynamics of the droplet-based bacterial populations. Total population growth rates and doubling times were calculated. Droplet population size distributions were measured, and it was explored how these distributions evolved as a function of time. The time at which visible bacterial populations were driven to extinction was investigated as a function of antibiotic concentration, and also as a function of initial droplet population size. Finally, the relationship between initial and final droplet population size was investigated.

The uninhibited growth rate that we measured for RJA002 *E. coli* was found to be in agreement with those measured in bulk growth experiments[201]. Likewise, the MIC value for RJA002 grown in the presence of streptomycin was consistent with reported measurements using bulk growth techniques [48]. These measurements imply that the process of encapsulation and growth in microfluidic droplets does not inhibit bacterial growth in of itself.

A number of interesting and novel growth dynamics were observed. It was found that in experimental runs that exhibited net growth, the correlation between initial and final population size was weakly positive and independent of antibiotic concentration. This indicates a highly stochastic growth process. In the absence of streptomycin, the final droplet population size distributions exhibited extended tails due to the presence of droplets containing large populations. These extended tails were also observed at streptomycin concentrations below the MIC, however their length was reduced in comparison. This implies that at low concentrations, streptomycin limits the growth rate of fast growing droplet populations. At moderate streptomycin concentrations both around and above the MIC value, it was found that streptomycin inhibited some bacterial populations in a non-lytic manner (resulting in fluorescent but non-growing bacteria), whereas other bacterial populations underwent lysis. Also at moderate streptomycin concentrations around the MIC value, a bias against lysis for large droplet

populations was observed. At low streptomycin concentrations below the MIC value, it was found that streptomycin inhibited some bacterial populations without lysing them, whereas other bacterial populations were uninhibited.

8.2 Outlook

In the immediate future, there are a number of experimental studies that would be very interesting to carry out using our microfluidic system. Firstly, the uninhibited total population growth rate we measured was inconsistent between two experimental runs. The cause of this heterogeneity is unknown, and we would like to know if this growth rate variability persists across multiple replicate runs. Secondly, we are keen to understand why some droplets exhibit growth rates that far exceed the average growth rate observed across the total population. We believe it would be possible to use our microfluidic system to rapidly identify bacterial populations with large growth rates and then more closely observe their behaviour. Finally, it would be interesting to determine why certain droplet populations are inhibited strongly by streptomycin whilst others are unaffected. This could be achieved by categorising droplet populations according to their growth behaviour and further investigating if a common trait or behaviour links these categories. This type of study benefits from the use of a microfluidic device such as ours that can study large numbers of near identical bacterial populations simultaneously, with a high degree of accuracy.

A source of experimental error that may have been inadvertently introduced during our research was in the use of streptomycin that had been refrozen after being allowed to thaw (see section 3.2.8 for further information). It has been shown that numerous classes of antibiotics can lose efficacy over time whilst stored frozen. Furthermore, thawing and then re-freezing antibiotics has been shown to additionally degrade the activity of certain antibiotics[217]. To ensure that this variability does not impact the reliability of future repeat studies, any antibiotics used should only be thawed once and then disposed of.

More generally, we believe our system successfully bridges the gap between microfluidic devices that can quickly extract rudimentary growth metrics from large numbers of small bacterial populations[43][131], and microfluidic devices that can extract detailed growth metrics and parameters from a small number of small bacterial populations[137]. We hope that the modular and adaptable nature of this

microfluidic system allow it to be used for a wide variety of biological applications. In its current form, testing is already underway that could allow the device to be used in conjunction with flow cytometry techniques to screen for growth in samples comprising bacteria that have proven difficult to culture using standard procedures.

I believe that microfluidic technology has the power to dramatically and positively impact a wide range of academic fields. The benefits afforded by microfluidic systems are too numerous and significant to ignore, and given time I hope that the incorporation of microfluidic systems into bacterial studies will accelerate research that has the very real possibility of improving the lives of people outside the laboratory. Despite this, there is still a sizable barrier to entry to the non-specialist academic who is interested in using microfluidic systems. Current research appears to be trending toward the design and use of increasingly elaborate and complex microfluidic systems, when the widespread adoption of microfluidic technology is still limited by a lack of accessible information and research. In this thesis, we have developed a microfluidic system that is accessible to the non-specialist, both in fabrication and operation. The two microfluidic devices that constitute the system are modular and adaptable, with exceptional bio-compatibility. Using our microfluidic system we have observed novel bacterial growth behaviours in the presence of antibiotic that would not have been possible to see using bulk growth techniques. Further development of our microfluidic system will focus on refining and further simplifying our current microfluidic design. This will allow us to better understand and more accurately quantify the interesting growth dynamics that we have observed in small bacterial populations inhibited by streptomycin.

The work conducted in this thesis demonstrates that exciting and novel biological phenomena can be accurately quantified using a microfluidic system that is easy to understand and simple to operate. We hope this work will inspire others to integrate microfluidic systems and processes into their experimental arsenal, furthering the widespread adoption of microfluidic technology.

Bibliography

[1] Losee L. Ling et al. “A new antibiotic kills pathogens without detectable resistance”. In: *Nature* 517.7535 (2015).

[2] Stuart B Levy. “Microbial Resistance to Antibiotics: An Evolving and Persistent Problem”. In: *The Lancet* 320.8289 (1982).

[3] Eili Y Klein et al. “Global increase and geographic convergence in antibiotic consumption between 2000 and 2015.” In: *Proceedings of the National Academy of Sciences of the United States of America* 115.15 (2018).

[4] Simon J Howard et al. “Antibiotic resistance: global response needed”. In: *The Lancet Infectious Diseases* 13.12 (2013).

[5] Trudy M. Wassenaar. *Bacteria : the Benign, the Bad, and the Beautiful*. Wiley-Blackwell, 2012.

[6] T Vellai and G Vida. “The origin of eukaryotes: the difference between prokaryotic and eukaryotic cells.” In: *Proceedings. Biological sciences* 266.1428 (1999).

[7] Petra Anne Levin and Esther R Angert. “Small but Mighty: Cell Size and Bacteria.” In: *Cold Spring Harbor perspectives in biology* 7.7 (2015).

[8] Kaoru Ikuma and Boris L. T. Lau. *The Extracellular Bastions of Bacteria - A Biofilm Way of Life*. Nature Education Knowledge 4(2):2, 2013.

[9] Fredrik Bäckhed et al. “Host-Bacterial Mutualism in the Human Intestine”. In: *Science* 307.5717 (2005).

[10] Jose Ruben Morones et al. “The bactericidal effect of silver nanoparticles”. In: *Nanotechnology* 16.10 (2005).

[11] J W Bartholomew and T Mittwer. “The Gram stain.” In: *Bacteriological reviews* 16.1 (1952).

[12] Richard Coico. “Gram Staining”. In: *Current Protocols in Microbiology*. Vol. 00. 1. John Wiley & Sons, Inc., 2005.

[13] George A O'Toole. "Classic Spotlight: How the Gram Stain Works." In: *Journal of bacteriology* 198.23 (2016).

[14] James B. Kaper, James P. Nataro, and Harry L. T. Mobley. "Pathogenic Escherichia coli". In: *Nature Reviews Microbiology* 2.2 (2004).

[15] F R Blattner et al. "The complete genome sequence of Escherichia coli K-12." In: *Science* 277.5331 (1997).

[16] Jon L. Hobman, Charles W. Penn, and Mark J. Pallen. "Laboratory strains of Escherichia coli: model citizens or deceitful delinquents growing old disgracefully?" In: *Molecular Microbiology* 64.4 (2007).

[17] Koji Hayashi et al. "Highly accurate genome sequences of Escherichia coli K-12 strains MG1655 and W3110." In: *Molecular systems biology* 2 (2006).

[18] M. Riley et al. "Escherichia coli K-12: a cooperatively developed annotation snapshot–2005". In: *Nucleic Acids Research* 34.1 (2006).

[19] K F Jensen. "The Escherichia coli K-12 "wild types" W3110 and MG1655 have an rph frameshift mutation that leads to pyrimidine starvation due to low pyrE expression levels." In: *Journal of Bacteriology* 175.11 (1993).

[20] Lei Wang, Quan Wang, and Peter R. Reeves. *The Variation of O Antigens in Gram-Negative Bacteria*. Subcellular Biochemistry, 53, Springer, Dordrecht, 2010.

[21] M Achtman and G Pluschke. "Clonal Analysis of Descent and Virulence Among Selected Escherichia Coli". In: *Annual Review of Microbiology* 40.1 (1986).

[22] Stephen J. Hagen. "Exponential growth of bacteria: Constant multiplication through division". In: *American Journal of Physics* 78.12 (2010).

[23] Keiran Stevenson et al. "General calibration of microbial growth in microplate readers". In: *Scientific Reports* 6.1 (2016).

[24] Peter Jurtshuk. *Bacterial Metabolism*. University of Texas Medical Branch at Galveston, 1996.

[25] B A Haddock and C W Jones. "Bacterial respiration." In: *Bacteriological reviews* 41.1 (1977).

[26] G. A. Pankey and L. D. Sabath. "Clinical Relevance of Bacteriostatic versus Bactericidal Mechanisms of Action in the Treatment of Gram-Positive Bacterial Infections". In: *Clinical Infectious Diseases* 38.6 (2004).

[27] Michael A. Kohanski et al. “A Common Mechanism of Cellular Death Induced by Bactericidal Antibiotics”. In: *Cell* 130.5 (2007).

[28] Rustam I. Aminov. “A Brief History of the Antibiotic Era: Lessons Learned and Challenges for the Future”. In: *Frontiers in Microbiology* 1 (2010).

[29] Saswati Sengupta, Madhab K. Chattopadhyay, and Hans-Peter Grossart. “The multifaceted roles of antibiotics and antibiotic resistance in nature”. In: *Frontiers in Microbiology* 4 (2013).

[30] Eric D. Brown and Gerard D. Wright. “Antibacterial drug discovery in the resistance era”. In: *Nature* 529.7586 (2016).

[31] Kim Lewis. “Recover the lost art of drug discovery”. In: *Nature* 485.7399 (2012).

[32] Jennifer M. Andrews. “Determination of minimum inhibitory concentrations”. In: *Journal of Antimicrobial Chemotherapy* 48.Suppl 1 (2001).

[33] Kyriacos C Nicolaou and Stephan Rigol. “A brief history of antibiotics and select advances in their synthesis”. In: *The Journal of Antibiotics* 71.2 (2018).

[34] Maya A. Farha and Eric D. Brown. “Unconventional screening approaches for antibiotic discovery”. In: *Annals of the New York Academy of Sciences* 1354.1 (2015).

[35] Stuart B Levy and Bonnie Marshall. “Antibacterial resistance worldwide: causes, challenges and responses”. In: *Nature Medicine* 10.12s (2004).

[36] Mary Barber and Mary Rozwadowska-Dowzenko. “Infection by Penicillin - Resistant Staphylococci”. In: *The Lancet* 252.6530 (1948).

[37] J. Crofton and D. A. Mitchison. “Streptomycin resistance in pulmonary tuberculosis.” In: *British medical journal* 2.4588 (1948).

[38] Stuart B. Levy. “Antibiotic Resistance: Consequences of Inaction”. In: *Clinical Infectious Diseases* 33.s3 (2001).

[39] T Tsuchido and M Takano. “Sensitization by heat treatment of Escherichia coli K-12 cells to hydrophobic antibacterial compounds.” In: *Antimicrobial agents and chemotherapy* 32.11 (1988).

[40] Christopher P Randall et al. “The target of daptomycin is absent from Escherichia coli and other gram-negative pathogens.” In: *Antimicrobial agents and chemotherapy* 57.1 (2013).

[41] Jessica M. A. Blair et al. “Molecular mechanisms of antibiotic resistance”. In: *Nature Reviews Microbiology* 13.1 (2015).

[42] Shangshang Qin et al. “Identification of a Novel Genomic Island Conferring Resistance to Multiple Aminoglycoside Antibiotics in Campylobacter coli”. In: *Antimicrobial Agents and Chemotherapy* 56.10 (2012).

[43] Fengjiao Lyu et al. “Phenotyping antibiotic resistance with single-cell resolution for the detection of heteroresistance”. In: *Sensors and Actuators B: Chemical* 270 (2018).

[44] Jacob Poehlsgaard and Stephen Douthwaite. “The bacterial ribosome as a target for antibiotics”. In: *Nature Reviews Microbiology* 3.11 (2005).

[45] J. M. Berg, J. L. Tymoczko, and L. Stryer. *Biochemistry. 5th edition.* W. H. Freeman & Co Ltd., 2002.

[46] Brian Søgaard Laursen et al. “Initiation of protein synthesis in bacteria.” In: *Microbiology and molecular biology reviews : MMBR* 69.1 (2005).

[47] Daniel N. Wilson. “Ribosome-targeting antibiotics and mechanisms of bacterial resistance”. In: *Nature Reviews Microbiology* 12.1 (2014).

[48] Philip Greulich et al. “Growth-dependent bacterial susceptibility to ribosome-targeting antibiotics.” In: *Molecular systems biology* 11.3 (2015).

[49] Douglas B. Murphy and Michael W. Davidson. *Fundamentals of Light Microscopy and Electronic Imaging.* Hoboken, NJ, USA: John Wiley & Sons, Inc., 2012.

[50] Jay L. Nadeau. *Introduction to experimental biophysics: biological methods for physical scientists.* CRC Press, 2017.

[51] Osamu Shimomura, Frank H. Johnson, and Yo Saiga. “Extraction, Purification and Properties of Aequorin, a Bioluminescent Protein from the Luminous Hydromedusan,Aequorea”. In: *Journal of Cellular and Comparative Physiology* 59.3 (1962).

[52] Guohong Zhang, Vanessa Gurtu, and Steven R. Kain. “An Enhanced Green Fluorescent Protein Allows Sensitive Detection of Gene Transfer in Mammalian Cells”. In: *Biochemical and Biophysical Research Communications* 227.3 (1996).

[53] Fan Yang, Larry G. Moss, and George N. Phillips. “The molecular structure of green fluorescent protein”. In: *Nature Biotechnology* 14.10 (1996).

[54] John Davison. “Genetic Exchange between Bacteria in the Environment”. In: *Plasmid* 42.2 (1999).

[55] W. Walthall et al. “Cell-cell interactions in the guidance of late-developing neurons in Caenorhabditis elegans”. In: *Science* 239.4840 (1988).

[56] Brendan P. Cormack, Raphael H. Valdivia, and Stanley Falkow. “FACS-optimized mutants of the green fluorescent protein (GFP)”. In: *Gene* 173.1 (1996).

[57] Oliver Scholz et al. “Quantitative analysis of gene expression with an improved green fluorescent protein”. In: *European Journal of Biochemistry* 267.6 (2000).

[58] S. James Remington. “Negotiating the speed bumps to fluorescence”. In: *Nature Biotechnology* 20.1 (2002).

[59] Robert E Campbell et al. “A monomeric red fluorescent protein.” In: *Proceedings of the National Academy of Sciences of the United States of America* 99.12 (2002).

[60] Adaobi Nwaneshiudu et al. “Introduction to Confocal Microscopy”. In: *Journal of Investigative Dermatology* 132.12 (2012).

[61] Michael J Rust, Mark Bates, and Xiaowei Zhuang. “Sub-diffraction-limit imaging by stochastic optical reconstruction microscopy (STORM)”. In: *Nature Methods* 3.10 (2006).

[62] Bo Huang et al. “Three-dimensional super-resolution imaging by stochastic optical reconstruction microscopy.” In: *Science* 319.5864 (2008).

[63] George M. Whitesides. “The origins and the future of microfluidics”. In: *Nature* 442.7101 (2006).

[64] Henrik Bruus. *Theoretical microfluidics*. Oxford University Press, 2008.

[65] Todd M. Squires and Stephen R. Quake. “Microfluidics: Fluid physics at the nanoliter scale”. In: *Reviews of Modern Physics* 77.3 (2005).

[66] E. M. Purcell. “Life at low Reynolds number”. In: *American Journal of Physics* 45.1 (1977).

[67] Kwang W. Oh et al. “Design of pressure-driven microfluidic networks using electric circuit analogy”. In: *Lab Chip* 12.3 (2012).

[68] Petra S. Dittrich and Andreas Manz. “Lab-on-a-chip: microfluidics in drug discovery”. In: *Nature Reviews Drug Discovery* 5.3 (2006).

[69] Johan Pihl, Mattias Karlsson, and Daniel T. Chiu. “Microfluidic technologies in drug discovery”. In: *Drug Discovery Today* 10.20 (2005).

[70] R. S. Ramsey And and J. M. Ramsey. “Generating Electrospray from Microchip Devices Using Electroosmotic Pumping”. In: *Analytical Chemistry* 69.6 (1997).

[71] Samuel M. Stavis et al. “Single molecule studies of quantum dot conjugates in a submicrometer fluidic channel”. In: *Lab on a Chip* 5.3 (2005).

[72] Petra S. Dittrich and Andreas Manz. “Single-molecule fluorescence detection in microfluidic channels—the Holy Grail in μTAS?” In: *Analytical and Bioanalytical Chemistry* 382.8 (2005).

[73] C. C. Lee. “Multistep Synthesis of a Radiolabeled Imaging Probe Using Integrated Microfluidics”. In: *Science* 310.5755 (2005).

[74] George M. Whitesides et al. “Soft Lithography in Biology and Biochemistry”. In: *Annual Review of Biomedical Engineering* 3.1 (2001).

[75] Douglas B. Weibel, Willow R. DiLuzio, and George M. Whitesides. “Microfabrication meets microbiology”. In: *Nature Reviews Microbiology* 5.3 (2007).

[76] T. M. Tran et al. “From tubes to drops: Droplet-based microfluidics for ultrahigh-throughput biology”. In: *Journal of Physics D: Applied Physics* 46.11 (2013).

[77] Chandra K. Dixit and Ajeet Kumar Kaushik. *Microfluidics for biologists: fundamentals and applications*. Springer International Publishing, 2016.

[78] Heekyung Jung, Myung-Suk Chun, and Mi-Sook Chang. “Sorting of human mesenchymal stem cells by applying optimally designed microfluidic chip filtration”. In: *The Analyst* 140.4 (2015).

[79] Adina Scott et al. “A microfluidic microelectrode array for simultaneous electrophysiology, chemical stimulation, and imaging of brain slices.” In: *Lab on a chip* 13.4 (2013).

[80] Kyung-Jin Jang and Kahp-Yang Suh. “A multi-layer microfluidic device for efficient culture and analysis of renal tubular cells”. In: *Lab Chip* 10.1 (2010).

[81] Ping Wang et al. “Robust Growth of Escherichia coli”. In: *Current Biology* 20.12 (2010).

[82] Burak Okumus, Sadik Yildiz, and Erdal Toprak. “Fluidic and microfluidic tools for quantitative systems biology”. In: *Current Opinion in Biotechnology* 25 (2014).

[83] Sung Sik Lee et al. “Whole lifespan microscopic observation of budding yeast aging through a microfluidic dissection platform.” In: *Proceedings of the National Academy of Sciences of the United States of America* 109.13 (2012).

[84] J. E. Keymer et al. “Bacterial metapopulations in nanofabricated landscapes”. In: *Proceedings of the National Academy of Sciences* 103.46 (2006).

[85] Q. Zhang et al. “Acceleration of Emergence of Bacterial Antibiotic Resistance in Connected Microenvironments”. In: *Science* 333.6050 (2011).

[86] V. Prasad P. B. Umbanhowar and D. A. Weitz. “Monodisperse Emulsion Generation via Drop Break Off in a Coflowing Stream”. In: *Langmuir* 16.2 (1999).

[87] G. F. Christopher and S. L. Anna. “Microfluidic methods for generating continuous droplet streams”. In: *Journal of Physics D: Applied Physics* 40.19 (2007).

[88] Chunfeng Zhou, Pengtao Yue, and James J. Feng. “Formation of simple and compound drops in microfluidic devices”. In: *Physics of Fluids* 18.9 (2006).

[89] Piotr Garstecki et al. “Formation of droplets and bubbles in a microfluidic T-junction - Scaling and mechanism of break-up”. In: *Lab on a Chip* 6.3 (2006).

[90] Shingo Okushima et al. “Controlled Production of Monodisperse Double Emulsions by Two-Step Droplet Breakup in Microfluidic Devices”. In: *Langmuir* 20.23 (2004).

[91] J. H. Xu et al. “Correlations of droplet formation in T-junction microfluidic devices: from squeezing to dripping”. In: *Microfluidics and Nanofluidics* 5.6 (2008).

[92] Todd Thorsen et al. “Dynamic Pattern Formation in a Vesicle-Generating Microfluidic Device”. In: *Physical Review Letters* 86.18 (2001).

[93] Luoran Shang, Yao Cheng, and Yuanjin Zhao. “Emerging Droplet Microfluidics”. In: *Chemical Reviews* 117.12 (2017).

[94] Shia Yen Teh et al. “Droplet microfluidics”. In: *Lab on a Chip* 8.2 (2008).

[95] Takasi Nisisako, Toru Torii, and Toshiro Higuchi. "Droplet formation in a microchannel network". In: *Lab Chip* 2.1 (2002).

[96] Charles N. Baroud, Francois Gallaire, and Rémi Dangla. "Dynamics of microfluidic droplets". In: *Lab on a Chip* 10.16 (2010).

[97] Gordon F. Christopher et al. "Experimental observations of the squeezing-to-dripping transition in T-shaped microfluidic junctions". In: *Physical Review E* 78.3 (2008).

[98] M. De Menech et al. "Transition from squeezing to dripping in a microfluidic T-shaped junction". In: *Journal of Fluid Mechanics* 595 (2008).

[99] Mario De Menech. "Modeling of droplet breakup in a microfluidic T-shaped junction with a phase-field model". In: *Physical Review E* 73.3 (2006).

[100] Volkert van Steijn, Michiel T. Kreutzer, and Chris R. Kleijn. "μ-PIV study of the formation of segmented flow in microfluidic T-junctions". In: *Chemical Engineering Science* 62.24 (2007).

[101] Maartje L. J. Steegmans, Karin G. P. H. Schroën, and Remko M. Boom. "Characterization of Emulsification at Flat Microchannel Y Junctions". In: *Langmuir* 25.6 (2009).

[102] Pierre Guillot and Annie Colin. "Stability of parallel flows in a microchannel after a T junction". In: *Physical Review E* 72.6 (2005).

[103] Woon Seob Lee et al. "Predictive model on micro droplet generation through mechanical cutting". In: *Microfluidics and Nanofluidics* 7.3 (2009).

[104] Krzysztof Churski, Jacek Michalski, and Piotr Garstecki. "Droplet on demand system utilizing a computer controlled microvalve integrated into a stiff polymeric microfluidic device". In: *Lab Chip* 10.4 (2010).

[105] S. M. Sohel Murshed et al. "Microdroplet formation of water and nanofluids in heat-induced microfluidic T-junction". In: *Microfluidics and Nanofluidics* 6.2 (2009).

[106] Piotr Garstecki et al. "Formation of monodisperse bubbles in a microfluidic flow-focusing device". In: *Applied Physics Letters* 85.13 (2004).

[107] Shelley L. Anna and Hans C. Mayer. "Microscale tipstreaming in a microfluidic flow focusing device". In: *Physics of Fluids* 18.12 (2006).

[108] Ashleigh B. Theberge et al. “Microdroplets in microfluidics: An evolving platform for discoveries in chemistry and biology”. In: *Angewandte Chemie - International Edition* 49.34 (2010).

[109] A. S. Utada et al. “Monodisperse Double Emulsions Generated from a Microcapillary Device”. In: *Science* 308.5721 (2005).

[110] Thomas Ward et al. “Microfluidic flow focusing: Drop size and scaling in pressure versus flow-rate-driven pumping”. In: *Electrophoresis* 26.19 (2005).

[111] Ralf Seemann et al. “Droplet based microfluidics”. In: *Reports on Progress in Physics* 75.1 (2012).

[112] B Rotman. “Measurement of activity of single molecules of beta - D - galactosidase.” In: *Proceedings of the National Academy of Sciences of the United States of America* 47.12 (1961).

[113] Dan S. Tawfik and Andrew D. Griffiths. “Man-made cell-like compartments for molecular evolution”. In: *Nature Biotechnology* 16.7 (1998).

[114] Venkatachalam Chokkalingam et al. “Optimized droplet-based microfluidics scheme for sol–gel reactions”. In: *Lab on a Chip* 10.13 (2010).

[115] Max Chabert, Kevin D. Dorfman, and Jean-Louis Viovy. “Droplet fusion by alternating current (AC) field electrocoalescence in microchannels”. In: *Electrophoresis* 26.19 (2005).

[116] Assaf Rotem et al. “Single-cell ChIP-seq reveals cell subpopulations defined by chromatin state”. In: *Nature Biotechnology* 33.11 (2015).

[117] Craig Priest, Stephan Herminghaus, and Ralf Seemann. “Controlled electrocoalescence in microfluidics: Targeting a single lamella”. In: *Applied Physics Letters* 89.13 (2006).

[118] Jae-Hoon Choi et al. “Designed pneumatic valve actuators for controlled droplet breakup and generation”. In: *Lab on a Chip* 10.4 (2010).

[119] Helen Song et al. “On-Chip Titration of an Anticoagulant Argatroban and Determination of the Clotting Time within Whole Blood or Plasma Using a Plug-Based Microfluidic System”. In: *Analytical Chemistry* 78.14 (2006).

[120] K. I. Sotowa et al. “Droplet Formation by the Collision of Two Aqueous Solutions in a Microchannel and Application to Particle Synthesis”. In: *Chemical Engineering & Technology* 30.3 (2007).

[121] Batoul Ahmed, David Barrow, and Thomas Wirth. “Enhancement of Reaction Rates by Segmented Fluid Flow in Capillary Scale Reactors”. In: *Advanced Synthesis & Catalysis* 348.9 (2006).

[122] Jeffrey D Winterton et al. “A novel continuous microfluidic reactor design for the controlled production of high-quality semiconductor nanocrystals”. In: *Journal of Nanoparticle Research* 10.6 (2008).

[123] Lucas Frenz et al. “Droplet-Based Microreactors for the Synthesis of Magnetic Iron Oxide Nanoparticles”. In: *Angewandte Chemie International Edition* 47.36 (2008).

[124] Alan Dove. “Drug screening—beyond the bottleneck”. In: *Nature Biotechnology* 17.9 (1999).

[125] Jean-Christophe Baret et al. “Fluorescence-activated droplet sorting (FADS): efficient microfluidic cell sorting based on enzymatic activity”. In: *Lab on a Chip* 9.13 (2009).

[126] Balint Kintses et al. “Microfluidic droplets: New integrated workflows for biological experiments”. In: *Current Opinion in Chemical Biology* 14.5 (2010).

[127] Jeremy J Agresti et al. “Ultrahigh-throughput screening in drop-based microfluidics for directed evolution.” In: *Proceedings of the National Academy of Sciences of the United States of America* 107.9 (2010).

[128] Kary B. Mullis and Fred A. Faloona. “[21] Specific synthesis of DNA in vitro via a polymerase-catalyzed chain reaction”. In: *Methods in Enzymology* 155 (1987).

[129] Yonghao Zhang and Hui-Rong Jiang. “A review on continuous-flow microfluidic PCR in droplets: Advances, challenges and future”. In: *Analytica Chimica Acta* 914 (2016).

[130] Helena Zec, Dong Jin Shin, and Tza-Huei Wang. “Novel droplet platforms for the detection of disease biomarkers”. In: *Expert Review of Molecular Diagnostics* 14.7 (2014).

[131] Witold Postek et al. “Microfluidic screening of antibiotic susceptibility at a single-cell level shows the inoculum effect of cefotaxime on E. coli”. In: *Lab on a Chip* 18.23 (2018).

[132] Evelien W. M. Kemna et al. “High-yield cell ordering and deterministic cell-in-droplet encapsulation using Dean flow in a curved microchannel”. In: *Lab on a Chip* 12.16 (2012).

[133] David J. Collins et al. “The Poisson distribution and beyond: methods for microfluidic droplet production and single cell encapsulation”. In: *Lab on a Chip* 15.17 (2015).

[134] Max Chabert and Jean-Louis Viovy. “Microfluidic high-throughput encapsulation and hydrodynamic self-sorting of single cells.” In: *Proceedings of the National Academy of Sciences of the United States of America* 105.9 (2008).

[135] Tengyang Jing et al. “Jetting microfluidics with size-sorting capability for single-cell protease detection”. In: *Biosensors and Bioelectronics* 66 (2015).

[136] Jung-uk Shim et al. “Simultaneous Determination of Gene Expression and Enzymatic Activity in Individual Bacterial Cells in Microdroplet Compartments”. In: *Journal of the American Chemical Society* 131.42 (2009).

[137] Pooja Sabhachandani et al. “Integrated microfluidic platform for rapid antimicrobial susceptibility testing and bacterial growth analysis using bead-based biosensor via fluorescence imaging”. In: *Microchimica Acta* 184.12 (2017).

[138] Sarah Köster et al. “Drop-based microfluidic devices for encapsulation of single cells”. In: *Lab on a Chip* 8.7 (2008).

[139] Amir Aharoni et al. “High-throughput screening methodology for the directed evolution of glycosyltransferases”. In: *Nature Methods* 3.8 (2006).

[140] Evan Z. Macosko et al. “Highly Parallel Genome-wide Expression Profiling of Individual Cells Using Nanoliter Droplets”. In: *Cell* 161.5 (2015).

[141] Rapolas Zilionis et al. “Single-cell barcoding and sequencing using droplet microfluidics”. In: *Nature Protocols* 12.1 (2017).

[142] Grace X. Y. Zheng et al. “Massively parallel digital transcriptional profiling of single cells”. In: *Nature Communications* 8.1 (2017).

[143] Xiannian Zhang et al. “Comparative Analysis of Droplet-Based Ultra-High-Throughput Single-Cell RNA-Seq Systems”. In: *Molecular Cell* 73.1 (2019).

[144] I Brook. “Inoculum effect.” In: *Reviews of infectious diseases* 11.3 (1989).

[145] Rajendrani Mukhopadhyay. “When PDMS isn’t the best”. In: *Analytical Chemistry* 79.9 (2007).

[146] Samuel K. Sia and George M. Whitesides. “Microfluidic devices fabricated in poly(dimethylsiloxane) for biological studies”. In: *Electrophoresis* 24.21 (2003).

[147] Cheolmin Park Jessamine Ng Lee and George M. Whitesides. “Solvent Compatibility of Poly(dimethylsiloxane)-Based Microfluidic Devices”. In: *Analytical Chemistry* 75.23 (2003).

[148] C. Holtze et al. “Biocompatible surfactants for water-in-fluorocarbon emulsions”. In: *Lab on a Chip* 8.10 (2008).

[149] Jean Christophe Baret. “Surfactants in droplet-based microfluidics”. In: *Lab on a Chip* 12.3 (2012).

[150] Helen Song L. Spencer Roach and Rustem F. Ismagilov. “Controlling Nonspecific Protein Adsorption in a Plug-Based Microfluidic System by Controlling Interfacial Chemistry Using Fluorous-Phase Surfactants”. In: (2004).

[151] Jenifer Clausell-Tormos et al. “Droplet-Based Microfluidic Platforms for the Encapsulation and Screening of Mammalian Cells and Multicellular Organisms”. In: *Chemistry and Biology* 15.5 (2008).

[152] Linas Mazutis et al. “Single-cell analysis and sorting using droplet-based microfluidics”. In: *Nature Protocols* 8.5 (2013).

[153] Masahito Hosokawa et al. “Droplet-based microfluidics for high-throughput screening of a metagenomic library for isolation of microbial enzymes”. In: *Biosensors and Bioelectronics* 67 (2015).

[154] Trinh Lam et al. “Femtoliter droplet confinement of Streptococcus pneumoniae: bacterial genetic transformation by cell–cell interaction in droplets”. In: *Lab on a Chip* 19.4 (2019).

[155] Minsoung Rhee et al. “Versatile on-demand droplet generation for controlled encapsulation”. In: *Biomicrofluidics* 8.3 (2014).

[156] Xin LI et al. *PicoSurf Patent (WO2017203280)*. 2017.

[157] Takasi Nisisako, Shingo Okushima, and Toru Torii. “Controlled formulation of monodisperse double emulsions in a multiple-phase microfluidic system”. In: *Soft Matter* 1.1 (2005).

[158] Dhananjay Bodas and Chantal Khan-Malek. “Hydrophilization and hydrophobic recovery of PDMS by oxygen plasma and chemical treatment—An SEM investigation”. In: *Sensors and Actuators B: Chemical* 123.1 (2007).

[159] Say Hwa Tan et al. “Oxygen plasma treatment for reducing hydrophobicity of a sealed polydimethylsiloxane microchannel”. In: *Biomicrofluidics* 4.3 (2010).

[160] Michael J. Owen and Patrick J. Smith. “Plasma treatment of polydimethylsiloxane”. In: *Journal of Adhesion Science and Technology* 8.10 (1994).

[161] H. Hillborg et al. “Crosslinked polydimethylsiloxane exposed to oxygen plasma studied by neutron reflectometry and other surface specific techniques”. In: *Polymer* 41.18 (2000).

[162] S. Bhattacharya et al. “Studies on surface wettability of poly(dimethyl) siloxane (PDMS) and glass under oxygen-plasma treatment and correlation with bond strength”. In: *Journal of Microelectromechanical Systems* 14.3 (2005).

[163] Dhananjay Bodas and Chantal Khan-Malek. “Formation of more stable hydrophilic surfaces of PDMS by plasma and chemical treatments”. In: *Microelectronic Engineering* 83.4-9 (2006).

[164] Stefano Begolo et al. “New family of fluorinated polymer chips for droplet and organic solvent microfluidics”. In: *Lab Chip* 11.3 (2011).

[165] Carson T. Riche et al. “Fluoropolymer surface coatings to control droplets in microfluidic devices”. In: *Lab Chip* 14.11 (2014).

[166] Adam R. Abate et al. “Glass coating for PDMS microfluidic channels by sol–gel methods”. In: *Lab on a Chip* 8.4 (2008).

[167] Steve C. C. Shih et al. “A droplet-to-digital (D2D) microfluidic device for single cell assays”. In: *Lab on a Chip* 15.1 (2015).

[168] Diarmuid P. Lloyd and Rosalind J. Allen. “Competition for space during bacterial colonization of a surface”. In: *Journal of The Royal Society Interface* 12.110 (2015).

[169] Elise Darmon et al. “Repair on the Go: E. coli Maintains a High Proliferation Rate while Repairing a Chronic DNA Double-Strand Break”. In: *PLoS ONE* 9.10 (2014).

[170] Michael B. Elowitz et al. “Stochastic gene expression in a single cell.” In: *Science* 297.5584 (2002).

[171] Lourdes Cabrera Yun-Seok Heo and Shuichi Takayama. “Characterization and Resolution of Evaporation-Mediated Osmolality Shifts That Constrain Microfluidic Cell Culture in Poly(dimethylsiloxane) Devices”. In: *Analytical Chemistry* 79.3 (2007).

[172] Sadettin S. Ozturk and Bernhard O. Palsson. “Effect of medium osmolarity on hybridoma growth, metabolism, and antibody production”. In: *Biotechnology and Bioengineering* 37.10 (1991).

[173] J Lin et al. “Enhanced monoclonal antibody production by gradual increase of osmotic pressure.” In: *Cytotechnology* 29.1 (1999).

[174] Jonathan Shemesh et al. “Stationary nanoliter droplet array with a substrate of choice for single adherent/nonadherent cell incubation and analysis.” In: *Proceedings of the National Academy of Sciences of the United States of America* 111.31 (2014).

[175] NE-1002X Programmable Microfluidics Syringe Pump Product Page (accessed 02-03-19). *http://www.syringepump.com/Micro.php*.

[176] Mark A Eddings, Michael A Johnson, and Bruce K Gale. “Determining the optimal PDMS–PDMS bonding technique for microfluidic devices”. In: *Journal of Micromechanics and Microengineering* 18.6 (2008).

[177] David C. Duffy et al. “Rapid Prototyping of Microfluidic Systems in Poly(dimethylsiloxane)”. In: *Analytical Chemistry* 70.23 (1998).

[178] Da Yang et al. “Analysis of Factors Limiting Bacterial Growth in PDMS Mother Machine Devices.” In: *Frontiers in microbiology* 9 (2018).

[179] Metafluidics - open repository for fluidic systems (accessed 29-08-19). *https://metafluidics.org/*.

[180] KLayout documentation and user manual (accessed 16-07-19). *https://www.klayout.de/doc.html*.

[181] Emmanuel Delamarche et al. “Stability of molded polydimethylsiloxane microstructures”. In: *Advanced Materials* 9.9 (1997).

[182] Younan Xia and George M. Whitesides. “Soft Lithography”. In: *Annual Review of Materials Science* 28.1 (1998).

[183] Michelle R Bringer et al. “Microfluidic systems for chemical kinetics that rely on chaotic mixing in droplets.” In: *Philosophical transactions. Series A, Mathematical, physical, and engineering sciences* 362.1818 (2004).

[184] M. Schwertner, M. J. Booth, and T. Wilson. “Specimen-induced distortions in light microscopy”. In: *Journal of Microscopy* 228.1 (2007).

[185] I. D. Vladescu et al. “Filling an emulsion drop with motile bacteria”. In: *Physical Review Letters* 113.26 (2014).

[186] 3M Fluorinert Electronic Liquid FC-40 Product Information (accessed 29-08-19). *https://multimedia.3m.com/mws/media/64888O/fluorinert-electronic-liquid-fc-40.pdf*.

[187] Vladimír Ulman et al. "An objective comparison of cell-tracking algorithms". In: *Nature Methods* 14.12 (2017).

[188] Jonathan W. Young et al. "Measuring single-cell gene expression dynamics in bacteria using fluorescence time-lapse microscopy". In: *Nature Protocols* 7.1 (2012).

[189] Adrien Ducret, Ellen M. Quardokus, and Yves V. Brun. "MicrobeJ, a tool for high throughput bacterial cell detection and quantitative analysis". In: *Nature Microbiology* 1.7 (2016).

[190] J. Klein et al. "TLM-Tracker: software for cell segmentation, tracking and lineage analysis in time-lapse microscopy movies". In: *Bioinformatics* 28.17 (2012).

[191] Robert S Fischer et al. "Microscopy in 3D: a biologist's toolbox." In: *Trends in cell biology* 21.12 (2011).

[192] MATLAB 2019a documentation (accessed 16-07-19). *https://uk.mathworks.com/help/images/ref/imfindcircles.html*.

[193] Rafael C. Gonzalez, Richard E. Woods, and Steven L. Eddins. *Digital Image processing using MATLAB*. McGraw Hill, 2011.

[194] HK Yuen et al. "Comparative study of Hough Transform methods for circle finding". In: *Image and Vision Computing* 8.1 (1990).

[195] John C. Crocker and David G. Grier. "Methods of Digital Video Microscopy for Colloidal Studies". In: *Journal of Colloid and Interface Science* 179.1 (1996).

[196] Jana Schwarz-Linek et al. "Escherichia coli as a model active colloid: A practical introduction". In: *Colloids and Surfaces B: Biointerfaces* 137 (2016).

[197] Begoña Heras et al. "The antigen 43 structure reveals a molecular Velcro-like mechanism of autotransporter-mediated bacterial clumping." In: *Proceedings of the National Academy of Sciences of the United States of America* 111.1 (2014).

[198] H Hasman, T Chakraborty, and P Klemm. "Antigen-43-mediated autoaggregation of Escherichia coli is blocked by fimbriation." In: *Journal of bacteriology* 181.16 (1999).

[199] S. Takeuchi et al. “An Axisymmetric Flow-Focusing Microfluidic Device”. In: *Advanced Materials* 17.8 (2005).

[200] W.-H. Tan and S. Takeuchi. “Monodisperse Alginate Hydrogel Microbeads for Cell Encapsulation”. In: *Advanced Materials* 19.18 (2007).

[201] Craig Watson et al. “Reduced adhesion between cells and substrate confers selective advantage in bacterial colonies”. In: *EPL (Europhysics Letters)* 123.6 (2018).

[202] James Q. Boedicker, Meghan E. Vincent, and Rustem F. Ismagilov. “Microfluidic confinement of single cells of bacteria in small volumes initiates high-density behavior of quorum sensing and growth and reveals its variability”. In: *Angewandte Chemie - International Edition* 48.32 (2009).

[203] Gerardo Cárcamo-Oyarce et al. “Quorum sensing triggers the stochastic escape of individual cells from Pseudomonas putida biofilms”. In: *Nature Communications* 6 (2015).

[204] Cheng-Feng Chiang et al. “Green Fluorescent Protein Rendered Susceptible to Proteolysis: Positions for Protease-Sensitive Insertions”. In: *Archives of Biochemistry and Biophysics* 394.2 (2001).

[205] Erik Lee Snapp. “Fluorescent proteins: a cell biologist’s user guide.” In: *Trends in cell biology* 19.11 (2009).

[206] J B Andersen et al. “New unstable variants of green fluorescent protein for studies of transient gene expression in bacteria.” In: *Applied and environmental microbiology* 64.6 (1998).

[207] X Li et al. “Generation of destabilized green fluorescent protein as a transcription reporter.” In: *The Journal of biological chemistry* 273.52 (1998).

[208] Lina Boulos et al. “LIVE/DEAD® BacLight™: application of a new rapid staining method for direct enumeration of viable and total bacteria in drinking water”. In: *Journal of Microbiological Methods* 37.1 (1999).

[209] Michael Berney et al. “Assessment and interpretation of bacterial viability by using the LIVE/DEAD BacLight Kit in combination with flow cytometry.” In: *Applied and environmental microbiology* 73.10 (2007).

[210] G Nebe-von-Caron et al. “Analysis of bacterial function by multi-colour fluorescence flow cytometry and single cell sorting”. In: *Journal of Microbiological Methods* 42.1 (2000).

[211] Fabien Joux and Philippe Lebaron. “Use of fluorescent probes to assess physiological functions of bacteriaat single-cell level”. In: *Microbes and Infection* 2.12 (2000).

[212] Sephra N Rampersad. “Multiple applications of Alamar Blue as an indicator of metabolic function and cellular health in cell viability bioassays.” In: *Sensors (Basel, Switzerland)* 12.9 (2012).

[213] S. Sieuwerts et al. “A simple and fast method for determining colony forming units”. In: *Letters in Applied Microbiology* 47.4 (2008).

[214] Silvio D. Brugger et al. “Automated Counting of Bacterial Colony Forming Units on Agar Plates”. In: *PLoS ONE* 7.3 (2012). Ed. by Stefan Bereswill.

[215] B D Davis. “Mechanism of bactericidal action of aminoglycosides.” In: *Microbiological reviews* 51.3 (1987).

[216] Diarmuid Padraig Lloyd. “Microscopic studies of surface growing bacterial populations”. PhD thesis. 2015.

[217] Lieve Okerman, Johan Van Hende, and Lieven De Zutter. “Stability of frozen stock solutions of beta-lactam antibiotics, cephalosporins, tetracyclines and quinolones used in antibiotic residue screening and antibiotic susceptibility testing”. In: *Analytica Chimica Acta* 586.1-2 (2007).